LBL-38492
UC-401

Lawrence Berkeley Laboratory
UNIVERSITY OF CALIFORNIA

Accelerator & Fusion Research Division

Development of a High-Resolution Soft X-Ray (30 - 1500 eV) Beamline at the Advanced Light Source and Its Use for the Study of Angle-Resolved Photoemission Extended Fine Structure

W.R.A. Huff
(Ph.D. Thesis)

February 1996

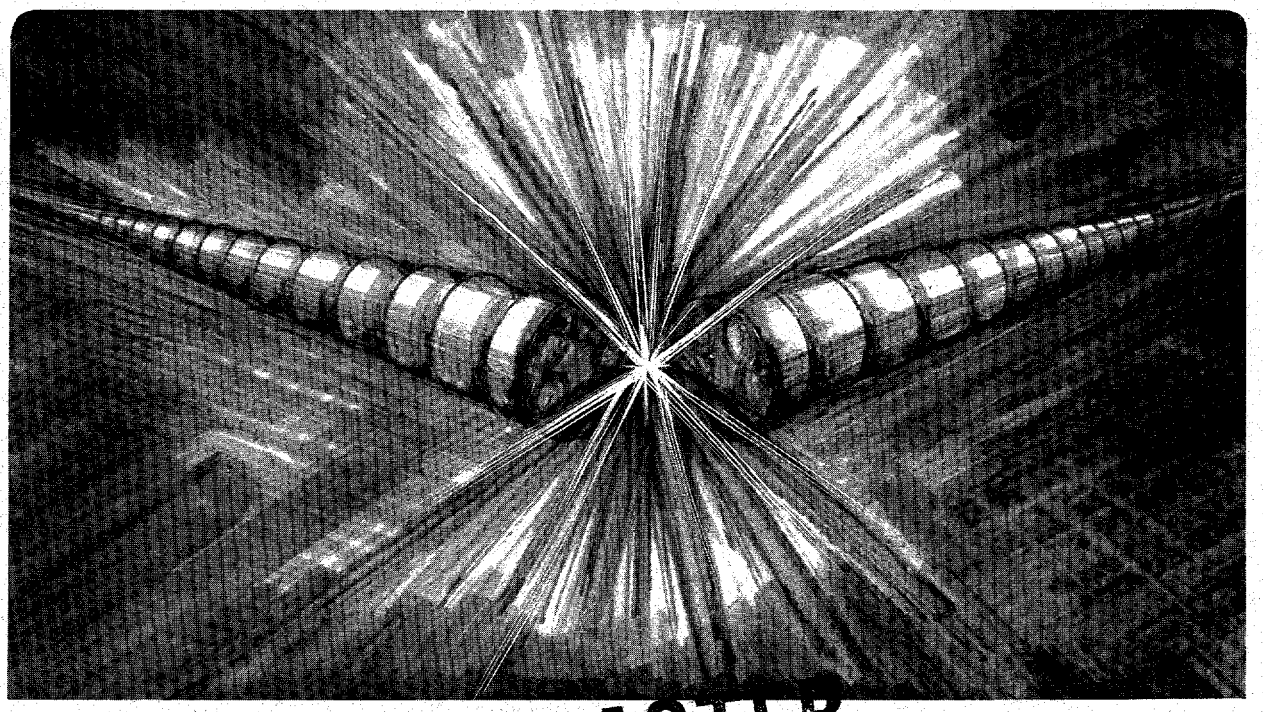

Prepared for the U.S. Department of Energy under Contract Number DE-AC03-76SF00098

LBL-38492
LSBL-317
UC-401

DEVELOPMENT OF A HIGH-RESOLUTION SOFT X-RAY (30 - 1500 EV) BEAMLINE AT THE ADVANCED LIGHT SOURCE AND ITS USE FOR THE STUDY OF ANGLE-RESOLVED PHOTOEMISSION EXTENDED FINE STRUCTURE*

Welcome Rex Anthony Huff
Ph.D. Thesis

DEPARTMENT OF CHEMISTRY
University of California, Berkeley

and

Accelerator Fusion and Research Division
Ernest Orlando Lawrence Berkeley National Laboratory
University of California
Berkeley, CA 94720

FEBRUARY 1996

*This work was supported by the Director, Office of Energy Research, Office of Basic Energy Sciences, Chemical Sciences Division, of the U.S. Department of Energy, under Contract No. DE-AC03-76SF00098.

Development of a High-Resolution Soft X-Ray (30 - 1500 eV) Beamline at the Advanced Light Source and its use for the Study of Angle-Resolved Photoemission Extended Fine Structure

by

Welcome Rex Anthony Huff

B.S. (Indiana University) 1989

A dissertation submitted in partial satisfaction of the

requirements for the degree of

Doctor of Philosophy

in

Chemistry

of the

GRADUATE DIVISION

of the

UNIVERSITY of CALIFORNIA, BERKELEY

Committee in Charge:

Professor David A. Shirley, Chair
Professor A. Paul Alivisatos, Co-Chair
Professor Gabor A. Somorjai
Professor Zahid Hussain
Professor David T. Attwood

1996

Development of a High-Resolution Soft X-Ray (30 - 1500 eV) Beamline at the Advanced Light Source and Its Use for the Study of Angle-Resolved Photoemission Extended Fine Structure

by

Welcome Rex Anthony Huff

ABSTRACT

Development of a High-Resolution Soft X-Ray (30 - 1500 eV) Beamline at the Advanced Light Source and its use for the Study of Angle-Resolved Photoemission Extended Fine Structure

by

Welcome Rex Anthony Huff

Doctor of Philosophy in Chemistry

University of California, Berkeley

Professor David A. Shirley, Chair

Bending magnet beamline 9.3.2 at the ALS was designed for high resolution spectroscopy with the capability for delivering circularly polarized light. The fixed included-angle SGM uses three gratings to access photon energies from 30 - 1500 eV. Circularly polarized radiation is obtained by inserting an aperture to select the beam above or below the horizontal plane. The photocurrent from the upper and lower jaws of the entrance slit sets a Piezoelectric drive feedback loop on the vertically deflecting mirror to maintain a stable beam intensity. The end station has a movable platform enabling the synchrotron radiation to be directed to either chamber without breaking vacuum.

With photoemission data collected at the Stanford Synchrotron Radiation Laboratory, the structure of c(2x2)P/Fe(100) was determined using angle-resolved photoemission extended fine structure (ARPEFS). The data were collected normal and 45° off-normal from the (100) surface. Multiple-scattering spherical-wave (MSSW) calculations indicate that the P

atoms adsorb in four-fold hollow sites 1.02 Å above the first Fe layer. Self-consistent-field Xα scattered wave calculation results agree with this c(2x2)P/Fe(100) and the previously published c(2x2)S/Fe(100) structures, confirming the ARPEFS determination that the Fe_1-Fe_2 spacing is contracted for S/Fe but not for P/Fe. These structures are compared to atomic nitrogen and atomic oxygen adsorbed on Fe(100).

Final-state effects on ARPEFS curves were studied using previously published data from the S 1*s* and 2*p* core-levels of c(2x2)S/Ni(001). The curves are similar and ~180° out of phase; the Fourier transforms (FTs) are quite different. A Generalized Ramsauer-Townsend splitting is present in the 1*s* but not the 2*p* data. Based on MSSW calculations, an approximate method for analyzing ARPEFS data from a non-*s* initial-state using only the higher-ℓ partial wave was proposed and successfully tested.

ARPEFS data from clean surfaces were collected normal to Ni(111) (3*p* core-levels) and 5° off-normal from Cu(111) (3*s* and 3*p* core-levels). The two Cu curves are similar and ~180° out of phase. The FTs of these ARPEFS data resemble adsorbate systems, showing backscattering signals from atoms up to four layers below the emitters. The 3*p* FTs show scattering from the six nearest neighbors in the same crystal layer as the emitters. MSSW calculation results indicate that the Cu 3*p* photoemission intensity has mostly *d*-wave character. Evidence was seen in the FTs for double-scattering and for single-scattering from laterally distant atoms. Calculations indicate that the signal is dominated by photoemission from the first two crystal layers.

TABLE OF CONTENTS

LIST OF TABLES

LIST OF FIGURES

ACKNOWLEDGMENTS

This work has been completed with the assistance of many people. Dave Shirley and Zahid Hussain have been excellent advisors throughout my entire graduate school life. Eddie Moler and Scot Kellar have been helpful and supportive from the data collection to the manuscript completion. Yu Zheng and Yufeng Chen have offered great assistance with the theoretical modeling and interpretation of the results. Pat McKean insured the safe and successful beamline move and reassembly. Without the help of these people, there is no doubt that I would not have completed this work.

Special thanks must also be given to Barry Petersen and Ajith Kaduwela for many helpful discussions regarding photoelectron holography and electron scattering. Chuck Fadley and his group as well as Shirley Group members too numerous to mention have contributed to this work.

The experiments were performed at the Stanford Synchrotron Radiation Laboratory, the National Synchrotron Light Source, and the Advanced Light Source. These synchrotron radiation facilities are supported by the Department of Energy's Office of Basic Energy Sciences. At each of these facilities, Lou Terminello has freely offered his assistance experimentally and scientifically. Also, Joe Katz has been instrumental in the completion of each experiment, if not in person then in spirit.

Much of the success of BL 9.3.2 is due to the financial, technical, and engineering assistance of the Advanced Light Source. The generous technical staff was key to the beamline assembly and operation. This work was supported by the Director, Office of Energy Research, Office of Basic Energy Sciences, Chemical Sciences Division of the U.S. Department of Energy under Contract No. DE-AC03-76SF00098.

Chapter 1

High-Resolution Soft X-Ray ($h\nu$ = 30 - 1500 eV) Bending Magnet Beamline 9.3.2 with Circularly Polarized Radiation Capability at the Advanced Light Source: Design, Performance, and Operation

ABSTRACT

Bending magnet beamline 9.3.2 at the Advanced Light Source (ALS) was designed for high resolution spectroscopy with the capability for delivering circularly polarized light. The monochromator is a fixed included-angle SGM having three interchangeable gratings to access photon energies from 30 eV to 1500 eV. A Kirkpatrick-Baez configuration is used to deflect the beam to the monochromator. The water-cooled pre-mirror is a horizontally deflecting ($2\theta = 5°$) tangential cylinder collecting 7.5 mrads of the horizontal radiation fan and focusing it near the exit slit of the monochromator. The vertically diverging radiation is collected by a vertically deflecting spherical mirror ($2\theta = 5°$) accepting 1.2 mrad of vertical radiation and focuses onto the entrance slit of the monochromator with a 0.60 magnification.

Circularly polarized radiation is obtained by inserting a water-cooled movable aperture in front of the vertically focusing mirror to allow selecting the beam either above or below the horizontal plane. To maintain a stable beam intensity through the entrance slit, the photocurrent signals from the upper and lower jaws of the entrance slit are utilized to set a feedback loop with a Piezoelectric drive on the vertically deflecting mirror. The beamline end station has a movable platform that accommodates two experimental chambers and enables the synchrotron radiation to be directed to either one of the two experimental chambers without breaking vacuum.

I. INTRODUCTION

BL 9.3.2 is a Rowland circle SGM installed on a bending magnet at the Advance Light Source (ALS), Lawrence Berkeley National Laboratory.[1,2] Originally BL 6-1 on a 55-pole wiggler at SSRL, BL 9.3.2 was developed as a prototype for insertion device monochromators at the ALS.[3] Heimann et al.[4] describe the beamline design and performance while installed at SSRL.

For operations at the ALS, the plane horizontally deflecting premirror and the toroidal vertically deflecting mirror[3] were replaced with a Kirkpatrick-Baez configuration of two separate, crossed mirrors.[5,6] The Kirkpatrick-Baez configuration allows for minimizing the optical aberrations by using a single mirror for the horizontal focusing and a separate, single mirror for the vertical focusing. The horizontally deflecting cylindrical pre-mirror focuses in the horizontal plane ~19 m from the mirror, which is ~3 m upstream from the center of the exit slit (S2) travel. The Kirkpatrick-Baez configuration is completed by the vertically deflecting spherical mirror (comparatively very high precision) focusing in the vertical plane 8.4 m downstream from this mirror which is at the center of the entrance slit (S1) travel. See figures 1 and 2.

Each slit is based on a flexure design allowing a side-driven micrometer to push the jaws open vertically against spring tension continuously from ≤3 μm to 1500 μm. The jaws are maintained parallel (within ±1 mrad) over the full horizontal width of the beam, ≤10 mm. Both slits, S1 and S2, are translatable along the beam path by 600 mm and 1000 mm, respectively. This allows the Rowland circle condition to be satisfied over a wide energy range. The focus condition can be satisfied over the

entire energy range of the monochromator. Note that this is a fixed included-angle SGM. An alternate design is a variable included-angle SGM, but such monochromators do not conform to the Rowland circle geometry.[7]

Using one of three gratings, the accessible energy range is 30 eV to 1500 eV. The gratings are kinematically mounted onto a carriage attached to a rail by ball bearing rollers and their rotation is monitored with a laser interferometer.[3] Each spherical grating is designed to have a 55 m radius. The fixed included angle is 174°.

The refocusing mirror is a bendable cylinder with a fixed small (sagittal) radius (10 cm) and an adjustable large (meridian) radius (80 m - ∞). The bending mechanism is based on a design by Howells[8] and will allow for moving the meridian focus from 1.5 m to ∞ downstream of the refocusing mirror.

Section II of this work discusses the monochromator optics and section III discusses the monochromator slits. Section IV discusses several improvements made to the beamline during its construction at the ALS. Section V discusses some photon beam stability considerations. Appendix A gives a summary of the quality of each optical element as well as the manufacturers and materials used. Appendix B steps through the foci calculations for M1, M2, and M3. Appendix C steps through the monochromator focus calculations for the Rowland circle condition and the focus condition as well as applies the contribution of the important optical aberrations to the monochromator resolution.[9-11] Appendix D presents circular polarization calculations and measurements. Appendix E presents ray tracing calculation results to illustrate the beam image at the sample for each grating. Finally, Appendix F discusses the beamline control systems.

II. OPTICS

Figure 1 is a schematic of the beamline which operates under ultra-high vacuum and has a base pressure better than 60 nPa($\sim 5\times10^{-10}$ torr or $\sim 6\times10^{-10}$ mbar). For earthquake safety, the vacuum chambers are supported by the ALS orthogonal six-strut system designed to withstand 1 g of lateral acceleration (0.7 g is the ALS requirement). The stands for the mirrors and slits have a first vibrational mode higher than 30 Hz.

The grating tank stand legs are 30 cm outer diameter with a 2.5 cm wall thickness and are filled with water for thermal stability. The grating tank stand was only partially redesigned in moving to the ALS and the first mode of vibration is 23 Hz. All six struts supporting the grating tank, as well as the vertical struts of S1 and S2, are made of invar for stable energy calibration and reproducibility.

Fiducial points on each optical component are referenced to points on each respective vacuum tank for alignment. The ALS Surveyors aligned the optics to within 100 μm of the desired position based on ray tracing analyses of the beamline. Further alignment was completed by measuring the $N_{2(g)}$ $1s$ to π^* resonance to monitor the resolution as well as scanning the intensity at various points along the beamline.[4]

When discussing optic alignment and position, BL 9.3.2 conforms to the ALS standard notation regarding optical alignment. 'X' is horizontal motion perpendicular to the photon path. 'Pitch' is rotation about the X-axis. 'Y' is vertical motion. 'Yaw' is rotation about the Y-axis. 'Z' is motion along the photon path. 'Roll' is rotation about the Z-axis. Figure 2 is a schematic of the BL 9.3.2 optical layout.

A. Kirkpatrick-Baez Deflection Mirrors

Because BL 9.3.2 is a bending magnet beamline, the source is a wide fan of radiation. M1 is a water-cooled tangential cylinder accepting 7.5 mrads of the horizontal radiation fan; this is determined by its length (1.2 m) and its location (7 m from the source) and the radiation incidence angle (2.5°). M1 focuses the beam horizontally near the exit slit (S2) with a magnification of 2.68. The M1 radius was designed to be 242 m; the delivered radius was 234 m. The focus was thus moved closer to the mirror by 2.8 m. Appendix B discusses the optical equations for each mirror.

The divergence angles are small which means M1 has a large depth of field. Subsequently, the effects of the slightly wrong radius are small. The present M1 has a fixed geometry. However, if one wished to optimize the radius, M1 and the front end could be designed such that it included an attached bender thus allowing the M1 radius to be adjusted. Such a bender is used during the polishing process. An alternative option is to employ a type of mirror recently designed by Malcolm Howells where the entire mirror is constructed as a flexure.[8]

Completing the Kirkpatrick-Baez design is the spherical mirror M2 (242 m radius) which focuses the beam vertically at the midpoint of the entrance slit (S1) travel with a magnification of 0.60. M2 accepts 1.2 mrads of the vertical radiation fan ($2\theta = 5°$). The vertical beam should be focused at S1 to obtain high throughput with a narrow slit width for maximum resolution. The M2 focal point was measured using a photodiode directly downstream of S1. With S1 at 10 μm, the M2 pitch was adjusted to scan the photon beam profile across the slit gap. The S1 position was changed after each scan and thus the focal point was experimentally determined to be 8.52

m downstream of M2 (0.07 m toward the grating tank from the design specification). Figure 3 illustrates this effect with S1 at each of the travel extremes as well as at the M2 focal point. The M2 radius is fixed; thus, the focal point is only very slightly adjustable by changing its elevation which changes the angle of incidence.

B. Gratings

Using one of three gratings, the accessible energy range is 30 eV to 1500 eV. The gratings are kinematically mounted onto a carriage attached to a rail by ball bearing rollers and their rotation is monitored with a laser interferometer.[3] Figure 4 plots the flux vs. energy for each grating as measured from a gold photodiode downstream from S2.[12] Each spherical grating is designed to have a 55 m radius. The fixed included angle is 174°. The fact that the flux from the high energy grating does not drop off indicates a large scattered light component and a possible problem with the grating. This is presently under investigation.

The grating alignment with respect to the photon beam has been described previously by McKinney *et al.*[3] After installation of the grating tank and prior to connecting the vacuum hardware from the slits, a HeNe laser beam was directed along the synchrotron beam path at the center of the grating. The roll and yaw of the gratings were adjusted until the zeroth and ±1 orders of diffraction fell on the same spot on a screen several meters away from the gratings. The 'Y' was adjusted so that this spot was stationary while changing the pitch, which is the motion used to scan the photon energy. It is extremely important that the gratings rotate about a grating line on the grating surface to maintain energy calibration and resolution.

C. The Refocusing Mirror, M3

The refocusing mirror is a bendable cylinder with a fixed small (sagittal) radius (10 cm) and an adjustable large (meridian) radius (80 m - ∞). The bending mechanism is based on a design by Howells[8] and will allow for moving the meridian focus from 1.5 m to ∞ downstream of the refocusing mirror. Appendix B discusses the optical equations as applied to the refocusing mirror.

III. SLITS

Each slit is based on a flexure design allowing a side-driven micrometer to push the jaws open vertically against spring tension continuously from ≤3 μm to 1500 μm. The jaws are maintained parallel (within ±1 mrad) over the full horizontal width of the beam, ≤10 mm. The jaws must also be parallel with the grating lines or else the slit width is effectively widened and the energy resolution is degraded.

The vertical struts on the entrance and exit slits are almost 1.3 m long on average. To maintain high stability in the energy calibration and energy resolution, the slits have to be vertically stable and thermal expansion of these struts was a concern. Thus, the vertical struts on the entrance and exit slits are constructed from invar so that the thermal expansion is negligible.

To satisfy the Rowland circle condition over a wide energy range, the entrance and exit slits are translatable over 600 mm and 1000 mm, respectively. BL 9.3.2 has three modes of operation: fixed slits, scanned slits (Rowland circle), and scanned exit slit (focus condition). The fixed slits mode is appropriate when a small energy range is being scanned. For best

resolution, the slits should be set as close to the Rowland circle or the focus condition as possible. Appendix C discusses the Rowland circle condition and the focus condition as well as the effects of the important optical aberrations on the resolution. The full energy range of each grating can be reached under the focus condition by moving S1 away from the M2 focus and thus sacrificing some flux. The following table gives the energy range for each grating under the focus condition and the Rowland circle condition. These ranges are limited by the entrance slit's translation limits.

Energy Range of Beamline 9.3.2

Grating ($^{lines}/_{mm}$)	Focus Condition Energy Range (eV)	Rowland Circle Energy Range (eV)
100	30 - 150	45 - 77
600	200 - 800	270 - 460
1200	400 - 1500	540 - 920

It is critical that the slits' translation lie along the photon beam path. If S1 does not, then more or less of the beam centroid will be accepted which will adversely affect the flux. This is especially true for higher photon energies where the vertical divergence is less and effective size of the beam at S1 is smaller. If the S2 pitch is wrong, then the S2 position will be incorrect for a given photon energy. Additionally, if S1 and/or S2 do not travel along the beam path, then the energy calibration will change due to the changing included angle.

Satisfying the focus condition and closing S1 and S2 to 10 μm each, the resolving power is $^{E}/_{\Delta E} \geq 7{,}000$. Figure 5 plots the $N_2(g)$ 1s to π^* resonance using first order (inside) light from the 600 $^{lines}/_{mm}$ grating. For

this spectrum, the slit positions were set to satisfy the grating focus condition and remained fixed during the scan.

IV. BEAMLINE ATTRIBUTES

A. Circular Polarization

Bending magnet synchrotron radiation is linearly polarized with the polarization vector in the orbit plane. Viewing at any angle other than in the orbit plane, however, the perpendicular component of the polarization vector becomes non-zero. The net polarization is thus elliptical at any viewing angle other than in the orbit plane. The helicity of the elliptically polarized light changes when changing the viewing angle from above to below the orbit plane. Additionally, the degree of circular polarization increases as the out of plane viewing angle increases. Of course, the flux decreases for these larger angles. The optimum balance between circular polarization and flux within the limitations imposed by the beamline geometry must be determined before carrying out experiments using circularly polarized light.[13,14]

A water-cooled aperture which can be positioned with 1 μm resolution to select the beam centroid for linearly polarized light is installed upstream of the vertically deflecting mirror. Alternatively, the aperture can be positioned above or below the beam center to select circularly or elliptically polarized light.

A 0.5 mm slit below the selection aperture is used to determine the beam centroid; the degree of linear polarization through this slit was measured to be 0.99 at the endstation.[15,16] The degree of circular

polarization as measured at the endstation is over 0.8 at 700 eV with the circular polarization flux ≥30% of the total flux.[16] Figure 6 illustrates a schematic of this selection aperture. Appendix D discusses the circular polarization calculations and measurements in more detail.[17-20]

B. Photodiodes

A photodiode is installed downstream from each optical component to aid alignment and storage ring diagnostics. These are electrically isolated to allow for photocurrent measurements and/or coated with phosphor for viewing the beam. The parts used to collect photocurrent signals expose a clean gold surface to the beam. Thus, absolute flux calculations can be performed.

C. I-zero

Directly downstream of M3 are a gold grid and a copper grid (>85% transmission). Evaporators for each metal are maintained so that a fresh layer can be deposited on the respective grid and a clean I-zero signal can be collected. These grids are electrically isolated and the I-zero photocurrent can be measured directly. A potential may be applied to an electrically isolated wire loop surrounding the face of the grids to collect all photoelectrons and thus improve the stability and accuracy of the measured photocurrent. Alternatively, one can measure total yield by using a channeltron positioned 90° to the beam.

D. Rotating Platform Endstation

Mounted on a rotating platform are two different endstations. The platform rotates manually through 60° in <5 minutes allowing the beam to be directed to either endstation without breaking the vacuum. Figure 7 shows a schematic of this double-chamber rotating platform. The two halves of the platform are vibrationally decoupled from one another to allow assembly of one endstation while the other takes beam. The rotation stops have been designed to align the chambers upon successive rotations. For structural stability, the chambers are bolted through the platform to pods secured to the floor. This removes the 'drum-head' effect of the large platform.

Permanently mounted at station one is the Advanced Photoelectron Spectrometer/Diffractometer (APESD)[21] with an angle resolving Scienta SES 200 hemispherical electron energy analyzer for doing a variety of surface science experiments. These include high resolution photoelectron diffraction (scanned angle and/or energy) and x-ray photoelectron spectroscopy (XPS) of surfaces and interfaces. Additionally, magnetic circular dichroism (MCD) as well as x-ray total-reflection XPS studies are being performed at station one.

Mounted at station two is the Applied Materials Chamber[22] with a partial yield electron and fluorescence detector for near-edge x-ray absorption fine structure (NEXAFS) and MCD studies. An angle integrating electron energy analyzer is used for XPS studies. Alternately mounted at station two is the Angle-Resolved PhotoEmission Spectrometer (ARPES) with a movable electrostatic hemispherical electron energy analyzer (mean radius of 50 mm) used for studying surfaces and interfaces.[23] This system is

mainly used for studying angle-resolved photoemission extended fine structure (ARPEFS - scanned energy photoelectron diffraction).

A third endstation is mounted upstream of M3. A deflecting mirror is used to direct the photon beam through the gas cell to the Fourier Transform Soft X-Ray (FTSX) spectrometer.[24] The FTSX spectrometer will be used for ultra-high resolution spectroscopic studies of gas-phase core-levels from hν = 40 - 120 eV.

E. Active Feedback on M2 Pitch

A beam position locking system was developed to correct for photon beam fluctuations. The most notable cause has been temperature variations of the low conductivity water (LCW) which is used to cool the ALS magnets and some optics. LCW temperature must not vary more than ±0.1 C° to maintain a stable photon beam.

The beamline is controlled by the Experimental Physics and Industrial Controls Systems (EPICS). The Proportional, Integral, and Derivative (PID) algorithm in EPICS[25] is used to control this beam position locking system. The upper and lower entrance slit jaws are electrically isolated from each other and from ground. The photocurrent from each jaw is measured. In conjunction with the PID logic, this photocurrent is used to generate an error function, E_f,

$$E_f = \frac{I_U - I_L}{I_U + I_L} \qquad (1)$$

where I_U and I_L are the photocurrent signals from the upper and lower jaws, respectively. This error function is utilized to automatically adjust a piezoelectric drive that changes the M2 pitch. The feedback routinely operates at 10 Hz.

Figure 8 plots the error function used for the feedback loop as a function of time. Without the feedback loop in operation, the photon beam can drift. This beam drift causes changes in the photocurrent collected from each jaw. However, when in operation, the feedback loop effectively locks the beam position thus stabilizing the flux at the endstation to better than 1% (see next section).

V. OTHER PHOTON BEAM STABILITY CONSIDERATIONS

A. Temperature Variations of the Low-Conductivity Water

Temperature variations of the low-conductivity water (LCW) used to cool both the storage ring magnets and the optics can cause instabilities in the photon beam. Figure 9 illustrates how dramatic these effects can be at the endstation. Originally, the LCW temperature was allowed to vary ±0.5 C°. The top panel in figure 9 shows that this variation was sufficient to cause ~±1% oscillations in the relative intensity of the photon beam measured at I-zero. The noise level is approximately two parts per thousand; the high frequency ±0.5% oscillations are not random noise. This is illustrated by the bottom panel of figure 9 which shows the Fourier transform of the relative intensity curve and has a strong peak at a 37 s period. The large, low frequency oscillations show a 14 min. period. This effect was also detected on BL 7.0, BL 8.0, and BL 9.0.

Successful efforts were made to constrain the LCW temperature to within ±0.1 C°. The lower curve in the top panel of figure 9 illustrates the complete improvement in photon flux stability at I-zero. Not only are the low frequency oscillations removed (less than 0.2%), but the high frequency oscillations are also no longer present as illustrated by the Fourier transform.

It is important to note that the photon stability should be continually monitored by the users. System components sometimes fail to work properly and the users will be the first affected. Rapid notification of the control room almost always results in a rapid correction of the problem. Continually recording the I-zero signal will help to prevent wasting beam time by collecting data when the beam is unstable.

B. Changing Undulator Gaps

Normal operation of the ALS allows user control of the undulator gaps. Ultimately, there will be ten insertion devices installed in the ALS. The users on these beamlines have control of the insertion device operating parameters and will be adjusting the parameters as dictated by their experiments. Typically, the flux at BL 9.3.2 is stable regardless of how the insertion devices are being moved.

Once in a while, a spurious intensity change has been correlated with a changing undulator gap. Figure 10 illustrates such an occurrence. During this scan, I-zero was being monitored over time to investigate the beam instabilities due to the temperature variation described previously. The feedback system with M2 was not installed at the time the spectrum in figure 10 was acquired. The step loss was due to a change in an undulator gap as indicated. One can see that after the change, the high frequency noise

increased dramatically. This effect is perhaps correlated with the value of the insertion device gap. At smaller gaps (higher fields), the electron beam will be more sensitive to changes.

These effects were investigated with the cooperation of users on BL 7.0, BL 8.0, and BL 9.0, but no reproducible results were obtained. In fact, detecting an undulator gap change at the BL 9.3.2 endstation seems to be a rarity. The conclusion is again that the flux should be continually monitored so that any spectra affected by such a spurious event can be corrected or reacquired.

C. Stored Electron Beam Energy

The ALS is capable of operating at any energy between 1.0 GeV and 1.9 GeV. At beamline 9.3.2, the photon beam centroid can shift as much as 600 μm at 14 m from the source depending upon the stored electron beam energy. Typically, these beam shifts are not a problem because the active feedback loop steers the photon beam through the entrance slit. For experiments involving circular polarization, the photon beam centroid is experimentally measured and the aperture positions are referenced to this measured value.

Due to the inherent stability of the ALS, a local steering magnet to bump the beam at 9.3.2 could be installed to correct for the beam position shift. A one-time calibration and subsequent incorporation into the ALS operating parameters would insure that the beam is always at the same spot regardless of the storage ring configuration. This would also help to eliminate any effects of changing undulator gaps.

VI. CONCLUSION

Beamline 9.3.2 at the Advanced Light Source is a high resolving power ($E/\Delta E \geq 7{,}000$) beamline which can access photon energies from 30 eV to 1500 eV by using one of three gratings. The Kirkpatrick-Baez configuration was adopted for the pre-mirror assembly. The beamline utilizes a 55 m fixed included-angle SGM with movable entrance and exit slits.

It has been measured that the synchrotron radiation beam is highly polarized (99.9%) in the horizontal plane; the upper limit to the unpolarized component is ≤0.1%. Circularly polarized radiation to a desired degree is obtained by inserting a water-cooled movable aperture in front of the vertically focusing mirror.

To maintain a stable beam intensity through the entrance slit, the photocurrent signals from the upper and lower jaws of the entrance slit are utilized to set a closed-loop feedback with a Piezoelectric drive which adjusts the pitch of the vertically deflecting mirror. This has increased the photon beam stability at the endstation to two parts per thousand if temperature variations of the LCW are controlled.

The beamline end station also has a movable platform that accommodates two experimental chambers and enables the synchrotron radiation to be directed to either one of the two experimental chambers without breaking vacuum. A deflection mirror upstream of M3 directs the photon beam to a permanently mounted third endstation.

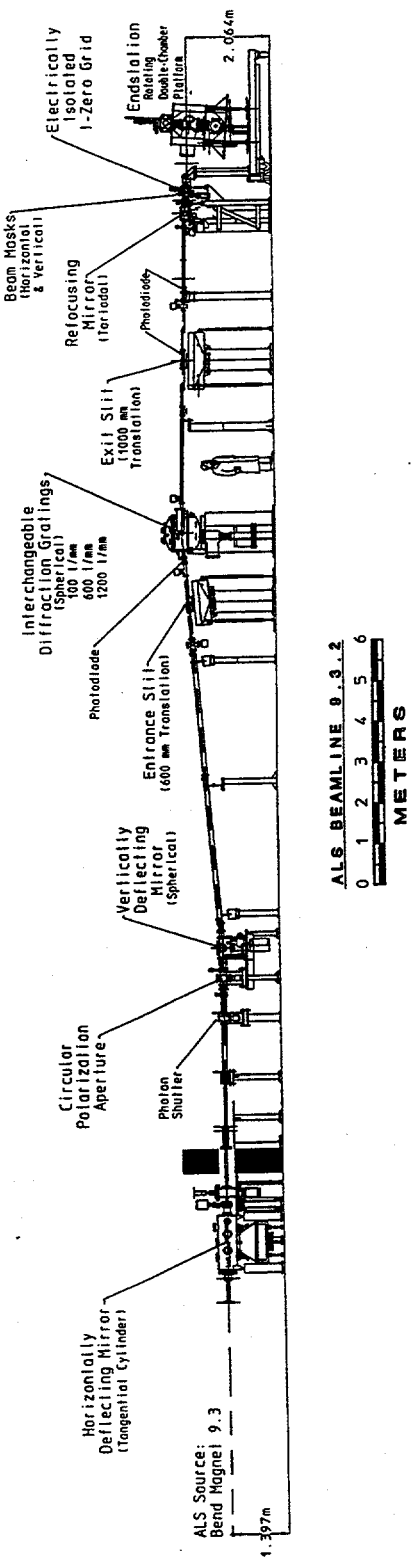

XBD 9601-00159.BIM

Engineering Schematic of BL 9.3.2 at the ALS
Figure 1

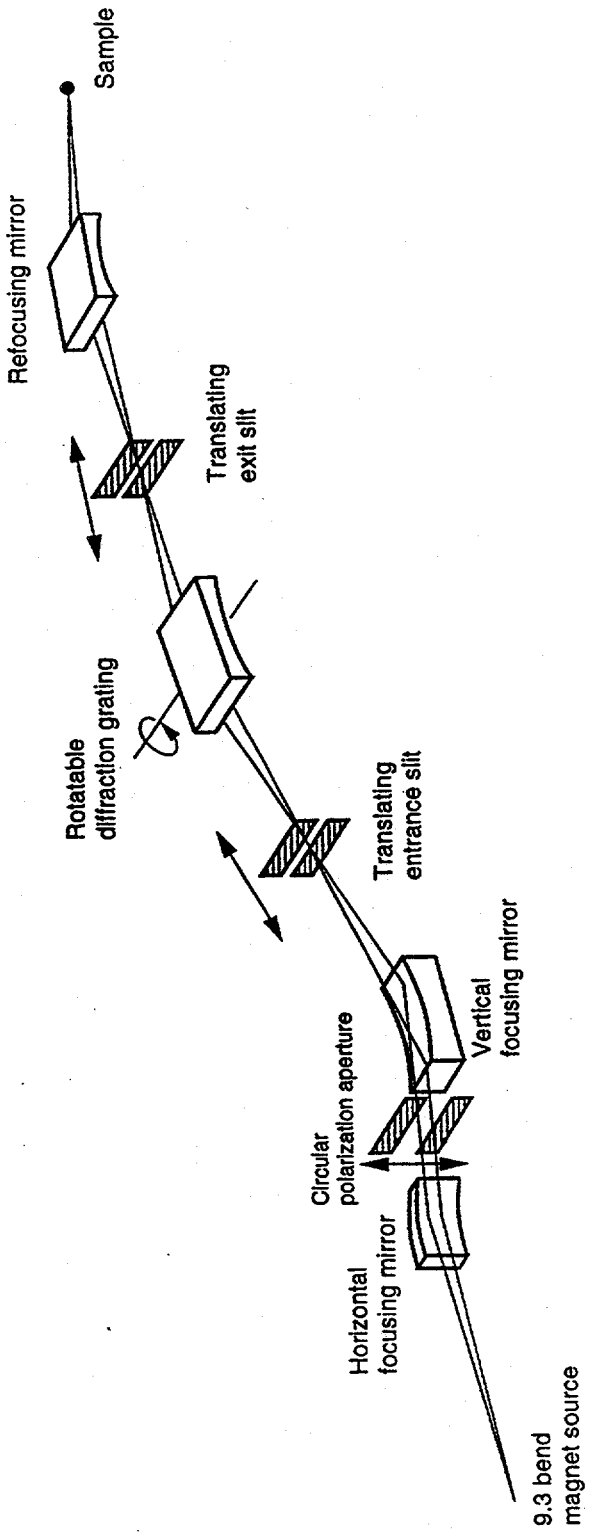

XBD 9602-00396.BIM

Optical Layout Schematic of BL 9.3.2 at the ALS
Figure 2

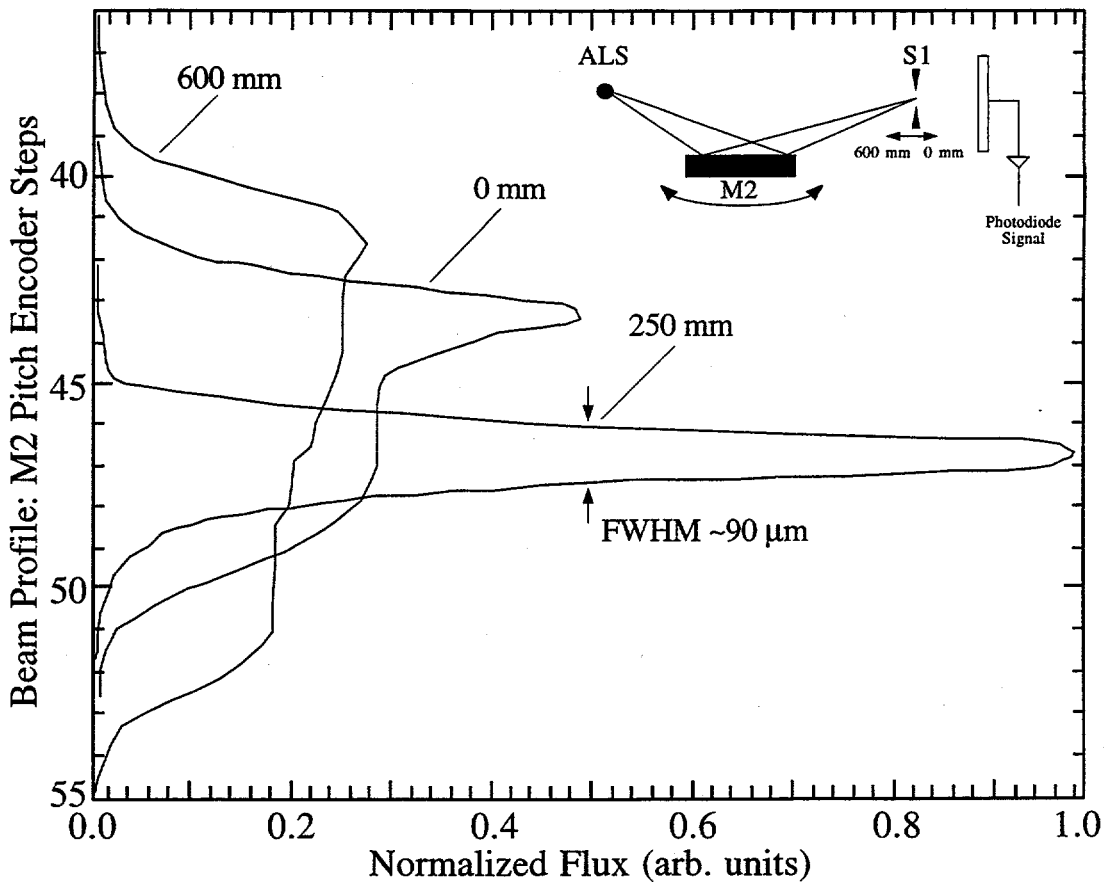

With S1 at 10 μm, the M2 pitch was adjusted to scan the photon beam profile across the slit gap. The S1 position was changed after each scan and thus the focal point was experimentally determined to be 8.52 m from M2 (0.07 m toward the grating tank from the design specification). At the S1 travel extremes, the photon beam is out of focus shown by the broad, low intensity curves.

Figure 3

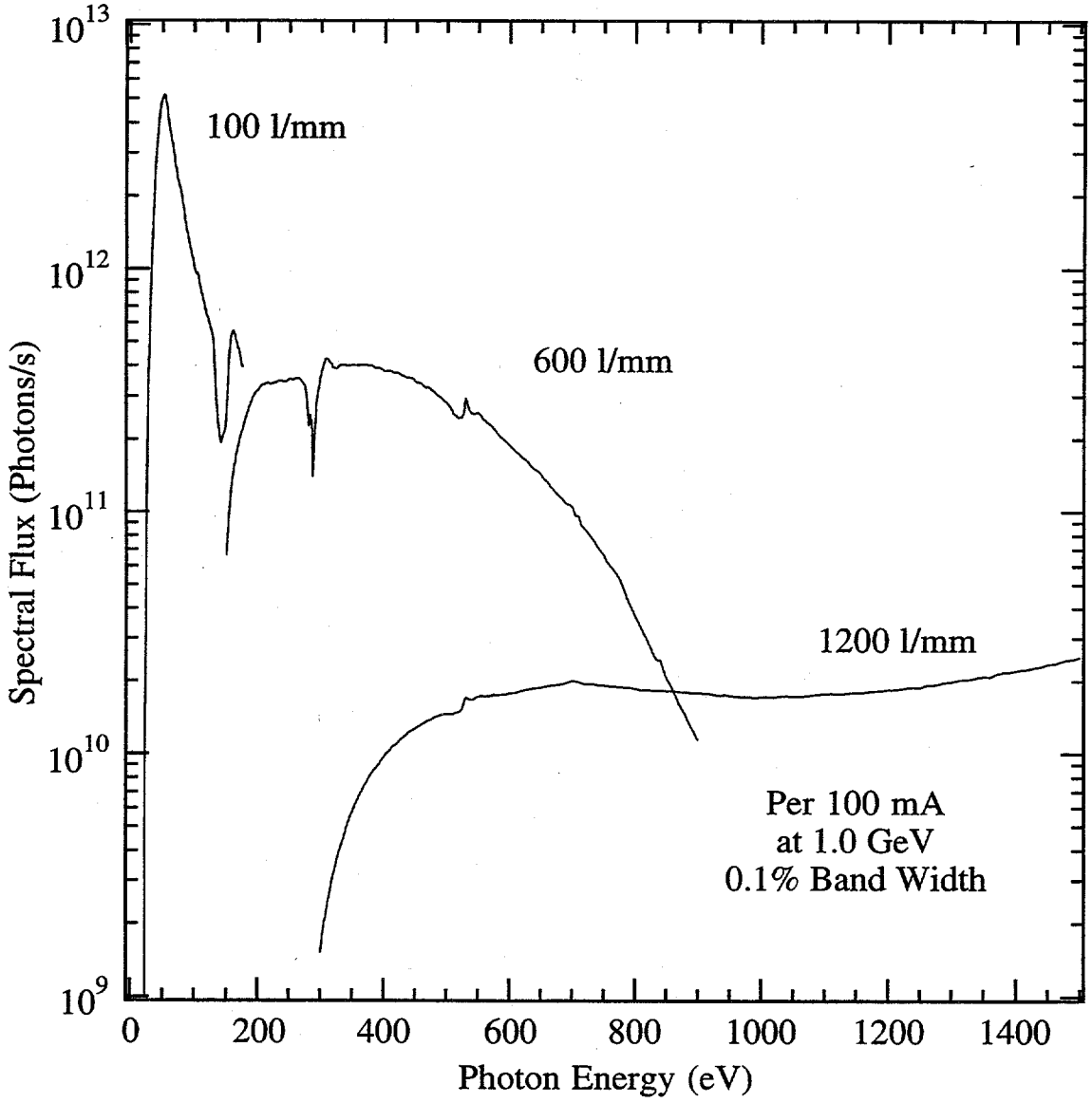

Spectral flux (photons/second) vs. photon energy (eV) for each grating (0.1% bandwidth) as measured from a gold photodiode downstream from S2. The fact that the flux from the high energy grating does not drop off indicates a large scattered light component.

Figure 4

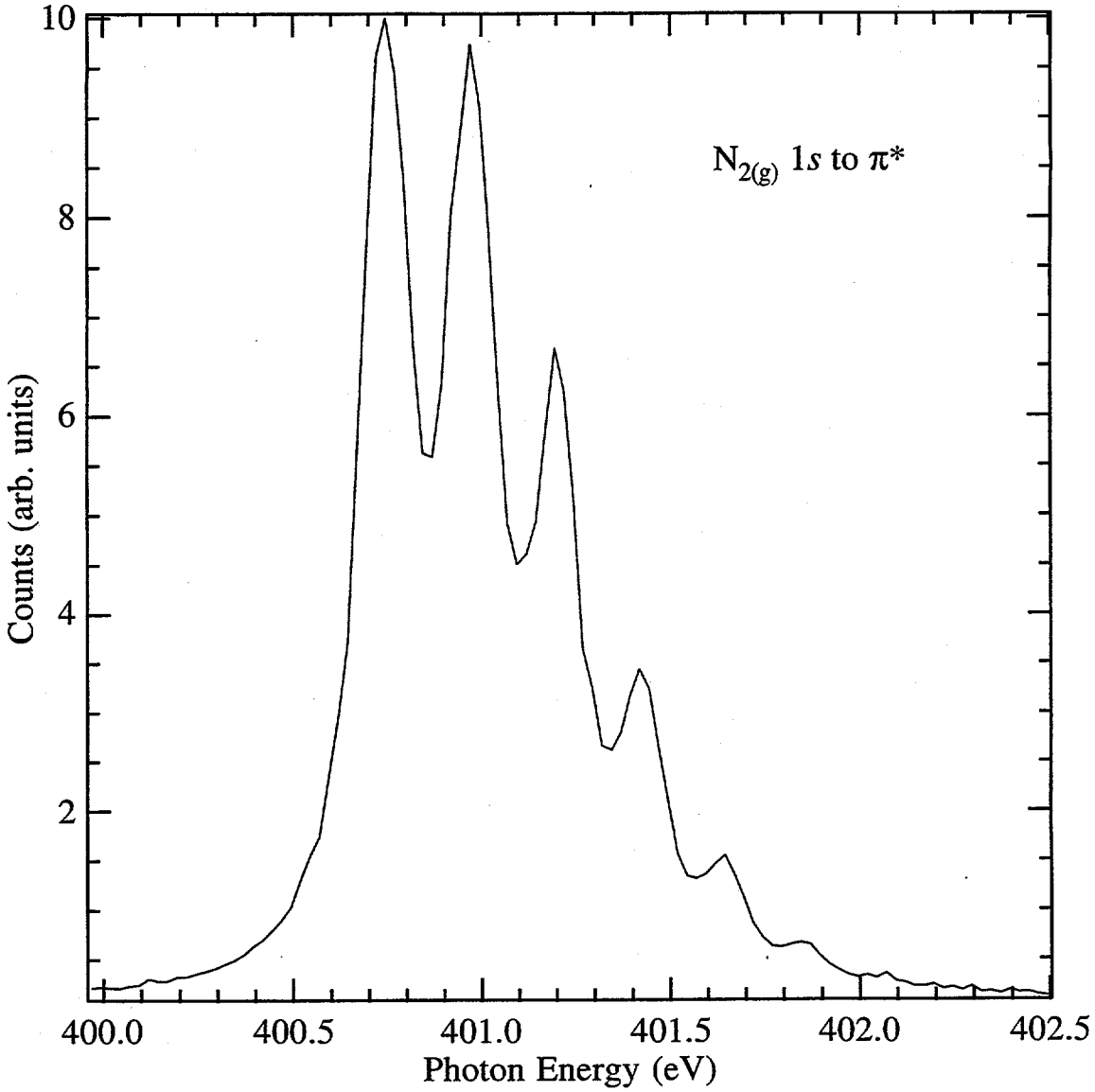

The $N_{2(g)}$ 1s to π* resonance using first order (inside) light from the 600 $^{lines}/_{mm}$ grating shows a resolving power is $^{E}/_{\Delta E} \geq 7{,}000$ with S1 and S2 each set to 10 μm. For this spectrum, the slit positions were set to satisfy the grating focus condition and remained fixed during the scan.

Figure 5

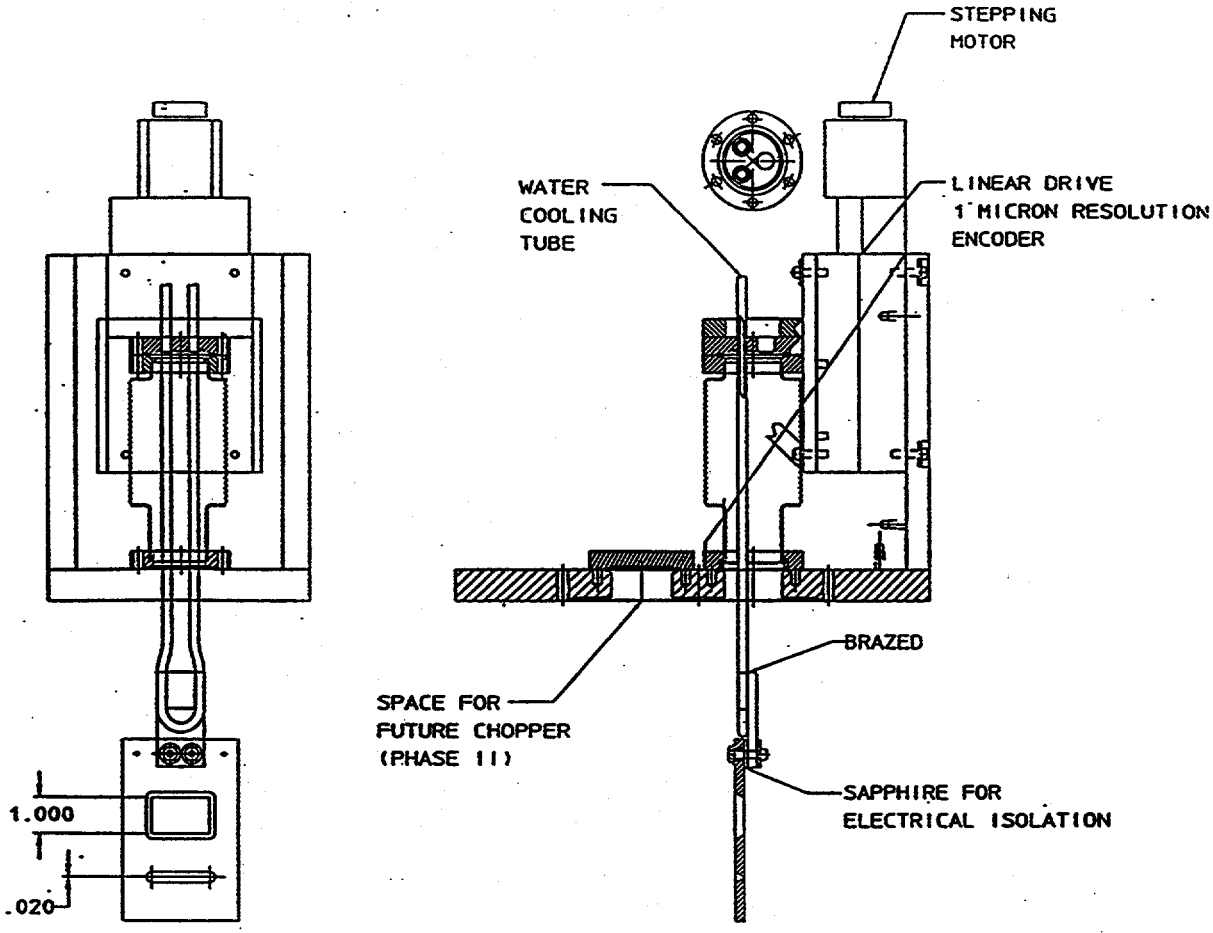

XBD 9601-00161.BIM

Circular polarization selection aperture schematic. The movable aperture is constructed of a water cooled, gold plated copper block. The large aperture is 25 mm vertically. The small aperture for determining the photon beam centroid is 0.5 mm vertically.

Figure 6

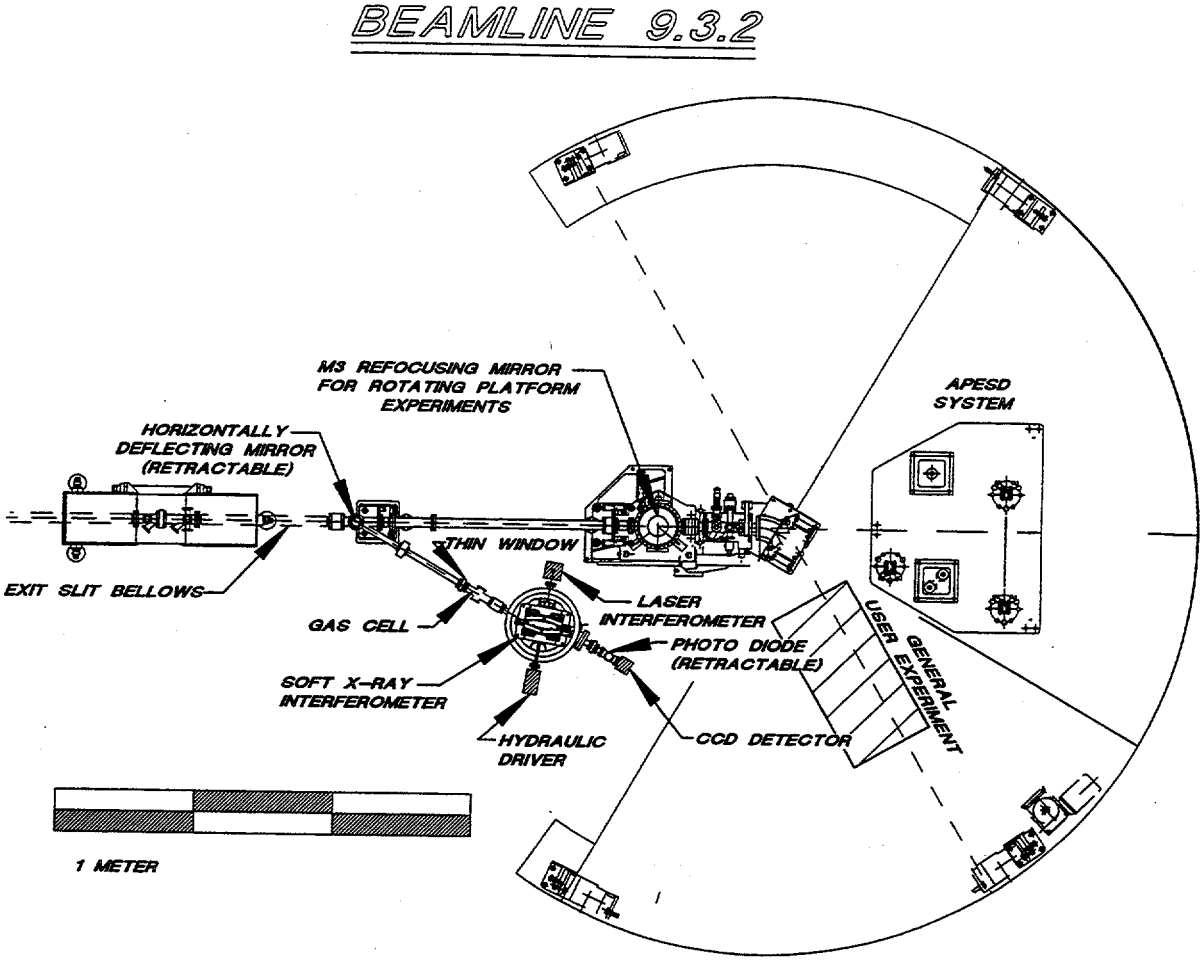

XBD9601-00160.BIM

The two halves of the platform are vibrationally decoupled from one another to allow assembly of one end station while the other takes beam. The platform rotates manually through 60° in <5 min.; the electronics have been connected appropriately. The rotation stops have been designed to align the chambers upon successive rotations. For structural stability, the chambers are bolted to pods secured to the floor removing the 'drum-head' effect of the large platform.

Figure 7

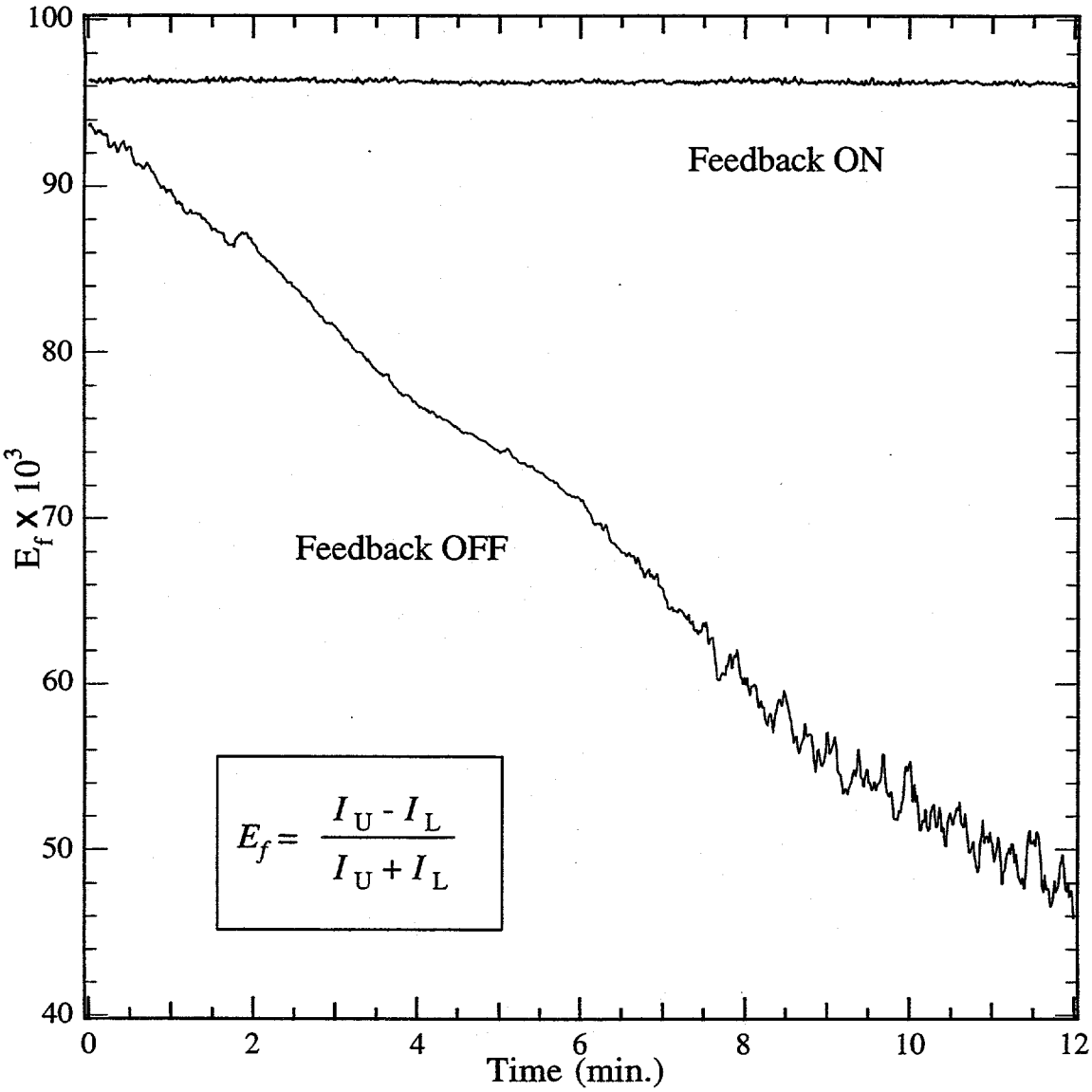

The upper and lower jaws of the entrance slit are electrically isolated from each other and from ground. Thus, the photocurrent from each jaw at a given slit width can be monitored. This signal then goes through an active feedback loop (PID logic) which is used to automatically adjust a Piezoelectric drive. This drive changes the pitch of the vertically deflecting mirror.

Figure 8

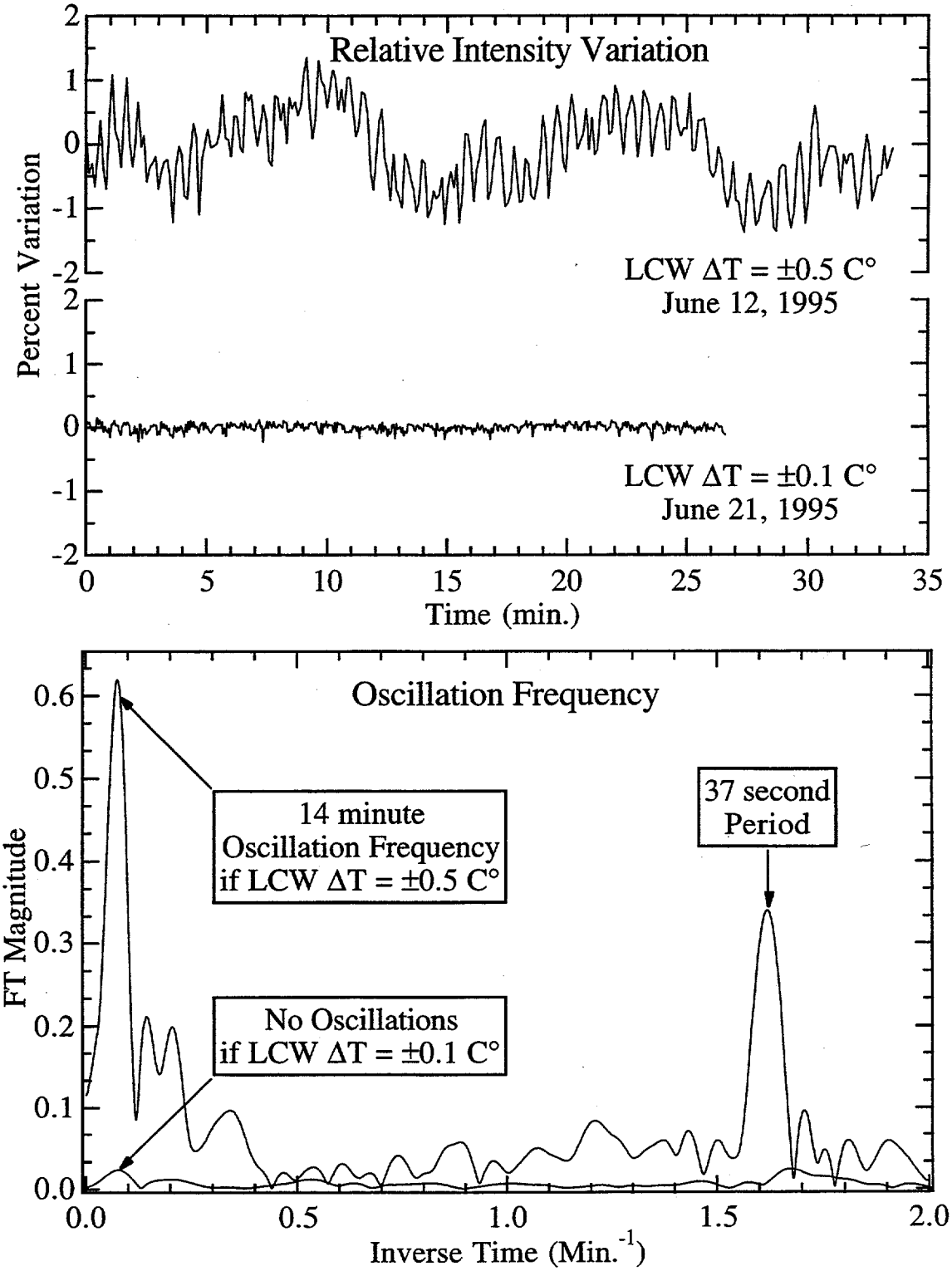

Originally, the low conductivity water temperature was allowed to vary ±0.5 C° which caused large fluctuations in the photon beam--an intensity oscillation ~±1% with a ~14 min. period. Successful efforts constrained the LCW temperature to ±0.1 C° and the photon beam has become extremely stable (±0.1%).

Figure 9

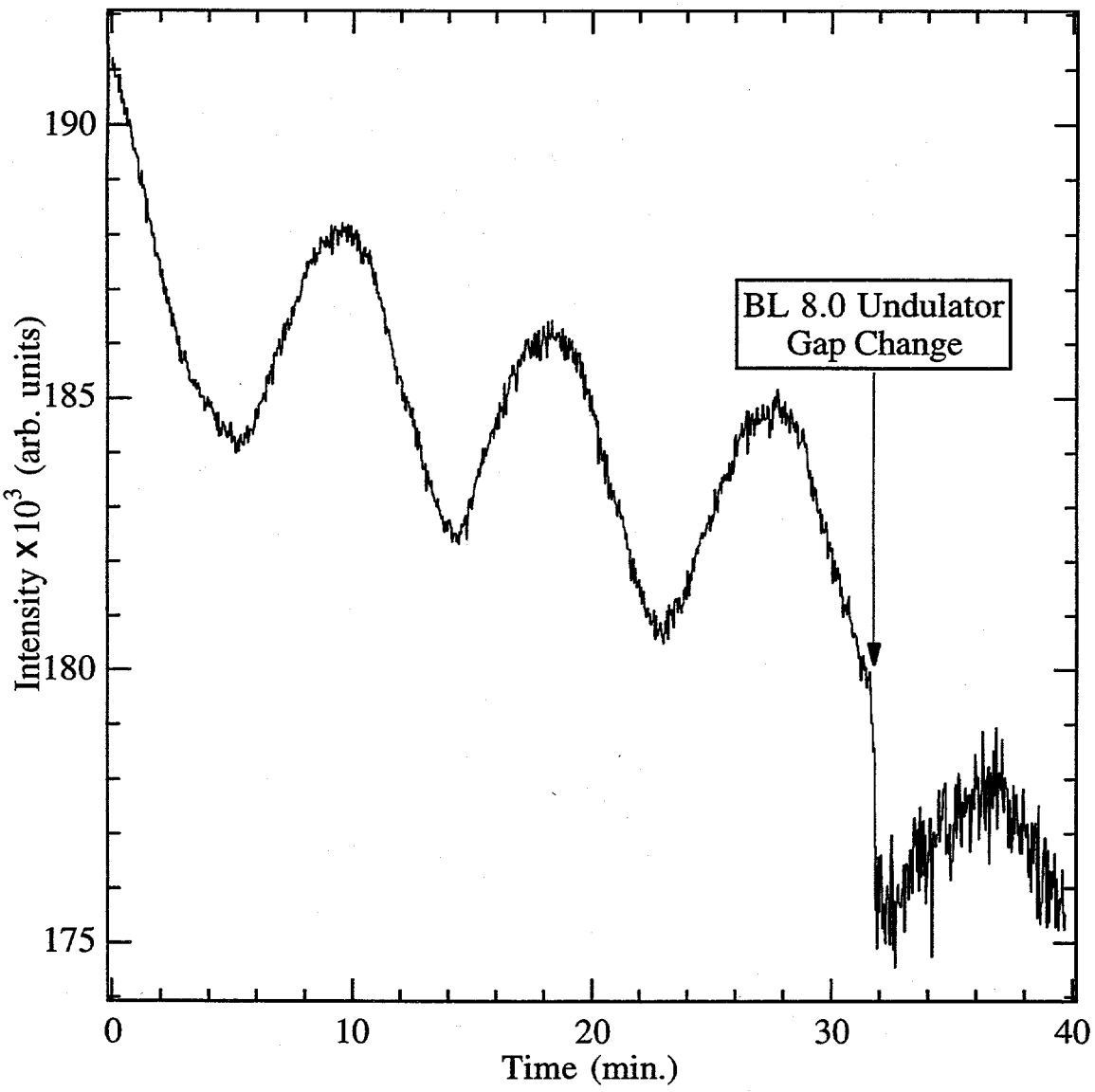

A spurious intensity change correlated with a changing undulator gap. The feedback system with M2 was not installed at the time this spectrum was acquired. After the undulator gap change, the high frequency noise increased dramatically. This effect is perhaps correlated with the value of the insertion device gap. At smaller gaps (higher fields), the electron beam will be more sensitive to changes.

Figure 10

REFERENCES

[1]Z. Hussain, W.R.A. Huff, S.A. Kellar, E.J. Moler, P.A. Heimann, W. McKinney, C. Cummings, T. Lauritzen, J.P. McKean, F.J. Palomares, H. Wu, Y. Zheng, A.T. Young, H.A. Padmore, C.S. Fadley and D.A. Shirley, Rev. Sci. Instrum. to be published (1996).

[2]Z. Hussain, W.R.A. Huff, S.A. Kellar, E.J. Moler, P.A. Heimann, W. McKinney, H.A. Padmore, C.S. Fadley and D.A. Shirley, J. Electron Spectrosc. to be published (1996).

[3]W.R. McKinney, M.R. Howells, T. Lauritzen, J. Chin, R. DiGennaro, E. Fong, W. Gath, J. Guigli, H. Hogrefe, J. Meneghetti, D. Plate, P.A. Heimann, L. Terminello, Z. Ji, D.A. Shirley and F. Senf, Nucl. Instr. and Meth. **A291**, 221(1990).

[4]P.A. Heimann, F. Senf, W. McKinney, M. Howells, R.D. van Zee, L.J. Medhurst, T. Lauritzen, J. Chin, J. Meneghetti, W. Gath, H. Hogrefe and D.A. Shirley, Physica Scripta **T31**, 127(1990).

[5]C. Kunz, *Topics in Current Physics: Synchrotron Radiation, Techniques and Applications*, (Springer-Verlag, Berlin, 1979).

[6]A.G. Michette, *Optical Systems for Soft X-Rays*, (Plenum Press, New York, 1986).

[7]H. Petersen, F. Senf, F. Schäfers and J. Bahrdt, Rev. Sci. Instrum. **66**, 1777(1995).

[8]M.R. Howells, *Bending Mechanisms*, Unpublished, (1995).

[9]H. Hogrefe, M.R. Howells and E. Hoyer, SPIE **733**, 274(1986).

[10]J. Kirz, D.T. Attwood, B.L. Henke, M.R. Howells, K.D. Kennedy, K.-J. Kim, J.B. Kortright, R.C. Perera, P. Pianetta, J.C. Riordan, J.H. Scofield, G.L. Stradling, A.C. Thompson, J.H. Underwood, D. Vaughan, G.P. Williams and H. Winick, *X-Ray Data Booklet*, Center for X-Ray Optics, Lawrence Berkeley Laboratory, PUB-490 Rev. (1986).

[11]T. Reich, Z. Hussain, E. Moler, M. Blackwell, G. Kaindl, D.A. Shirley and M.R. Howells, Rev. Sci. Instrum. **64**, 2552(1993).

[12]M. Krumrey and E. Tegeler, Rev. Sci. Instrum. **63**, 797(1992).

[13]H.A. Padmore, Z. Hussain and Y. Zheng, *Selection of the Optimum Aperture Sizes for Circularly Polarized Spectroscopy on Beamline 9.3.2*, Lawrence Berkeley Laboratory, LSBL #218 (1993).

[14]K. Green, *Proposal for a National Synchrotron Light Source*, Brookhaven National Laboratory, BNL 50595 (1977).

[15]J.B. Kortright, M. Rice and K.D. Franck, Rev. Sci. Intrum. **66**, 1567(1995).

[16]J.B. Kortright, M.A. Rice, Z. Hussain, H.A. Padmore, A.T. Young, A. Adamson, W.R.A. Huff, E.J. Moler, S.A. Kellar, R.X. Ynzunza, F.J. Palomares, H. Diamon, E.D. Tober and C.S. Fadley, Rev. Sci. Instrum. to be published, (1996).

[17]H. Kimura, M. Yamamoto, M. Yanagihara, T. Maehara and T. Namioka, Rev. Sci. Intrum. **63**, 1379(1992).

[18]S. Di Fonzo, W. Jark, F. Schafers, H. Petersen, A. Gaupp and J.H. Underwood, Appl. Optics **33**, 2624(1994).

[19]E. Collett, *Polarized Light*, (Marcel Dekker, Inc., New York, 1993).

[20]R. Carr, J.B. Kortright, M. Rice and S. Lidia, Rev. Sci. Intrum. **66**, 1862(1995).

[21]R.X. Ynzunza, E.D. Tober, F.J. Palomares, Z. Wang, H. Xiao, F. Zhang, Z. Hussain and C.S. Fadley, (to be published).

[22]S.A. Kellar, N. Hartman, Z. Hussain, W.R.A. Huff, E.J. Moler and D.A. Shirley, (to be published).

[23]S.D. Kevan, *Ph.D. Thesis*, The University of California, Berkeley, LBL-11017(1980).

[24]E.J. Moler, Z. Hussain, R.M. Duarte and M.R. Howells, J. Electron Spectrosc. to be published (1996).

[25]J.B. Anderson and M.R. Kraimer, *EPICS IOC Reference Manual*, Los Alamos National Laboratory, p. 103 (1992).

APPENDIX A: Summary of Each Optical Element

	MIRRORS			GRATINGS		
	M1	M2	M3	G100	G600	G1200
Shape	Tangential Cylinder	Sphere	Bent Cylinder	Sphere	Sphere	Sphere
Radius (m)	243 (design) 234 (actual)	243 (design) 242 (actual)	80 - ∞ (meridian) 0.1 (sagittal)	55	55	55
Incidence Angle	2.5°	2.5°	1° to 3°	Variable	Variable	Variable
Size (mm^3)	1200 × 100 × 65	400 × 75 × 70	400 × 40 × 7	188 × 100 × 50	188 × 100 × 50	188 × 100 × 50
Water Cooling	Yes	No	No	Yes	No	Yes
Bulk Material	Glidcop	Glidcop	ULE Quartz	Glidcop	ULE Quartz	Glidcop
Surface Material	250 Å Pt	250 Å Pt	250 Å Pt	250 Å Pt	250 Å Au	250 Å Pt
RMS Slope Error	<10 μrad	<0.6 μrad	≤5 μrad	≤1 μrad	≤1 μrad	≤1 μrad
RMS Roughness	5 Å	3 Å	5 Å	5 Å	5 Å	5 Å
Magnifi-cation	2.68	0.6	0.23 (meridian) 0.34 (sagittal)	---	---	---
Manufac-turer	Rockwell Internat'l	Rockwell Internat'l	Conti-nental Optics	Hyperfine	Ferranti Astron Ltd.	Hughes
Delivered Date	1993	1993	1996	1991	1988	1994

APPENDIX B: Foci Calculations

A. Horizontally Deflecting/Focusing Mirror, M1

The horizontally deflecting mirror, M1, is a tangential cylinder. It is curved in the horizontal plane which allows for horizontal focusing of the photon beam. This can be considered a two dimensional optical component and the meridian focal length, f_{m}, is defined by[1]

$$f_{\mathrm{m}} = \frac{R \sin \theta_{\mathrm{i}}}{2} \tag{B1}$$

where R is the radius of curvature and θ_{i} is the angle of incidence as measured from the surface tangent at the mirror center. Using equation (B1) together with

$$\frac{1}{d_{\mathrm{obj}}} + \frac{1}{d_{\mathrm{img}}} = \frac{1}{f} \tag{B2}$$

where d_{obj} and d_{img} are the distances from the mirror center to the object and the image, respectively, the parameters for M1 can be calculated. It is important to note that these calculations are for the optical path. The vertical deflections of M2, the gratings, and M3 will cause the optical path length to differ slightly from the floor distance. Also, note that the calculations presented here are approximate in that they do not consider the effects of the other optical elements. The actual parameters were obtained from calculations using SHADOW which included all of the optical elements.

The distance from the source to the mirror, $d_{\text{obj-M1}}$, is 7.00 m. It was desirable to position the M1 focal point at the center of the exit slit travel. Given that $2\theta = 5°$ for both M1 and M2, and the grating included angle is 174° (causing a net downward deflection of 1° from the grating center to the center of M3), the optical path length from the M1 center to the S2 travel center, $d_{\text{img-M1,design}}$, is 21.60 m. Using equation (B2), the desirable M1 meridian focal length is $f_{\text{m-M1,design}} = 5.29$ m. Rearranging equation (B1) and solving for the radius, $R_{\text{M1,design}} = 243$ m.

In fact, the actual M1 radius, $R_{\text{M1,actual}}$, is 234 m. The result of this -9 m deviation from the design value causes the actual meridian focal length, $f_{\text{m-M1,actual}}$, to be 5.10 m. Thus, the actual M1 focal point is $d_{\text{img-M1,actual}} = 18.79$ m, which is 2.8 m upstream of the S2 travel center.

The magnification, M, can be calculated by taking the ratio of the object and image distances.

$$M = \frac{d_{\text{img}}}{d_{\text{obj}}} \tag{B3}$$

Thus, M1 magnifies the source by a factor of 2.68.

B. Vertically Deflecting/Focusing Mirror, M2

The vertically deflecting mirror, M2, is spherical and completes the Kirkpatrick-Baez design.[1] It is curved in the vertical plane which allows for vertical focusing of the photon beam. As with M1, the meridian focal length, f_{m}, is defined by equation (B1).

It is desirable to vertically focus the photon beam at the center of the entrance slit travel to obtain high throughput with a narrow slit width for maximum resolution. Taking account of the 5° horizontal deflection of M1, the distance from the source to the M2 center, $d_{\text{obj-M2}}$, is 14.22 m. The distance from the M2 center to the S1 travel center, $d_{\text{img-M2,design}}$, is 8.45 m. Using equation (B2), the desired meridian focal length, $f_{\text{m-M2,design}}$, is thus 5.30 m. Using equation (B1), the desired radius, $R_{\text{M2,design}}$, is 243 m. It is purely coincidence that the M2 radius turns out to be the same as the M1 radius. The actual M2 radius is 242 m which causes the focal point to move closer to the mirror by a negligible 0.07 m.

In fact, the focal point of M2 is slightly adjustable by changing its elevation. Because M2 is spherical, $\theta_i = 2.5°$ only at the mirror center. Lowering M2 causes θ_i to become larger (more incidence) which moves the focal point *away* from the mirror. Raising M2 causes θ_i to become smaller (more glancing) which moves the focal point *toward* the mirror. As described in the text, it was experimentally determined that $d_{\text{img-M2,actual}} = 8.52$ m downstream from M2 (see figure 3 in main text). Using equation (B3), the magnification of M2 is 0.60 (the photon beam is $< \frac{2}{3}$ of the source size at the M2 focus).

The fact that M2 is three dimensional must be considered. That is, the spherical surface will also cause focusing in the horizontal plane which is described by the sagittal focal length, f_s, where[1]

$$f_s = \frac{R}{2\sin\theta_i} \qquad \text{(B4)}$$

Given that $R_{M2,actual} = 242\,m$ and $\theta_i = 2.5°$, $f_{s\text{-}M2} = 2774\,m$. Using equation (B2), the sagittal focal point, $d_{s,img\text{-}M2}$, is -14.29 m (14.29 m upstream of M2). This results is some astigmatism at the entrance slit.[1]

The astigmatism would not have been present if a tangential cylinder had been used for M2 instead of a sphere. However, manufacturing considerations made a spherical mirror the better choice. A spherical mirror can be polished to much higher quality than a tangential cylinder. The aberrations at the focal point are a minor consideration when compared with the higher optical quality of the spherical mirror.

C. Refocusing Mirror, M3

The refocusing mirror, M3, is used to focus the beam both vertically and horizontally to the same point. It is desirable to have this point the same for each endstation on the platform. This will minimize the switch-over time between experimental stations. As determined by the permanently mounted Advanced Photoelectron Spectrometer/Diffractometer,[2] the focal point should be 2.17 m downstream from the M3 center. At the largest angle of incidence, M3 deflects the beam vertically by -3° (in addition to the net -1° downstream of the grating). Since 4° is such a small angle, this floor distance and the optical path length are the same to the nearest 0.01 m.

To place both the meridian and sagittal focal points at the same place in space, the vertical and horizontal curvatures must be different. To accomplish this task with a single mirror, either a toroid or a bent cylinder must be used. Manufacturing costs and delivery times dictated the choice of using a bent cylinder. The large (meridian) radius is adjustable while the small (sagittal) radius is fixed.

Because M3 is a vertically deflecting mirror, equations (B1) and (B2) can be used to determine the desired long radius and thus the bending parameters. The focal distance, $d_{\text{m,img-M3}}$, is 2.17 m as stated. The object distance, $d_{\text{m,obj-M3}}$, is the distance from the M3 center to the travel center of S2 (the closest vertically defining aperture) which is 3.60 m. Thus, the meridian focal length of M3, $f_{\text{m-M3}}$, should be 1.35 m. With $\theta_{\text{i}} = 1.5°$, the long (meridian) radius of M3, $R_{\text{m-M3}}$, should thus be bent to 103 m.

Similarly, equations (B4) and (B2) can be used to determine the desired short radius of M3. The focal distance $d_{\text{s,img-M3}}$, is also 2.17 m as stated. The object distance $d_{\text{s,obj-M3}}$, is the distance from the M3 center to the grating center, 7.80 m. Thus, the sagittal focal length of M3, $f_{\text{s-M3}}$, should be 1.70 m. With $\theta_{\text{i}} = 1.5°$, the short (sagittal) radius of M3, $R_{\text{s-M3}}$, should thus be polished to 0.09 m.

The vertical and horizontal magnifications can be calculated using equation (B3) and the distances already mentioned. The vertical magnification, $M_{\text{m-M3}} = {}^{d_{\text{m,img-M3}}}\!/_{d_{\text{m,obj-M3}}}$, is 0.60 while the horizontal magnification, $M_{\text{s-M3}} = {}^{d_{\text{s,img-M3}}}\!/_{d_{\text{s,obj-M3}}}$, is 0.28. These multiply to the exit slit width and the horizontal size at the grating respectively.

REFERENCES

[1]A.G. Michette, *Optical Systems for Soft X-Rays*, (Plenum Press, New York, 1986).

[2]R.X. Ynzunza, E.D. Tober, F.J. Palomares, Z. Wang, H. Xiao, F. Zhang, Z. Hussain and C.S. Fadley, (to be published).

APPENDIX C: Monochromator Calculations

Michette[1] and Kunz *et al.*[2] are good references for a detailed discussion of the Rowland circle optical configuration, including image distortion and focusing. Here, the Rowland circle will be discussed with regard to BL 9.3.2. Figure C1 illustrates how the Rowland circle applies to BL 9.3.2. The grating radius, R_G, is fixed at 55 m; thus, the Rowland circle radius, $R_G/2$, is fixed at 27.5 m.

For a spherical concave grating, the grating equation is the same as that for a plane grating[2]

$$\sin\alpha + \sin\beta = \frac{(\pm m)\lambda}{d} \tag{C1}$$

where α and β are the incident and reflected angles, respectively, as measured normal to the grating surface at its center, λ is the wavelength of the light, m is an integer specifying the diffraction order and is positive if $|\alpha| > |\beta|$, and d is the spacing between lines on the grating. For the 100 $^{\text{lines}}/_{\text{mm}}$ grating, d is 1.00×10^5 Å; for the 600 $^{\text{lines}}/_{\text{mm}}$ grating, d is 1.67×10^4 Å; for the 1200 $^{\text{lines}}/_{\text{mm}}$ grating, d is 8.33×10^3 Å.

BL 9.3.2 is a fixed included-angle Rowland circle spherical grating monochromator (SGM). The condition holds that

$$\alpha - \beta = 2\theta \tag{C2}$$

where 2θ is the included angle ($2\theta = 174°$ for BL 9.3.2). An alternative design, the variable included-angle SGM, does not conform to the Rowland

circle geometry.[3] The included angle is determined by considering such things as the grating radius and the desired reflectivity, i.e., the highest desired photon energy for a given line spacing. Equation (C2) is written $\alpha - \beta$ because β is defined to be negative. This sign convention follows from the definitions of the outside order and the inside order.[1,2,4]

By using the trigonometric identity

$$\sin\alpha + \sin\beta = 2\sin\left[\tfrac{1}{2}(\alpha+\beta)\right]\cos(\alpha-\beta) \tag{C3}$$

equations (C1) and (C2) can be solved simultaneously and to determine α and β.

$$\alpha = \sin^{-1}\left[\frac{m\lambda}{2d\cos\theta}\right] + \theta \tag{C4a}$$

$$\beta = \sin^{-1}\left[\frac{m\lambda}{2d\cos\theta}\right] - \theta \tag{C4b}$$

For a known line density and a known inclusion angle, the slit positions can now be calculated for given photon energy. The focus condition for the Rowland circle mounted SGM in the dispersion plane is defined as

$$\frac{\cos^2\alpha}{r_{S1}} - \frac{\cos\alpha}{R_G} + \frac{\cos^2\beta}{r_{S2}} - \frac{\cos\beta}{R_G} = 0 \tag{C5}$$

where r_{S1} and r_{S2} are the distances from the grating center to S1 and S2 respectively.

The Rowland circle condition is a special case of the focus condition where

$$r_{S1} = R_G \cos\alpha \tag{C6a}$$

$$r_{S2} = R_G \cos\beta \tag{C6b}$$

The effects of aberrations on the resolution, including the primary coma, the spherical aberration, the line curvature and the slit-width, can be calculated using the discussion by Hogrefe, *et al.*[4] along with a discussion by Howells in section 5 of the X-Ray Data Booklet.[5] The wavelength broadening due to the *primary coma* is described by

$$\Delta\lambda_{PC} = \frac{3w^2 d}{2m}\Sigma\left(\frac{T_{S1}\sin\alpha}{r_{S1}}\right) \tag{C7}$$

The wavelength broadening due to the *spherical aberration* is described by

$$\Delta\lambda_{SA} = \frac{w^3 d}{2m}\Sigma\left(\frac{4T_{S1}\sin^2\alpha}{(r_{S1})^2} - \frac{(T_{S1})^2}{r_{S1}} + \frac{S_{S1}}{(R_G)^2}\right) \tag{C8}$$

Assuming a point source illumination, the wavelength broadening due to the *line curvature* is described by

$$\Delta\lambda_{LC} = \frac{\ell^2 d}{2m}\left[\Sigma\left(\frac{S_{S1}\sin\alpha}{r_{S1}}\right) - \frac{2\sin\beta}{r_{S1}}\Sigma(S_{S1}) + \sin\beta\left(\Sigma(S_{S1})\right)^2\right] \tag{C9}$$

When discussing the broadening due to the finite slit width, Hogrefe, *et al.*[4] consider the entrance slit. However, Reich, *et al.* suggest that the slit-width limited resolution is due to the exit slit for a toroidal grating.[6] From experience, it is known that both slit-widths affect the resolution. By quadratically summing the contribution from each slit, the *slit-width* limited resolution is described by

$$\Delta\lambda_{SW} = \sqrt{\Sigma\left[\left(\frac{W_{S1} d \cos\alpha}{m r_{S1}}\right)^2\right]} \qquad \text{(C10)}$$

where W_{S1} is the width of the entrance slit. For these equations, the Σ indicates that a second term must be added to the first term such that $r_{S1} \Rightarrow r_{S2}$, $\alpha \Rightarrow \beta$, $T_{S1} \Rightarrow T_{S2}$, $S_{S1} \Rightarrow S_{S2}$, and $W_{S1} \Rightarrow W_{S2}$. The variables T and S are described by

$$T_{S1} = \frac{\cos^2\alpha}{r_{S1}} - \frac{\cos\alpha}{R_G(w)} \qquad \text{(C11a)}$$

$$S_{S1} = \frac{1}{r_{S1}} - \frac{\cos\alpha}{R_G(\ell)} \qquad \text{(C11b)}$$

Note that a sphere is a special case of a toroid where $R_G(\ell) = R_G(w)$.

As discussed in the text, BL 9.3.2 operates in one of three modes: Fixed Slits, Fixed Entrance Slit, and Rowland Circle. Using equations (C7), (C8), (C9), and (C10), the theoretical resolution of the monochromator is plotted in figures C3, C4, and C5. The resolving power is defined as

$$\text{Resolving Power} = \frac{\lambda}{\Delta\lambda} = \frac{E}{\Delta E} \qquad \text{(C12)}$$

thus allowing for calculating in terms of wavelength and then converting to energy for a convenient plot. The conversion factor for converting eV to Å is 12398.54 eV·Å. Figures C3, C4, and C5 plot ΔE_{FWZH} (Full-Width Zero Height) vs. E for each aberration and the slit-width limit as well as the sum of all the effects for each grating. One can see in figures C3, C4, and C5 that the slit limited resolution can be approached only when the Rowland circle condition is satisfied. The entrance and exit slit widths were fixed at 10 μm for all calculations. Note that 'G' indicates the grating center.

Figure C2 plots the theoretical resolution for the 100 $^{lines}/_{mm}$ grating. The calculation in C2a was completed with both slits fixed; S1 was fixed 1.95 m upstream from G and S2 was fixed 3.81 m downstream from G. These slit positions satisfy the Rowland circle condition for 70 eV as can be seen on the plot (the primary coma drops to zero). The calculation in C2b was completed in the Fixed Entrance Slit mode. S1 was fixed at the M2 focus, 1.68 m upstream from G. The exit slit was allowed to scan from 3.7 m to 4.7 m downstream from G to maintain the focus condition dictated by equation (C5). With the entrance slit fixed at 1.68 m upstream from G, the Rowland circle condition is satisfied at 54.4 eV. The calculation in C2c satisfies the Rowland circle condition by allowing both slits to move as dictated by equations (C6a) and (C6b). Although the total energy range calculated matched the range for figures C2a and C2b, the Rowland circle condition was only satisfied from 44.9 eV to 76.7 eV due to the limited travels of S1 and S2. The entrance slit was allowed to vary from 1.43 m to 2.03 m upstream of the grating; the exit slit travel limits were the same as figure C3b. Note that for figures C2b and C2c, when a slit position was calculated to be outside the allowed travel range, it was simply fixed at the extremum closest to the calculated value.

Figure C3 plots the theoretical resolution for the 600 $^{lines}/_{mm}$ grating. The calculation in C3a was completed with both slits fixed; S1 was fixed 1.90 m upstream from G and S2 was fixed 3.85 m downstream from G. These slit positions satisfy the Rowland circle condition for 400 eV as can be seen on the plot (the primary coma drops to zero). The calculation in C3b was completed in the Fixed Entrance Slit mode. S1 was fixed at the M2 focus, 1.68 m upstream from G. The exit slit was allowed to scan from 3.7 m to 4.7 m downstream from G to maintain the focus condition dictated by equation (C5). With the entrance slit fixed at 1.68 m upstream from G, the Rowland circle condition is satisfied at 326 eV. The calculation in C3c satisfies the Rowland circle condition by allowing both slits to move as dictated by equations (C6a) and (C6b). Although the total energy range calculated matched the range for figures C3a and C3b, the Rowland circle condition was only satisfied from 269.7 eV to 460.3 eV due to the limited travels of S1 and S2. The entrance slit was allowed to vary from 1.43 m to 2.03 m upstream of the grating; the exit slit travel limits were the same as figure C3b. Note that for figures C3b and C3c, when a slit position was calculated to be outside the allowed travel range, it was simply fixed at the extremum closest to the calculated value.

Figure C4 plots the theoretical resolution for the 1200 $^{lines}/_{mm}$ grating. The calculation in C4a was completed with both slits fixed; S1 was fixed 1.90 m upstream from G and S2 was fixed 3.85 m downstream from G. These slit positions satisfy the Rowland circle condition for 800 eV as can be seen on the plot (the primary coma drops to zero). The calculation in C4b was completed in the Fixed Entrance Slit mode. S1 was fixed at the M2 focus, 1.68 m upstream from G. The exit slit was allowed to scan from 3.7 m to 4.7 m downstream from G to maintain the focus condition dictated by

equation (C5). With the entrance slit fixed at 1.68 m upstream from G, the Rowland circle condition is satisfied at 652 eV. The calculation in C4c satisfies the Rowland circle condition by allowing both slits to move as dictated by equations (C6a) and (C6b). Although the total energy range calculated matched the range for figures C4a and C4b, the Rowland circle condition was only satisfied from 539.4 eV to 920.5 eV due to the limited travels of S1 and S2. The entrance slit was allowed to vary from 1.43 m to 2.03 m upstream of the grating; the exit slit travel limits were the same as figure C4b. Note that for figures C4b and C4c, when a slit position was calculated to be outside the allowed travel range, it was simply fixed at the extremum closest to the calculated value.

REFERENCES

[1]A.G. Michette, *Optical Systems for Soft X-Rays*, (Plenum Press, New York, 1986).

[2]C. Kunz, *Topics in Current Physics: Synchrotron Radiation, Techniques and Applications*, (Springer-Verlag, Berlin, 1979).

[3]H. Petersen, F. Senf, F. Schäfers and J. Bahrdt, Rev. Sci. Instrum. **66**, 1777(1995).

[4]H. Hogrefe, M.R. Howells and E. Hoyer, SPIE **733**, 274(1986).

[5]J. Kirz, D.T. Attwood, B.L. Henke, M.R. Howells, K.D. Kennedy, K.-J. Kim, J.B. Kortright, R.C. Perera, P. Pianetta, J.C. Riordan, J.H. Scofield, G.L. Stradling, A.C. Thompson, J.H. Underwood, D. Vaughan, G.P. Williams and H. Winick, *X-Ray Data Booklet*, Center for X-Ray Optics, Lawrence Berkeley Laboratory, PUB-490 Rev., (1986).

[6]T. Reich, Z. Hussain, E. Moler, M. Blackwell, G. Kaindl, D.A. Shirley and M.R. Howells, Rev. Sci. Instrum. **64**, 2552(1993).

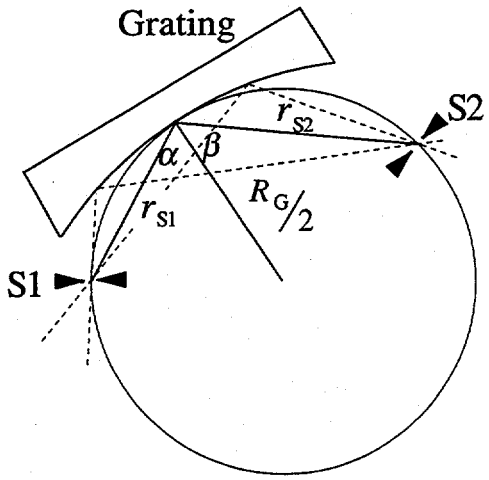

Illustration of how the Rowland circle applies to BL 9.3.2. The grating radius, R_G, is fixed at 55 m; thus, the Rowland circle radius, $R_G/2$, is fixed at 27.5 m.

Figure C1

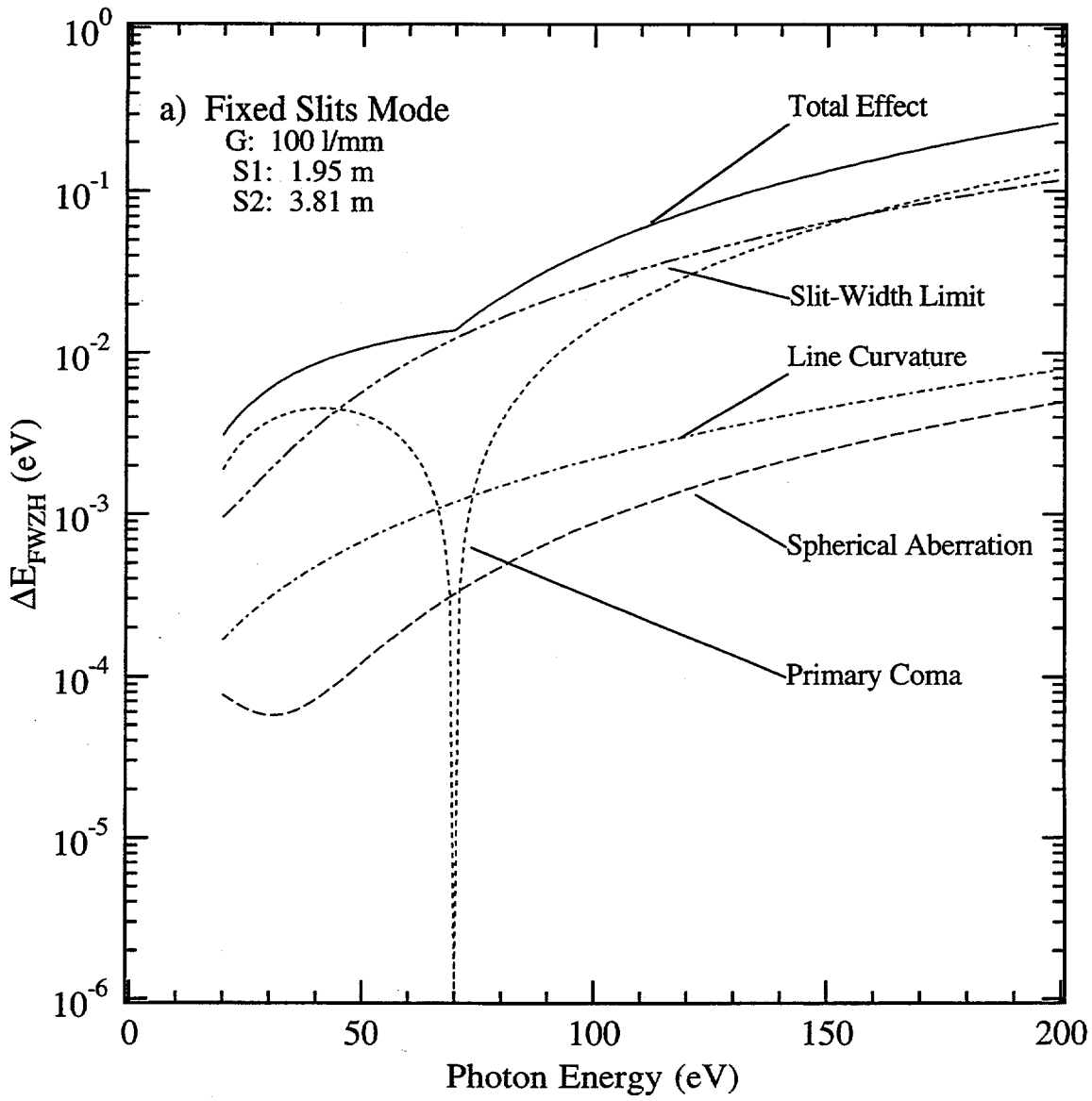

Calculation in Fixed Slits mode for the 100 $^{lines}/_{mm}$ grating. S1 was fixed at 1.95 m upstream from G and S2 was fixed at 3.81 m downstream from G. These positions satisfy the Rowland circle condition at 54.4 eV as evidenced by the primary coma dropping to zero at this energy. The entrance and exit slit widths were set to 10 μm.

Figure C2a

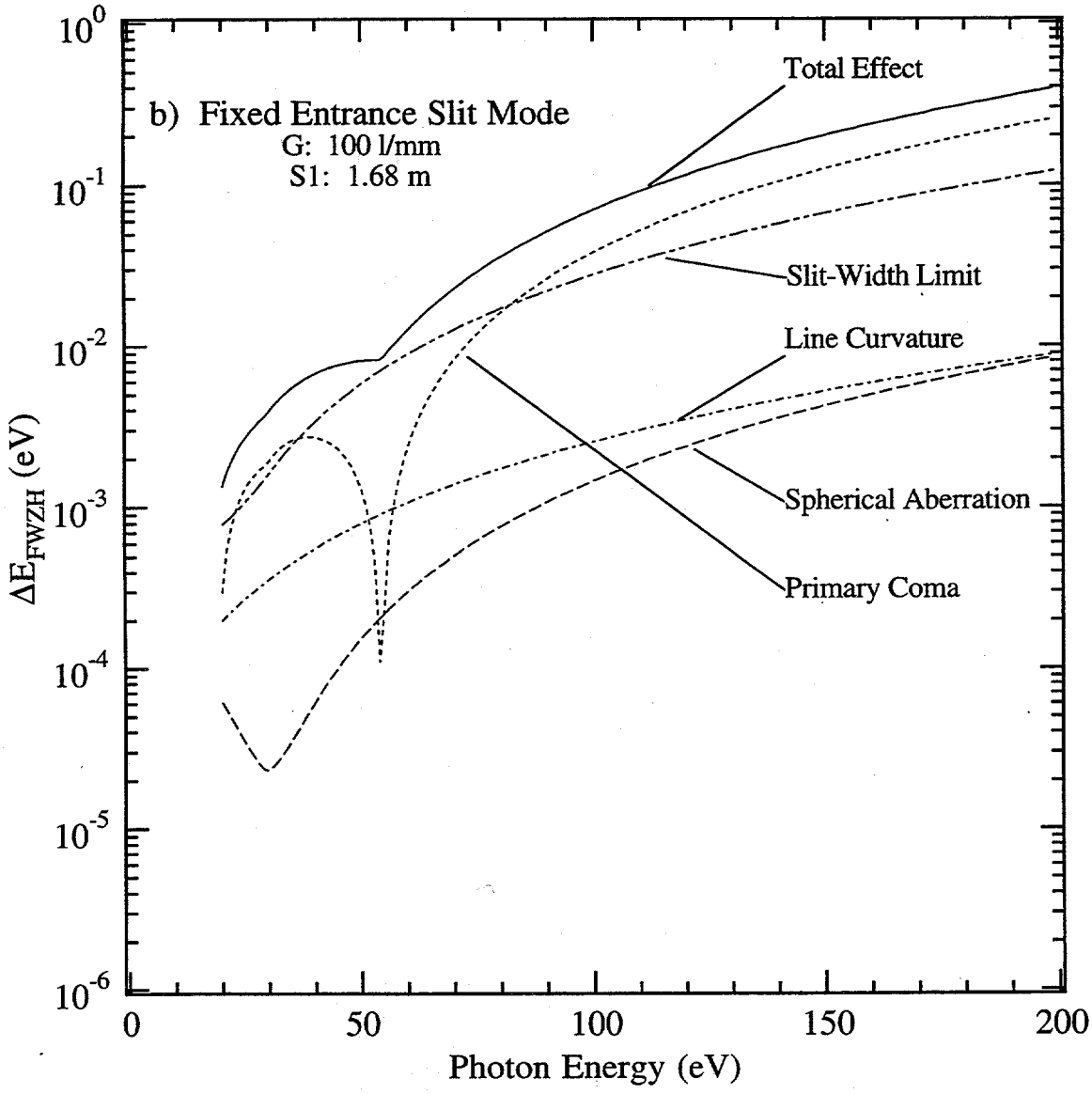

Calculation in Fixed Entrance Slit mode for the 100 $^{lines}/_{mm}$ grating. S1 was fixed at the M2 focus, 1.68 m upstream from G, and S2 was allowed to vary from 3.7 m to 4.7 m downstream from G. With S1 at 1.68 m, the Rowland circle condition is satisfied at 400 eV as evidenced by the primary coma dropping to zero at this energy. If the S2 position was calculated to be outside the allowed travel range, it was fixed at the extremum closest to the calculated value. The entrance and exit slit widths were set to 10 μm.

Figure C2b

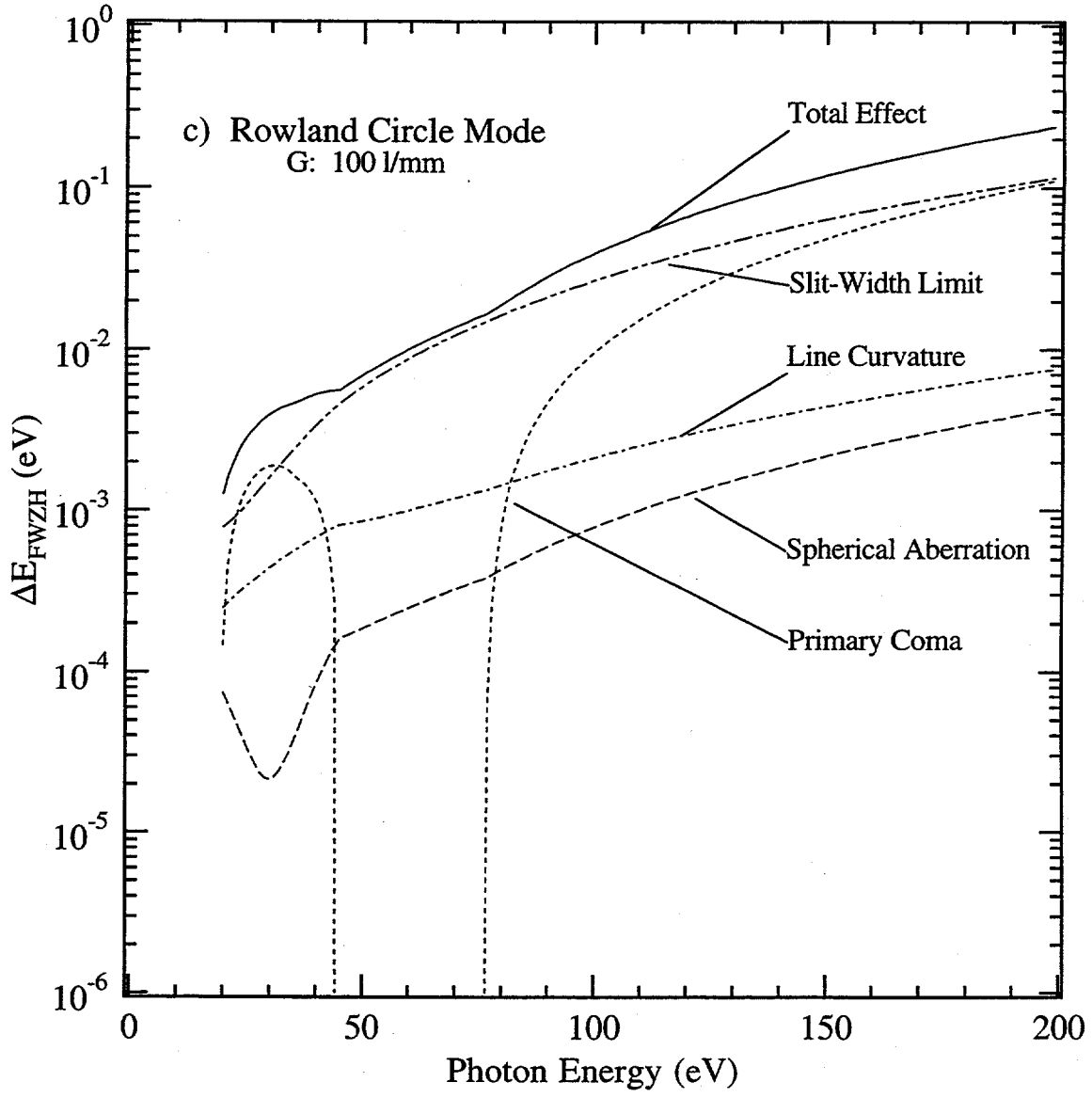

Calculation in Rowland Circle mode for the 100 $^{lines}/_{mm}$ grating. S1 was allowed to vary 1.43 m to 2.03 m upstream from G and S2 was allowed to vary 3.7 m to 4.7 m downstream from G. Although the energy range calculated matched that for figures C2a and C2b, the Rowland circle condition was only satisfied from 44.9 eV to 76.7 eV as evidenced by the primary coma dropping to zero in this range. If the S1 or the S2 position was calculated to be outside the allowed travel range, it was fixed at the extremum closest to the calculated value. The S1 and S2 slit widths were set to 10 μm.

Figure C2c

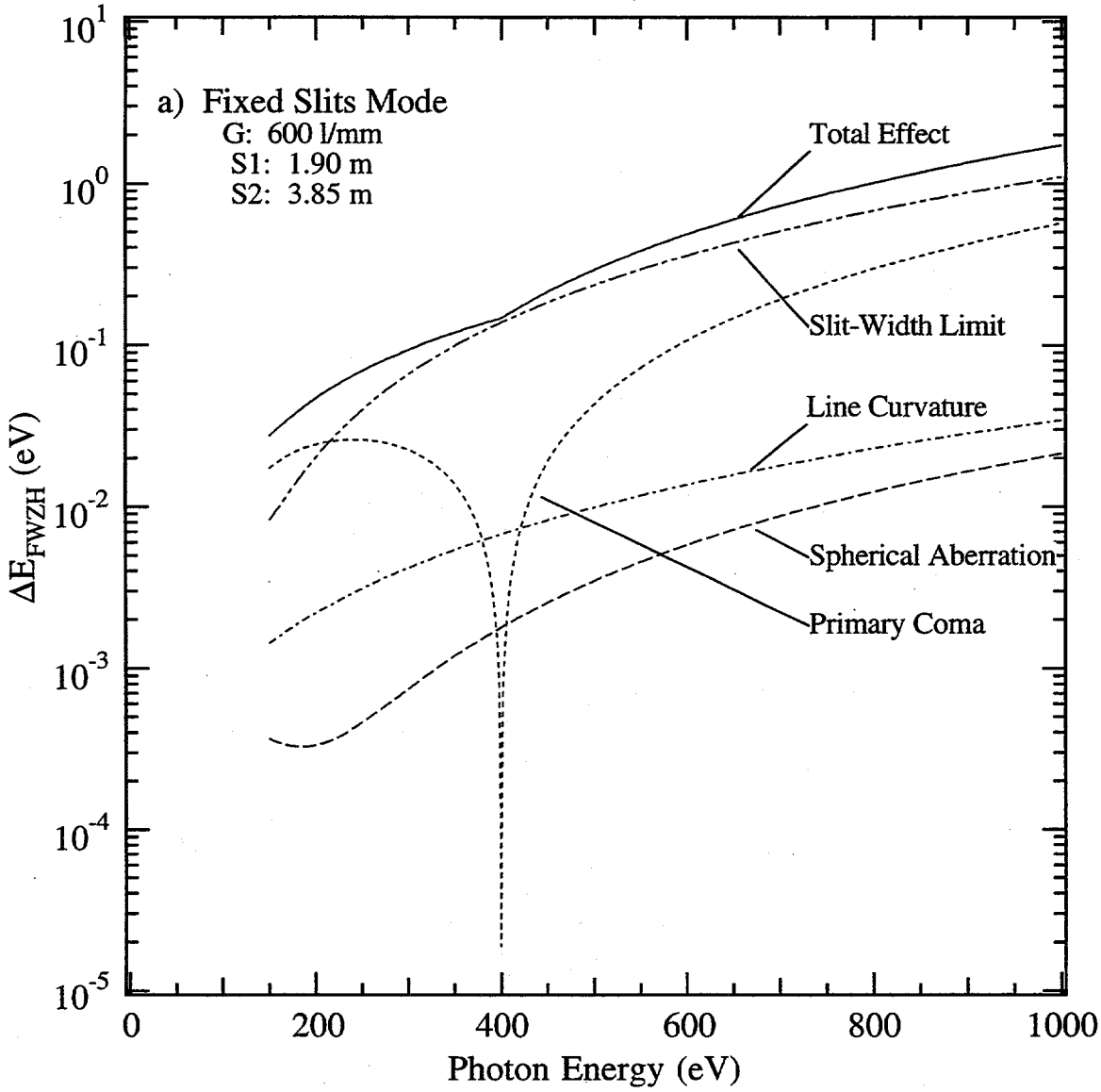

Calculation in Fixed Slits mode for the 600 $^{lines}/_{mm}$ grating. S1 was fixed at 1.90 m upstream from G and S2 was fixed at 3.85 m downstream from G. These positions satisfy the Rowland circle condition at 400 eV as evidenced by the primary coma dropping to zero at this energy. The entrance and exit slit widths were set to 10 μm.

Figure C3a

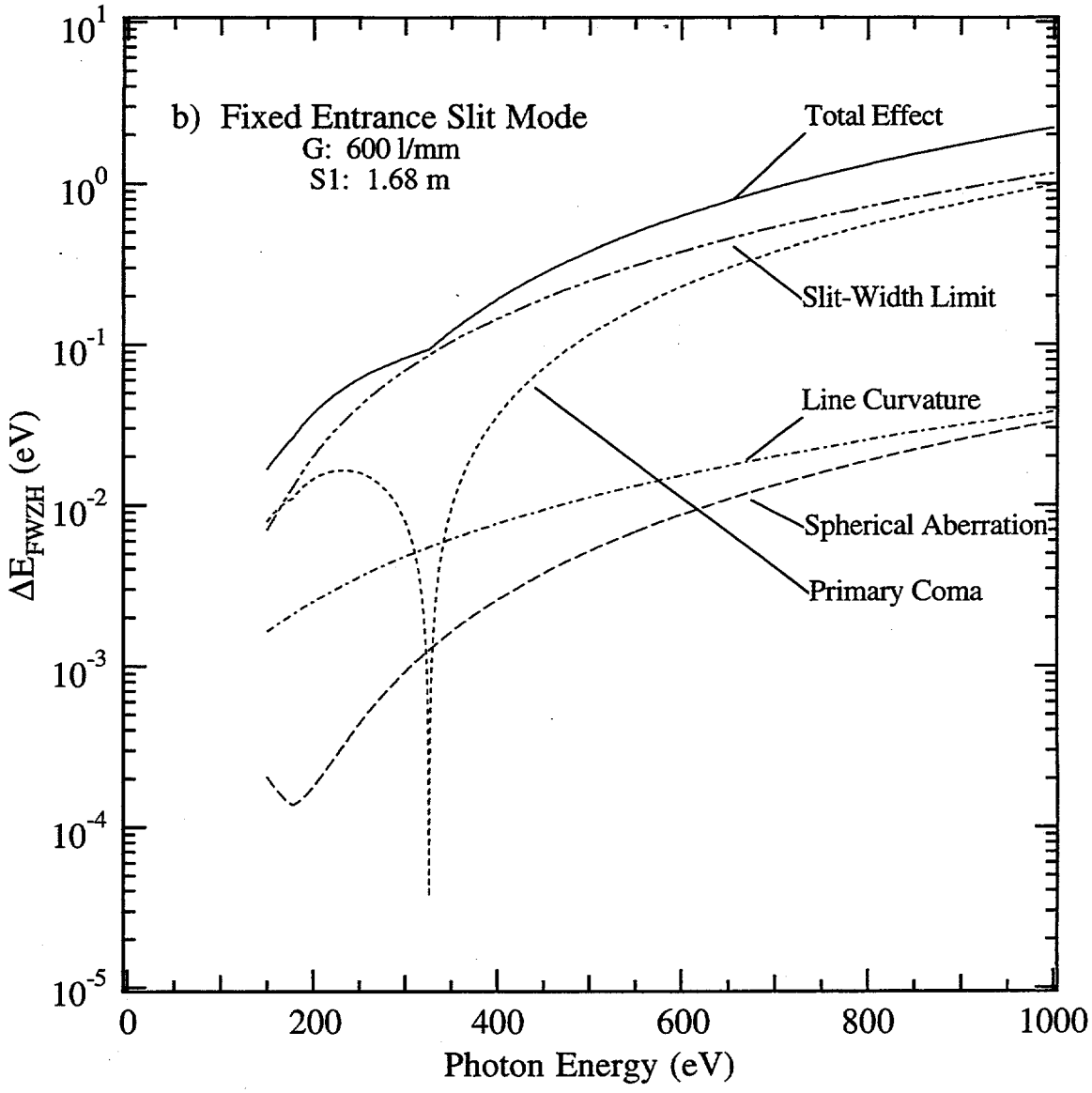

Calculation in Fixed Entrance Slit mode for the 600 $^{lines}/_{mm}$ grating. S1 was fixed at the M2 focus, 1.68 m upstream from G, and S2 was allowed to vary from 3.7 m to 4.7 m downstream from G. With S1 at 1.68 m, the Rowland circle condition is satisfied at 326 eV as evidenced by the primary coma dropping to zero at this energy. If the S2 position was calculated to be outside the allowed travel range, it was fixed at the extremum closest to the calculated value. The entrance and exit slit widths were set to 10 μm.

Figure C3b

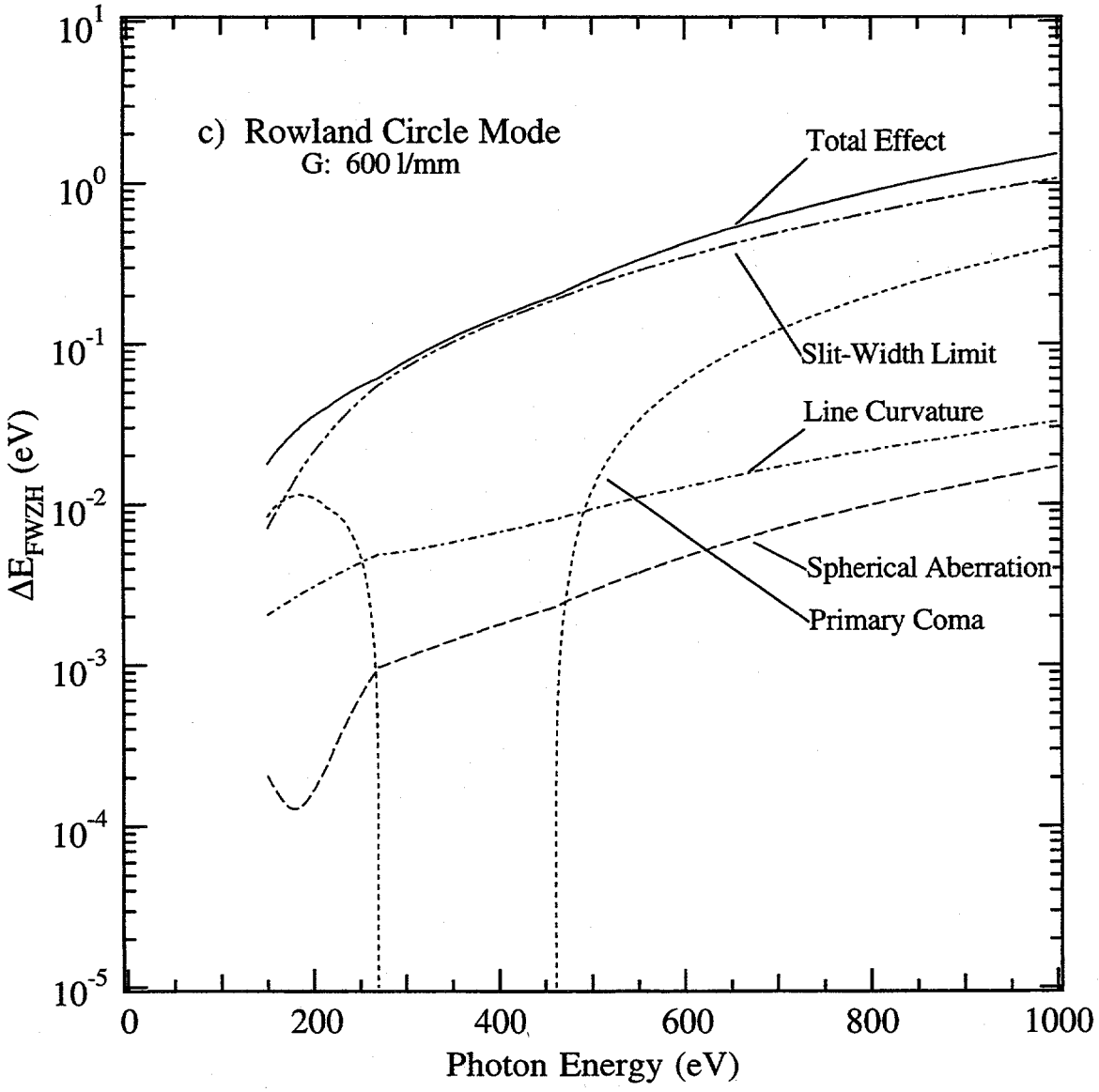

Calculation in Rowland Circle mode for the 600 $^{lines}/_{mm}$ grating. S1 was allowed to vary 1.43 m to 2.03 m upstream from G and S2 was allowed to vary 3.7 m to 4.7 m downstream from G. Although the energy range calculated matched that for figures C3a and C3b, the Rowland circle condition was only satisfied from 269.7 eV to 460.3 eV as evidenced by the primary coma dropping to zero in this range. If the S1 or the S2 position was calculated to be outside the allowed travel range, it was fixed at the extremum closest to the calculated value. The S1 and S2 slit widths were set to 10 μm.

Figure C3c

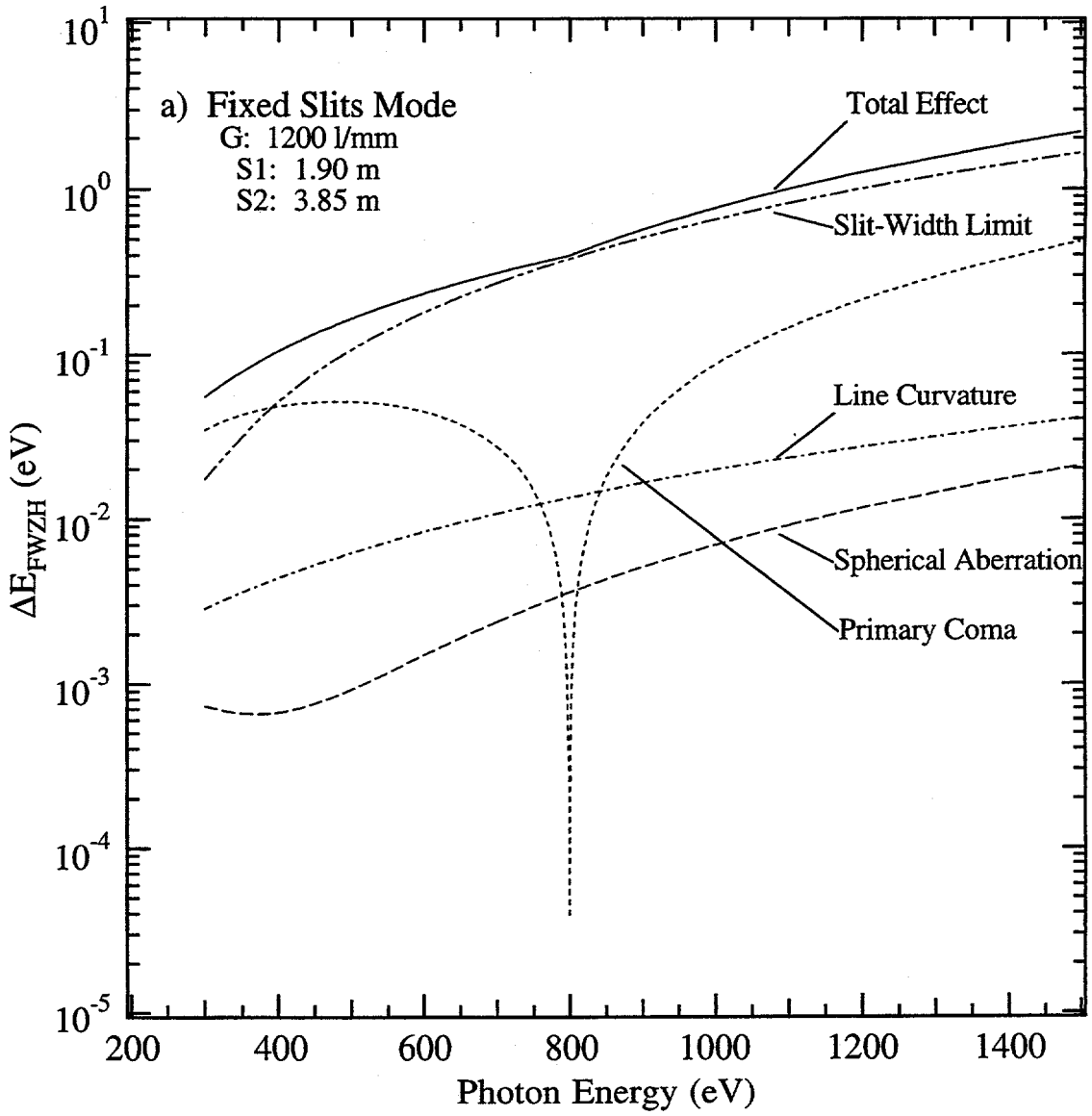

Calculation in Fixed Slits mode for the 1200 $^{lines}/_{mm}$ grating. S1 was fixed at 1.90 m upstream from G and S2 was fixed at 3.85 m downstream from G. These positions satisfy the Rowland circle condition at 800 eV as evidenced by the primary coma dropping to zero at this energy. The entrance and exit slit widths were set to 10 μm.

Figure C4a

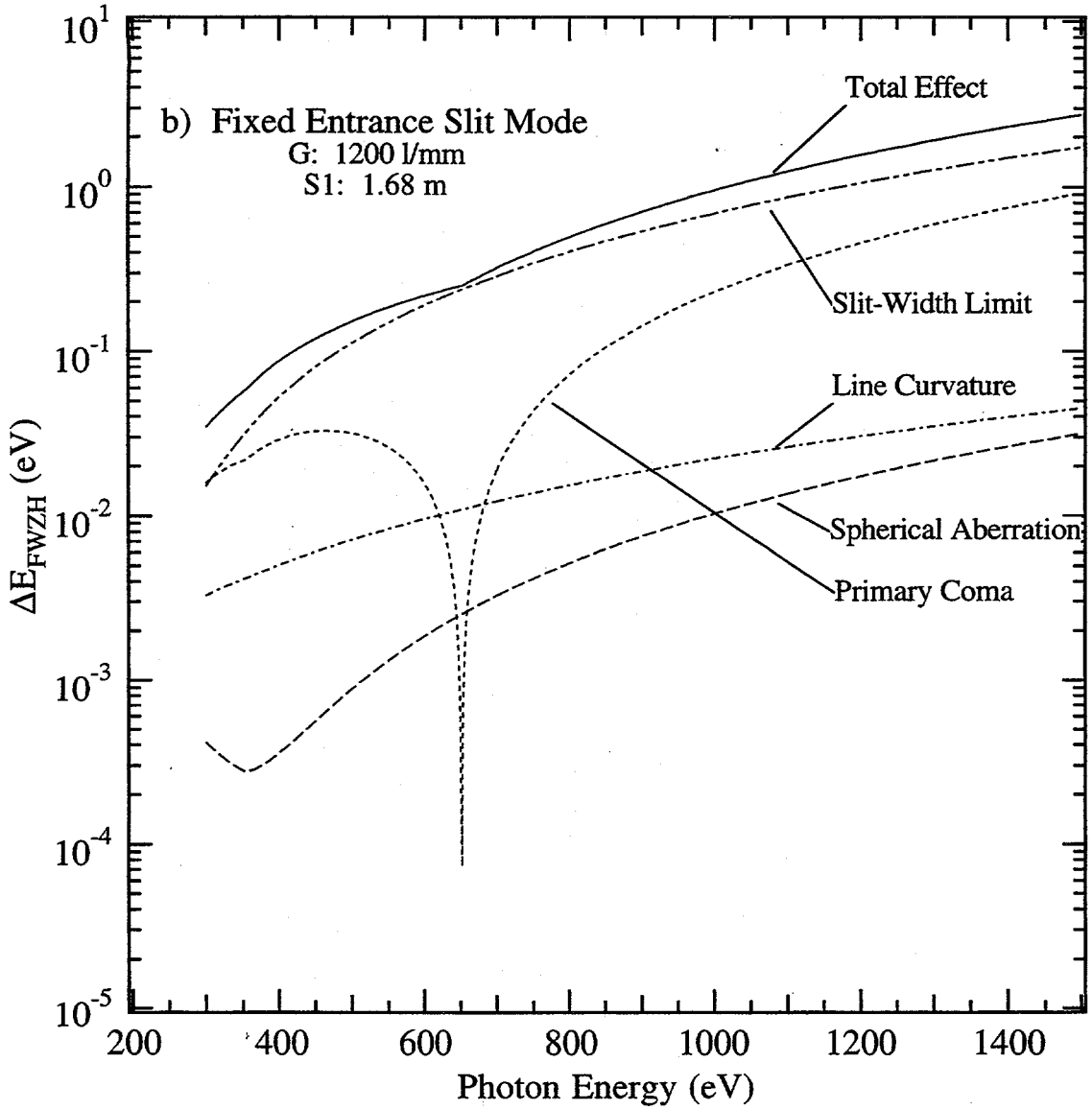

Calculation in Fixed Entrance Slit mode for the 1200 $^{lines}/_{mm}$ grating. S1 was fixed at the M2 focus, 1.68 m upstream from G, and S2 was allowed to vary from 3.7 m to 4.7 m downstream from G. With S1 at 1.68 m, the Rowland circle condition is satisfied at 652 eV as evidenced by the primary coma dropping to zero at this energy. If the S2 position was calculated to be outside the allowed travel range, it was fixed at the extremum closest to the calculated value. The entrance and exit slit widths were set to 10 μm.

Figure C4b

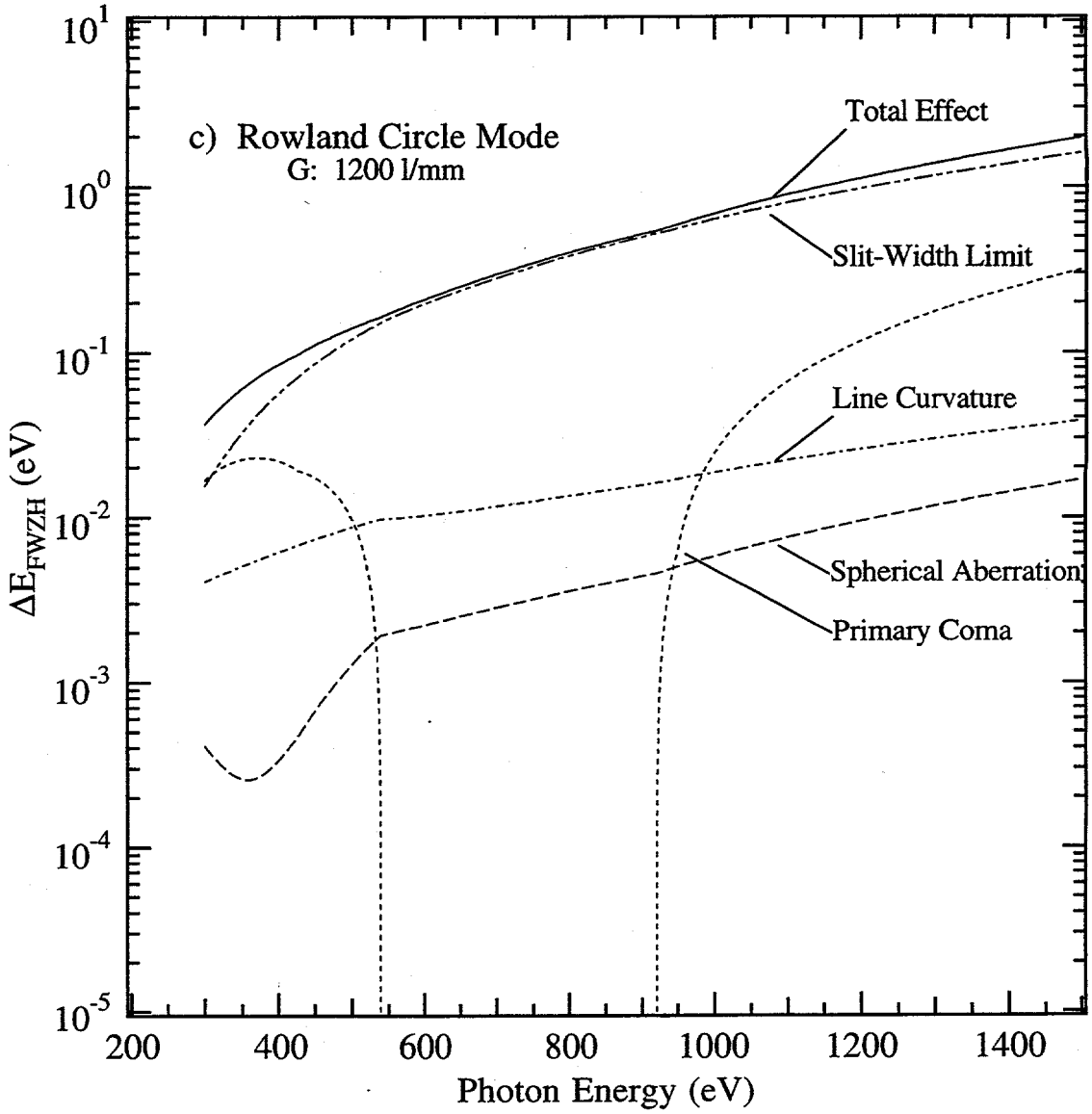

Calculation in Rowland Circle mode for the 1200 $^{lines}/_{mm}$ grating. S1 was allowed to vary 1.43 m to 2.03 m upstream from G and S2 was allowed to vary 3.7 m to 4.7 m downstream from G. Although the energy range calculated matched that for figures C4a and C4b, the Rowland circle condition was only satisfied from 539.4 eV to 920.5 eV as evidenced by the primary coma dropping to zero in this range. If the S1 or the S2 position was calculated to be outside the allowed travel range, it was fixed at the extremum closest to the calculated value. TheS1 and S2 slit widths were set to 10 μm.

Figure C4c

APPENDIX D: Circular Polarization Calculations and Measurements

A. Calculations

Calculations were performed to determine how the flux and the degree of circular polarization vary as a function of photon energy for different beam-stop sizes introduced in the orbit plane. This beam-stop is used to exclude the horizontal polarization component.[1] As discussed in the text, different beam-stop sizes are introduced by a water-cooled, movable aperture which defines the lower (or upper) acceptance angle. The parallel polarized component (s) is at a maximum in the orbit plane and the perpendicular polarized component (p) is zero in the orbit plane but maximum at a small angle out of the plane. The value of the small angle where this maximum occurs is dependent on the photon energy. The beamline accepts radiation in the vertical direction from a lower angle, Ψ_l, defined by the position of the movable aperture to an upper angle, Ψ_u, defined by a mirror, a grating, or perhaps a real aperture. The flux through the aperture, F_a, is defined by

$$F_a = \int_{\Psi_l}^{\Psi_u} \frac{dF}{d\Psi} d\Psi \qquad \text{(D1)}$$

where $\frac{dF}{d\Psi}$ is the flux per unit vertical aperture as a function of the out of plane angle Ψ and depends on the machine energy, the photon energy, the critical photon energy, the bending field strength, as well as the s and p polarized light components.[2]

$$\frac{dF}{d\psi} = 1.327 \times 10^{13} \left[\frac{VE}{E_c} \right]^2 \times \left[1 + X^2 \right] \times \left[A_h^2 + A_v^2 \right] \qquad \text{(D2)}$$

where V (GeV) is the machine energy, E (eV) is the photon energy, and E_c (eV) is the critical photon energy. For a bending magnet, $E_c = 655 V^2 B$ where $B(V,\rho)$ (T) is the bending magnet field strength and ρ (m) is the bend radius, 4.8 m for the *non*-superconducting magnets at the ALS. $X = \gamma\psi$ where $\gamma \equiv {}^{V}/_{m_e c^2}$, m_e is the electron mass $\left(5.11 \times 10^{-4}\ {}^{GeV}/_{c^2}\right)$ and c is the velocity of light. A_h and A_v represent the s and p polarized light components, respectively, such that

$$A_h = K_{2/3}(\xi) \qquad \text{(D3a)}$$

$$A_v = \frac{X}{\sqrt{1+X^2}} K_{1/3}(\xi) \qquad \text{(D3b)}$$

where

$$\xi = \frac{E}{2E_c}\left(1+X^2\right)^{3/2} \qquad \text{(D4)}$$

and the K's are modified Bessel functions of the second kind.

Considering only half-apertures above (or below--the argument is the same with simply the 'upper' and 'lower' reversed) the plane of the ring, ψ_ℓ is defined by the position of the aperture. The aperture is 13.4 m downstream from the source and is indicated on figure 1 of the main text. ψ_u is defined by the acceptance of M2, ϕ_{M2}, which is constant (0.6 mrad) or the acceptance of the grating, ϕ_G, which is a function of the photon

energy, the grating width, and the beamline geometry. Accounting for the magnification of M2 (discussed in Appendix B),

$$\phi_G = \frac{w}{r_{S1,G}} \cos\left(\alpha \frac{r_{M2,S1}}{r_{S,M2}} \right) \tag{D5}$$

where w is the illuminated width of the grating and α is the angle of incidence on the grating (see Appendix C for a discussion). $r_{S,M2}$ is the source to M2 distance, $r_{M2,S1}$ is the M2 to entrance slit distance, and $r_{S1,G}$ is the entrance slit to grating distance. Although one may think in terms of 'length' being the longitudinal size of the grating, w (indicative of the number of illuminated grooves) was chosen to be consistent with the resolution calculations discussed in Appendix C and references therein. Thus, ψ_u is defined by the lesser of the two values ϕ_{M2} and ϕ_G. It should be noted that for the polarization measurements discussed below, M3 was a defining aperture at lower photon energies because its longitudinal length was so short. For the calculations compared with these measurements, an effective $\phi_{M2-eff} = 0.5$ mrad was used. M3 has since been replaced with a larger mirror and is no longer an aperture.

Figure D1 graphs the total calculated flux from equation (D1) considering a grating line density of 600 $^{lines}/_{mm}$, a fixed included angle of 174°, and operated in the $m = +1$ diffraction order. Figure D2 plots the calculated fraction of the total emitted flux accepted by the aperture. The half-apertures of the central stop are shown ranging from 0.0 to 0.5 mrads. Larger central stop sizes cause a significant flux reduction, especially at high energies.

The degree of circular polarization, P_C, where

$$P_C = \sqrt{1 - \left(\frac{F_s - F_p}{F_s + F_p}\right)^2} \tag{D6}$$

and F_s and F_p are the s and p polarized fluxes, respectively, was calculated as a weighted average of the circular polarization over the aperture. The weighting is due to the change in intensity of the s and p polarized components across the aperture. Thus,

$$\langle P_C \rangle_a = \frac{1}{F_a} \int_{\psi_l}^{\psi_u} P_c(\psi) \frac{dF}{d\psi} d\psi \tag{D7}$$

Figure D3 plots the calculated average degree of circular polarization for the aperture. For the largest stop size, the degree of circular polarization is greater than 0.9. Even with no stop, it is typically greater than 0.6 throughout the energy range.

To optimize the balance between the flux and the circular polarization, it is useful to calculate the merit function as described by

$$M = \langle P_C \rangle_a \sqrt{F_a / F_t} \tag{D8}$$

where F_t is the total flux radiated by the source at the defined photon energy (see figure D4). The half-apertures of the central stop are shown ranging from 0.0 to 0.5 mrads. The merit functions over the half-aperture sizes 0.0, 0.1, and 0.2 mrads are within 10% of each other over the entire energy range. This insensitivity is caused by the balance of decreasing flux and increasing degree of circular polarization.

B. Measurements

Polarization and intensity measurements as a function of the vertical aperture were made using a recently developed multilayer polarimeter.[3,4] The polarimeter can utilize both a transmission multilayer phase retarder and a reflection polarizer or analyzer. Some recent polarimetry measurements using multilayers have used a retarder to help distinguish between possible unpolarized and circularly polarized radiation.[5,6] A retarder was not used for the measurements presented here; the degree of unpolarized radiation was found to be immeasurably small. The retarder also enables the distinction between left and right circularly polarized radiation, which is not problematic for bend-magnet radiation.

Three multilayers with constant period were mounted on the polarizer stage. These were translatable to illuminate the different optics allowing polarimetry measurements at 367 eV and 722 eV without breaking vacuum. The beamline was tuned to these photon energies using the 600 $^{lines}/_{mm}$ grating; the storage ring was operating at 1.9 GeV. The polarimeter was mounted in tandem with the APESD chamber. Fine adjustment of the polarimeter was accomplished with its own translation and tilt stages. Because the polarimeter was not at the M3 focus, the vertical position of its 2 mm entrance pinhole was re-optimized as the upstream vertical aperture position was changed to maximize flux through the pinhole.

Standard rotating analyzer ellipsometry techniques and expressions were used to collect and analyze the data.[7] The data collected were the intensity entering the polarimeter (measured as a mesh current) and analyzer scans which record the intensity reflected from the polarizer as it rotates

azimuthally about the beam direction. The reflected intensity normalized by the incident intensity as a function of azimuthal angle, α, is given by

$$I(\alpha) = S_0 \frac{R_s + R_p}{2} + \left[S_1 \cos(2\alpha) + S_2 \sin(2\alpha)\right] \frac{R_s - R_p}{2} \qquad \text{(D9)}$$

where R_s and R_p are the reflectivities of the s and p polarized radiation component from the polarizer. S_0, S_1, and S_2 are the first three of four Stokes parameters which define the intensity and polarization state of the beam. Thus, the degree of linear polarization, P_L, was measured directly.

$$P_L = \frac{\left(S_1^2 + S_2^2\right)^{1/2}}{S_0} \qquad \text{(D10)}$$

For all measurements reported here, the linear component at ±45°, S_2, is negligible compared to the linear component at 0° and 90°, S_1.

Circular polarization is represented by the fourth Stokes parameter, S_3. The degree of circular polarization, P_C, is

$$P_C = \frac{S_3}{S_0} \qquad \text{(D11)}$$

P_C is determined from

$$P_L^2 + P_C^2 + (\text{amount of unpolarized radiation}) = 1 \qquad \text{(D12)}$$

but the amount of unpolarized radiation was negligibly small. Since P_L and P_C add in quadrature, they can be regarded as representing the amplitudes of

the different polarization types and it is correct to refer to them as the *degree* of polarization and not the *percent* of polarization.

Polarimetry data taken as the narrow horizontal slit is stepped vertically across the beam are useful to determine the orbit plane, to set an upper limit on the amount of unpolarized radiation, and to measure the variation of polarization state with aperture position. Since the radiation is most linearly polarized in the plane of the electron orbit, measuring P_L as the narrow slit is scanned unambiguously determines the orbit plane. Using the maximum in an intensity measurement to determine the orbit plane can be misleading if the measurement is made downstream of optics that are poorly aligned with respect to the beam. Careful vertical alignment of each optical element in succession (using intensity signals) was conducted prior to polarimetry measurements presented below. After alignment, both intensity and polarization signals indicated that the optics were reasonably well centered on the beam.

Experimental and theoretical values for P_L and P_C vs. ψ at 367 eV and 722 eV are shown in figures D5a and D5b, respectively. In comparing theory with experiment, it was assumed that the incidence angles ($\leq$2.5°) at the beamline optics introduce negligible changes in the beam's polarization. At each energy, there is good agreement between measurement and theory out to large ψ values. This confirms that the beamline optics are well aligned. A more rapid fall in P_L with ψ is evident at higher energy as expected.

An upper limit to the degree of unpolarized radiation can be estimated from the experimental data alone. This is accomplished by determining the most linearly polarized portion of the beam measured and assuming that the remaining portion is unpolarized.[8] Assuming that this degree of unpolarized

radiation is constant with ψ allows a lower limit to P_C to be determined, even in the presence of possible unpolarized radiation. However, the theoretical calculations for a perfectly polarized source yield P_L values in excellent agreement with the measured values. This indicates that the remaining radiation is not unpolarized, but rather is the small amount of circularly polarized radiation entering the narrow slit due to its non-zero size. Thus, in this experimental determination of P_C from equation (D12), it is assumed that the amount of unpolarized radiation is zero. The true amount of unpolarized radiation present is less than the uncertainty in the measurement. With the narrow slit at $\psi = 0$ mrad, the theoretical value for P_L is 0.9993 and 0.991 for 367 and 722 eV, respectively.

Polarization and flux response to blocking the beam from above and below the horizon using the larger semi-aperture were investigated. Figures D6a and D6b show P_L, P_C, and the fractional flux measured at 367 eV and 722 eV, respectively, as a function of the semi-aperture position in the beam. For $\psi > 0$, the semi-aperture blocks the beam below the horizon; for $\psi < 0$, the semi-aperture blocks the beam above the horizon. Calculations were completed over an angular aperture roughly corresponding to that measured. An upper ψ limit of 0.5 and 0.6 mrad for 367 eV and 722 eV was assumed, respectively. At lower photon energies, the changing focal position of the spherical grating overfilled M3, causing it to act as an effective aperture. The flux data are the fraction of flux passing through the aperture normalized to the total flux if the aperture were positioned to pass the entire beam. Thus, the fractional flux has a value of 0.5 at $\psi = 0$ mrad.

The measured quantities are in generally good agreement with the theoretical calculations, although not as good as for the narrow slit. This is because the narrow slit has precisely determined edges defining a beam

which entirely enters the polarimeter entrance pinhole. For the semi-aperture, the high-angle limit is less well known and a smaller fraction of the wider beam actually enters the polarimeter. At 367 eV (figure D6a), the measured fractional flux falls more rapidly than that calculated. This results because radiation reflected from the ends of the overfilled M3 are not within the phase space acceptance of the polarimeter. Such a loss of intensity for off-axis rays systematically affects polarimetry results. This causes an increased P_L and decreased P_C as compared to calculations which ignore such effects. This systematic departure of measured results from calculated results is evident in figure D6a; a similar departure is evident at high positive ψ at 722 eV (figure D6b).

The values of P_L and P_C in figures D6a and D6b at $\psi = 0$ mrad equal those measured for a wide open aperture passing the entire vertical fan. Thus, radiation from different parts of the vertical fan add incoherently at the experiment, as expected. This results in a beam with a significant degree of linear as well as both left and right circularly polarized components. Experimenters should be aware of the presence of these different polarization components when accepting a wide vertical aperture.

The semi-aperture data allowed the investigation and optimization of the merit function described by equation D8. Using P_C and the fractional flux from figures D6a and D6b, the merit function was calculated for each semi-aperture position. These experimentally determined results are plotted along with the theoretical values for 367 eV and 722 eV in figures D7a and D7b, respectively. A shallow minimum at $\psi = 0$ mrad is predicted but does not appear to be observed experimentally. The systematic departure of measured results from calculated results mentioned above cause the measured merit function to fall more rapidly with ψ than predicted. The

merit function is optimized with the semi-aperture at or just beyond $\psi = 0$ mrad. If this merit function overrides other experimental considerations, experiments using left or right circular polarization are best illuminated with only roughly a factor of 2 loss in total intensity. For some experiments, a high value of P_C may be of greater value than this merit function, in which case a more restricted off-axis vertical aperture may be selected.

REFERENCES

[1]H.A. Padmore, Z. Hussain and Y. Zheng, *Selection of the Optimum Aperture Sizes for Circularly Polarized Spectroscopy on Beamline 9.3.2*, Lawrence Berkeley Laboratory, LSBL #218, (1993).

[2]K. Green, *Proposal for a National Synchrotron Light Source*, Brookhaven National Laboratory, BNL 50595, (1977).

[3]J.B. Kortright, M.A. Rice, Z. Hussain, H.A. Padmore, A.T. Young, A. Adamson, W.R.A. Huff, E.J. Moler, S.A. Kellar, R.X. Ynzunza, F.J. Palomares, H. Diamon, E.D. Tober and C.S. Fadley, Rev. Sci. Instrum. to be published, (1996).

[4]J.B. Kortright, M. Rice and K.D. Franck, Rev. Sci. Intrum. **66**, 1567(1995).

[5]H. Kimura, M. Yamamoto, M. Yanagihara, T. Maehara and T. Namioka, Rev. Sci. Intrum. **63**, 1379(1992).

[6]S. Di Fonzo, W. Jark, F. Schafers, H. Petersen, A. Gaupp and J.H. Underwood, Appl. Optics **33**, 2624(1994).

[7]E. Collett, *Polarized Light*, (Marcel Dekker, Inc., New York, 1993).

[8]R. Carr, J.B. Kortright, M. Rice and S. Lidia, Rev. Sci. Intrum. **66**, 1862(1995).

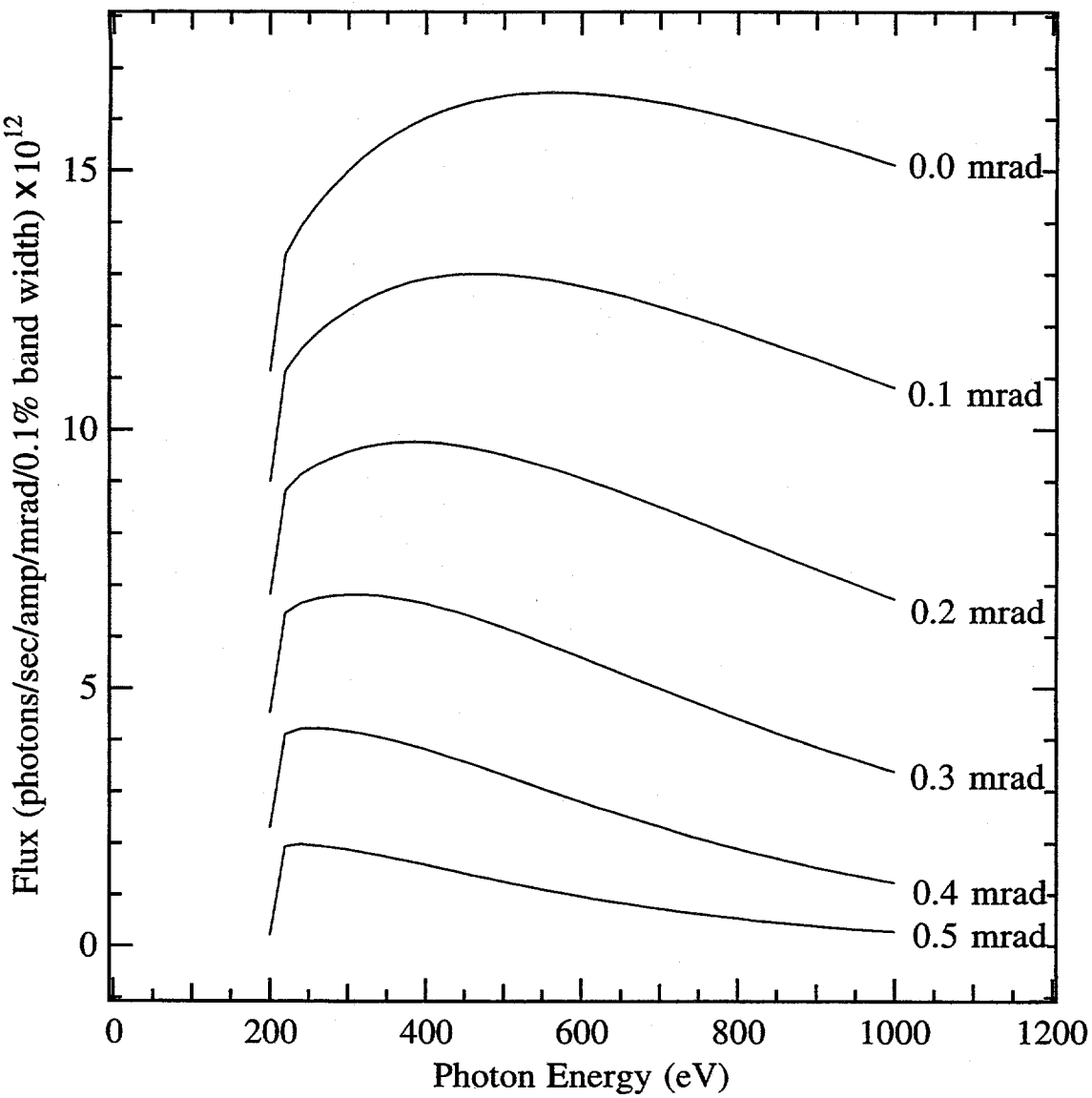

Total calculated flux from equation (D1) considering a grating line density of 600 $^{lines}/_{mm}$, a fixed included angle of 174°, and operated in the m=+1 diffraction order.

Figure D1

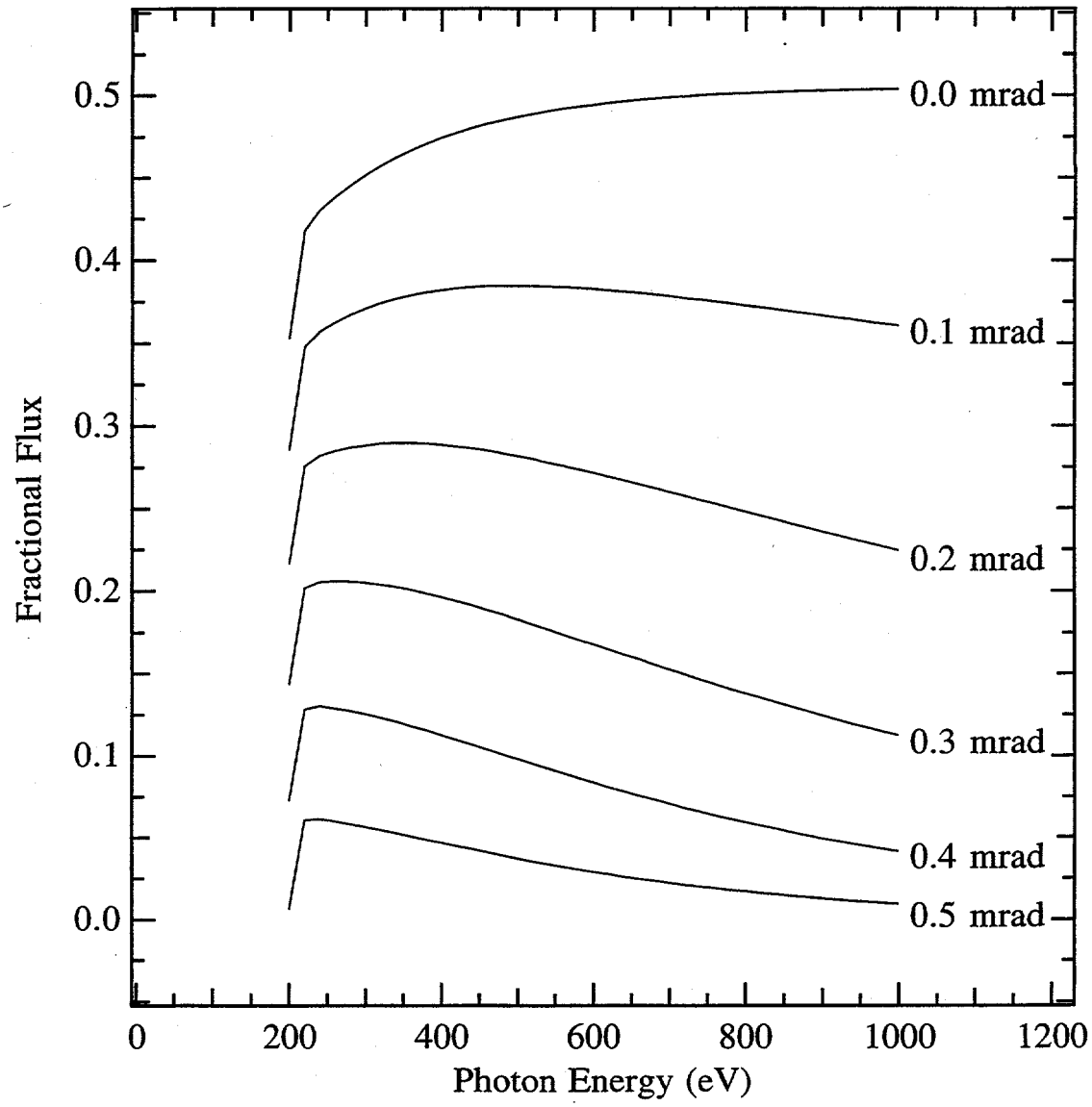

Calculated fraction of the total emitted flux accepted by an aperture defined by a lower value given by a central stop while the upper value is given by either the aperture of the horizontally deflecting mirror or the aperture of the grating. The half-apertures of the central stop are shown ranging from 0.0 to 0.5 mrads. Larger central stop sizes cause a significant flux reduction, especially at high energies.

Figure D2

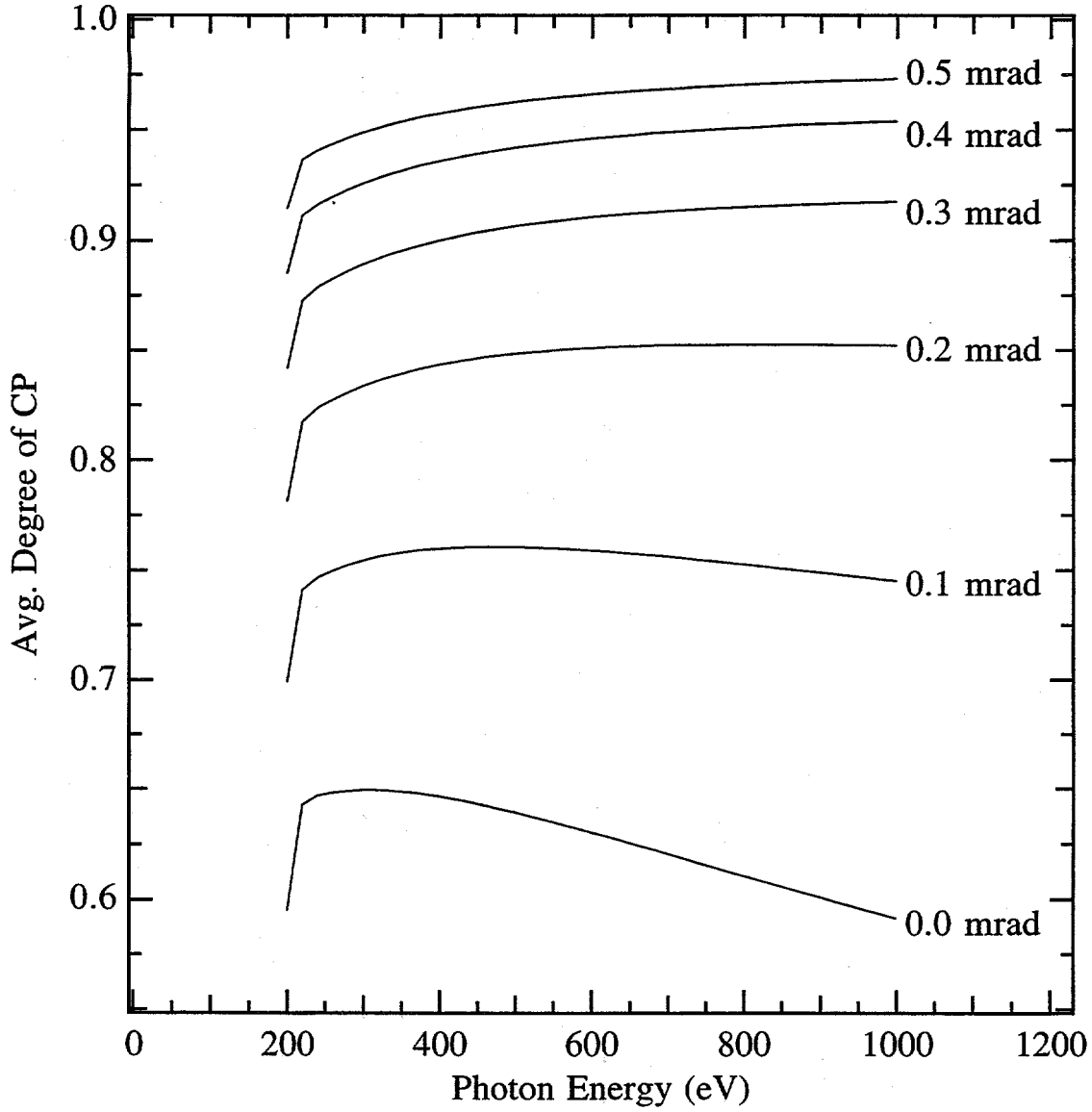

Calculated average degree of circular polarization for an aperture defined by a lower value given by a central stop while the upper value is given by either the aperture of the horizontally deflecting mirror or the aperture of the grating. The half-apertures of the central stop are shown ranging from 0.0 to 0.5 mrads. For the largest stop size, the degree of circular polarization is greater than 0.9. Even with no stop, it is typically greater than 0.6 throughout the energy range.

Figure D3

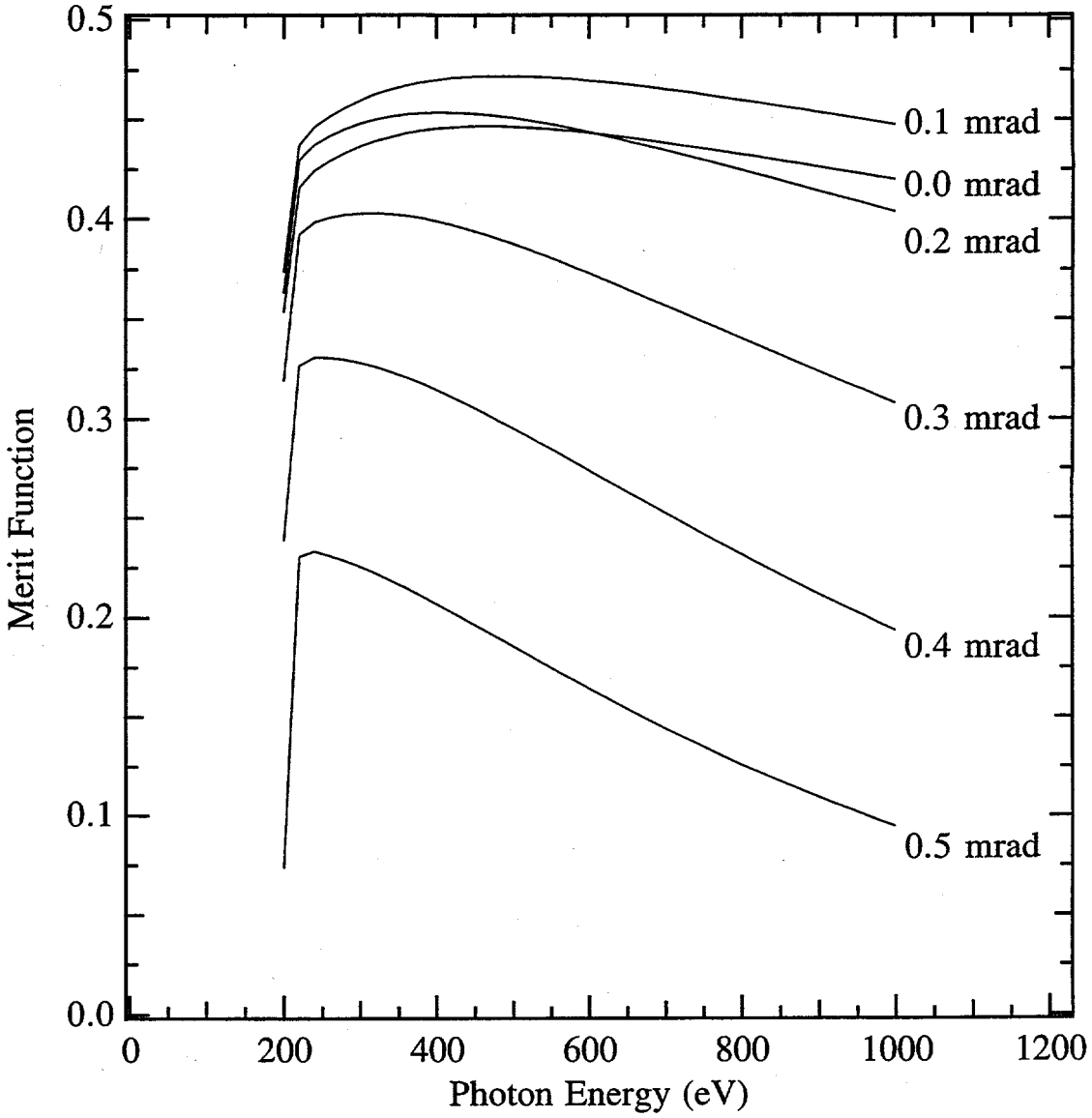

Calculated merit function for an aperture defined by a lower value given by a central stop while the upper value is given by either the aperture of the horizontally deflecting mirror or the aperture of the grating. The half-apertures of the central stop are shown ranging from 0.0 to 0.5 mrads. The merit function weights the average degree of circular polarization with the fraction of the total emitted flux actually accepted. The merit functions over the half-aperture sizes 0.0, 0.1, and 0.2 mrads are within 10% of each other over the entire energy range. This insensitivity is caused by the balance of decreasing flux and increasing degree of circular polarization.

Figure D4

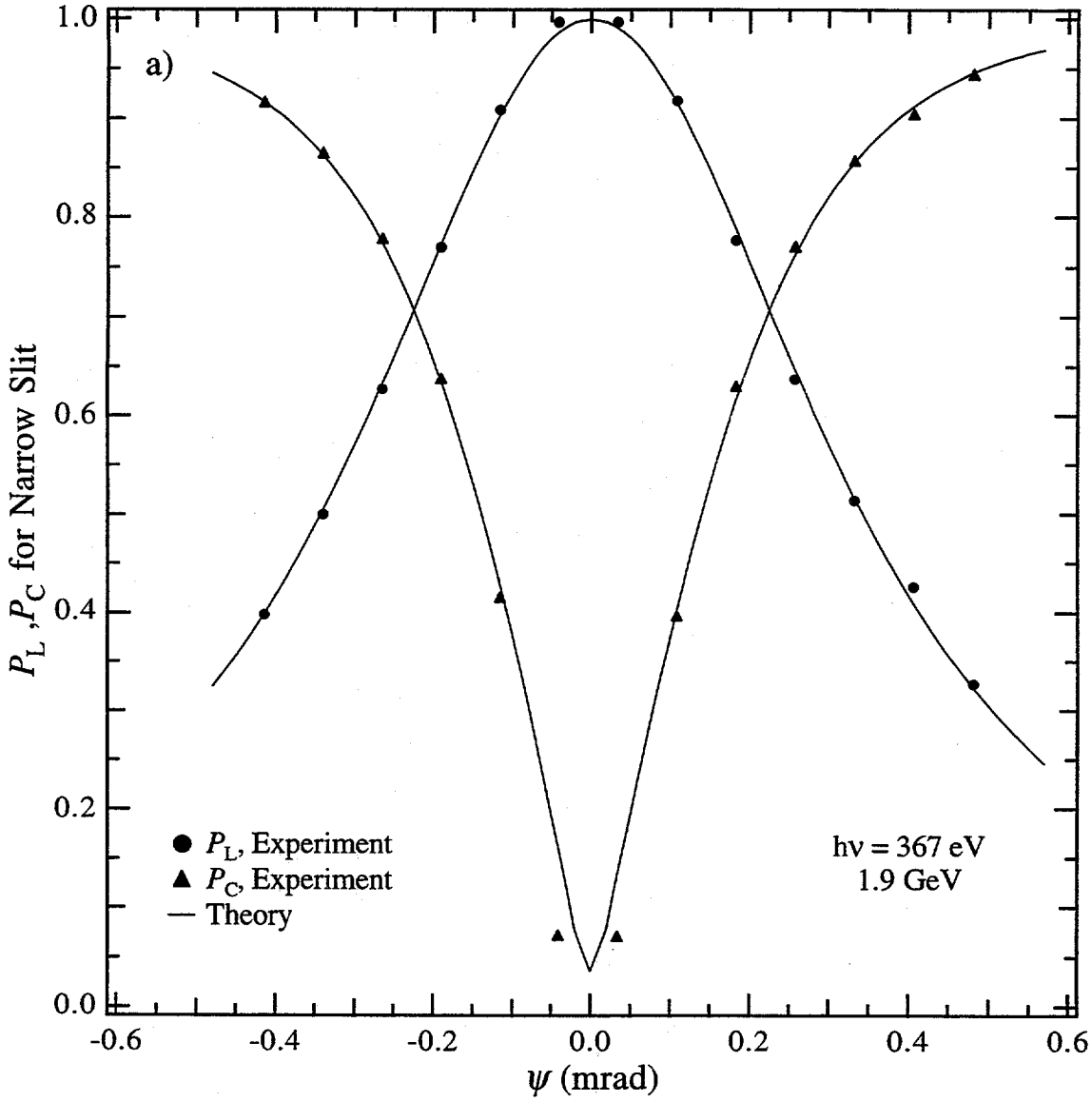

The degree of linear (P_L) and circular (P_C) polarization as the narrow slit (0.037 mrad) was stepped across the vertical opening angle for 367 eV photon energy. Symbols represent the experimental values; experimental P_C values were obtained by assuming that the amount of unpolarized radiation was zero. Lines represent the calculated values. Even with the slit at ψ = 0 mrad, there is a small amount of circular polarization transmitted due to the non-zero slit width.

Figure D5a

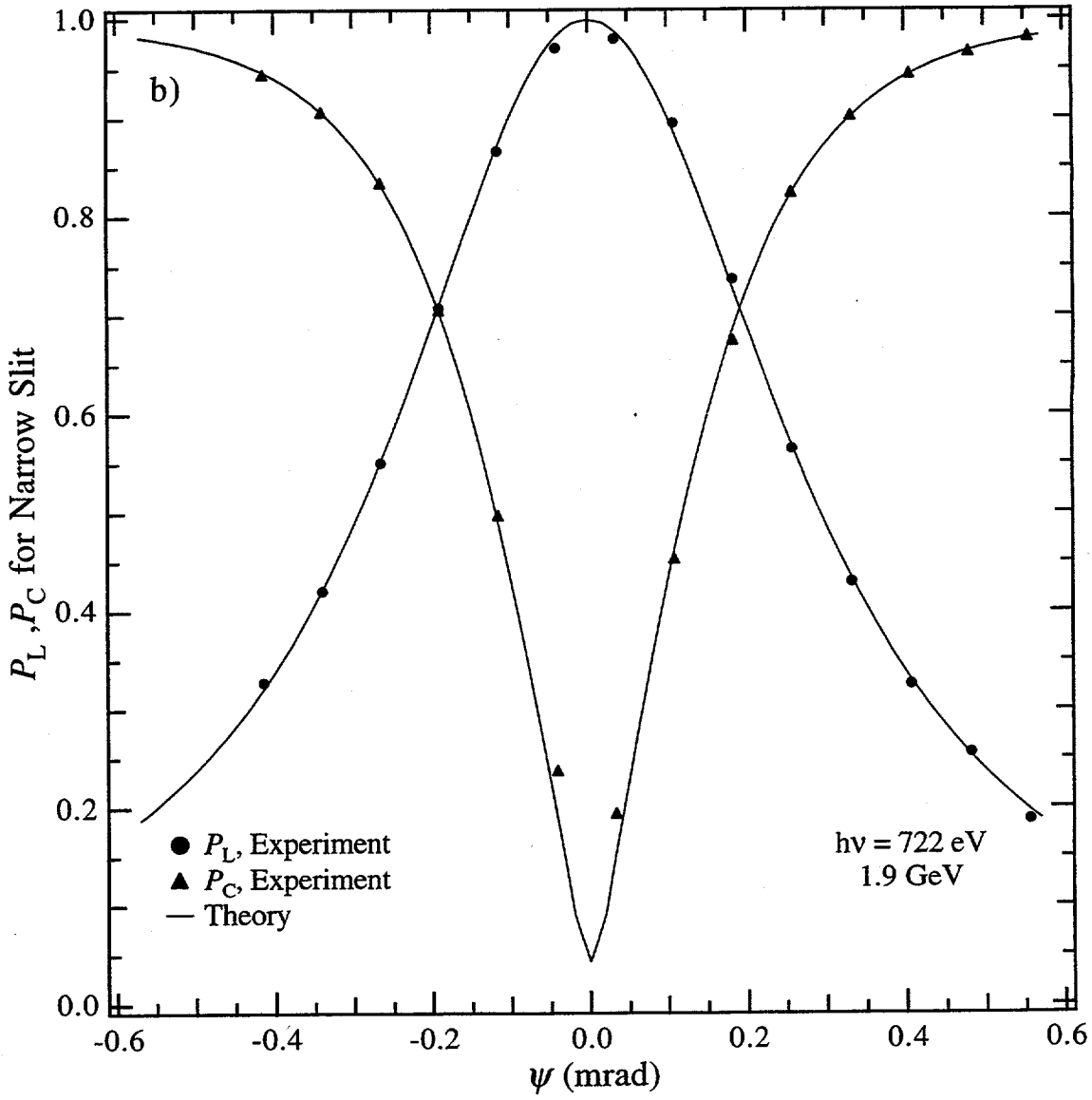

The degree of linear (P_L) and circular (P_C) polarization as the narrow slit (0.037 mrad) was stepped across the vertical opening angle for 722 eV photon energy. Symbols represent the experimental values; experimental P_C values were obtained by assuming that the amount of unpolarized radiation was zero. Lines represent the calculated values. Even with the slit at ψ = 0 mrad, there is a small amount of circular polarization transmitted due to the non-zero slit width.

Figure D5b

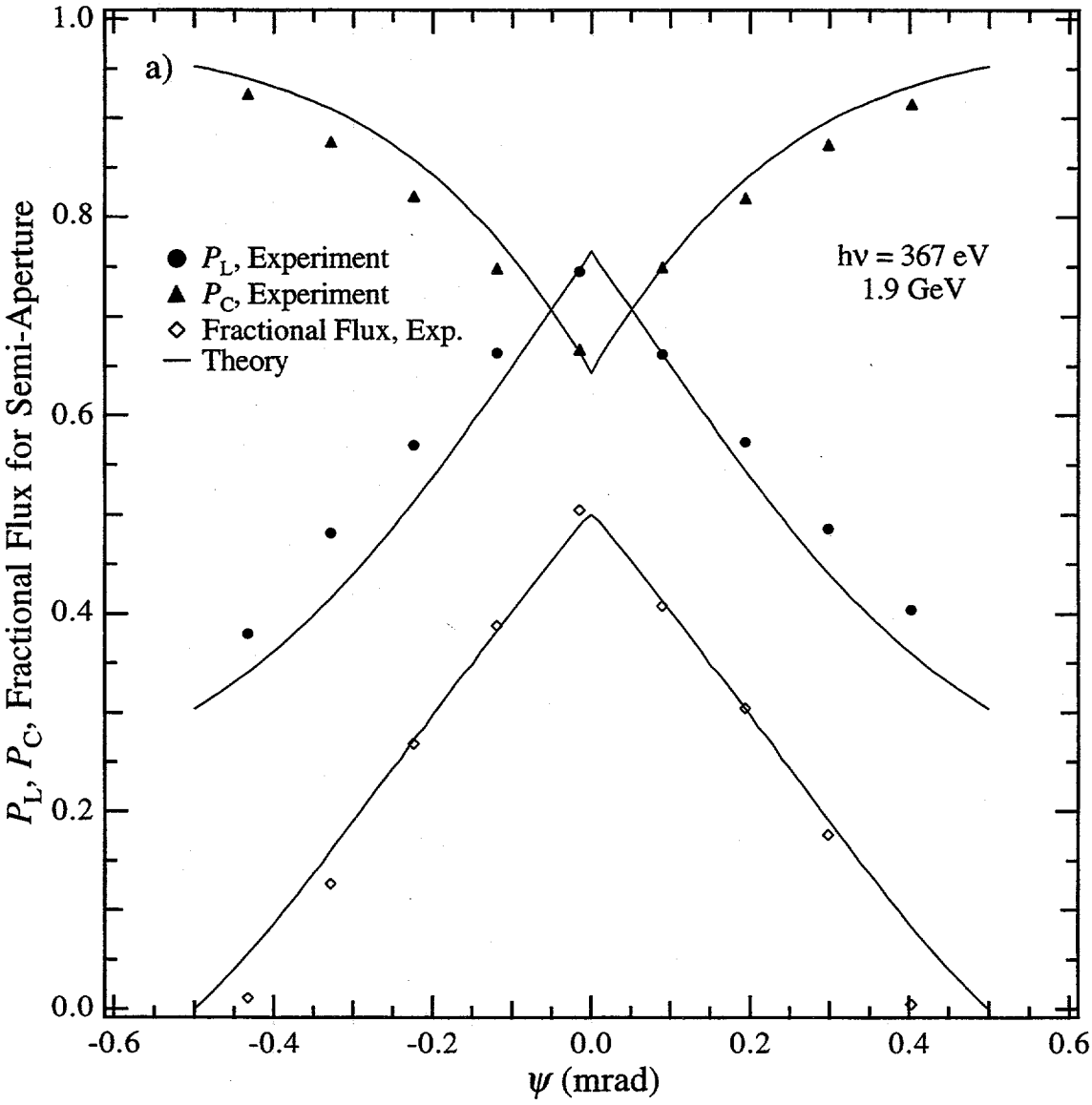

The degree of linear (P_L) and circular (P_C) polarization and the fractional flux as the wide semi-aperture was stepped across the vertical opening angle for 367 eV photon energy. For $\psi > 0$, the semi-aperture blocks the beam below the horizon; for $\psi < 0$, the semi-aperture blocks the beam above the horizon. Symbols represent the experimental values; experimental P_C values were obtained by assuming that the amount of unpolarized radiation was zero. Lines represent the calculated values. With the semi-aperture removed to transmit the entire beam, the measured P_L and P_C values equal those measured with the aperture edge at $\psi = 0$ mrad.

Figure D6a

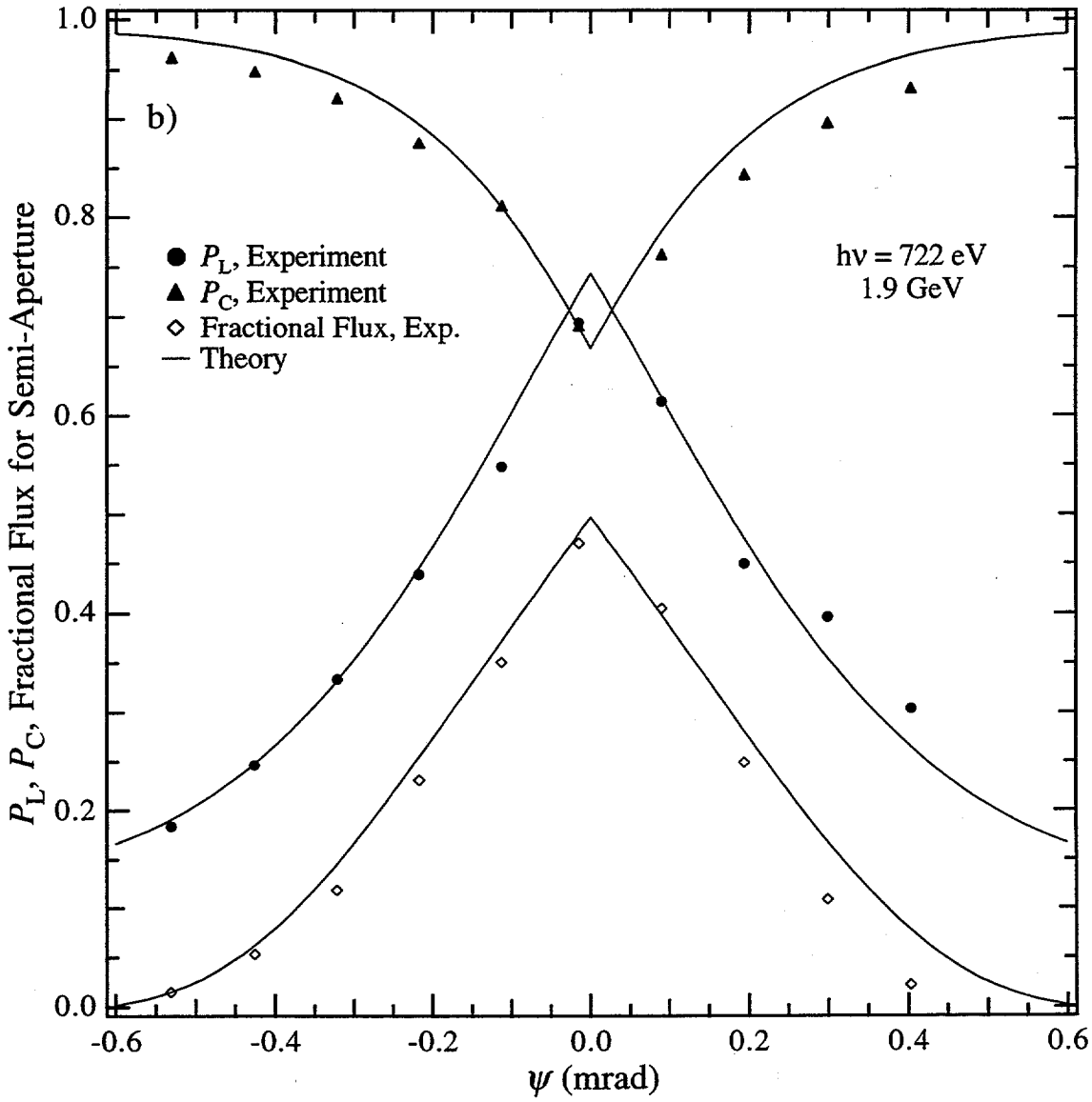

The degree of linear (P_L) and circular (P_C) polarization and the fractional flux as the wide semi-aperture was stepped across the vertical opening angle for 722 eV photon energy. For $\psi > 0$, the semi-aperture blocks the beam below the horizon; for $\psi < 0$, the semi-aperture blocks the beam above the horizon. Symbols represent the experimental values; experimental P_C values were obtained by assuming that the amount of unpolarized radiation was zero. Lines represent the calculated values. With the semi-aperture removed to transmit the entire beam, the measured P_L and P_C values equal those measured with the aperture edge at $\psi = 0$ mrad.

Figure D6b

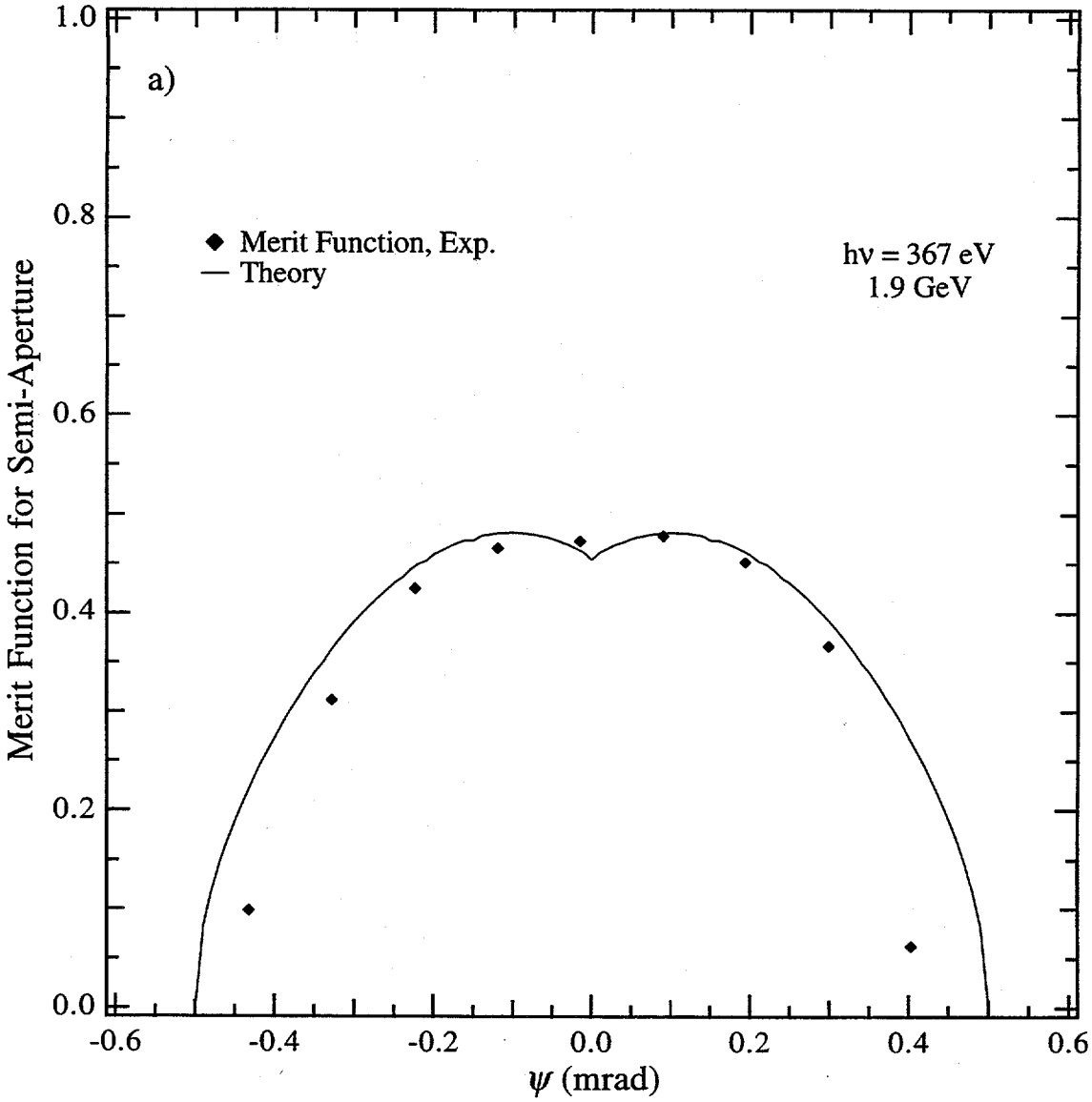

The merit function given by equation (D8) as the semi-aperture was stepped across the vertical opening for 367 eV photon energy. Symbols represent the experimental values. Lines represent the calculated values. The merit function is optimized with the semi-aperture blocking roughly half of the total intensity.

Figure D7a

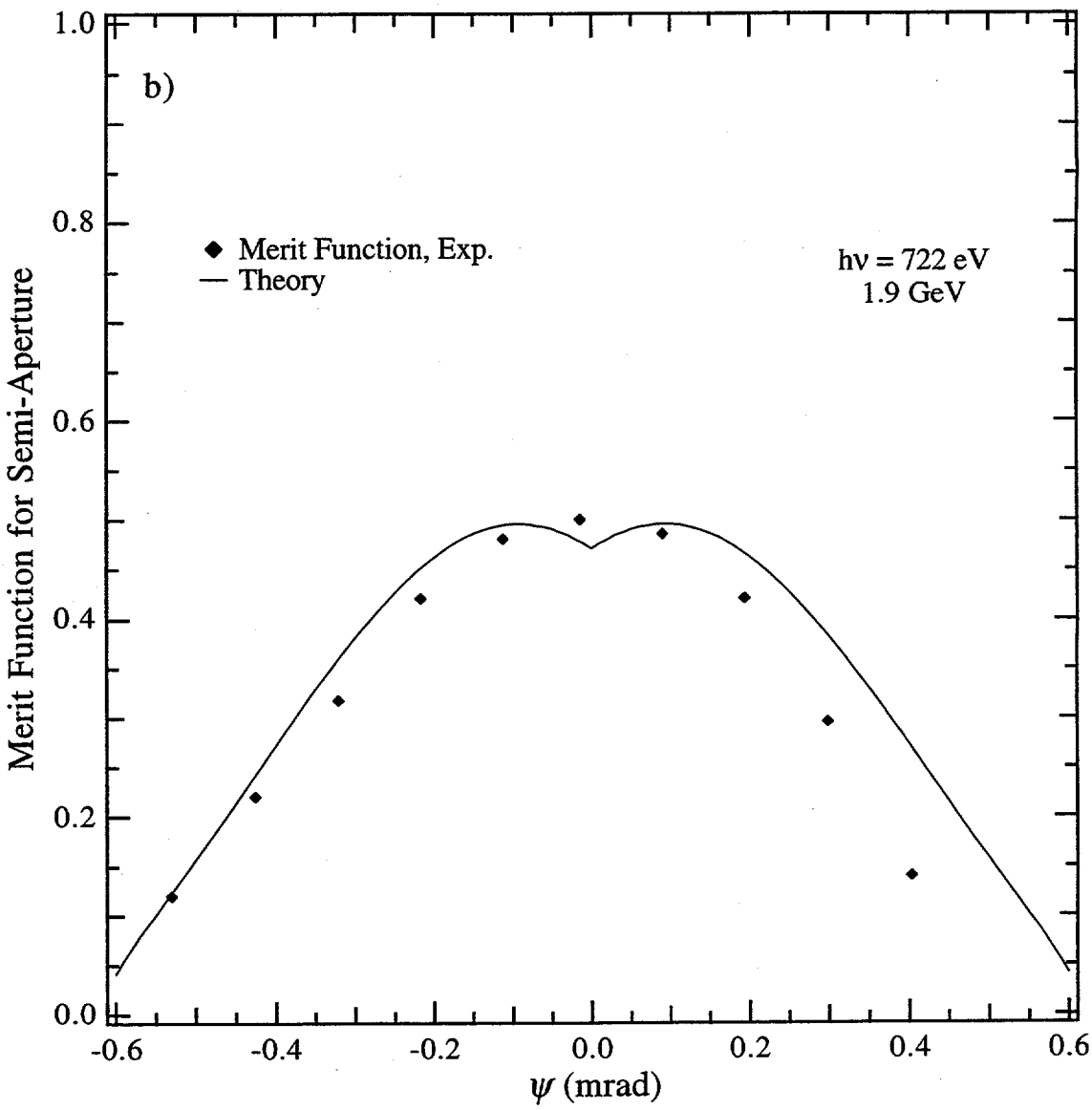

The merit function given by equation (D8) as the semi-aperture was stepped across the vertical opening for 722 eV photon energy. Symbols represent the experimental values. Lines represent the calculated values. The merit function is optimized with the semi-aperture blocking roughly half of the total intensity.

Figure D7b

APPENDIX E: Ray Tracing Calculations

Using the ray-tracing program SHADOW, calculations were performed to illustrate how the photon beam focus at the endstation depends on the exit slit position and the photon energy. Figure 2 in the main text shows the optical geometry. The mirror dimensions and geometries are listed in Appendix A.

For the calculation results presented here, the angle of incidence on the refocusing mirror, M3, was 1.8°. The M3 meridian radius was fixed at 87.0 m to vertically focus the beam 2.17 m downstream of M3 when the exit slit, S2, is at 423 mm. This position satisfies the focus condition at 400 eV when the entrance slit, S1, is at 250 mm. The slit positions noted here are in units of millimeters as would be set by the user. To horizontally focus the beam 2.17 m downstream of M3, the sagittal M3 radius was fixed at 0.10 m because the M1 horizontal focus is 1.47 m downstream of the grating center (6.33 m upstream of the M3 center). Refer to Appendices B and C for an explanation of the foci calculations and the focus condition.

Using the 600 $^{lines}/_{mm}$ grating, calculations were performed at three different energies. S1 was fixed at 250 mm for all of the calculations; this is the M2 vertical focus. S2 was set to satisfy the focus condition for each photon energy. At the lower limit of the grating, 200 eV, S2 was at 746 mm (see figure E1). As stated above, the conditions for 400 eV were used to fix the M3 geometry and S2 was at 423 mm (see figure E2). The exit slit maximum travel, 1000 mm, was reached at 740 eV (see figure E3). Comparing figures E1, E2, and E3, one can see that the beam comes into and out of focus if the M3 geometry and orientation is fixed. However, this effect turns out to be negligible when doing photoemission experiments.

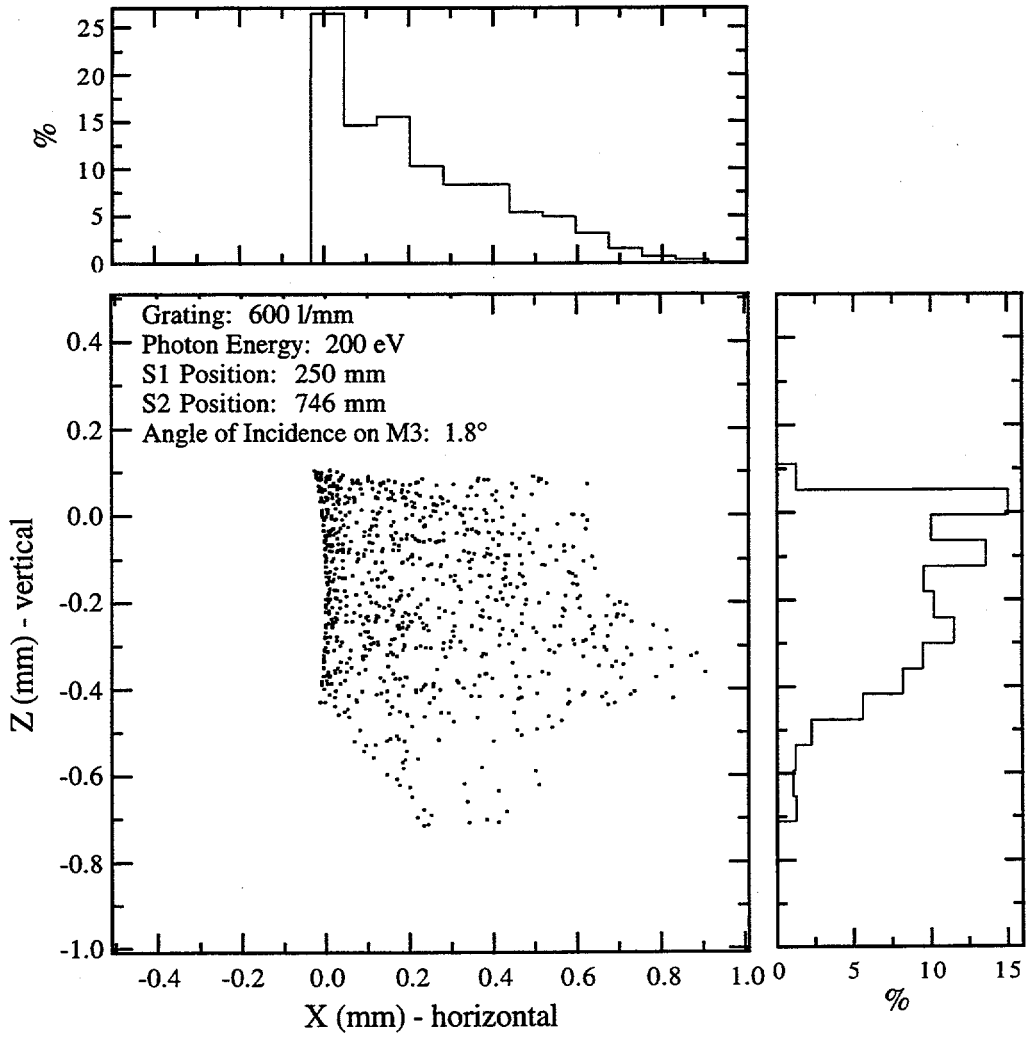

Focal spot for hν = 200 eV using the 600 $^{lines}/_{mm}$ grating. The slit positions satisfy the focus condition. The angle of incidence on M3 was 1.8°. As shown by the histograms, the majority of the flux falls within a beamsize ~0.5 x 0.4 mm.

Figure E1

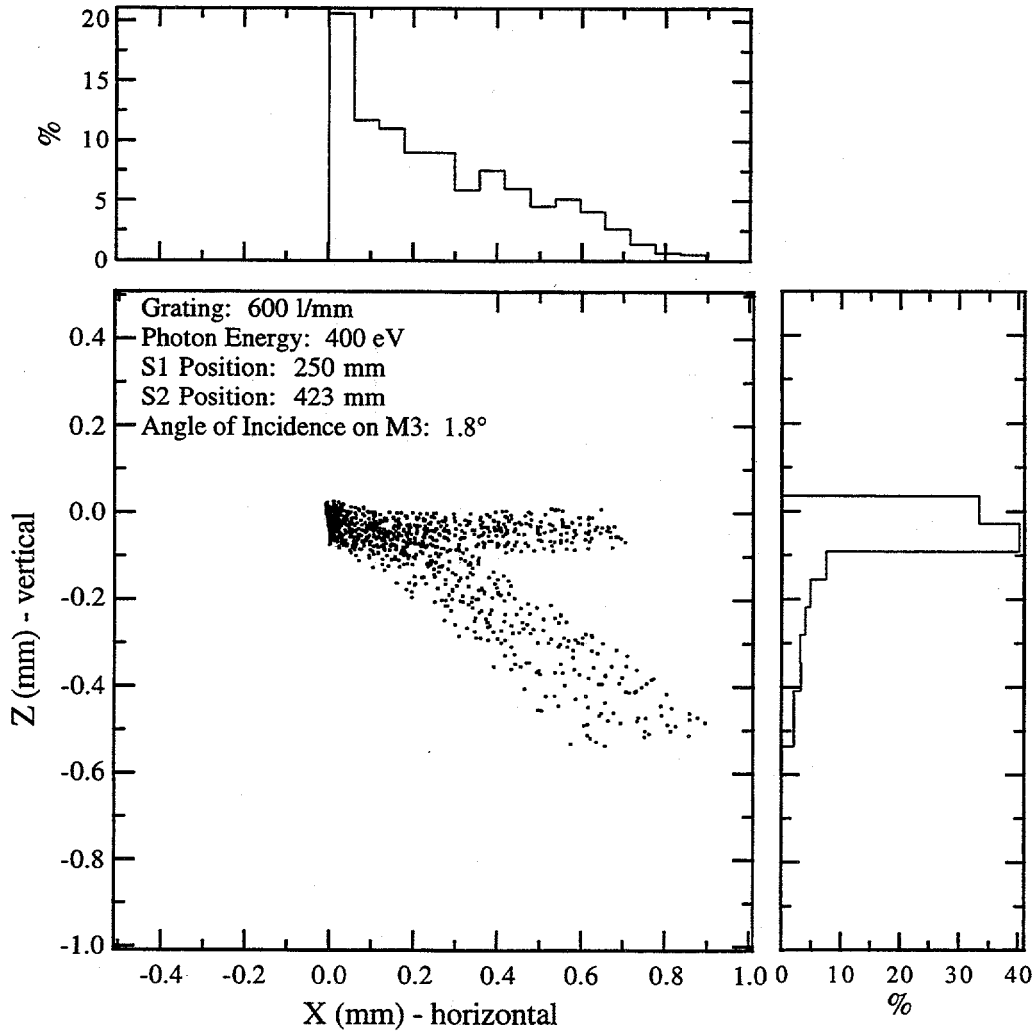

Focal spot for hν = 400 eV using the 600 $^{lines}/_{mm}$ grating. The slit positions satisfy the focus condition. The angle of incidence on M3 was 1.8°. As shown by the histograms, the majority of the flux falls within a beamsize ~0.5 x 0.2 mm.

Figure E2

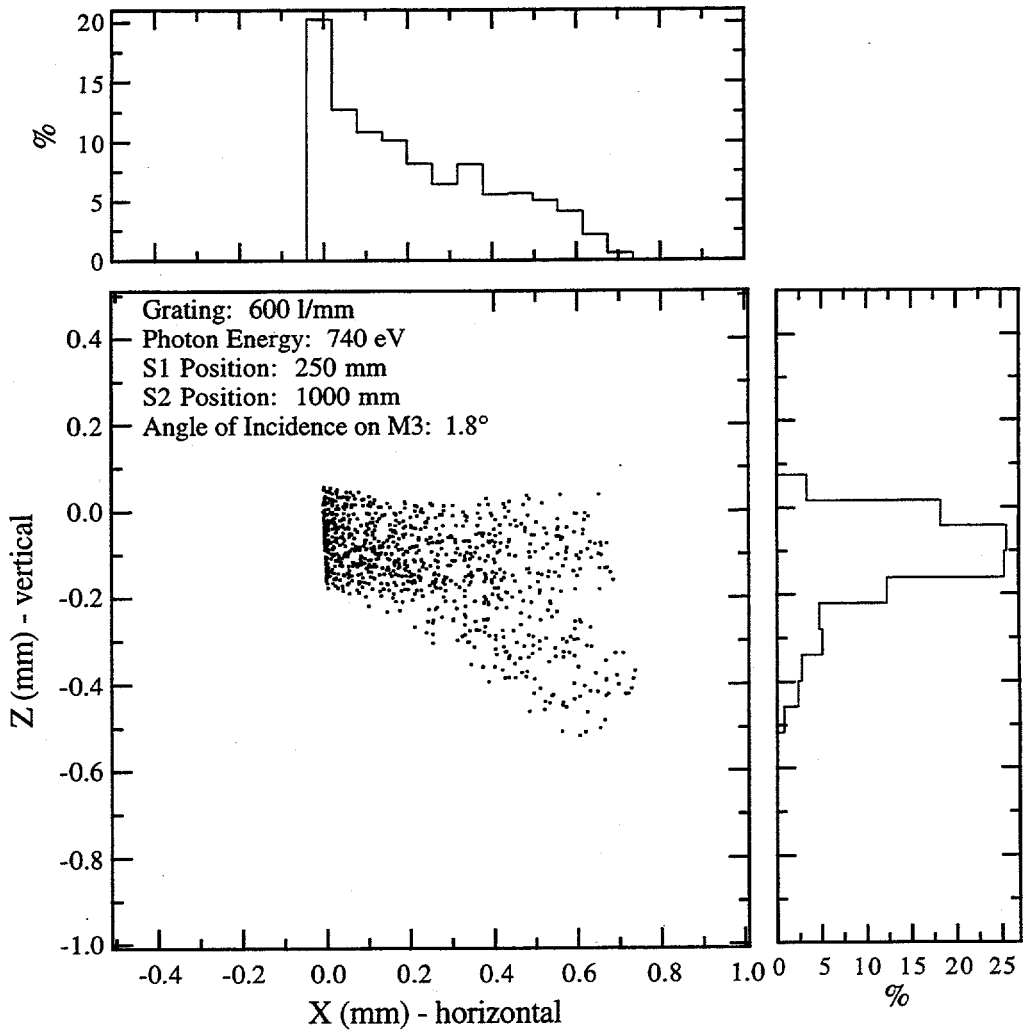

Focal spot for hν = 740 eV using the 600 $^{lines}/_{mm}$ grating. The slit positions satisfy the focus condition. The angle of incidence on M3 was 1.8°. As shown by the histograms, the majority of the flux falls within a beamsize ~0.5 x 0.3 mm.

Figure E3

APPENDIX F: BEAMLINE CONTROL SYSTEMS

A Sun Workstation connected to a networked VME Crate is used to control the BL 9.3.2 stepping motors on the mirrors, gratings, slits, and circular polarization aperture. The user controls the beamline through EPICS window displays which are organized to allow visiting users the control they need with a minimum amount of instruction. Additionally, serial ports are available so that visitors can control the monochromator with their own computer.

The username and password for the beamline computer are

username: `bl932usr`

password: `Zahid1Ø1`

Note that the Unix operating system is case sensitive. After a few moments, the *Beam Line 9.3.2 Main Control Panel* (figure F1) will open. This window displays the present operating parameters and is the access point for all of the other control windows. If this window is accidentally closed, there is a window utility that can be used to reopen the main control panel. Alternatively, at the prompt, one can type

```
1>bl93-102.als:bl932usr% dm bl932.dl&
```

From the *Beam Line 9.3.2 Main Control Panel* pictured in figure F1, the monochromator energy is set by typing under *Requests* an *Energy (eV)* or a *Lambda (nm)*. The *order* must also be set. For example, if the user wants hν = 700 eV in second order, the *Energy (eV)* should be set to *700* and the

order should be set to *2*. The monochromator will go to the same position as if hν = 350 eV was requested in first order.

The user can choose the desired *Slit Move Mode* simply by clicking on *Exit Slit Only*, *Rowland Circle*, or *No Slit Moves*. These operating modes have been discussed previously. Similarly, the user must tell the computer which *Grating* is being utilized. This information is used by the computer when the user requests an energy. Note that this is completely independent of which grating is actually in the photon beam path. It is the user's responsibility to manually choose the correct grating. The 100 $^{lines}/_{mm}$ is the one away from the ring, the 600 $^{lines}/_{mm}$ is the one in the center, and the 1200 $^{lines}/_{mm}$ is the one toward the ring.

The main control panel also monitors (with no control option) the *Position* of the grating (via *Lambda*), the *Entrance Slit*, and the *Exit Slit*. These can be manually controlled by accessing the *Motors* menu. Choosing *Grating Motor*, opens the *BL9.3.2, SGM1* window pictured in figure F2. This allows the user to move the grating in units of micrometers. This function is useful to find the zero-order position (see below) and *HOME* the grating. The grating must be homed whenever the *Laser Status* is red and reads *ERROR*. This window also allows the user to *KILL MOVE* if for some reason that becomes necessary.

Choosing *Entrance Slit (SLT1) Motor* opens the *BL9.3.2, SLIT1* window pictured in figure F3. This allows the user to set the entrance slit position in units of millimeters which has been discussed previously. This is useful in the *Exit Slit Only* and the *No Slit Moves* modes. Choosing *Exit Slit (SLT2) Motor* opens the *BL9.3.2, SLIT2* window pictured in figure F4. This allows the user to set the exit slit position in units of millimeters which has been discussed previously. This is useful in the *No Slit Moves* mode. Both

the entrance slit and exit slit motor windows have the *KILL MOVE* option available which becomes useful if an input is typed incorrectly.

Under the *Calibration* menu is the *Grating Calibration*. Choosing this opens the *Grating: Calibration* window pictured in figure F5. This window is useful if the user needs to find the *Zero Order Offset* of a grating to re-calibrate the photon energy. The value of the *Zero Order Offset* (in meters) should be multiplied by 10^6 and entered in the *BL9.3.2, SGM1* window (recall that the units are in micrometers). Small deviations from this position can then be entered if the value has changed.

Zero order of a grating is that position where the grating simply acts as a mirror and reflects all energies through the exit slit ($\alpha = \beta$). When going to zero order, great care should be taken to be certain that the high voltage for the I-zero channeltron is turned off. Additionally, the general user should never over-write the *def.parms* file for a grating calibration.

The main control panel also allows the user to visually monitor the *Beam Current* in the storage ring and the *I-zero* signal being collected just downstream of M3. The I-zero signal is also available under the *M2 Pitch* option under the *More...* menu which opens the *Beam Line 9.3.2: M2 Control* window pictured in figure F6. This window is the control panel for the M2 Piezo control discussed previously. To operate this, the user should choose *supervisory* from the *Loop Enable* option. The *Piezo Drive Voltage* should then be set to *0.00 V*. Subsequently, the flux at I-zero can be optimized manually. Care should be taken that the signals on *Slit 1 Upper* and *Slit 1 Lower* have the same sign and, hopefully, similar magnitudes. Once these are satisfactory, the user enables the feedback loop by pressing *GO FeedBack*.

The *Circ. Pol.* option is also available under the *More...* menu in the main control panel. This opens the *BL9.3.2, CIRC.* window pictured in figure F7. From this window, the user can select linear polarized radiation by positioning the aperture to -34170 μm. For ~0.8 degree of circularly polarized radiation, typical operating positions are -18542 μm for left-circularly polarized radiation and -49542 μm for right-circularly polarized radiation. Alternatively, the user can position the narrow slit to any desired position; for the photon beam center to go through the narrow slit, it should be positioned at about -77250 μm.

Finally, the main control menu allows the user to access a display of some undulator gaps, the window opened by choosing the *Undulator Gaps* option under *More...* This window is pictured in figure F8 and shows a display of the current gap for the undulators on beamlines 7.0, 8.0, and 9.0. Visually monitoring these values is useful to stay informed about the happenings around the ring.

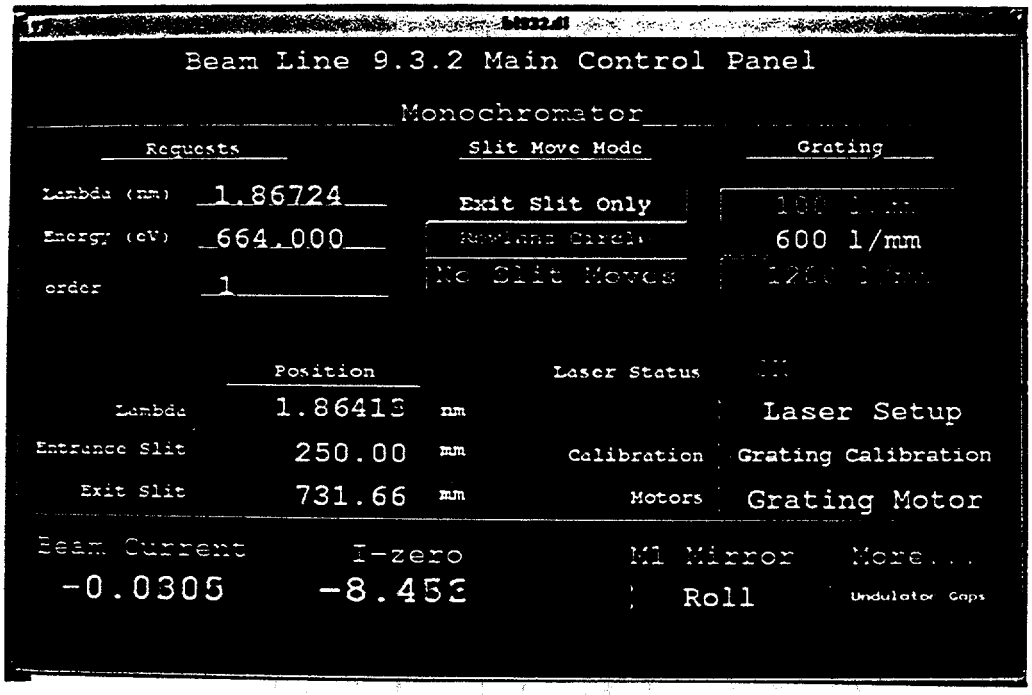

XBB 961-215

Beam Line 9.3.2 Main Control Panel
Figure F1

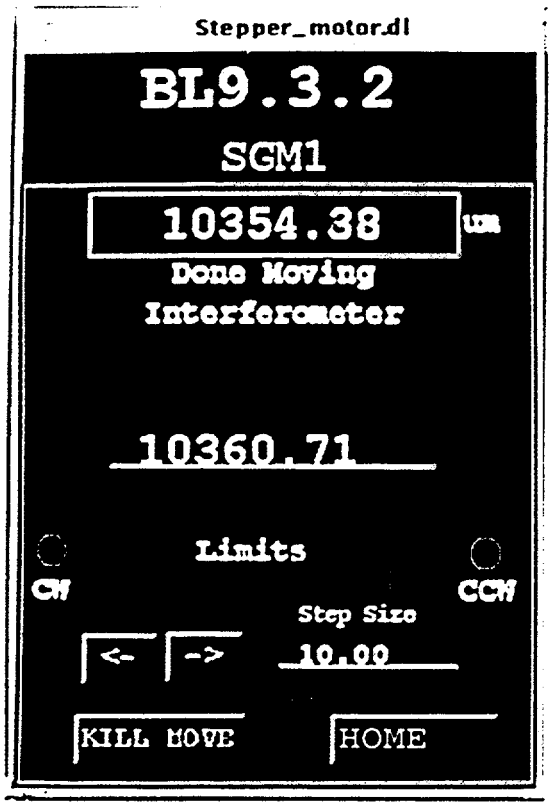

XBB 961-208

BL9.3.2, SGM1 Motor Control
Figure F2

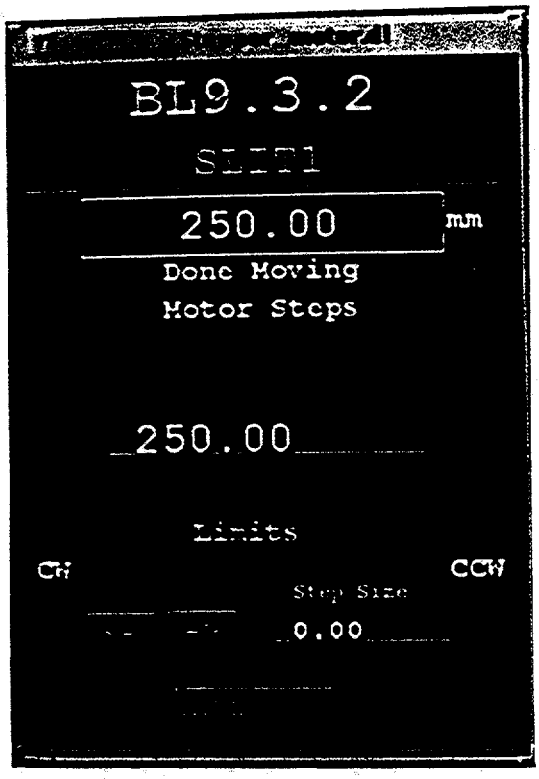

XBB 961-210

BL9.3.2, SLIT1 Motor Control
Figure F3

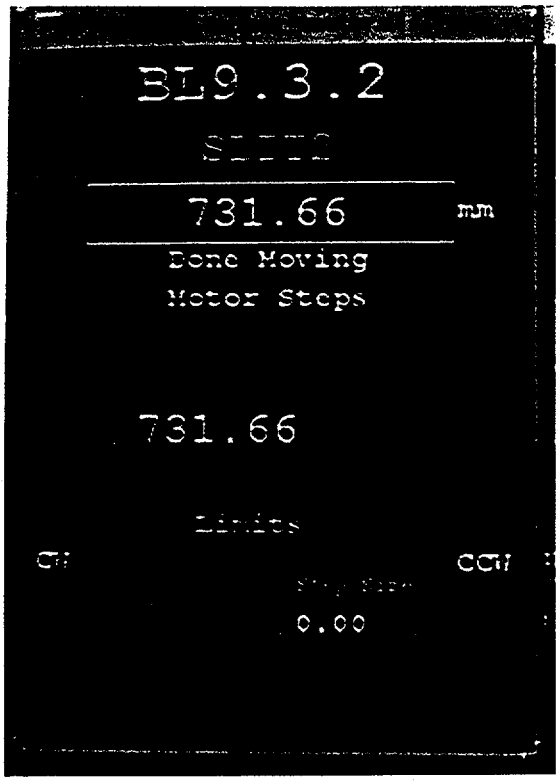

XBB 961-212

BL9.3.2, SLIT2 Motor Control
Figure F4

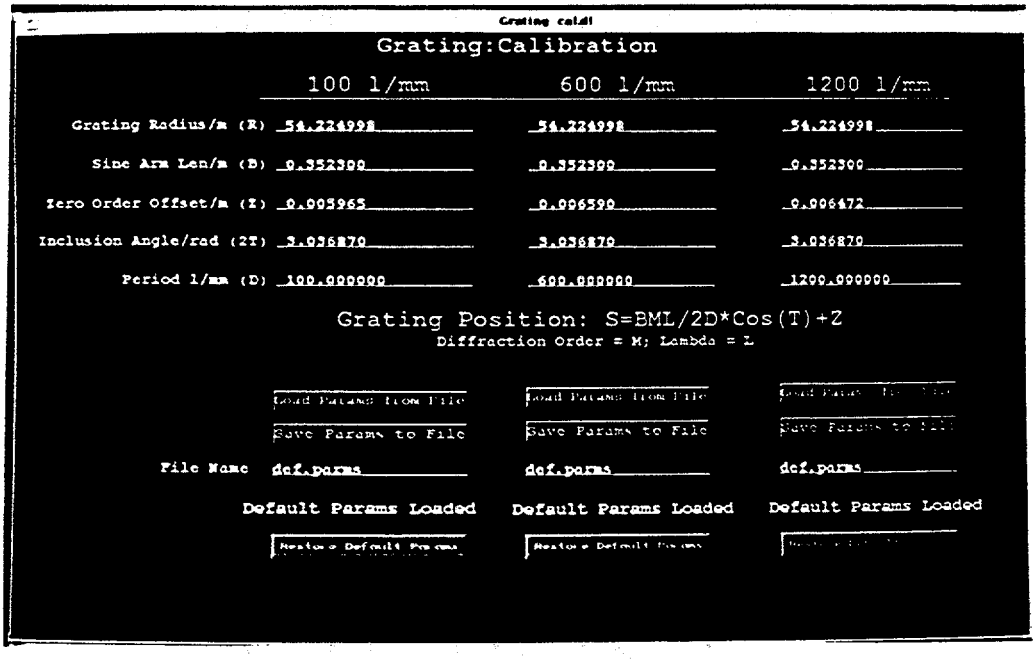

XBB 961-216

Grating: Calibration Control Panel
Figure F5

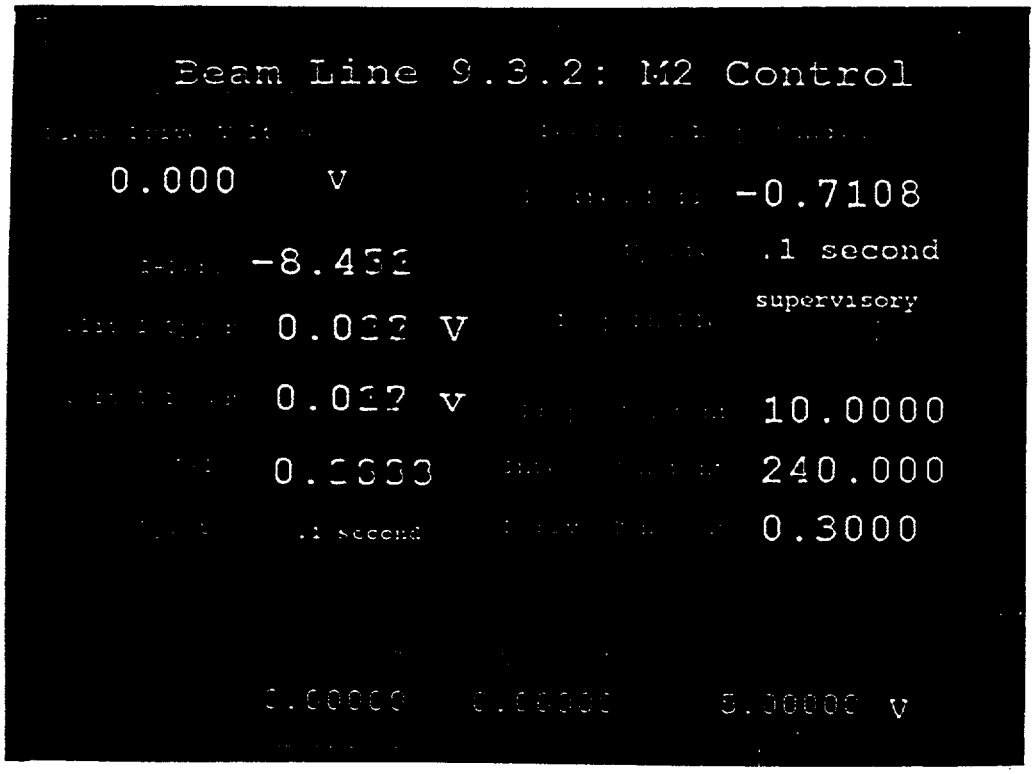

XBB 961-213

Beam Line 9.3.2: M2 Control
Figure F6

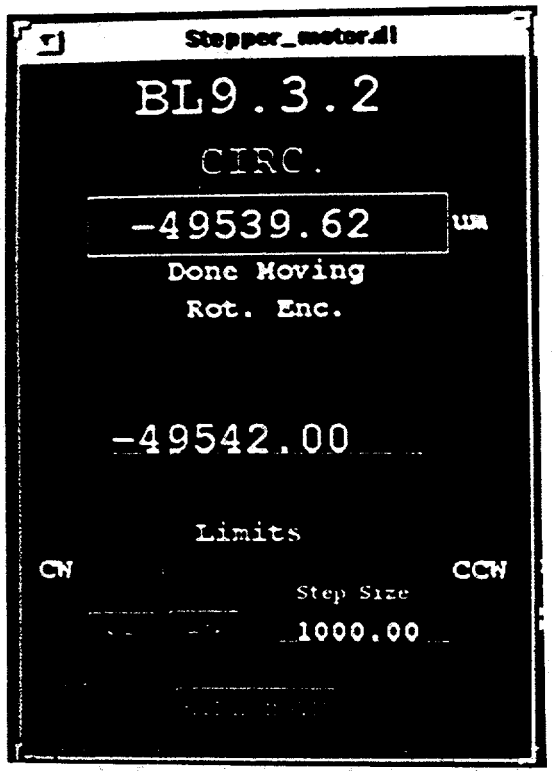

XBB 961-207

Beam Line 9.3.2: CIRC. Motor Control
Figure F7

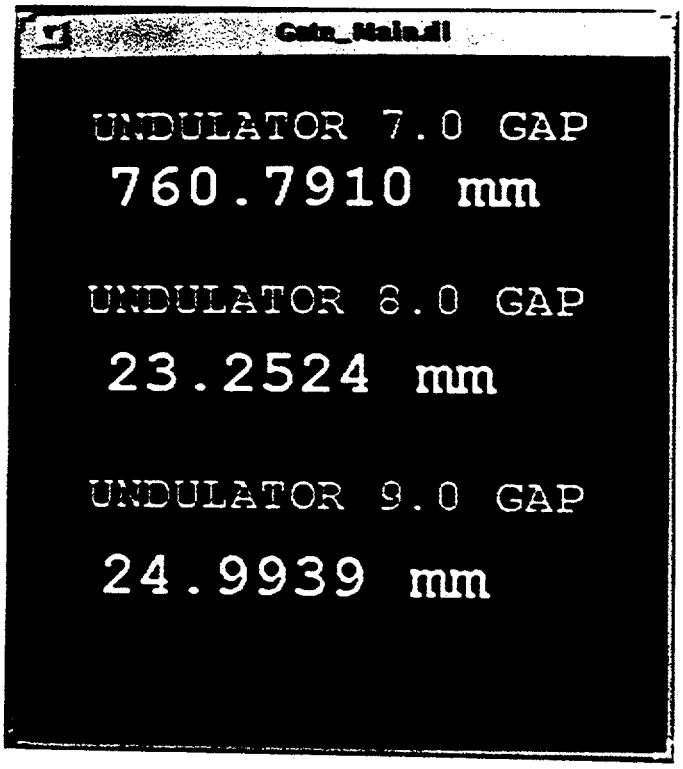

XBB 961-209

Undulator Gap Display Panel
Figure F8

Chapter 2

Structure Determination of Chemisorbed c(2x2)P/Fe(100) using Angle-Resolved Photoemission Extended Fine Structure and Self-Consistent-Field Xα Scattered Wave Calculations: Comparison with c(2x2)S/Fe(100)

ABSTRACT

Angle-resolved photoemission extended fine structure was used to determine the structure of c(2x2)P/Fe(100) for the first time. Photoemission data were collected normal to the (100) surface and 45° off-normal along the [011] direction at room temperature. A close analysis of the auto-regressive linear prediction based Fourier transform indicates that the P atoms adsorb in the high-coordination four-fold hollow sites. Curved-wave multiple scattering calculations confirmed the four-fold hollow adsorption site. The P atoms were determined to bond 1.02 Å above the first layer of Fe atoms and the Fe-P-Fe bond angle is 140.6°. Additionally, it was determined that there was no expansion of the Fe surface. Self-consistent-field Xα scattered wave calculations were performed for the c(2x2)P/Fe(100) and the c(2x2)S/Fe(100) systems. These independent results are in excellent agreement with this P/Fe structure and the S/Fe structure previously published, confirming the ARPEFS determination that the Fe_1-Fe_2 interlayer spacing is contracted from the bulk value for S/Fe but not for P/Fe. Finally, this structure is compared to structures from the literature of atomic nitrogen, atomic oxygen, and sulfur adsorbed on the Fe(100) surface.

I. INTRODUCTION

From the viewpoint of materials science, catalysis, and magnetism, a detailed knowledge of iron and its interaction with other elements and compounds is very important. There have been many theoretical studies of the structure and embrittlement of iron grain boundaries due to the presence of phosphorus, a common impurity.[1-5] The electronic and magnetic properties of Fe surfaces and thin films have been studied extensively as well.[6-11] Egert *et al.*[6] seem to be the first to observe the c(2x2) LEED pattern when P is adsorbed on the Fe(100) surface, but the structure determination using LEED I-V curves has not been done to date.

The structures of atomic nitrogen,[12] atomic oxygen,[13,14] and sulfur[15-17] adsorbed on the Fe(100) surface have been published. Using angle-resolved photoemission extended fine structure (ARPEFS), we present the first structure determination of chemisorbed c(2x2)P/Fe(100). These four adsorbate structures are summarized and compared in the discussion.

Also known as energy-scanned photoelectron diffraction[18], ARPEFS is a technique proven to yield accurate, local structural information of atomic and molecular adsorbates on single crystal surfaces to very high precision.[17,19-24] In addition to determining the adsorbate structure, ARPEFS is able to detect any relaxation of the first few layers of the substrate. By analyzing the auto-regressive linear prediction (ARLP) based Fourier transform (FT),[25,26] the binding site and a reasonably accurate structure can be determined. This allows for a close estimate of the structure without the need for any theoretical calculations. Using this estimate as a starting point, curved-wave multiple scattering calculations can then be used to determine the structure to very high precision (~±0.02 Å).

Photoemission data were collected normal to the (100) surface and 45° off-normal along the [011] direction at room temperature. A close analysis of the ARLP based FT indicates that the P atoms adsorb in the high-coordination four-fold hollow sites. The curved-wave multiple scattering calculations which simulate the photoelectron diffraction confirmed the four-fold hollow adsorption site. By simultaneously fitting both ARPEFS data sets, the P atoms were determined to bond 1.02 Å above the first layer of Fe atoms. The Fe-P-Fe bond angle is thus 140.6°. Assuming the radius of the Fe atoms is 1.24 Å, the effective P radius is 1.03 Å. To test this fitting method, each data set was fit individually and these results were in good structural agreement.

Additionally, self-consistent-field Xα scattered wave (SCF-Xα-SW or Xα-SW) calculations were performed for the c(2x2)P/Fe(100) and the c(2x2)S/Fe(100)[17] systems. These independent results are in excellent agreement with this P/Fe structure and the S/Fe structure previously published, confirming the ARPEFS determination that the Fe_1-Fe_2 interlayer spacing is contracted from the bulk value for S/Fe but not for P/Fe.

II. EXPERIMENTAL

The experiments were performed in an ultra-high vacuum chamber[27] at pressures ≤60 nPa using beamline 3-3 (Jumbo, the Ge(111) double crystal monochromator[28]) at the Stanford Synchrotron Radiation Laboratory. This beamline was chosen so that photoemission data could be acquired from the P 1*s* core-level which has a binding energy of 2149 eV. The photon energy was scanned from 2200 eV to 2700 eV, the energy resolution was 1.0~2.0 eV FWHM, and the degree of linear polarization was ~0.98.

The Fe crystal (6mm diameter and 2 mm thick) was cut from a boule using an electronic discharge machine. The (100) surface was oriented to ±1° precision by Laue backscattering. Before chemical etching, the final polishing was accomplished with a 0.5 μm mesh Al_2O_3 powder. The sample was mounted on a high precision (x, y, z, θ, ϕ) manipulator.

The crystal was cleaned by repetitive cycles of Ar^+ ion sputtering (beam voltage 1.0 kV, emission current 20 mA) and subsequent annealing by electron bombardment from behind to ~970 K. Iron undergoes a bcc to fcc phase transition at ~1180 K so it was important not to approach this temperature. The temperature was monitored with a chromel-alumel thermocouple attached near the sample and calibrated with an infrared pyrometer. After 5 weeks of these sputter-anneal cycles, the near-surface region was depleted of C, O, and S, and the surface could be cleaned after each set of experiments by sputtering with a 0.5 kV beam voltage and annealing to only ~820 K.

The LEED pattern of the clean surface showed a clear and sharp (1x1) pattern. The bulk contaminants C, O, and S were monitored with Auger Electron Spectroscopy (AES) using four-grid LEED optics in the retarding field mode. The surface contamination level was within the noise level of the measurements both before and after the data acquisition. The c(2x2) phosphorus overlayer was prepared by exposing the surface to PH_3 gas (from Matheson Inc.) using an effusive beam doser and then annealing the sample to 770 K. In segregation studies of P in Fe, Shell and Rivière[29] obtained an Auger peak ratio of $P_{LMM}(119\ eV)/Fe_{L_3VV}(47\ eV) = 0.932$ whereas Egert *et al.*[6] who observed the c(2x2) LEED pattern obtained the Auger peak ratio $P_{LMM}/Fe_{L_3VV} = 1.0$. For the data presented here, the Auger peak ratio was $P_{LMM}/Fe_{L_3VV} = 1.45$.

The photoemission spectra were collected using an angle-resolving electrostatic hemispherical electron energy analyzer (mean radius of 50 mm) which is rotatable 360° around the sample's vertical axis and 100° around the sample's horizontal axis. The analyzer pass energy was set to 160 eV and the energy resolution was approximately 1.6 eV FWHM. The angular resolution of the double einzel input lens was ±3°.

III. DATA ACQUISITION AND ANALYSIS

The photoemission data were collected in two different experimental geometries. In the first data set, the photoemission angle was normal to the Fe(100) surface, i.e. the [001] direction, and the photon polarization vector was 35° from the surface normal. This geometry gives information which is most sensitive to the Fe atoms directly below the P atoms. It could be a first layer Fe atom if P adsorbs in an atop site or a second layer Fe atom if P adsorbs in a four-fold hollow site. If P adsorbs in a bridge site, then the data will be very different. The second set of photoemission data was collected along the [011] direction, i.e. 45° off normal toward the (110) crystallographic plane, and the photon polarization vector was oriented parallel to the emission angle. By taking ARPEFS data off-normal, the structure parallel to the surface is enhanced. Thus, curves from the three possible adsorption sites listed above will appear significantly different. Analyzed together, the two different experimental geometries allow for an accurate determination of interlayer spacings, bond lengths, and bond angles.

ARPEFS raw data are a series of photoemission spectra with changing photoelectron kinetic energy which was varied from 60 eV to 600 eV (4 $Å^{-1}$ to 12.5 $Å^{-1}$, recorded in equal 0.1 $Å^{-1}$ steps). Each photoemission spectrum

was a 20 eV window with the P 1*s* photopeak located at the center. The peak was fit with a Voigt function to model the natural linewidth as well as the experimental broadening.[30]

The purpose of fitting the spectra is to extract the most accurate area from the peaks to construct the $\chi(k)$ diffraction curve containing the structural information. $\chi(k)$ is defined by[31]

$$\chi(k) = \frac{I(k)}{I_0(k)} - 1 \qquad (1)$$

where $I(k)$ is the peak area plotted as a function of the peak position in k-space. $I_0(k)$ is a smooth, slowly varying function with an oscillation frequency much lower than $I(k)$ and stems from the contribution of the inelastic scattering processes and the varying atomic cross section. It is adequate to use a simple polynomial function of energy to fit $I_0(k)$.[30] The experimental ARPEFS data thus obtained are plotted in figure 1 along with a schematic of the respective experimental geometries. The dashed curves in figure 1 are the best-fit results from the multiple scattering modeling calculations which will be discussed later.

A. Fourier Analysis

At this point, it is interesting to take the auto-regressive linear prediction based Fourier transform (ARLP-FT) to move from momentum space to real space. In ARPEFS, the positions of the strong peaks in ARLP-FTs from adsorbate/substrate systems can be predicted with fairly good accuracy using the single-scattering cluster (SSC) model together with the concept of strong backscattering from atoms located within a cone around

180° from the emission direction. The effective solid angle of this backscattering cone is ca. 30°-40°; it is not unique, but is operationally defined simply by opening the angle until it can account for the observed FT peaks based on the crystal geometry. Signals from scattering atoms very close to the source atom may be observable even if the scatterers lie outside the nominal backscattering cone.

These FT peaks correspond to path-length differences (PLDs), ΔR_j, between the component of the photoemitted wave that propagates directly to the detector and the components which are first scattered by the atomic potentials within this backscattering cone.[19] Thus, the peak positions are

$$\Delta R_j = r_j\left(1-\cos\theta_j\right)+\phi_j \qquad (2)$$

where r_j is the bond length, θ_j is the scattering angle (180° for exact backscattering), and ϕ_j is the atomic scattering phase shift. The scattering takes place inside the crystal and the ARPEFS data must be shifted from the measured $\chi\left(k_{\text{outside-crystal}}\right)$ to $\chi\left(k_{\text{inside-crystal}}\right)$ to account for the inner potential. In ARPEFS modeling calculations, the inner potential is treated as an adjustable parameter and is typically 0 - 15 eV. The inner potential for c(2x2)S/Fe(100) was determined to be 14.5 eV.[17] Thus, before Fourier transformation, the ARPEFS data presented here were shifted by 14 eV to higher kinetic energy.

Without knowing anything about the structure, an analysis of the normal and off-normal ARLP-FTs can yield insight to the adsorption site as well as to the bond distance. The sharp c(2x2) LEED pattern suggests that the monolayer coverage is 50% and that the P atoms adsorb on a high symmetry site such as atop, bridge, or four-fold hollow. Using the bulk Fe

interlayer spacing, 1.43 Å, the strong peak at 4.77 Å in the [001] FT can be used as a calibration to calculate the distance between the P layer and the first Fe layer for each adsorption site. This estimation ignores the small phase shift effects. The PLDs for the strong scattering events can then be calculated and the results for each adsorption site can compared to the [001] and [011] data FTs as is done in figure 2. The dashed vertical lines in figure 2 indicate expected peak positions for each respective geometry. The numbers with units of degrees indicate the scattering angles representative of these lines.

The calculated peak positions for the atop adsorption site are shown in figure 2a. Using the [001] FT peak at 4.77 Å for calibration, the P-Fe_1 interlayer spacing would be 2.39 Å. Calculating prominent PLDs shows reasonable agreement for the [001] FT except there is no way to account for the feature at 3.50 Å. Although the peak positions are in agreement, examining the [011] FT shows that an atop adsorption site is unlikely because the strongest feature in the data is the peak at 3.76 Å. The only Fe atom giving rise to this PLD would be at a scattering angle $\theta_j = 85°$. Since ARPEFS is dominated by backscattering events,[19,25] the data peak at 7.57 Å should dominate the FT if P adsorbs in an atop geometry.

When considering a bridge adsorption site, there are two possible P-Fe_1 interlayer spacings, depending on which atom one chooses for calibration of the 4.77 Å [001] data peak. Figure 2b indicates a spacing of 2.17 Å obtained if one believes that scattering from the *first* layer Fe atoms gives rise to this peak. Figure 2c indicates a spacing of 0.74 Å obtained if one believes that scattering from the *second* layer Fe atoms gives rise to this peak. In each case, only one of two possible bridge sites can be occupied with a c(2x2) LEED pattern. These sites are degenerate for the [001] FT but

become distinct for the [011] FT. For the off-normal case, the strong backscattering peak will be either from a first layer Fe atom or from a second layer Fe atom. Due to the symmetry of the (100) crystal face, each bridge site is energetically degenerate. Thus, in an experimental situation, domains of each will occur and [011] ARPEFS data from $\theta = 45°$, $\phi = 0°$ would be identical to ARPEFS data where $\theta = 45°$, $\phi = 90°$. The FT would show peaks from each domain. Therefore, if P adsorbed onto a bridge site, many more peaks would be expected in the [011] FT than are actually there. What this discussion implies is that ARPEFS is unable to distinguish the two domains of c(2x2) from a p(1x1) coverage in which both bridge sites were occupied equally. Unless, of course, the adsorbate-adsorbate interaction significantly effects the adsorbate-substrate bonding in the denser coverage.

As with the bridge site, two P-Fe_1 interlayer spacings are possible with the four-fold hollow site. If the data peak at 4.77 Å is due to scattering from a *first* layer Fe atom, then the layer spacing would be 1.96 Å. These calculated PLDs are shown in figure 2d. However, if this was the correct geometry, an intense peak due to backscattering from the second layer Fe atoms is expected at 6.79 Å. Additionally, the [011] FT would be dominated by a backscattering PLD at 5.22 Å. The scattering angle for the line at 3.19 Å would be 98° which is not expected to be so strong as described above.

Alternatively, if the P adsorbs in a four-fold hollow site and the data peak at 4.77 Å is due to backscattering from the *second* layer Fe atoms, then the P-Fe_1 interlayer spacing would be 0.95 Å. These calculated PLDs are shown in figure 2e. For this proposed geometry, the calculated PLDs are in good agreement with the data and the scattering angles are reasonable for the relative strengths of each peak.

In fact, from the structure analysis of c(2x2)S/Fe,[15-17] it is expected that the P atoms adsorb in the four-fold hollow sites and are ~1 Å above the first layer Fe atoms. It is possible to extend this estimate by calibrating the P-Fe_1 interlayer spacing to each strong data peak and then averaging the results. Doing this estimation, the P-Fe_1 interlayer spacing would be 1.19 Å. Noting that this distance is significantly expanded over the S/Fe value of 1.09 Å[17] and that this process neglects phase shifts, one should realize that 1.19 Å is probably too large.

Modeling calculations to be described in the next section are necessary to obtain highly precise bond distances. However, with no modeling calculations, it has already been determined that P adsorbs in the high coordination four-fold hollow sites and the P-Fe_1 interlayer spacing is between 0.95 Å and 1.19 Å. The ARLP-FTs for both the [001] and the [011] data sets are presented in figure 3. Also shown in figure 3 is a schematic of the crystal with the backscattering cone for each emission direction superimposed; the labeled atoms correspond to labeled peaks in each FT . The solid lines indicate the scattering atoms for [001] photoemission while the dashed lines indicate the scattering atoms for [011] photoemission. Peaks arise in the FT due to scattering from atoms up to five layers below the emitting atoms. The depth sensitivity of ARPEFS has been described previously[32] and was found to be enhanced by multiple-scattering effects.

B. Multiple Scattering Analysis

Modeling calculations were performed to simulate the ARPEFS $\chi(k)$ curve and obtain a structure more precise than yielded by the FT analysis. Using the single-scattering model of ARPEFS,[19,31] $\chi(k)$ can be written as

$$\chi(k) = \sum_j A_j(k) \cos\left[k\left(R_j - R_j \cos\theta_j\right) + \phi_j\right] \qquad (3)$$

where $A_j(k)$ contains experimental geometry factors including the photon polarization direction and the electron emission direction as well as the scattering amplitude, aperture integration, and thermal averaging.

A new code developed by Chen, Wu, and Shirley[33] based on the Rehr-Albers formalism[34] was used for the multiple-scattering spherical-wave calculations presented here. This new code differs from the Kaduwela/Fadley code[35] and is sufficiently fast that multi-curve fitting calculations can be performed.

The calculations require both structural and nonstructural input parameters. The initial structural parameters were determined from the FT analysis. The nonstructural parameters included were the initial state, the atomic scattering phase shifts, the crystal temperature, the inelastic mean free path, the emission and polarization directions, the electron analyzer acceptance angle, and the inner potential. The fitting procedure allowed the structure to vary as well as the inner potential such that a best fit was obtained.

To account for vibration effects of the bulk atoms, the mean square relative displacement (MSRD) was calculated using equation (33) by Sagurton *et al.*[36]

$$\left\langle u_i^2 \right\rangle \propto \frac{1}{M_i \theta_{\mathrm{D},i}} \left(1 + \frac{cT^2}{\theta_{\mathrm{D},i}^2} \cdots\right) \qquad (4)$$

where M_i is the atomic mass, $\theta_{D,i}$ is the correlated Debye temperature, T is the sample temperature, and c is a coefficient that varies slowly with temperature. For calculating the MSRD of the bulk Fe atoms, $\theta_{D,i}$ was set to 400 K.

Accounting for the surface atomic vibration is not as straightforward. The relation between the MSRD and different atomic masses has been given by Allen *et al.*[37]

$$\langle u_i^2 \rangle \sqrt{M_i} = \langle u_j^2 \rangle \sqrt{M_j} \qquad (T \approx 0\ \mathrm{K}) \tag{5}$$

$$\langle u_i^2 \rangle = \langle u_j^2 \rangle \qquad (T \to \infty) \tag{6}$$

Correlating equations (5) and (6) with equation (4), an effective surface atomic mass is introduced such that

$$\langle u_{i,\mathrm{bulk}}^2 \rangle \sqrt{M_{i,\mathrm{bulk}}} \cong \langle u_{j,\mathrm{surface}}^2 \rangle \sqrt{M_{j,\mathrm{effective}}} \tag{7}$$

where $M_{j,\mathrm{effective}} = M_{j,\mathrm{surface}}$ if $T/\theta_{D,i} << 1$ or $M_{j,\mathrm{effective}} = M_{j,\mathrm{bulk}}$ if $T/\theta_{D,i} > 1$. For $T/\theta_{D,i} \approx 1$, $M_{j,\mathrm{effective}}$ is allowed to vary between the surface and bulk atomic masses. For this study where $T = 300$ K and $\theta_{D,i} = 400$ K, it was found that the calculated $\chi(k)$ diffraction curve was insensitive to the surface atomic mass, so $M_{j,\mathrm{effective}}$ was set to the atomic mass of P, 31 a.u.

The atomic-scattering phase shifts were calculated in situ by using the atomic potentials tabulated by Moruzzi *et al.*[38] The emission and polarization directions and the electron analyzer acceptance angle were set to match the experiment as described earlier. The inelastic mean free path (IMFP) was included using the exponential damping factor $e^{-r/\lambda}$ where λ was calculated using the Tanuma, Powell, and Penn (TPP-2) formula.[39] The

IMFP calculation is important in obtaining a close fit to the data and in determining the depth sensitivity of ARPEFS. The TPP-2 formula seems to be the most accurate method to determine the IMFP, especially below 200 eV.

The 'multi-curve fitting' feature means that multiple data curves can be fit simultaneously as explained later. Figure 1 illustrates the best fit (dashed lines) to both the [001] and the [011] ARPEFS data sets (solid lines) by simultaneous fitting. For these fits, a 76 atom cluster was used and the P-Fe_1 interlayer spacing was determined to be 1.02(2) Å. The inner potential was 15.0 eV. The fitting also determined that there was no relaxation of the first or second Fe layers from the bulk 1.43 Å interlayer spacing.

Each data curve was also fit individually to compare the results. For the [001] individual fit, a 76 atom cluster was used and the P-Fe_1 interlayer spacing was determined to be 1.02(2) Å. For the [011] individual fit, a 75 atom cluster was used and the P-Fe_1 interlayer spacing was determined to be 1.01(2) Å. The inner potential was the same as with the simultaneous fits. Neither of the individual fits showed any relaxation of the first two Fe layers. These results confirm the validity of the multi-curve fitting method.

Finally, an attempt was made to fit the ARPEFS data using an atop adsorption site and a bridge adsorption site. For each site, the [001] and [011] curves were fit simultaneously. The results are presented in figure 4.

Simple visual inspection is sufficient to rule out the atop and bridge adsorption sites. The [001] atop fit is quite good, as is expected due to the symmetry similarities with the four-fold hollow site. When viewing off-normal, however, this symmetry is broken. This is shown by the [011] fit which is better for the four-fold hollow site than for the atop site (e.g., at

~6.5 $Å^{-1}$ and ~9 $Å^{-1}$). The bridge best fits are not competitive with the other two possible sites, especially when viewing off-normal.

These comparisons further prove that the P atoms adsorb in the four-fold hollow sites as concluded from the FT analysis. Additionally, they illustrate the importance of acquiring ARPEFS data in at least two different emission directions to be certain of the adsorption site. The four-fold hollow adsorption site and the P-Fe_1 interlayer spacing for this c(2x2)P/Fe(100) structure correlate well with the structure for chemisorbed c(2x2)S/Fe(100).[15-17]

C. Discussion of Error

The best fit is determined by an R-factor minimization. A three-step fitting process is used to determine the true R-factor minimum to prevent convergence to a local minimum. The initial coarse-fitting minimizes the $\tilde{R}$-factor, $\tilde{R} = R_a$ where

$$R_a = \frac{\sum_i \left[\chi_{i,c}(k) - \chi_{i,e}(k)\right]^2}{\sum_i \left[\chi_{i,c}^2(k) + \chi_{i,e}^2(k)\right]} \tag{8}$$

using a simple net search.[33] $\chi_{i,c}(k)$ and $\chi_{i,e}(k)$ are the points in the calculated and experimental $\chi(k)$ curves respectively. Second, the code again minimizes $\tilde{R} = R_a$ using the Downhill Simplex Method in Multidimensions.[40] Finally, the code minimizes $\tilde{R} = R$ where

$$R = \frac{\sum_i \left[\chi_{i,c}(k) - \chi_{i,e}(k)\right]^2}{\sum_i \chi_{i,e}^2(k)} \qquad (9)$$

using the Nonlinear Marquardt Method.[40]

When using the multi-curve fitting feature, $\tilde{R}$-factors from each fit must be considered. For this, the sum of the individual $\tilde{R}$-factors, $\tilde{R}_{\text{total}}$, is used. Thus, if fitting N ARPEFS curves simultaneously, then

$$\tilde{R}_{\text{total}} = \sum_j \frac{1}{N} \tilde{R}_j \qquad (10)$$

Note that the code is flexible such that a weighted sum could be used if justification could be made for giving preference to the $\tilde{R}$-factor of one ARPEFS curve over another.

While fitting, the largest effects stem from changes in the inner potential and the P-Fe_1 interlayer spacing. Figure 5 shows a contour plot of the R-factor as the inner potential and P-Fe_1 interlayer spacing are varied. Analysis of figure 5 indicates that the precision of ARPEFS is ~±0.02 Å, but only if the inner potential is known very well. If, however, the inner potential is allowed to float without constraint, the precision of ARPEFS drops to ~±0.03 Å.

IV. SCF-Xα-SW Calculations

The chemisorption structure of c(2x2)P/Fe(100) and c(2x2)S/Fe(100)[17] from the experimental determination may be further confirmed by theoretical calculations in an appropriate model. In this

section, SCF-Xα-SW (or Xα-SW) calculations are presented for two atomic clusters, PFe_9 and SFe_9, which represent the two chemisorption systems P/Fe and S/Fe, respectively.

The SCF-Xα-SW formalism developed by Slater[41] and Johnson[42,43] seems to be a convenient compromise between the need for rigorous calculations and the limitations of computing resources. The SCF equation is solved numerically. Basis sets are utilized only in the sense that there is a choice of maximum ℓ value allowed on each center. The numerical solution is made possible by the Xα approximation for the exchange contribution to the total potential and the muffin-tin approximation for molecular potential and charge densities. Studies of a range of molecular properties have shown that this method has better performance than semiempirical MO methods and gives results of roughly double-zeta *ab initio* quality.[44-49] The tremendous orbital sizes in these clusters make *ab initio* methods virtually impossible to apply and so the Xα-SW method is the highest level of theory practically available for this work. In fact, the Xα-SW method is particularly appropriate because of the high symmetry of the clusters for the calculations.

Due to the limitations of the muffin-tin approximation, the Xα-SW method may not provide a very accurate calculation of reaction energetics such as the adsorption energy of the P/Fe or S/Fe system. However, the error introduced by the muffin-tin approximation can be overcome to some extent by the use of overlapping atomic spheres.[50] Therefore, it is expected that the relative changes of the total energy can be described to desirable accuracy, especially those involved in small structural variations near the equilibrium positions. Of course, the standard parameters should be used for

this purpose and the predicted equilibrium structures should not be sensitive to the values of the parameters.

All standard non-empirical parameters for the calculations were used. The radii of atomic spheres were chosen according to Norman[51] and the α exchange parameters were taken from Schwarz's[52] tabulations. In the intersphere and outersphere regions, an average value of α, obtained from a valence-weighted average of the α's for the atoms in the cluster, is employed. Figure 6 shows the structures of the two clusters PFe_9 and SFe_9. The overall symmetry for each cluster is C_{4v}. The four Fe atoms in the top layer are labeled by Fe_1 and the five Fe atoms in the second layer are labeled by Fe_2. The distance of the adsorbed atom P (or S) to the plane formed by the Fe_1 atoms is P-Fe_1 (or S-Fe_1) and the distance between the first and the second layers of Fe atoms is Fe_1-Fe_2. The total energies of the clusters were calculated at several P-Fe_1 (S-Fe_1) distances embracing the experimental equilibrium distance while the Fe_1-Fe_2 interlayer distance was kept at the experimental value. The total energy for a different Fe_1-Fe_2 interlayer distance was also calculated at the experimental P-Fe_1 (S-Fe_1) distance to compare the structural difference in the Fe_1-Fe_2 layer between the P/Fe and the S/Fe systems. The calculation results are presented in tables 1 and 2 for PFe_9 and SFe_9, respectively.

It is seen in table 1 that the P-Fe_1 interlayer distance at the energy minimum is around 1.01 Å with the Fe_1-Fe_2 interlayer distance set at the bulk value of 1.43 Å. This result is consistent with the experimentally obtained structure. Table 2 similarly shows good agreement between the calculations and experiment for the S/Fe^{17} system where the S-Fe_1 interlayer distance at the energy minimum is around 1.09 Å with the Fe_1-Fe_2 interlayer distance set at the experimentally determined value of 1.40 Å.

These calculation results confirm the ARPEFS determination that the Fe_1-Fe_2 interlayer spacing is contracted from the bulk value for S/Fe but not for P/Fe. If the Fe_1-Fe_2 interlayer spacing is contracted to 1.40 Å for the P/Fe system, the total energy is raised by 1.38 eV. Similarly, if the Fe_1-Fe_2 interlayer spacing is fixed at the 1.43 Å bulk value for the S/Fe system, the total energy is raised by 3.82 eV.

V. DISCUSSION

In this section, the structure determined here for c(2x2)P/Fe(100) is compared with atomic c(2x2)N/Fe(100),[12] atomic p(1x1)O/Fe(100),[13,14] and c(2x2)S/Fe(100).[15-17] These four elements border each other on the periodic table and their interaction with iron is very important in materials science, catalysis, and magnetism.

In table 3, a summary of these four structures is presented along with the structure of the clean Fe(100) surface.[17,53] The structure of atomic O adsorbed on the Fe(100) surface is interesting because the coverage is p(1x1), unlike atomic N, P, or S. Also, using first principles calculations, Chubb and Pickett[14] predict a very large expansion of the first layer Fe atoms. A smaller (by a factor of three) but significant expansion was experimentally determined by Legg *et al.* using LEED.[13] Figure 7 shows a schematic of both proposed oxygen structures (experiment on left, theory on right) as well as the structures for N, P, and S. Because of its ability to accurately determine the near-surface reconstruction of the substrate, ARPEFS should be used to study the p(1x1)O/Fe(100) structure.

VI. CONCLUSION

Angle-resolved photoemission extended fine structure was used to determine the structure of c(2x2)P/Fe(100) for the first time. Photoemission data were collected normal to the (100) surface and 45° off-normal along the [011] direction at room temperature. A close analysis of the ARLP based FT indicates that the P atoms adsorb in the high-coordination four-fold hollow sites. The FT analysis also allowed the bond distances to be estimated with surprisingly high accuracy. The curved-wave multiple scattering calculations which simulate the photoelectron diffraction confirmed the four-fold hollow adsorption site. By simultaneously fitting both ARPEFS data sets, the P atoms were determined to bond 1.02(2) Å above the first layer of Fe atoms. The Fe-P-Fe bond angle is thus 140.6°. Assuming the radius of the Fe atoms is 1.24 Å, the effective P radius is 1.03 Å. The inner potential was 15.0 eV. It was also determined that there was no relaxation of the first or second Fe layers from the bulk 1.43 Å interlayer spacing. To test this fitting method, each data set was fit individually and these results were in good structural agreement.

Additionally, self-consistent-field Xα scattered wave calculations were performed for the c(2x2)P/Fe(100) and the c(2x2)S/Fe(100)[17] systems. These independent results are in excellent agreement with this P/Fe structure and the S/Fe structure previously published, confirming the ARPEFS determination that the Fe_1-Fe_2 interlayer spacing is contracted from the bulk value for S/Fe but not for P/Fe.

SCF-Xα-SW Calculation Results for PFe_9

P-Fe_1 Interlayer Spacing (Å)	Total Energy (eV)	ΔE (eV)
1.06	-318411.46	1.89
1.04	-318412.48	0.87
1.01	-318413.35	0
0.99	-318410.35	3.00
1.01	-318411.97	1.38

Variations of the total energy and the relative energy of PFe_9 with the P-Fe_1 interlayer distance from Xa-SW calculations (Fe_1-Fe_2 was fixed at 1.43 Å). The last row lists the calculated energy with Fe_1-Fe_2 fixed at 1.40 Å.

Table 1

SCF-Xα-SW Calculation Results for SFe_9

S-Fe_1 Interlayer Spacing (Å)	Total Energy (eV)	ΔE (eV)
1.14	-319983.03	2.39
1.12	-319984.57	0.85
1.09	-319985.42	0
1.07	-319984.40	1.02
1.04	-319982.77	2.65
1.09	-319981.60	3.82

Variations of the total energy and the relative energy of SFe_9 with the S-Fe_1 interlayer distance from Xα-SW calculations (Fe_1-Fe_2 was fixed at 1.40 Å). The last row lists the calculated energy with Fe_1-Fe_2 fixed at 1.43 Å.

Table 2

Adsorbate Structure on an Fe(100) Substrate

	Clean Surface	Atomic Nitrogen	Atomic Oxygen[b]	Phosphorus	Sulfur
Coverage	--	c(2x2)	p(1x1)	c(2x2)	c(2x2)
$r_{eff}[X]$ (Å)	--	0.59	0.78	1.03	1.06
$r_{eff}[Fe]$ (Å)	1.24	1.24	1.24	1.24	1.24
$d_{\perp}[X\text{-}Fe_1]$ (Å)	--	0.27	0.48 0.38	1.02	1.09
$d_{\perp}[Fe_1\text{-}Fe_2]$ (Å)	1.41 (-1.4%)[a]	1.54 (+7.7%)	1.54 (+7.7%) 1.76 (+23%)	1.43	1.40 (-2.1%)
$d_{\perp}[Fe_2\text{-}Fe_3]$ (Å)	1.43	1.43	1.43	1.43	1.46 (+2.1%)
$d_{\perp}[X\text{-}Fe_2]$ (Å)	--	1.81	2.02 2.14	2.45	2.49
Bond Angle Fe-X-Fe	--	164.8°	153.3° 158.7°	140.6°	123.4°

[a]Percent expansion from the bulk 1.43 Å value.
[b]Upper value from reference 13; Lower value from reference 14.

Structures of clean Fe(100), c(2x2)N/Fe(100), p(1x1)O/Fe(100), c(2x2)P/Fe(100), and c(2x2)S/Fe(100). For the Fe_1-Fe_2 interlayer spacing, the percent expansion from the 1.43 Å bulk value is indicated. For O/Fe, the upper value indicates the experimental results while the lower value indicates the theoretically predicted structure. *"X"* indicates the adsorbate.

Table 3

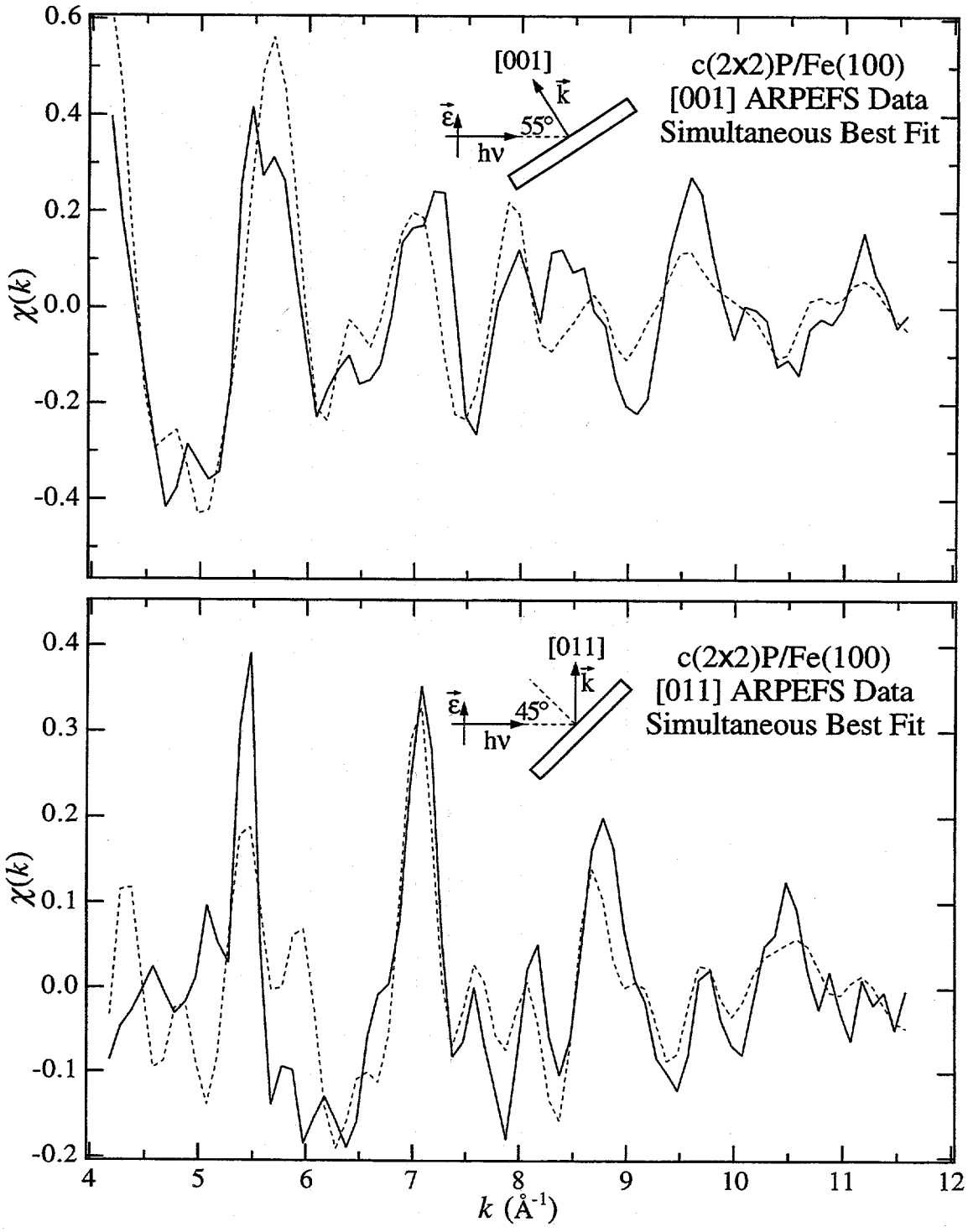

ARPEFS data for c(2x2)P/Fe(100) in the [001] and [011] directions. Also, schematics of each experimental geometry are shown. The dashed lines are the best-fit multiple-scattering modeling calculation results obtained by fitting both data sets simultaneously.

Figure 1

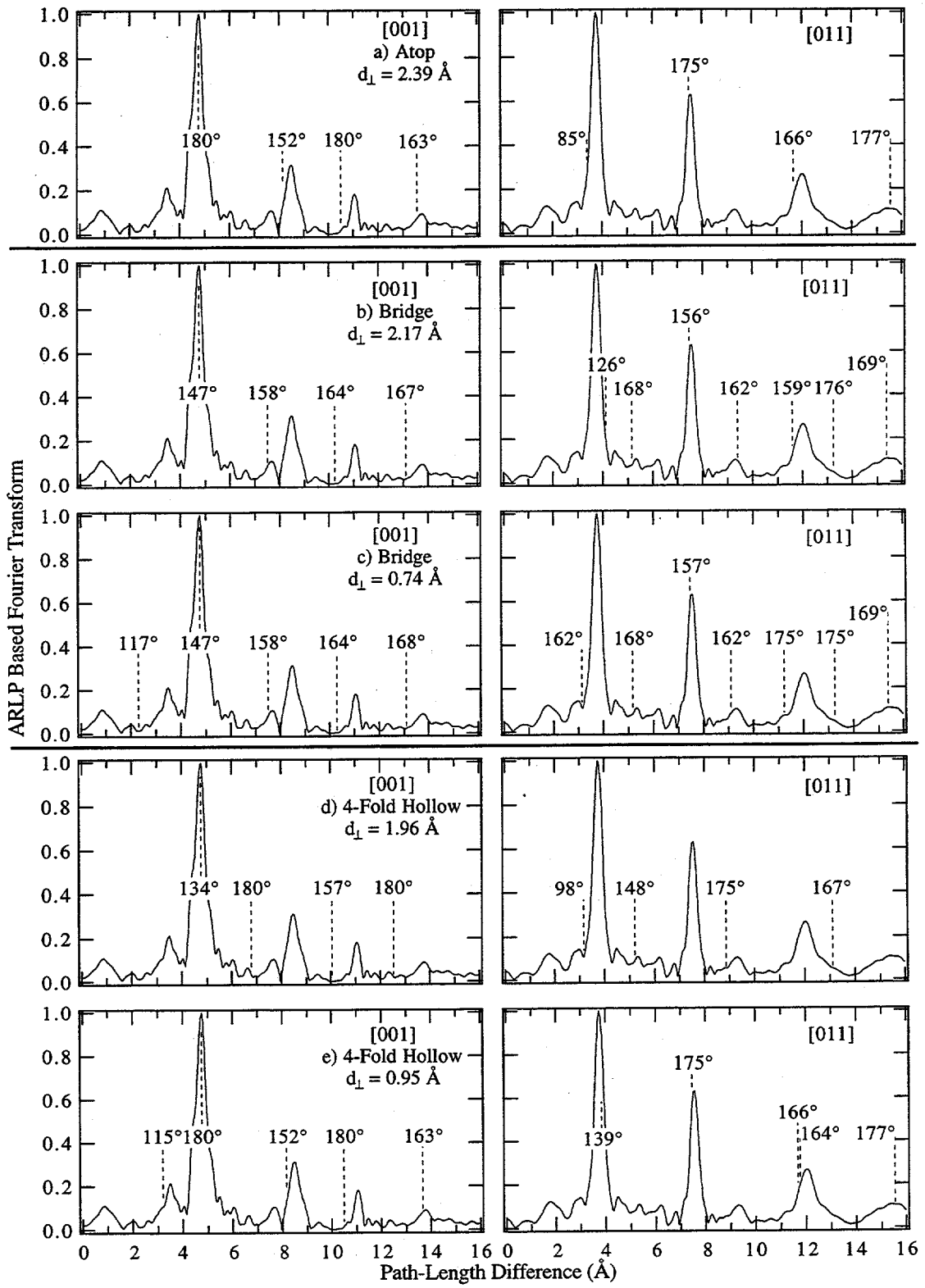

ARLP-FTs of the ARPEFS [001] data (left) and [011] data (right). Expected peak positions and scattering angles are shown for a) atop, $d_\perp$ = 2.39 Å; b) bridge, $d_\perp$ = 2.17 Å; c) bridge, $d_\perp$ = 0.74 Å; d) four-fold hollow, $d_\perp$ = 1.96 Å; e) four-fold hollow, $d_\perp$ = 0.95 Å.

Figure 2

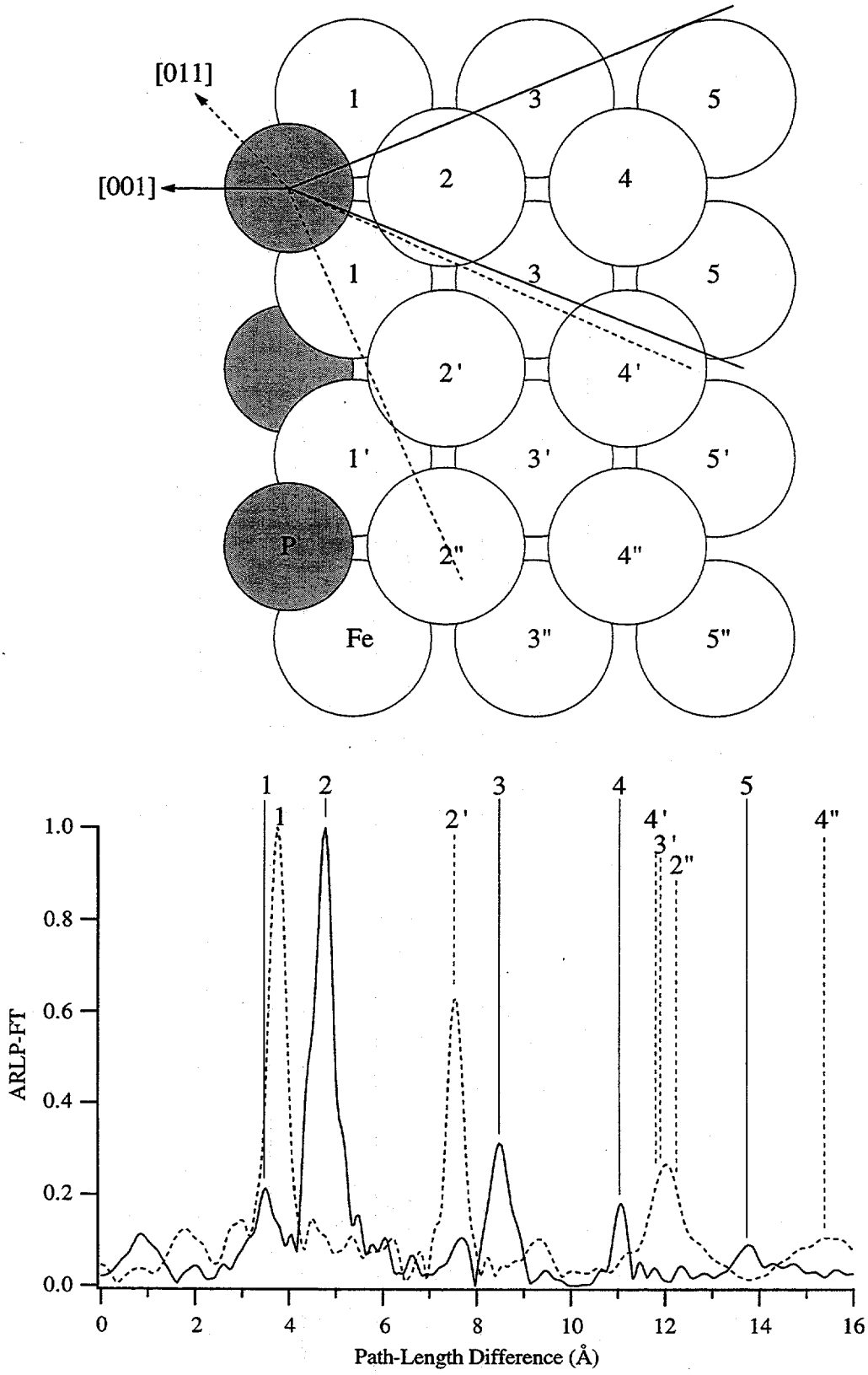

ARLP-FTs of the ARPEFS [001] (solid line) and [011] (dashed line) data. Each peak corresponds to an atom in the lattice; a backscattering cone for each direction is shown.

Figure 3

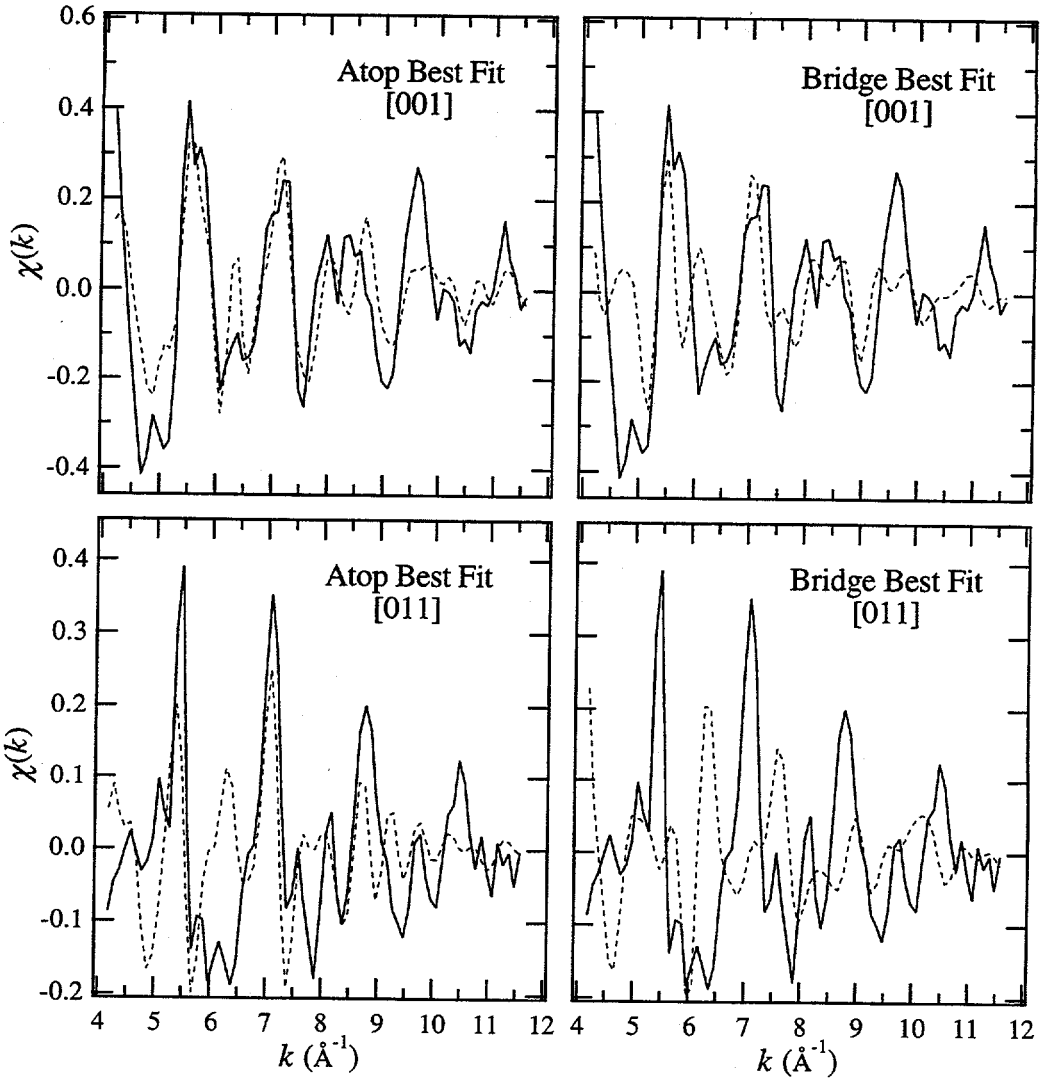

Best fit (dashed lines) to the [001] and [011] ARPEFS data by assuming an atop adsorption site or a bridge adsorption site.

Figure 4

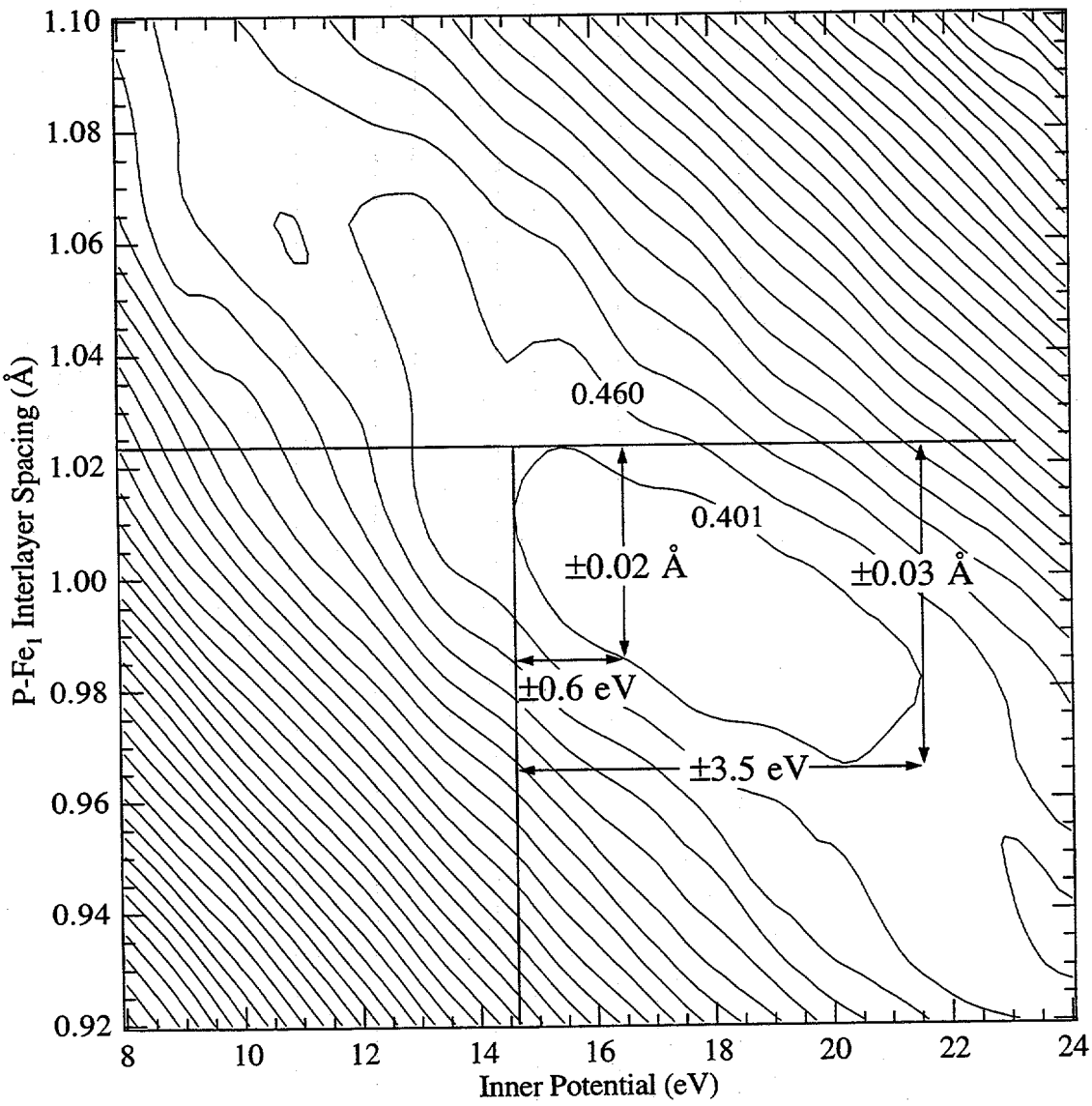

Contour plot showing how the *R*-factor varies with the P-Fe_1 interlayer spacing and the inner potential when simultaneously fitting the [001] and [011] ARPEFS data.

Figure 5

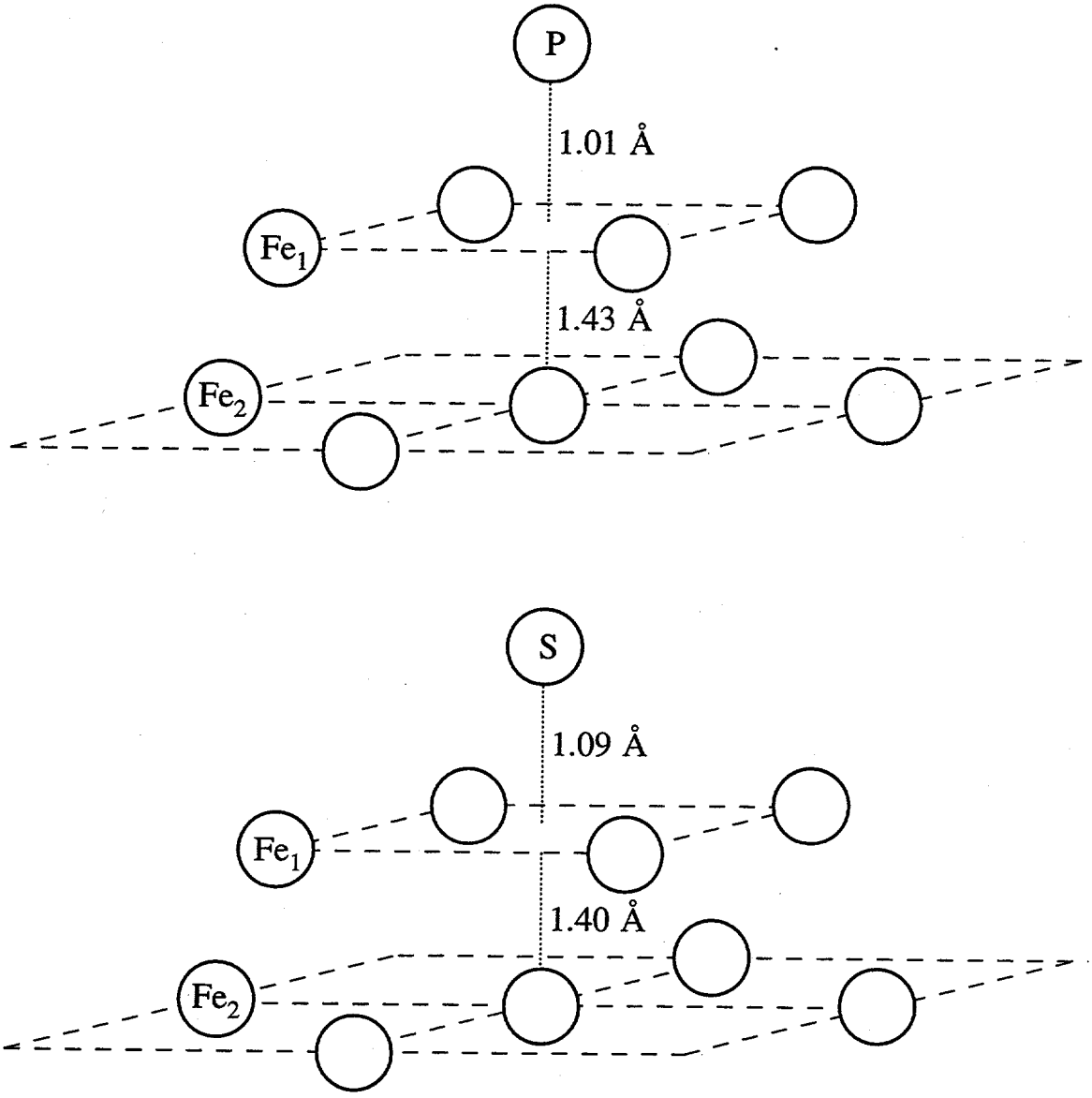

Structure of the two clusters PFe_9 and SFe_9 used for the Xα-SW calculations.
Figure 6

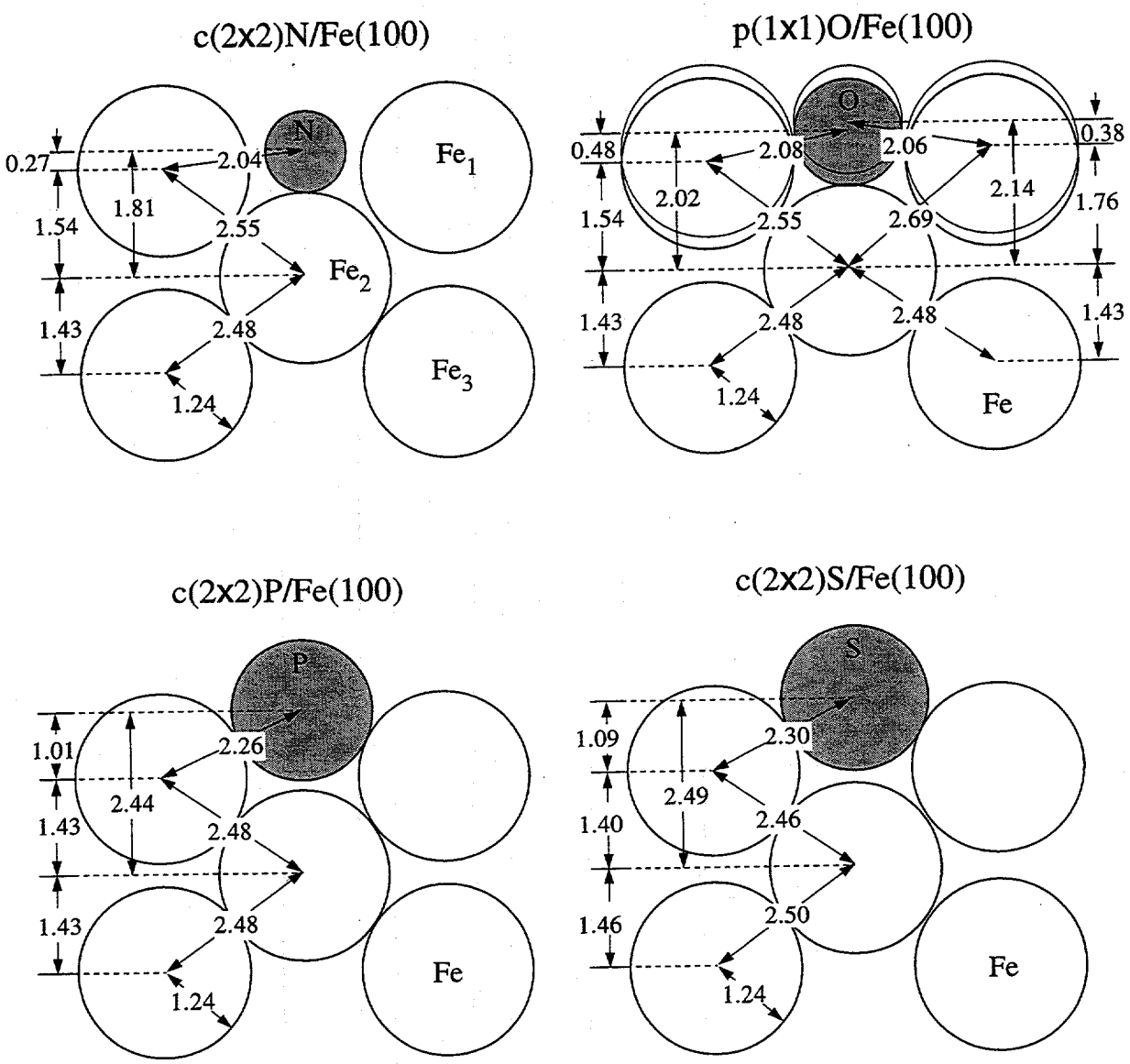

Schematics of the structures of atomic c(2x2)N/Fe(100), atomic p(1x1)O/Fe(100) (experiment on left, theory on right), c(2x2)P/Fe(100), and c(2x2)S/Fe(100).

Figure 7

REFERENCES

[1]G.L. Krasko and G.B. Olson, Solid State Commun. **76**, 247(1990).
[2]R. Wu, A.J. Freeman and G.B. Olson, J. Mater. Res. **7**, 2403(1992).
[3]S. Tang, A.J. Freeman and G.B. Olson, Phys. Rev. B **47**, 2441(1993).
[4]R. Wu, A.J. Freeman and G.B. Olson, Phys. Rev. B **47**, 6855(1993).
[5]R. Wu, A.J. Freeman and G.B. Olson, Phys. Rev. B **50**, 75(1994).
[6]B. Egert and G. Panzner, Surf. Sci. **118**, 345(1982).
[7]S. Ohnishi, A.J. Freeman and M. Weinert, Phys. Rev. B **28**, 6741(1983).
[8]Y. Sakisaka, Y.N. Rhodin, B. Egert and H. Grabke, Solid State Commun. **49**, 579(1984).
[9]C.L. Fu and A.J. Freeman, Phys. Rev. B **35**, 925(1987).
[10]S.R. Chubb and W.E. Pickett, Phys. Rev. B **38**, 10227(1988).
[11]R. Wu and A.J. Freeman, Phys. Rev. B **47**, 3904(1993).
[12]R. Imbihl, R.J. Behm, G. Ertl and W. Moritz, Surf. Sci. **123**, 129(1982).
[13]K.O. Legg, F. Jona, D.W. Jepsen and P.M. Marcus, Phys. Rev. B **16**, 5271(1977).
[14]S.R. Chubb and W.E. Pickett, Solid State Commun. **62**, 19(1987).
[15]K.O. Legg, F. Jona, D.W. Jepsen and P.M. Marcus, Surf. Sci. **66**, 25(1977).
[16]R.A. DiDio, E.W. Plummer and W.R. Graham, J. Vac. Sci. Technol. **A2**, 983(1984).
[17]X.S. Zhang, L.J. Terminello, S. Kim, Z.Q. Huang, A.E. Schach von Wittenau and D.A. Shirley, J. Chem. Phys. **89**, 6538(1988).
[18]D.P. Woodruff, D. Norman, B.W. Holland, N.V. Smith, H.H. Farrell and M.M. Traum, Phys. Rev. Lett. **41**, 1130(1978).
[19]J.J. Barton, C.C. Bahr, S.W. Robey, Z. Hussain, E. Umbach and D.A. Shirley, Phys. Rev. B **34**, 3807(1986).
[20]S.W. Robey, J.J. Barton, C.C. Bahr, G. Liu and D.A. Shirley, Phys. Rev. B **35**, 1108(1987).
[21]L.J. Terminello, K.T. Leung, Z. Hussain, T. Hayashi, X.S. Zhang and D.A. Shirley, Phys. Rev. B **41**, 12787(1990).
[22]L.Q. Wang, A.E. Schach von Wittenau, L.S. Wang Z.G. Ji, Z.Q. Huang and D.A. Shirley, Phys. Rev. B **44**, 1292(1991).
[23]Z.Q. Huang, Z. Hussain, W.T. Huff, E.J. Moler and D.A. Shirley, Phys. Rev. B **48**, 1696(1993).
[24]Z.Q. Huang, L.Q. Wang, A.E. Schach von Wittenau, Z. Hussain and D.A. Shirley, Phys. Rev. B **47**, 13626(1993).

[25]J.J. Barton, C.C. Bahr, Z. Hussain, S.W. Robey, J.G. Tobin, L.E. Klebanoff and D.A. Shirley, Phys. Rev. Lett. **51**, 272(1983).

[26]J.J. Barton, Z. Hussain and D.A. Shirley, Phys. Rev. B **35**, 933(1987).

[27]S.D. Kevan, *Ph.D. Thesis*, The University of California, Berkeley, LBL-11017(1980).

[28]Z. Hussain, E. Umbach, D.A. Shirley, J. Stohr and J. Feldhaus, Nucl. Instrum. Methods **195**, 115(1982).

[29]C.A. Shell and J.C. Rivière, Surf. Sci. **40**, 1496(1973).

[30]J.J. Barton, *Ph.D. Thesis*, The University of California, Berkeley, LBL-19215(1985).

[31]J.J. Barton, S.W. Robey and D.A. Shirley, Phys. Rev. B **34**, 778(1986).

[32]Y. Zheng and D.A. Shirley, Chem. Phys. Lett. **203**, 114(1993).

[33]Y. Chen, H. Wu and D.A. Shirley, *CWMS Code - Unpublished*(1995).

[34]J.J. Rehr and R.C. Albers, Phys. Rev. B **41**, 8139(1990).

[35]A. Kaduwela, *Ph.D. Thesis*, University of Hawaii at Manoa, Honolulu(1991).

[36]M. Sagurton, E.L. Bullock and C.S. Fadley, Surf. Sci. **182**, 287(1987).

[37]R.E. Allen, G.P. Alldredge and F.W. de Wette, J. Chem. Phys. **54**, 2605(1971).

[38]V.L. Moruzzi, J.F. Janak and A.R. Williams, *Calculated Electronic Properties of Metals*, (Pergamon Press, Inc., New York, 1978).

[39]S. Tanuma, C.J. Powell and D.R. Penn, Surf. Interface Anal. **20**, 77(1993).

[40]W.H. Press, S.A. Teukolsky, W.T. Vetterling and B.P. Flannery, *Numerical Recipes in Fortran: The Art of Scientific Computing*, 2 ed., (University Press, Cambridge, 1992).

[41]J.C. Slater, Phys. Rev. **81**, 385(1951).

[42]K.H. Johnson, J. Chem. Phys. **45**, 3085(1966).

[43]K.H. Johnson, Adv. Quantum Chem. **7**, 143(1972).

[44]M. Cook and M. Karplus, J. Chem. Phys. **72**, 7(1980).

[45]D.A. Case, M. Cook and M. Karplus, J. Chem. Phys. **73**, 3294(1980).

[46]M.E. Eberhart, K.H. Johnson and D. Adler, Phys. Rev. B **26**, 3138(1982).

[47]J.S.-Y. Chao and K.D. Jordan, J. Phys. Chem. **91**, 5578(1987).

[48]M. Cook and C.T. White, Phys. Rev. B **38**, 9674(1988).

[49]H. Adachi and M. Takano, J. Solid State Chem. **93**, 556(1991).

[50]J.C. Slater, *Solid State and Molecular Theory: A Scientific Biography*, (Wiley, New York, 1975).

[51]Jr. J.G. Norman, Mol. Phys. **31**, 1191(1976).

[52]K. Schwarz, Phys. Rev. B **5**, 2466(1972).

[53]K.A.R. Mitchell, Surf. Sci. **100**, 225(1980).

Chapter 3

Final-State Effects in the Angle-Resolved Photoemission Extended Fine Structure of c(2x2)S/Ni(001)

ABSTRACT

Final-state effects on angle-resolved photoemission extended fine structure (ARPEFS) $\chi(k)$ curves were studied using previously published normal-emission experimental data from the S $1s$ and S $2p$ core levels of c(2x2)S/Ni(001). The two $\chi(k)$ curves appeared to be approximately 180° out of phase as predicted by Tong and Tang. However, in contrast to the expectations based on plane-wave theory, the Fourier transforms of the experimental S $1s$ and S $2p$ data sets are quite different, with a Generalized Ramsauer-Townsend splitting present in the $1s$ but not in the $2p$ data. Multiple-scattering spherical-wave calculations were carried out to study the final-state effects. Based on the calculations, an approximate method for analyzing ARPEFS data from a non-s initial-state using only the higher-ℓ partial wave was proposed and successfully tested with the experimental S $2p$ ARPEFS data.

I. INTRODUCTION

Angle-resolved photoemission extended fine structure (ARPEFS), in which angle-resolved core-level photoemission intensities from surface atoms are measured over a wide photoelectron kinetic-energy range, is a proven technique for surface/interface structure determination.[1-6] In the past few years, ARPEFS has been used successfully to study the local atomic structure around the adsorbate atoms and the adsorbate-induced relaxation of the substrates.[7-16] In these studies, Fourier transform (FT) analyses yielded qualitative and semi-quantitative surface structural information. The peaks in the ARPEFS-FT spectrum correspond to path-length differences (PLDs) between the direct wave and single-scattered waves, plus a phase shift. Additionally, multiple-scattering spherical-wave (MSSW) analyses of ARPEFS $\chi(k)$ data yielded quantitative surface structures.

Most of the above ARPEFS studies were based on photoemission data from atomic *s* core-level initial states, for which the selection rule $\Delta\ell_i = \pm 1$ gives a *p*-wave final state. Experience with ARPEFS data from non-*s* initial states and their FTs is very limited, however. For non-*s* initial states ($\ell_i \neq 0$), the photoelectron final state is made up of partial waves with orbital quantum numbers $\ell_i + 1$ and $\ell_i - 1$, and a phase relationship between them which leads to interference between the two partial waves. The partial wave transition matrix elements and the phase angle are in general energy-dependent. Despite these complications, there are a number of interesting experimental situations for which ARPEFS studies on a non-*s* initial state may confer some advantage. For this reason, as well as general curiosity, it was decided that a more careful comparison of the existing data on the c(2x2)S/Ni(001) system should be made.

Two important results emerged. First, the Fourier transforms of the two data sets differed substantially, with a peak being split by the Generalized Ramsauer-Townsend Effect in one data set but not in the other. Second, the dominance of the $\ell_i + 1$ partial wave in the final state is so strong that the data could be analyzed with very good accuracy by using this wave alone, ignoring the $\ell_i - 1$ wave. A similar effect has been noted in extended x-ray absorption fine structure (EXAFS) studies.[17,18]

Tong and Tang[9,10] reported a theoretical study of the effect of final-state symmetry on normal photoelectron diffraction data, based on calculations of backscattering from sub-surface crystal layers. They derived the factor $(-1)^{\ell_i+1}$ to describe the phase relationship of ARPEFS $\chi(k)$ data from an arbitrary initial state. According to this factor, the ARPEFS $\chi(k)$ curves for initial states of odd ℓ_i are predicted to be 180° out of phase relative to those for initial states of even ℓ_i. Furthermore, their calculations showed for c(2x2)S/Ni(001) that, in their layer-scattering model, the ARPEFS $\chi(k)$ curves from different initial states would have the same frequencies, and the ARPEFS-FTs would therefore have the same peak positions. Tang[10] later examined the data, found quite good agreement, and concluded that these predictions were borne out.

In the present work, this issue has been reinvestigated in more detail. The same experimental S 1*s* and S 2*p* ARPEFS data from c(2x2)S/Ni(001) is used. Both data sets were measured normal to the crystal surface plane because in the early work the "normal photoelectron diffraction," or NPD, mode was regarded as special, consistent with the picture of backscattering off crystal planes rather than atoms. The photon polarization vectors were oriented 30° and 35° off the surface normal toward the [011] direction.[11,12]

II. DISCUSSION

Figure 1a compares these two ARPEFS data sets. The experimental S 1*s* and S 2*p* ARPEFS $\chi(k)$ curves are indeed approximately 180° out of phase as predicted by Tang and Tong. Again, it is noted that this prediction was made in the context of a scattering model of plane waves backscattering from sub-surface crystal layers. The FT of a normal-emission curve was regarded as yielding the distances to these layers. The current model is that of a curved photoelectron wave emanating from the source atom and scattering from neighboring atoms; the FT thus yields the path-length differences between the direct and scattered photoelectron waves.[6] Later studies have shown that the ARPEFS oscillations are dominated by atoms within a backscattering cone -- not just 180° backscattering. Hence, although the S 1*s* and S 2*p* ARPEFS data appear to be about 180° out of phase, the generality of the $(-1)^{\ell_i+1}$ factor for non-backscattering geometries is not established.

It is also important to ascertain whether these two ARPEFS data sets have the same frequencies and, therefore, the same peak positions in their FTs. Figure 1b compares the auto-regressive linear prediction (ARLP)-based FTs of the two $\chi(k)$ curves shown in figure 1a.[19] The ARPEFS-FTs from the 1*s* and 2*p* initial-states are, in fact, significantly different, contrasting expectations based on the earlier theory.[9,10]

First, figure 1b shows the Generalized Ramsauer-Townsend (GRT) peak-splitting of the peak near 4 Å in the 1*s* but not the 2*p* initial-state FT. Note that the GRT peak-splitting did not appear in the 1*s* initial-state FT in the early theory. The GRT splitting in the 1*s* initial-state ARPEFS-FT has been studied previously.[20] This splitting occurs because the scattering

amplitude goes nearly to zero at a given scattering angle and k, passing nearly through the origin in the complex plane and incurring a 180° phase shift. In the plane-wave approximation (PWA) used in the early theory, the atomic scattering factor, as described by

$$F_{\mathrm{PWA}}\left(\theta_j,k\right)=\tfrac{1}{k}\sum_{\ell=0}^{\ell_{\max}}(2\ell+1)e^{-i\delta_\ell}\sin\left(\delta_\ell\right)P_\ell\left(\cos\theta_j\right) \qquad (1)$$

is independent of the final state. Here δ_ℓ is the ion-core partial-wave phase shift, $P_\ell\left(\cos\theta_j\right)$ is a Legendre polynomial, and θ_j denotes the scattering angle of a scattering atom j at a distance R_j from the source atom. It has been shown that the PWA can only give approximate results in ARPEFS.[20,21] Because $F_{\mathrm{PWA}}\left(\theta_j,k\right)$ is independent of the final state, the present work, which is based on differences between the final states, again illustrates the importance of using the curved-wave approximation (CWA) in ARPEFS to make accurate surface-structural determinations.

Barton and Shirley[21] discussed the CWA for the atomic scattering factor for an arbitrary initial state. Additional studies of the initial-state dependence of the atomic scattering factor have been completed for both photoelectron diffraction and EXAFS.[7,8,22-27] Based on the CWA, atomic scattering factors for an arbitrary initial state are described in ARPEFS by

$$F_{\mathrm{CWA}}\left(\ell_{\mathrm{f}},\theta_j,k\right)\propto\frac{i^{\ell+1}kR_j}{e^{ikR_j}}h_\ell^+\left(kR_j\right)Y_{\ell_{\mathrm{f}}m_{\mathrm{i}}}\left(\hat{R}_j\right)F_{\mathrm{PWA}}\left(\theta_j,k\right)\left(1+\tfrac{\ell(\ell+1)}{2ikR_j}\right) \qquad (2)$$

where $h_\ell^+\left(kR_j\right)$ is the spherical Hankel function of the first kind and $Y_{\ell_{\mathrm{f}}m_{\mathrm{i}}}\left(\hat{R}_j\right)$ is the spherical harmonic evaluated at the angles given by the unit vector $\hat{R}_j$. Because F_{CWA} in equation (2) is dependent on the final state, a

given phenomenon, such as the GRT effect, may be present in the *p* final-state atomic scattering factor while at the same time being absent in the *s* or *d* final-state factor.

Figure 2 plots the final-state-dependent scattering factor in the complex plane. It is directly analogous to figure 3 in Ref. 20. The scattering factors were calculated for θ_j=130.5° (the normal-emission scattering angle off the sulfur atom's four nearest-neighbor nickel atoms). The tick marks indicate the photoelectron wave-number scale in Å^{-1}. Each scattering factor curve is also labeled with its respective photoelectron final state. The (real part of the) scattering amplitude for a given k is the distance from the origin to that k-point on the scattering factor curve. The phase shift for a given k is given by the angle between the positive real axis and that k-point on the scattering factor curve. For the *p* final state, the scattering amplitude is almost zero at $k \approx 7.5$ Å^{-1} and the phase shift changes abruptly by 180°. Hence, a GRT effect in the S 1*s* initial-state ARPEFS data would be predicted from this curve, in agreement with experiment.

Turning to the S 2*p* ARPEFS case, there is also a significant dip in the scattering amplitude and a fairly abrupt 180° phase shift change for the *s*-wave scattering factor. However, the *d*-wave scattering amplitude varies modestly throughout the entire k-range and even increases slightly at $k \approx 7$ Å^{-1}. Equally important, the *d*-wave scattering factor has no abrupt phase-shift changes. Thus no GRT effect would be possible for the *d*-wave alone. It will be shown that the final state in S 2*p* photoemission through this energy range is dominated by the *d*-wave and no GRT effect is predicted. The S 2*p* ARPEFS data and FT agree with this prediction as shown in fig. 1.

The second way that the FTs in figure 1b differ is that the 6 Å peak positions in the 1*s* and 2*p* initial-state ARPEFS-FTs are shifted. The shift is

much smaller for the higher path-length difference (PLD) peak at 10 Å. These results are easily understood within the CWA formulation of atomic scattering factors. The peak positions in the ARPEFS-FTs are affected differently by the respective atomic scattering phase shifts depicted in figure 2. Furthermore, as R_j increases (larger PLD), the CWA approaches the PWA. The differences in the peak positions become smaller as the atomic scattering factor becomes less dependent on the final state. To test this interpretation, FT curves were computed from the theoretical MSSW best fits to the data and they reproduced the shifts shown in figure 1b.

The ARPEFS data and FT from the $2p$ initial state require both s and d partial waves to describe the final state. The interference between these two partial waves was examined theoretically for c(2x2)S/Ni(001) using the Kaduwela-Fadley MSSW code,[8] which is based on the scattering formalism of Rehr and Albers.[25] Friedman and Fadley[28] have discussed this method and its application to photoelectron diffraction from arbitrary initial states.

For the calculations presented here, the radial dipole matrix elements, $R_{\ell_i \pm 1}$, and phase shifts, $\delta_{\ell_i \pm 1}$, were obtained from Goldberg *et al.*[29] These values describe the shape and phase relationship between the two partial waves, $\ell_i \pm 1$, and thus the true $s+d$ final state. The scattering phase shifts for sulfur and nickel were provided by Kaduwela and Fadley.[30] Structural and non-structural parameters of c(2x2)S/Ni(001) were taken from previous ARPEFS studies.[7,8] The S-Ni interlayer spacing, $d_\perp$, is 1.30 Å, and the first two nickel layers are separated by 1.86 Å. The second-to-third nickel interlayer spacing is the bulk value, 1.76 Å. Figure 3 compares the MSSW calculation to the experimental data. The agreement between theory and experiment is quite good.

The interference between the s and d partial waves was examined. Figure 4 compares the MSSW-ARPEFS curves calculated for the s and d partial waves, as well as for the actual s+d final state. The ratio of the S $2p$ radial dipole matrix elements, $\frac{R_{\ell_i+1}}{R_{\ell_i-1}}$, is greater than 3 throughout the ARPEFS energy range. Hence, in this particular case, it is expected that the ARPEFS data will be dominated by the ℓ_i+1, or d, partial wave. To further this idea, the ARPEFS data might be simulated to some reasonable level of accuracy by considering the d wave alone. This "ℓ_i+1 approximation" may be applicable more generally but shall be investigated here only for the S $2p$ case. In an ARPEFS study based on photoemission data from a non-s initial state, if the two partial waves in the final state give comparable contributions, then accurate information about both transition matrix elements, R_{ℓ_i+1} and R_{ℓ_i-1}, and their relative phase is required throughout the energy range to make accurate surface structural determinations. This information is available at various levels of approximation in the atomic photoemission theoretical literature.

On the other hand, if the ratio $\frac{R_{\ell_i+1}}{R_{\ell_i-1}}$ is large, it may be possible to analyze ARPEFS data to reasonable accuracy using contributions from only the single ℓ_i+1 partial wave. In this case, accurate information about the radial dipole matrix elements from the non-s initial states is not required. This approach has been successfully tested using the experimental S $2p$ ARPEFS data of c(2x2)S/Ni(001). Figure 5 shows the best fit of the experimental S $2p$ ARPEFS data with the MSSW calculations based on the actual s+d final state as well as the d partial wave alone. The quality of fit is measured by the R-factor, defined as:

$$R = \frac{\sum_i \left[\chi_{i,c}(k) - \chi_{i,e}(k)\right]^2}{\sum_i \chi_{i,e}^2(k)} \qquad (3)$$

where $\chi_e(k)$ denotes the experimental ARPEFS data points, and $\chi_t(k)$ denotes the MSSW calculation based on either the *s*+*d* final state or on the *d* partial wave. By fitting with the complete *s*+*d* final state, the derived interlayer spacing between the adsorbate S layer and the first Ni substrate layer was $d_\perp$=1.31 Å, in very good agreement with accepted value.[12] The *R*-factor value for this fit was 0.16, as shown in the inset in figure 5. By fitting over the same energy range with only the *d* partial wave, the values $d_\perp$=1.30 Å and *R*=0.30 were obtained.

III. CONCLUSION

The final-state effects in the ARPEFS study of adsorbed surfaces were investigated using experimental S 1*s* and S 2*p* ARPEFS data from c(2x2)S/Ni(001). The experimental 1*s* and 2*p* ARPEFS data appear to be approximately 180° out of phase as predicted by an early theoretical description. However, FTs of the experimental 1*s* and 2*p* ARPEFS $\chi(k)$ data are quite different due to the curved-wave characteristics and the scattering-factor differences of the photoelectron final states. MSSW calculations were carried out to study the final-state effects. Based on the calculations, it was found for this particular case that the ARPEFS data from this S 2*p* non-*s* initial state can be analyzed using the $\ell_i + 1$ partial *d*-wave contribution alone. For this case, the ratio of the radial dipole matrix elements, $\frac{R_{\ell_i+1}}{R_{\ell_i-1}}$, is relatively large, exceeding 3 throughout the energy range. This approach may have wider applicability for other core levels.

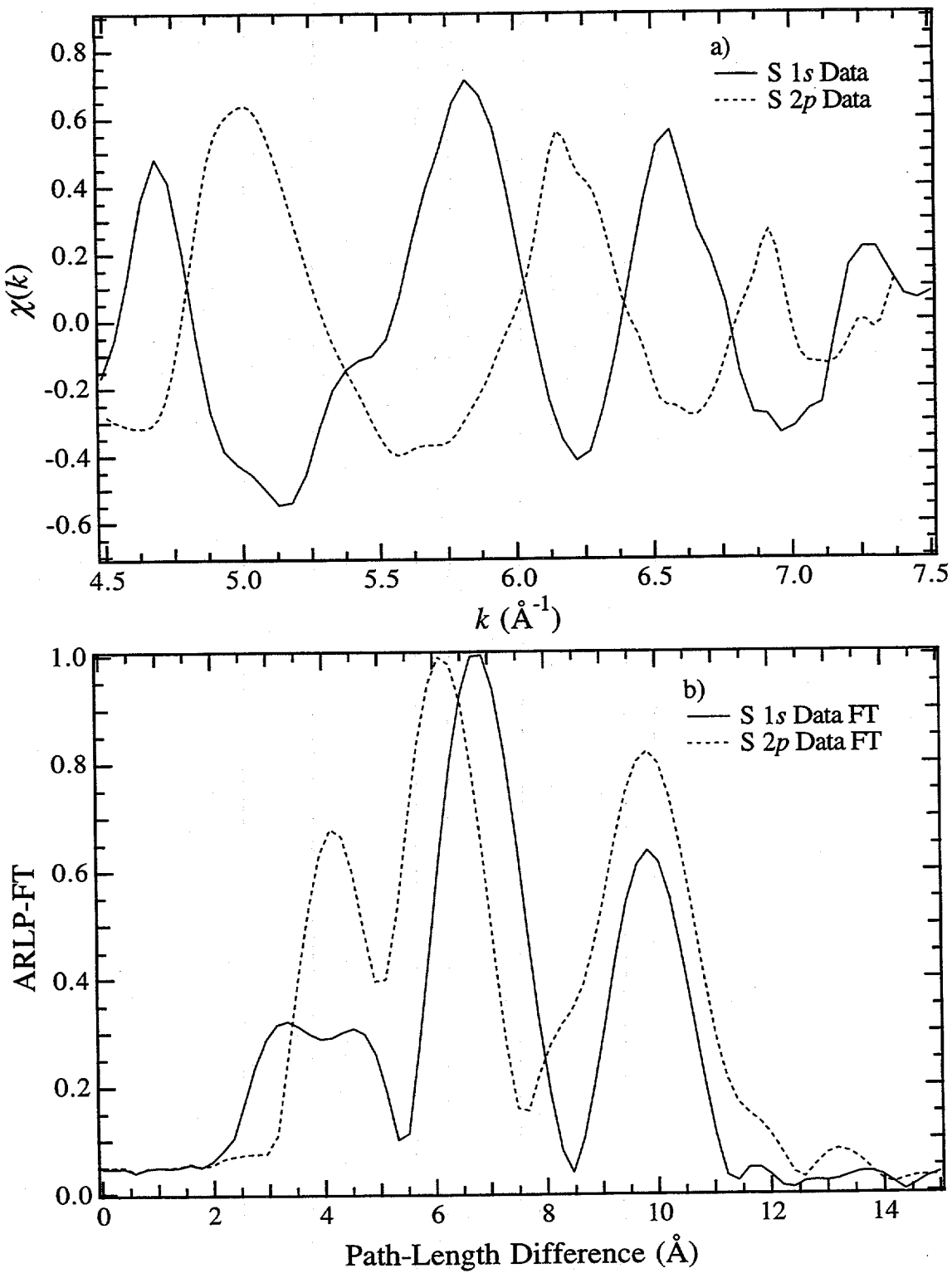

a) S 1*s* (solid line) and S 2*p* (dotted line) ARPEFS data of c(2x2)S/Ni(001); b) ARLP based FT of the S 1*s* (solid line) and S 2*p* (dotted line) ARPEFS data of c(2x2)S/Ni(001)
Figure 1

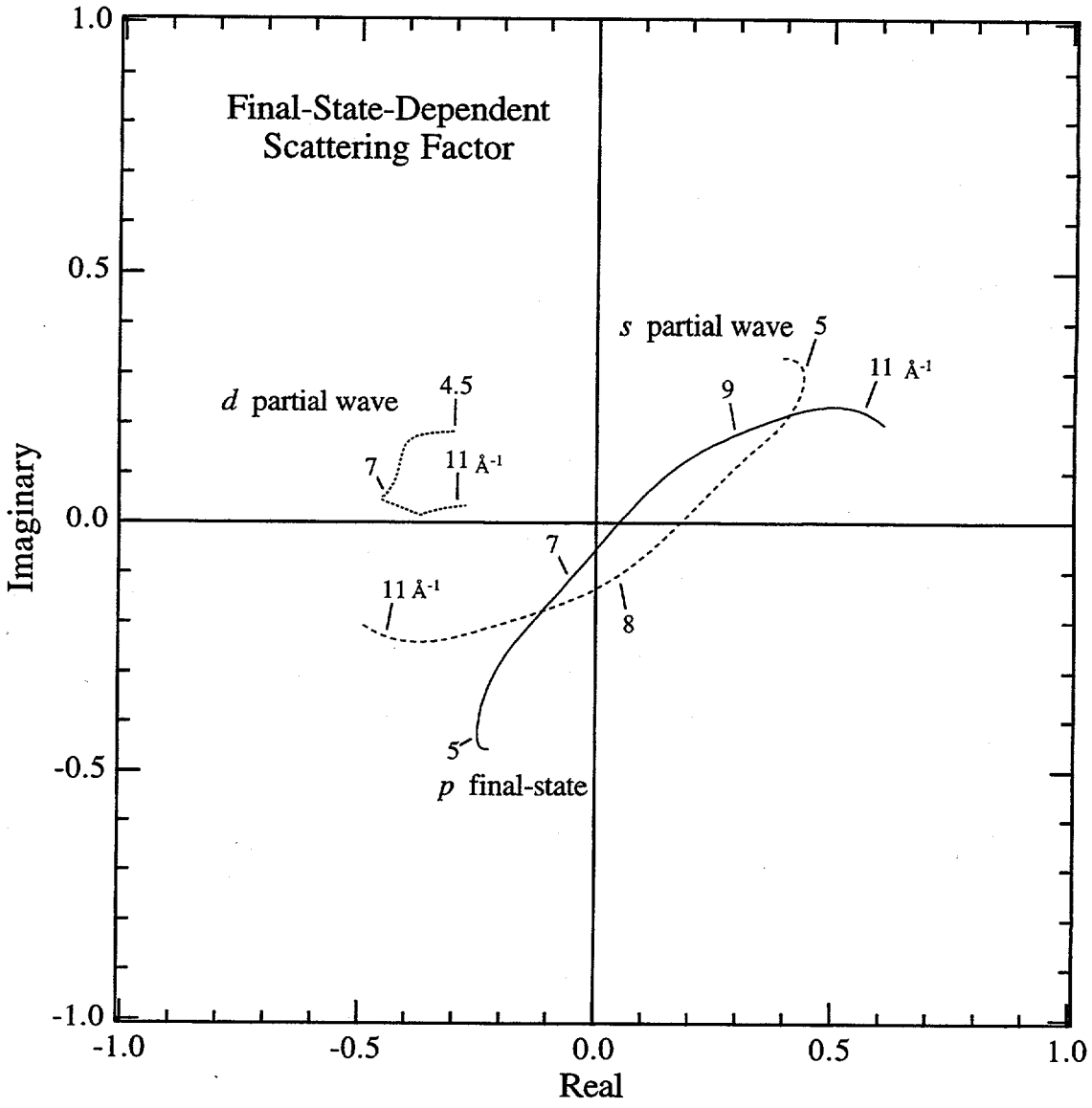

Final-state scattering factor calculations for *s* (dashed line), *p* (solid line), and *d* (dotted line) plotted in the complex plane (θ_j=130.5°). The tick marks indicate the photoelectron wave-number scale (Å^{-1}). The (real part of the) scattering amplitude for a given *k* is the distance from the origin to that *k*-point on the scattering factor curve. The phase shift for a given *k* is given by the angle between the real axis and that *k*-point on the scattering factor curve.

Figure 2

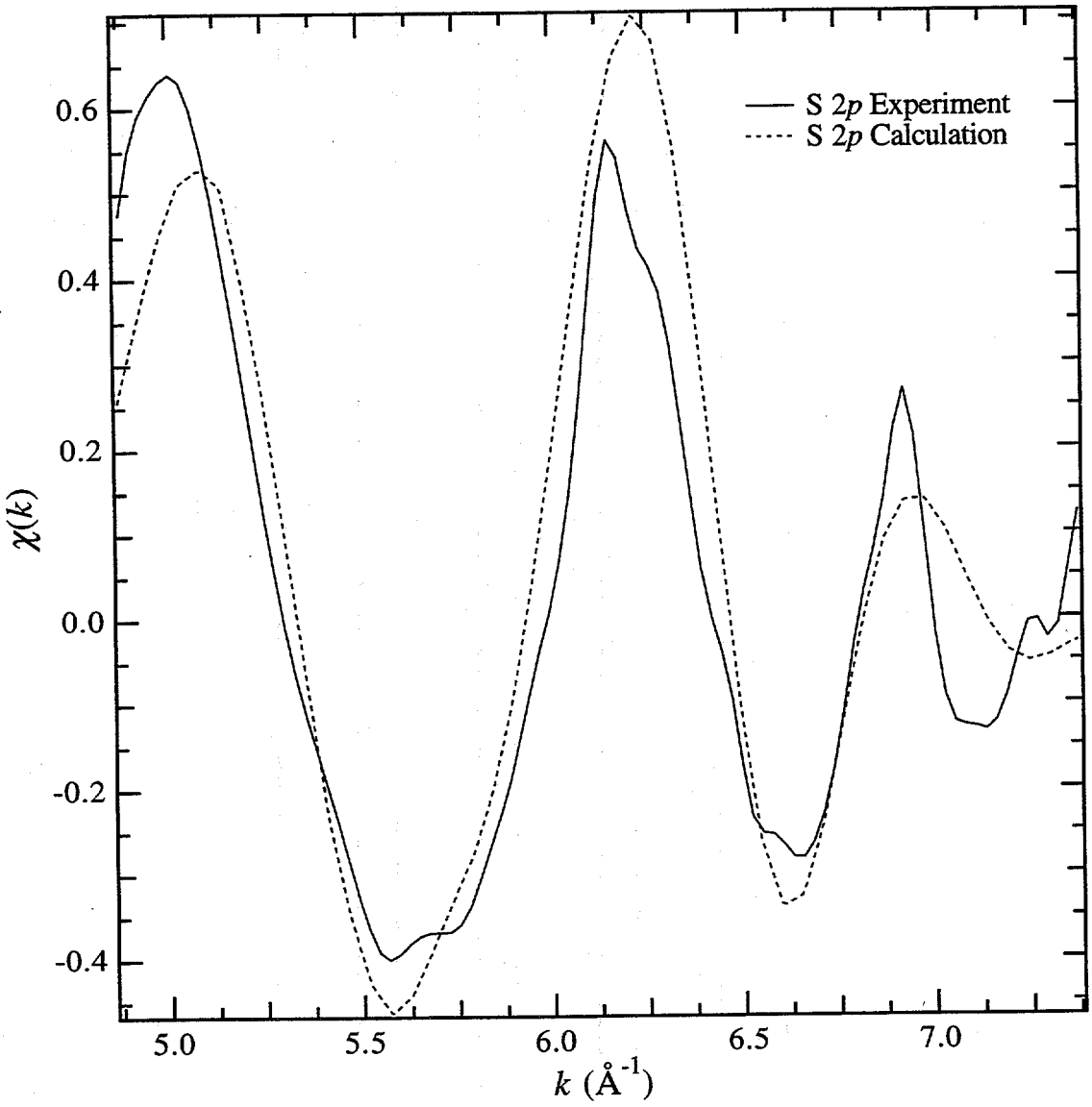

Comparison between the experimental S 2*p* ARPEFS data (solid line) and the MSSW calculation result (dotted line)

Figure 3

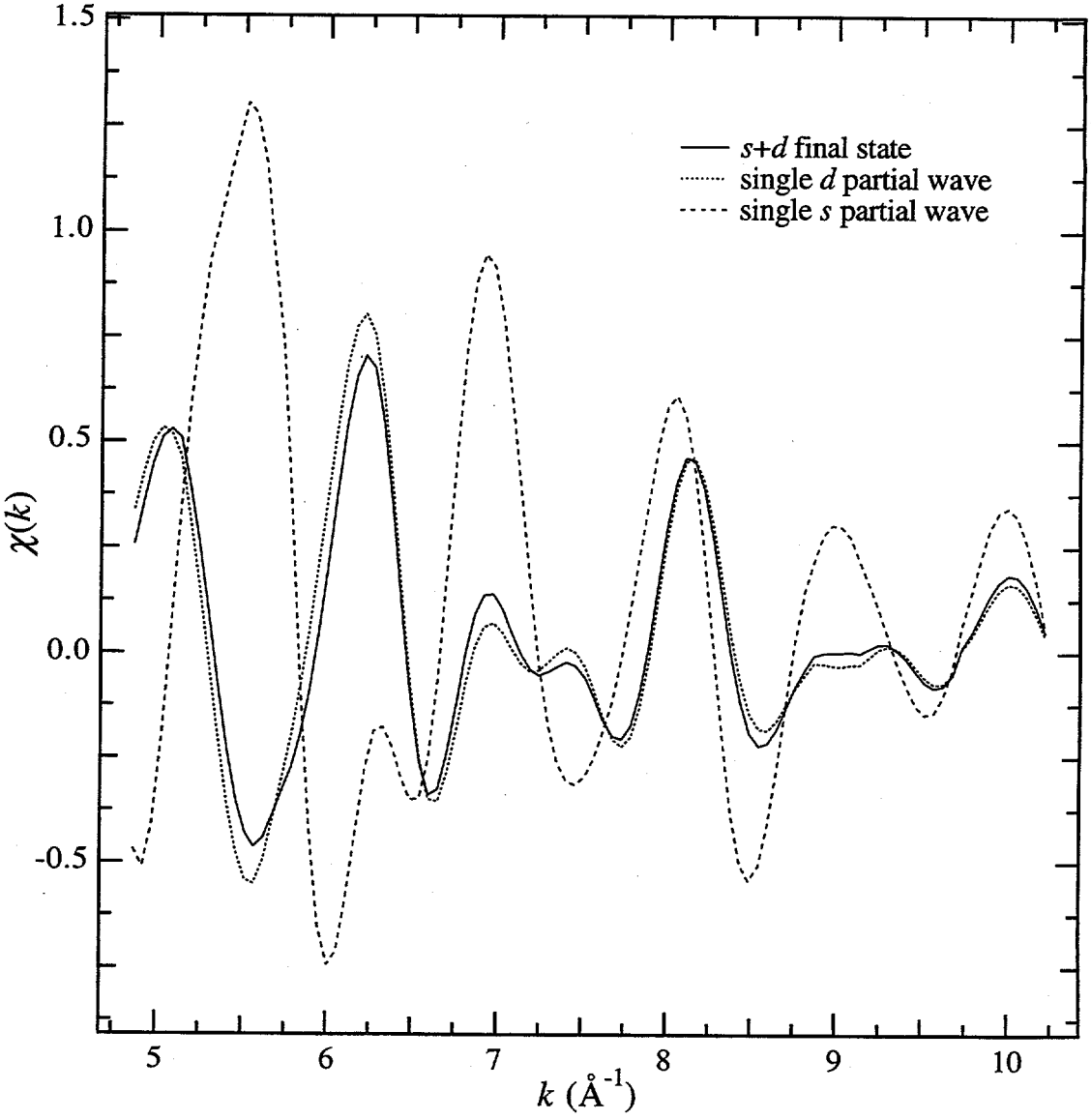

MSSW calculation results for the *s+d* final-state (solid line), the single *d* partial wave (dotted line), and the single *s* partial wave (dashed line)

Figure 4

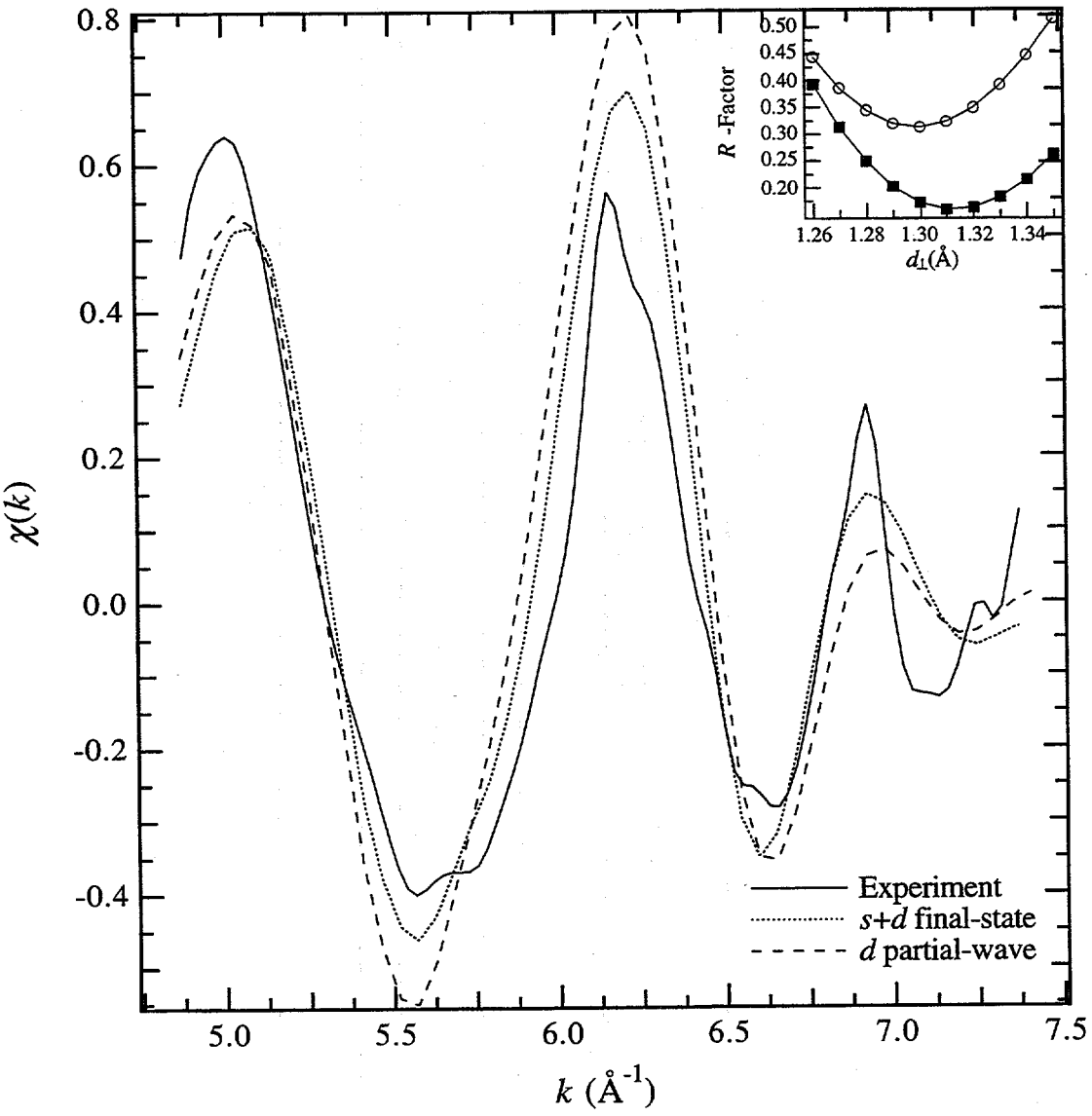

Comparison between the experimental S 2*p* ARPEFS data (solid line) and the best fit MSSW calculation result based on the actual *s*+*d* final-state (dotted line) and the single *d* partial wave (dashed line); The inset shows the *R*-factor versus $d_\perp$ for the actual *s*+*d* final-state (solid squares) and the single *d* partial wave (open circles).

Figure 5

REFERENCES

[1]A. Liebsch, Phys. Rev. Lett. **32**, 1203(1974).

[2]A. Liebsch, Phys. Rev. B **13**, 544(1976).

[3]S. Kono, C.S. Fadley, N.F.T. Hall and Z. Hussain, Phys. Rev. Lett. **41**, 117(1978).

[4]D.P. Woodruff, D. Norman, B.W. Holland, N.V. Smith, H.H. Farrell and M.M. Traum, Phys. Rev. Lett. **41**, 1130(1978).

[5]S.D. Kevan, D.H. Rosenblatt, D. Denley, B.C. Lu and D.A. Shirley, Phys. Rev. Lett. **41**, 1565(1978).

[6]J.J. Barton, C.C. Bahr, Z. Hussain, S.W. Robey, J.G. Tobin, L.E. Klebanoff and D.A. Shirley, Phys. Rev. Lett. **51**, 272(1983).

[7]J.J. Barton, *Ph.D. Thesis*, The University of California, Berkeley, LBL-19215(1985).

[8]A. Kaduwela, *Ph.D. Thesis*, University of Hawaii at Manoa, Honolulu(1991).

[9]S.Y. Tong and J.C. Tang, Phys. Rev. B **25**, 6526(1982).

[10]J.C. Tang, Chin. Phys. Lett. **4**, 321(1987).

[11]D.H. Rosenblatt, J.G. Tobin, M.G. Mason, R.F. Davis, S.D. Kevan, D.A. Shirley, C.H. Li and S.Y. Tong, Phys. Rev. B **23**, 3828(1981).

[12]J.J. Barton, C.C. Bahr, S.W. Robey, Z. Hussain, E. Umbach and D.A. Shirley, Phys. Rev. B **34**, 3807(1986).

[13]L.-Q. Wang, A.E. Schach von Wittenau, L.S. Wang Z.G. Ji, Z.Q. Huang and D.A. Shirley, Phys. Rev. B **44**, 1292(1991).

[14]L.-Q. Wang, Z. Hussain, Z.Q. Huang, A.E. Schach von Wittenau, D.W. Lindle and D.A. Shirley, Phys. Rev. B **44**, 13711(1991).

[15]Z.Q. Huang, L.Q. Wang, A.E. Schach von Wittenau, Z. Hussain and D.A. Shirley, Phys. Rev. B **47**, 13626(1993).

[16]Z.Q. Huang, Z. Hussain, W.T. Huff, E.J. Moler and D.A. Shirley, Phys. Rev. B **48**, 1696-1710(1993).

[17]S.M. Heald and E.A. Stern, Phys. Rev. B **16**, 5549(1977).

[18]B.-K. Teo and P.A. Lee, J. Am. Chem. Soc. **101**, 2815(1979).

[19]The ARLP-based FT of the S 1*s* ARPEFS data presented here agrees with Fig. 6 in Ref. 10. In this work, the ARLP-FT has lower resolution because the S 1*s* data range was reduced to match the S 2*p* data range.

[20]J.J. Barton, Z. Hussain and D.A. Shirley, Phys. Rev. B **35**, 933(1987).

[21]J.J. Barton and D.A. Shirley, Phys. Rev. B **32**, 1892(1985).

[22]A.G. McKale, G.S. Knapp and S.-K. Chan, Phys. Rev. B **33**, 841(1986).

[23]A.G. McKale, S.-K. Chan, B.W. Veal, A.P. Paulikas and G.S. Knapp, J. Phys. Colloq. **47**, C8(1986).

[24]A.G. McKale, B.W. Veal, A.P. Paulikas, S.-K. Chan and G.S. Knapp, J. Am. Chem Soc. **110**, 3763(1988).

[25]J.J. Rehr and R.C. Albers, Phys. Rev. B **41**, 8139(1990).

[26]J. Mustre de Leon, J.J. Rehr, C.R. Natoli, C.S. Fadley and J. Osterwalder, Phys. Rev. B **39**, 5632(1989).

[27]J. Mustre de Leon, J.J. Rehr, S.I. Zabinsky and R.C. Albers, Phys. Rev. B **44**, 4146(1991).

[28]D.J. Friedman and C.S. Fadley, J. Electron Spectrosc. Relat. Phenom. **51**, 689(1990).

[29]S.M. Goldberg, C.S. Fadley and S. Kono, J. Electron Spectrosc. Relat. Phenom. **21**, 285(1981).

[30]A. Kaduwela and C.S. Fadley (Private communication).

Chapter 4

A Study of Angle-Resolved Photoemission Extended Fine Structure as Applied to the Ni 3*p* Core-Level of a Clean Ni(111) Surface

ABSTRACT

The first non-*s* initial state angle-resolved photoemission extended fine structure (ARPEFS) study of a clean surface for the purpose of further understanding the technique is reported. The sample was a Ni(111) single crystal and normal photoemission data were taken from the Ni 3*p* core levels. The spin-orbit splitting between the Ni $3p_{3/2}$ and Ni $3p_{1/2}$ core-levels was not well resolved and yet an oscillatory ARPEFS curve was obtained with frequencies corresponding to scattering path-length differences as shown by the Fourier transform (FT). The clean surface ARPEFS data resemble data for adsorbate systems, showing strong backscattering signals from atoms up to four layers below the source atoms. Also, the data show a peak in the FT corresponding to scattering from the six nearest-neighbor atoms in the same crystal layer as the emitting atoms. This result has not been seen before because it is forbidden by symmetry for *s* initial state normal photoemission; however, it is expected for *p* initial state normal photoemission. Evidence was seen for single-scattering events from atoms laterally distant from the emitting atom as well as double-scattering events. Using a newly developed modeling code, the ARPEFS data were fit and the forward scattering and backscattering contributions were studied.

I. INTRODUCTION

Angle-resolved photoemission extended fine-structure (ARPEFS) is a proved technique for determining surface structures.[1-5] ARPEFS has been used to determine the structures of metal and non-metal atomic adsorbate systems as well as molecular adsorbates on conducting single crystal surfaces. ARPEFS yields accurate information about both the local structure around the adsorbates and the adsorbate-induced relaxation of the substrates.[6-12] These studies have shown that ARPEFS data from adsorbate/substrate systems, along with the Fourier transforms (FTs) of the data, can be described in terms of backscattering events. The positions of all the strong peaks in ARPEFS-FTs from adsorbed surfaces can be predicted from a trial structure with fairly good accuracy based on a single-scattering cluster (SSC) model together with the concept of a backscattering cone.

The purpose here is to explore the applicability of ARPEFS to non-*s* initial state photoemission of clean surfaces. The immediate goal is to observe and to understand the phenomenon in a simple, known system. The long-range goal is to develop a method for studying photoemission from an arbitrary initial state as well as to determine the atomic structure of interfaces, for which ARPEFS seems ideally suited. In favorable cases, atomic relaxation and reconstruction could be studied as well. In such studies, the elemental and chemical specificity of ARPEFS and its sensitivity to atomic layers that are several layers below the surface would confer certain advantages.

In using ARPEFS to study clean surfaces, the photoelectron signals from surface and bulk atoms will in some cases be resolvable, either directly or through fitting procedures. In these cases, the data analysis would be

based on two ARPEFS curves. For the more common case in which signals from different layers cannot be resolved, reconstruction or relaxation effects may still be modeled by fitting the single experimental ARPEFS curve. Due to the strength of the bulk signal, this curve may not be surface sensitive enough to yield a conclusion about possible surface reconstruction.

Most of the previous ARPEFS studies have been based on photoemission data from atomic *s* core-level initial states, for which the selection rules $\Delta\ell_i = \pm 1$, and $\Delta m_i = 0$ give a p_o-wave final state. Experience with ARPEFS data from non-*s* initial states and their FTs is very limited, however.[13-15] For non-*s* initial states ($\ell_i \neq 0$), the photoelectron final state is made up of partial waves with orbital quantum numbers $\ell_i + 1$ and $\ell_i - 1$, and a phase relationship between them which leads to interference between the partial waves. Note that the allowed m levels will be populated in the final state. Thus, with a *p* initial state, the partial waves consist of $\ell_f = 0$, $m_f = m_i = 0$ as well as $\ell_f = 2$, $m_f = m_i = 0, \pm 1$. The partial wave radial dipole matrix elements and the phase shifts are generally energy dependent. Despite these complications, there are a number of interesting experimental situations for which ARPEFS studies on a non-*s* initial state may be the only practical method of study.

The data presented here are photoemission from a clean Ni(111) surface, for which the surface and bulk 3*p* core-level peaks are unresolved. In fact, the spin-orbit splitting between the Ni $3p_{3/2}$ and Ni $3p_{1/2}$ peaks was not well resolved and yet an oscillatory ARPEFS curve was obtained with frequencies corresponding to scattering path-length differences as shown by the FT. The ARPEFS data resemble data for adsorbate systems and show strong backscattering signals from atoms up to four layers *below* the source atoms.

A new result was obtained in the FT analysis of this *p* initial state ARPEFS curve. In addition to the backscattering, the data show a peak in the FT corresponding to scattering from the six nearest neighbor atoms in the same crystal layer as the emitting atoms. This result is forbidden by symmetry for *s* initial state normal photoemission scattering from a point potential, but it is expected from *p* initial state photoemission. Additionally, evidence was seen for single-scattering events from atoms laterally distant from the emitting atom as well as double-scattering events.

In modeling these data, it is expected that the electron mean free path calculation is important in obtaining a close fit to the data. It is not yet clear which calculation method for determining the mean free path is the most accurate. Certainly, many emitters lie several layers below the surface region and their signal never escapes the crystal. The mean free path was calculated using the exponential damping factor $e^{-r/\lambda}$. The typically used $\lambda = ck$ formula is compared to the newer TPP-2 formalism.[16-18]

Finally, an adsorbate system, $\sqrt{3} \times \sqrt{3}R30°$Cl/Ni(111),[19] is compared with this Ni 3*p* data. Although this previously published data was photoemission taken from the Cl 1*s* core level, the data from the *s* versus *p* initial states agree in that they are roughly 180° out of phase. Additionally, the FTs are similar and the backscattering cone model is supported by this work.

It is appropriate to note here that photoelectron holography signals from clean surfaces are dominated by forward scattering, with atomic positions being imaged up to three layers *ahead* of the source atom.[20] A combination of these two photoelectron diffraction techniques would therefore provide a very good method for studying ordered interfaces.

II. EXPERIMENTAL

The experiments were performed at the National Synchrotron Light Source at Brookhaven National Laboratory on beamline U3-C, a soft x-ray beamline with a five meter extended range grasshopper monochromator having a fixed exit geometry. The gold coated spherical grating (1200 $^{lines}/_{mm}$ and 3.7 m radius) covered the photon energy range 150 - 1000 eV. The energy resolution was $\Delta E \approx 3$ eV with 40 μm slits.

The data were collected in an ultra-high vacuum chamber ($P \leq 60$ nPa) which has been described previously.[21] The chamber was equipped with standard ultra-high vacuum surface science sample cleaning and preparation tools including a Varian LEED/Auger system, a Phi Ar^+ sputter gun, a UTI residual gas analyzer, and a home-built gas inlet system as well as a material evaporation source for overlayer preparation. The crystal was spotwelded between two tungsten wires onto a Vacuum Generators high-precision manipulator (x, y, z, θ, ϕ) equipped with liquid-nitrogen cooling; the crystal was cleaned by repetitive cycles of Ar^+ sputtering and subsequent annealing by electron bombardment from behind to 700 °C. The sample cleanliness was monitored using x-ray photoelectron spectroscopy (XPS) and checking for carbon (1s), nitrogen (1s), oxygen (1s), and sulfur (2p); no contamination was detected before or after the data collection which lasted 9.5 hours.

The photoemission spectra were collected using an angle-resolving electrostatic hemispherical electron energy analyzer (mean radius of 50 mm) which is rotatable 360° around the sample's vertical axis and 100° around the sample's horizontal axis. The analyzer pass energy was set to 160 eV and

the energy resolution was ~1.6 eV FWHM. The angular resolution of the double einzel input lens was ~±3°.

Synchrotron radiation is ≥98% linearly polarized. The angle of incidence of the light on the crystal was oriented 55° from the surface normal away from the crystal (011) plane. The photon polarization vector, $\vec{\varepsilon}$, was thus oriented 35° from the surface normal and perpendicular to the crystal (011) plane (see illustration in figure 2). The analyzer was oriented normal to the Ni(111) surface and the crystal was cooled to ~100 K throughout the data collection.

III. DATA COLLECTION

The raw data were a series of x-ray photoemission spectra; the photoelectron kinetic energy was scanned from 97 - 416 eV. The lower limit was chosen to avoid Ni 3*p* peak interference with the strong Ni *MNN* auger peak at 61 eV. The scan was terminated at the upper limit because the flux became too low to obtain high quality spectra. Using the de Broglie relation

$$k\left(\text{Å}^{-1}\right) = 0.5123\sqrt{E(\text{eV})} \qquad (1)$$

this photoelectron energy range corresponds to the magnitude of the photoelectron wave vector range 5.05 - 10.45 Å^{-1}. The spectra were recorded across this range in equal 0.10 Å^{-1} steps. Note that this is the wave vector as measured by the analyzer (*outside* of the crystal). The scattering calculations to be described later take place *inside* the crystal and were adjusted for the inner potential of the solid. Although the exact value of the

inner potential is unknown, it is ~10 eV for nickel; it was allowed to float during the modeling calculations.

Each photoemission spectrum was a 29.5 eV window encompassing the Ni $3p_{3/2}$ and Ni $3p_{1/2}$ peaks as well as two satellite peaks. These satellites were shifted from the Ni $3p_{3/2}$ by 5.5 eV and 12 eV to lower kinetic energy. Figure 1 is an example of one of these spectra and includes the fit for each of the four peaks. Each peak was fit with a Lorentzian convoluted with a Gaussian, a Voigt function, to model the natural linewidth and the experimental broadening, respectively. Each Voigt function was added to a Fermi step-function with a step-height scaled to the respective peak intensity and a step-width taken as the Gaussian width of the respective peak. In this way, the step-function models the inelastic scattering background of the photoemission spectrum. Summing each of the four Voigt functions and adding the inelastic background gave the total fit which is the solid line through the data points in figure 1.

IV. DATA REDUCTION AND ANALYSIS

The purpose of fitting the spectra is to extract the most accurate area from the peaks. This allows the data to be reduced to the $\chi(k)$ diffraction curve which contains the structural information. $\chi(k)$ is defined by[22]

$$\chi(k) = \frac{I(k)}{I_0(k)} - 1 \qquad (2)$$

where $I(k)$ is the peak area plotted as a function of the peak position in k-space. $I_0(k)$ is a smooth, slowly varying function with an oscillation frequency much lower than $I(k)$; $I_0(k)$ stems from the contribution of the

inelastic scattering processes and the varying atomic cross section. It is adequate to use a simple polynomial function of energy to fit $I_0(k)$.[23]

Removing $I_0(k)$ results in a removal from the FT the peaks $\lesssim 2$ Å. Note that this study is of the clean nickel surface and thus photoemission occurred from atoms several layers below the surface. Many forward scattering path-length differences from sub-surface emitting atoms will be on the order of $\lesssim 2$ Å. This forward scattering signal is therefore removed during the data reduction along with the standard $I_0(k)$. The resulting experimental ARPEFS $\chi(k)$ curve is thus dominated by backscattering.

The peak area was determined by integrating the Voigt functions over the spectrum window. The total experimental energy resolution was approximately 3.4 eV, obtained by quadratically summing the beamline resolution with the analyzer resolution. The spin-orbit splitting between the Ni $3p_{1/2}$ and Ni $3p_{3/2}$ photoelectron peaks was not well resolved and thus there was much intensity mixing between the respective Voigt functions during the fitting process. For this reason, the sum of these two peak areas was plotted against the k-position of the Ni $3p_{3/2}$ peak to finally plot the experimental $\chi(k)$ curve shown in figure 2 (solid line). The best-fit result from the multiple-scattering modeling calculations is also shown in figure 2 (dashed line) and will be discussed later.

A. Fourier Analysis

At this point, it is useful to study the auto-regressive linear prediction based Fourier transform (ARLP-FT) to move from momentum space to real space. In ARPEFS, the positions of the strong peaks in ARLP-FTs from adsorbate/substrate systems can be predicted with fairly good accuracy using

the single-scattering cluster (SSC) model together with the concept of strong backscattering from atoms located within a cone around 180° from the emission direction. The effective solid angle of this backscattering cone is ~30° - 60°; it is not unique, but is operationally defined simply by opening the angle until it can account for the observed FT peaks based on the crystal geometry. Signals from scattering atoms very close to the source atom may be observable even if the scatterers lie outside the nominal backscattering cone.

These FT peaks correspond to path-length differences (PLDs), ΔR_j, between the component of the photoemitted wave that propagates directly to the detector and the components which are first scattered by the atomic potentials within this backscattering cone.[6] Thus, the peak positions are

$$\Delta R_j = r_j\left(1-\cos\theta_j\right)+\phi_j \tag{3}$$

where r_j is the bond length, θ_j is the scattering angle (180° for exact backscattering), and ϕ_j is the atomic scattering phase shift. The scattering takes place inside the crystal and the ARPEFS data must be shifted from the measured $\chi\left(k_{\text{outside-crystal}}\right)$ to $\chi\left(k_{\text{inside-crystal}}\right)$ to account for the inner potential. In ARPEFS modeling calculations, the inner potential is treated as an adjustable parameter and is typically 5 - 15 eV. Thus, before Fourier transformation, the ARPEFS data presented here were shifted by 10 eV to higher kinetic energy.

The ARLP-FT of the experimental ARPEFS data is plotted in figure 3. Also illustrated in figure 3 is a schematic of the Ni(111) single crystal, assuming a bulk-terminated fcc surface, with a backscattering cone superimposed. The FT shows peaks due to scattering from atoms up to four

layers below the emitting atoms. The depth sensitivity of ARPEFS has been described previously and was found to be enhanced by multiple-scattering effects.[5]

The labeled atoms correspond to the labeled peaks in figure 3. Using the bulk nearest-neighbor spacing, 2.49 Å, and assuming a bulk-terminated surface, the expected peak positions can be calculated using simple geometry. These expected peak positions along with the actual peak positions and their corresponding shifts are listed in table 1. Also listed in table one is an assignment of the peak to single-scattering (SS) or double-scattering (DS) events. Additionally, the number of atoms contributing to each peak is listed in table 1.

The origins of the peaks labeled 2, 3, 4, 5, and 6 are straightforward. If a line is drawn from a surface emitter into the crystal and normal to the (111) plane, peaks 2, 3, and 6 occur due to single-scattering from the three atoms closest to this line in layers 2, 3, and 5, respectively. Nickel is fcc and thus peak 4 is due to direct backscattering (θ_j=180°) from the #4 atom which is in layer 4. Peak 5 is due to single-scattering from the six nearest-neighbors to atom #4, the #5 atoms which are also in layer 4.

Peaks 2' and 3' may be attributed to atoms more laterally distant from the line described above. Peak 2' occurs due to single-scattering from the three second nearest-neighbors to this line in layer 2. Similarly, peak 3' occurs due to single-scattering from the three second nearest-neighbors to this line in layer 3.

Double-scattering may be detectable in the ARLP-FT as evidenced by peaks 2*, 3*, 4*, and 5*. The first event for peak 2*, for example, is scattering by the #2 atoms. The second event is scattering by the #2 atoms' six nearest-neighbors. Given that there are three #2 atoms, eighteen atoms

are available for the second scattering event to give peak 2*. An analogous process holds for the 3* peak. Because there is only one #4 atom for each emitter in the fcc ($\underset{\downarrow}{a}bc\underset{\downarrow}{a}bc$) geometry, only six atoms are in position for the second scattering event to give peak 4*. However, there are six #5 atoms and thus thirty-six atoms for the second scattering event to give peak 5*.

These assignments due to double-scattering are somewhat speculative. It is believed that peaks 4* and 5* have a higher relative amplitude as compared to 2* and 3* because waves scattering in the fourth layer can be forward focused by atoms in the surface layer. Also, the higher probability for the second scattering event of peak 5* due to the greater number of atomic potentials will increase its relative amplitude.

A new result is also noted in this ARLP-FT. In addition to the backscattering peaks, the peak labeled 1 is due to single-scattering of the photoemitted wave from the six nearest-neighbor atoms in the same (111) plane as the emitting atoms. This scattering path has not been observed previously for *s* initial state data or calculations because the photoemitted p_o wave destructively interferes with itself for the scattering angle θ_j=90° due to its negative parity. The photoemitted *d* and *s* waves which are interfering with themselves and with each other have positive parity; therefore, they do not cancel upon scattering from atoms in the same (111) plane as the emitting atoms. Thus, the frequency component labeled peak 1 is a physical part of the $\chi(k)$ diffraction curve and the appropriate PLD peak is observed. A peak that would be labeled 1' arising from scattering by the second nearest-neighbors in the same layer as the emitting atoms would be seen at ~4.31 Å. If present, this weak feature is dominated by peak 2.

B. Multiple-Scattering Analysis

It has become standard to perform modeling calculations in an attempt to simulate the ARPEFS $\chi(k)$ curve. Using the single-scattering model of ARPEFS,[6,22] $\chi(k)$ can be written as

$$\chi(k) = \sum_j A_j(k) \cos\left[k\left(R_j - R_j \cos\theta_j\right) + \phi_j\right] \qquad (4)$$

where $A_j(k)$ contains experimental geometry factors including the photon polarization direction and the electron emission direction as well as the scattering amplitude, aperture integration, and thermal averaging.

At θ_j = 0°, there is zero path-length difference (PLD) between the direct and scattered photoelectron waves. Hence, interference between the direct and scattered photoelectron waves is detectable only through amplitude and phase differences, not by modulation of the signal. For forward scattering through angles close to 0°, the scattering amplitude is quite large, but many PLD values are correspondingly small and do not show up in the FTs. Experience with ARPEFS data indicates that PLDs $\lesssim$2 Å will not show up in the FT analysis as discussed earlier. Modeling calculations are very useful because a variety of test cases can be used to better understand the scattering processes.

Typically, ARPEFS has been studied from an *s* initial state where the final state is a photoemitted p_0 wave. The multiple-scattering spherical-wave (MSSW) code developed by Barton and Shirley[6,22-24] has been proven accurate for *s* core-level photoemission.[6-11] However, the ARPEFS data and FTs from a *p* initial state require both *s* and *d* partial waves to describe the final state. A new code developed by Chen, Wu, and Shirley was used for

the calculations presented here.[25] This new code is based on the Rehr-Albers formalism.[26] Kaduwela and Fadley[27] developed a code based on this method which has been discussed and applied to photoelectron diffraction from arbitrary initial states by Friedman and Fadley.[28] This new code is sufficiently fast that fitting calculations can be performed for systems in which the photoemitters are in many layers and the core-level initial state has arbitrary angular momentum.

The radial dipole matrix elements, $R_{\ell_i \pm 1}$, and phase shifts, $\delta_{\ell_i \pm 1}$, were obtained from Goldberg, Fadley, and Kono[29] who developed them from Manson and Cooper's earlier work.[30] These values describe the shape and phase relationship between the two partial waves, $\ell_i \pm 1$, and thus the true $s+d$ final state as a function of the photoemitted electron kinetic energy.

To account for vibration effects of the bulk atoms, the mean square relative displacement (MSRD) was calculated using equation (33) by Sagurton *et al.*[4]

$$\left\langle u_i^2 \right\rangle \propto \frac{1}{M_i \theta_{\mathrm{D},i}} \left(1 + \frac{cT^2}{\theta_{\mathrm{D},i}^2} \cdots \right) \tag{5}$$

M_i is the atomic mass, $\theta_{\mathrm{D},i}$ is the correlated Debye temperature, T is the sample temperature, and c is a coefficient that varies slowly with temperature. For calculating the MSRD of the bulk Ni atoms, $\theta_{\mathrm{D},i}$ was 450 K and T was 80 K. Accounting for the surface atomic vibration has been discussed previously.[12,31]

The surface sensitivity of ARPEFS in the study of clean surfaces is strongly dependent on the inelastic mean free path (IMFP). Regarding modeling calculations, it is expected that the IMFP calculation is important

in obtaining a close fit to the data. Certainly, many emitters lie several layers below the surface region and their signal never escapes the crystal. The IMFP was included using the exponential damping factor $e^{-r/\lambda}$ where λ was calculated using the Tanuma, Powell, and Penn (TPP-2) formula.[18]

Powell[16] gives an overview of IMFP and attenuation length (AL) calculations and discusses the appropriate use of each. Powell also describes some of the problems and questions surrounding the IMFP and AL calculations. Application of IMFP calculations to x-ray photoelectron spectroscopy has been discussed by Jablonski and Powell.[17] Tanuma, Powell, and Penn[18] present a reasonable argument for using their TPP-2 formula to calculate the IMFP, λ (Å). They present the TPP-2 formula as

$$\lambda = \frac{E}{E_p^2\left[\beta \ln(\gamma E) - \frac{C}{E} + \frac{D}{E^2}\right]} \tag{6}$$

where E (eV) is the electron energy and E_p (eV) is the free electron plasmon energy as defined by

$$E_p = 28.8\left(\frac{N_v \rho}{M}\right)^{1/2} \tag{7}$$

N_v is the number of valence electrons per atom (or molecule), ρ $\left(g/cm\right)$ is the density, and M is the atomic (or molecular) weight. β, γ, C, and D are parameters defined as

$$\beta = -0.0216 + \frac{0.944}{\left(E_p^2 + E_g^2\right)^{1/2}} + 7.39 \times 10^{-4} \rho \tag{8}$$

$$\gamma = 0.191 \rho^{-0.50} \tag{9}$$

$$C = 1.97 - 0.91\left(\frac{N_v\rho}{M}\right) \quad (10)$$

$$D = 53.4 - 20.8\left(\frac{N_v\rho}{M}\right) \quad (11)$$

and E_g (eV) is the bandgap for non-conductors.

Figure 4 compares the TPP-2 formula for nickel and the $\lambda = ck$ formula where $c = 0.78$ Å^2 which has been used previously for ARPEFS modeling calculations.[32,33] The shape and magnitude for these IMFP curves are significantly different. However, also plotted in figure 4 is the $\lambda = ck$ formula for $c = 0.92$ Å^2 which adequately matches the TPP-2 formula for electron energies $\gtrsim$200 eV. Below 200 eV lies a significant amount of ARPEFS information and the effect of the different IMFP values is currently being studied.

Tanuma *et al.*[18] discuss why the TPP-2 formula is a good model and they also point out the causes of uncertainty. Angular anisotropies in the IMFP are another concern with respect to this study as well as with respect to fixed-energy, scanned angle photoelectron diffraction.[16] Certain crystallographic directions can enhance the depth sensitivity of ARPEFS due to forward focusing along a chain of atoms. It is not yet known how the angular anisotropies will affect the shape or magnitude of the curves shown in figure 4. It is certainly a more complicated problem to calculate a physically accurate signal loss due to inelastic scattering as a function of E, θ, and ϕ for a given sample and crystallographic surface.

The analyzer acceptance angle as well as the emission and polarization directions and were set to match the experiment as described earlier. The atomic-scattering phase shifts were calculated in situ by using the atomic potentials tabulated by Moruzzi *et al.*[34] Figure 2 plots the best fit

(dashed line) on top of the experimental ARPEFS data (solid line). For this fit, a 74 atom cluster was used and the inner potential was optimized at 9.8 eV. The spacing between the first two nickel layers was determined to be 2.06(1) Å -- a +1.5% expansion of the bulk value, 2.03 Å. By contrast, for clean Cu(111), LEED studies have detected a surface *contraction* of ~0.7% from the bulk value, 2.09 Å.[35,36]

C. Discussion of Error

The best fit is determined by an R-factor minimization. A three-step fitting process is used to determine the true R-factor minimum to prevent convergence to a local minimum. The initial coarse-fitting minimizes the $\tilde{R}$-factor, $\tilde{R} = R_a$ where

$$R_a = \frac{\sum_i \left[\chi_{i,c}(k) - \chi_{i,e}(k)\right]^2}{\frac{1}{2}\sum_i \left[\chi_{i,c}^2(k) + \chi_{i,e}^2(k)\right]} \tag{12}$$

using a simple net search.[25] $\chi_{i,c}(k)$ and $\chi_{i,e}(k)$ are the points in the calculated and experimental $\chi(k)$ curves respectively. Second, the code again minimizes $\tilde{R} = R_a$ using the Downhill Simplex Method in Multidimensions.[37] Finally, the code minimizes $\tilde{R} = R$ where

$$R = \frac{\sum_i \left[\chi_{i,c}(k) - \chi_{i,e}(k)\right]^2}{\sum_i \chi_{i,e}^2(k)} \tag{13}$$

using the Nonlinear Marquardt Method.[37]

While fitting, the largest effects stem from changes in the inner potential and the interlayer spacing between the first two Ni layers. Figure 5 shows a contour plot of the R-factor as the inner potential and Ni_1-Ni_2 interlayer spacing are varied. Even with an uncertainty of ±2.6 eV in the inner potential, the precision of ARPEFS is ±0.01 Å.

V. Ni 3*p* DATA COMPARED WITH $\sqrt{3}\times\sqrt{3}R30°$Cl/Ni(111) DATA

Figure 6 compares the Ni 3p data with $\sqrt{3}\times\sqrt{3}R30°$Cl/Ni(111) data published previously.[19] This comparison illustrates the differences and similarities between the s and the p core-level initial state ARPEFS data. The ARPEFS $\chi(k)$ curves are roughly 180° out of phase. This final-state effect is expected and has been seen previously.[13-15] Also, the FTs are remarkably similar, with ARLP-FT peaks for backscattering from layers below the source atom being resolved in both cases. There is a slight shift in lattice spacing between the two samples which is evident in the FT. Additionally, the Ni 3*p* data FT show a peak at ~2.5 Å due to effects described above whereas the Cl 1*s* data FT has no such peak.

The similarity of the two ARLP-FT spectra shows that ARPEFS of a clean crystal is dominated by backscattering. The ARPEFS intensity can be regarded as arising from the sum of contributions from source atoms in each layer as if it were the surface layer. If we neglect forward scattering from atoms in layers above the source atoms, the ARPEFS intensity is modulated due to backscattering from the atoms in layers below the source atoms. Due to the finite mean free path, the signal from the sub-surface layer atoms is damped.

VI. CONCLUSION

The first non-*s* initial state ARPEFS study of a clean surface for the purpose of further understanding the technique is reported. The clean surface ARPEFS data resemble data for adsorbate systems, showing strong backscattering signals from atoms up to four layers *below* the source atoms. In addition to the backscattering, the Ni 3*p* data show a peak in the FT at ~2.5 Å corresponding to scattering from the six nearest neighbor atoms in the same crystal layer as the emitting atoms. This result is forbidden by symmetry for *s* initial state photoemission scattering from a point source but is expected from *p* initial state photoemission. Evidence was also seen for single-scattering events from atoms laterally distant from the emitting atom as well as double-scattering events.

An adsorbate system, $\sqrt{3}\times\sqrt{3}R30°$Cl/Ni(111),[19] was compared with the clean Ni 3*p* data. Although this previously published data was photoemission taken from the Cl 1*s* core level, the data and FTs from *s* versus *p* initial states agree such that the backscattering cone model is supported by this work.

It has been shown that photoelectron holography signals from clean surfaces are dominated by forward scattering, with atomic positions being imaged up to three layers *ahead* of the source atom.[20] A combination of these two photoelectron diffraction techniques would therefore provide a very good method for studying ordered interfaces.

Calculated and Actual Scattering PLDs

Peak Number	Calculated PLD (Å)	Peak Position (Å)	Peak Shift (Å)	Scattering	# of Atoms Contributing
1	2.49	2.36	-0.13	SS	6
2	4.52	4.69	0.17	SS	3
2'	5.55	5.99	0.44	SS	3
2*	7.01	7.60	0.59	DS	3 × 6
3	8.37	8.45	0.08	SS	3
3'	9.04	9.07	0.03	SS	3
3*	10.86	10.18	-0.68	DS	3 × 6
4	12.18	12.51	0.33	SS	1
5	12.67	12.90	0.23	SS	6
4*	14.67	14.68	0.01	DS	1 × 6
5*	15.16	15.09	-0.07	DS	6 × 6
6	16.37	16.00	-0.37	SS	3

Scattering paths with the calculated PLD (based on 2.49 Å nearest neighbor spacing) along with the actual peak positions and the respective shifts. Layer 1 is defined as the same layer as the emitting atom.

Table 1

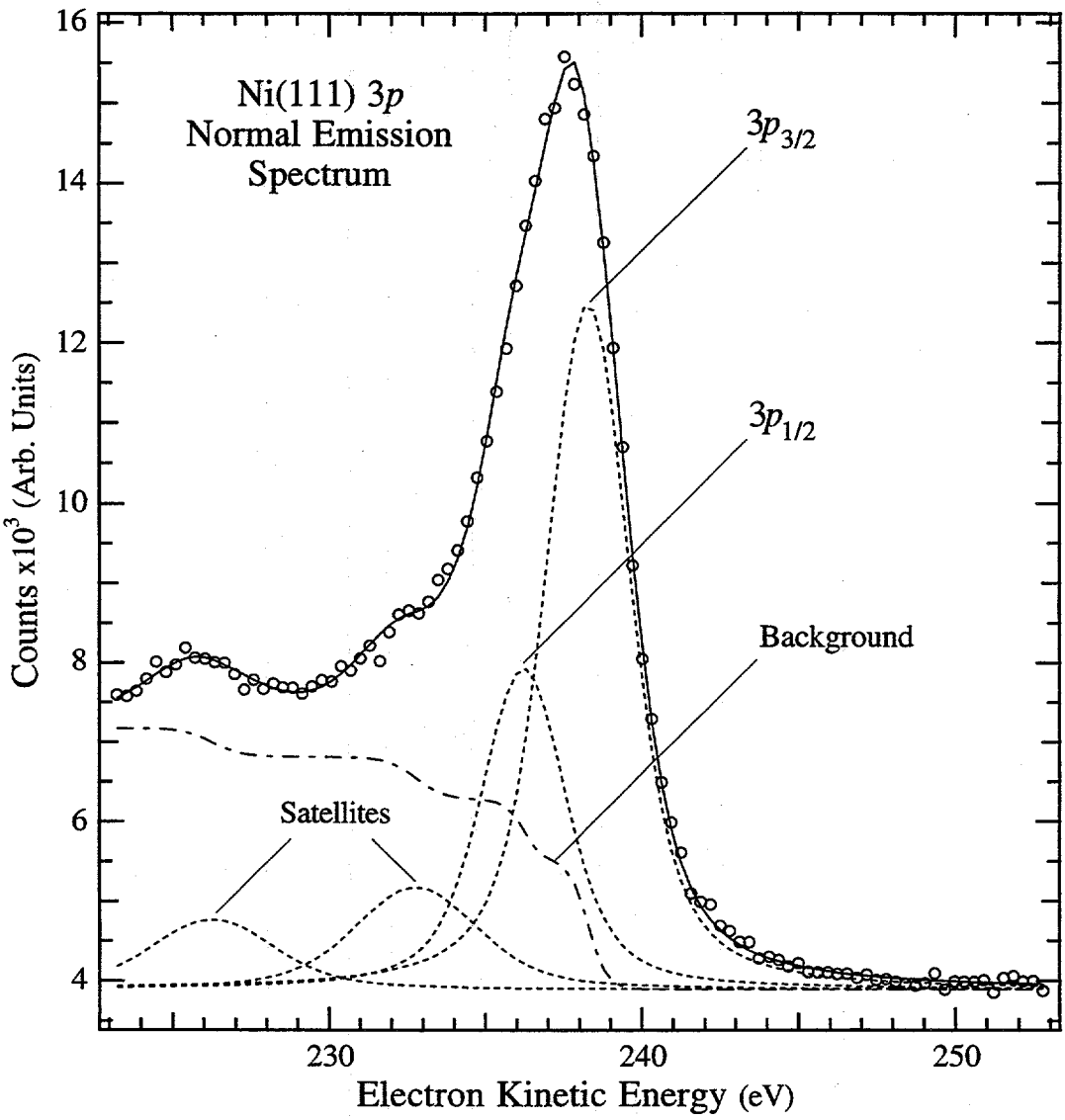

Example photoemission spectrum showing the data as well as the four Voigt functions and the step function used to fit the data.

Figure 1

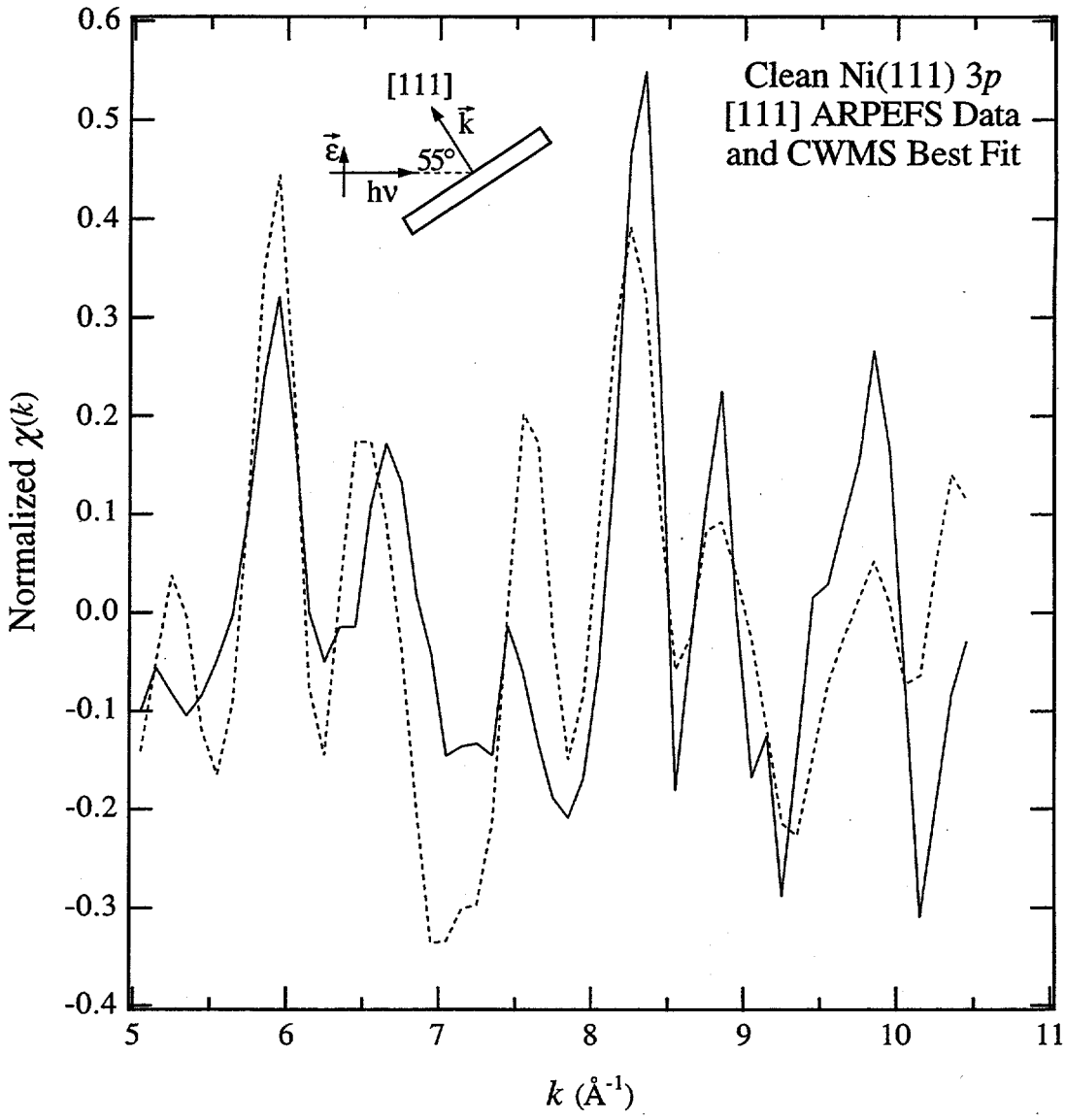

Normal emission Ni(111) 3*p* ARPEFS data (solid line) and best fit (dashed line). A schematic of the experimental geometry is shown.

Figure 2

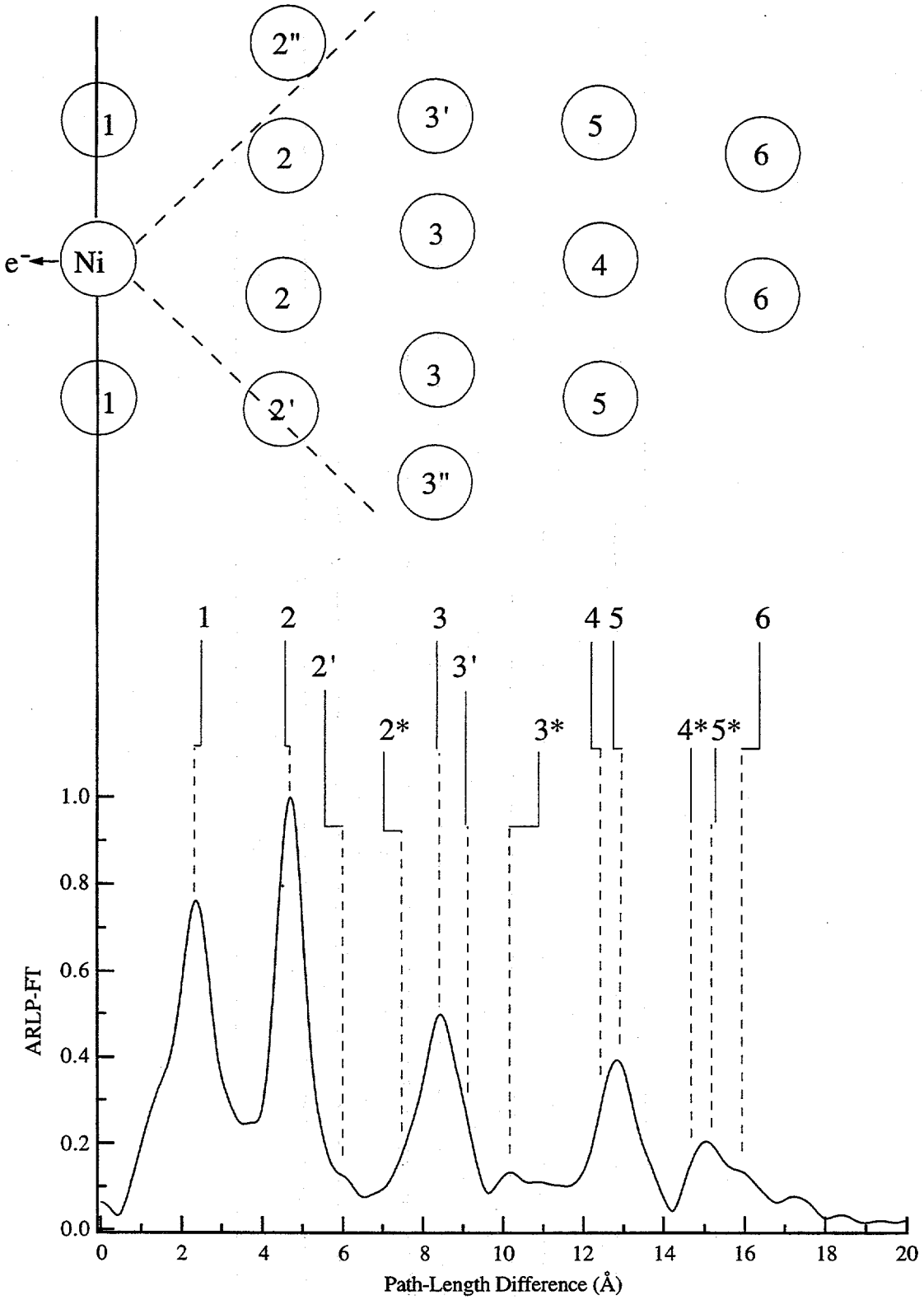

ARLP based FT of the Ni 3*p* ARPEFS data. A model of the lattice with the backscattering cone indicates the scattering atoms corresponding to the FT peaks.

Figure 3

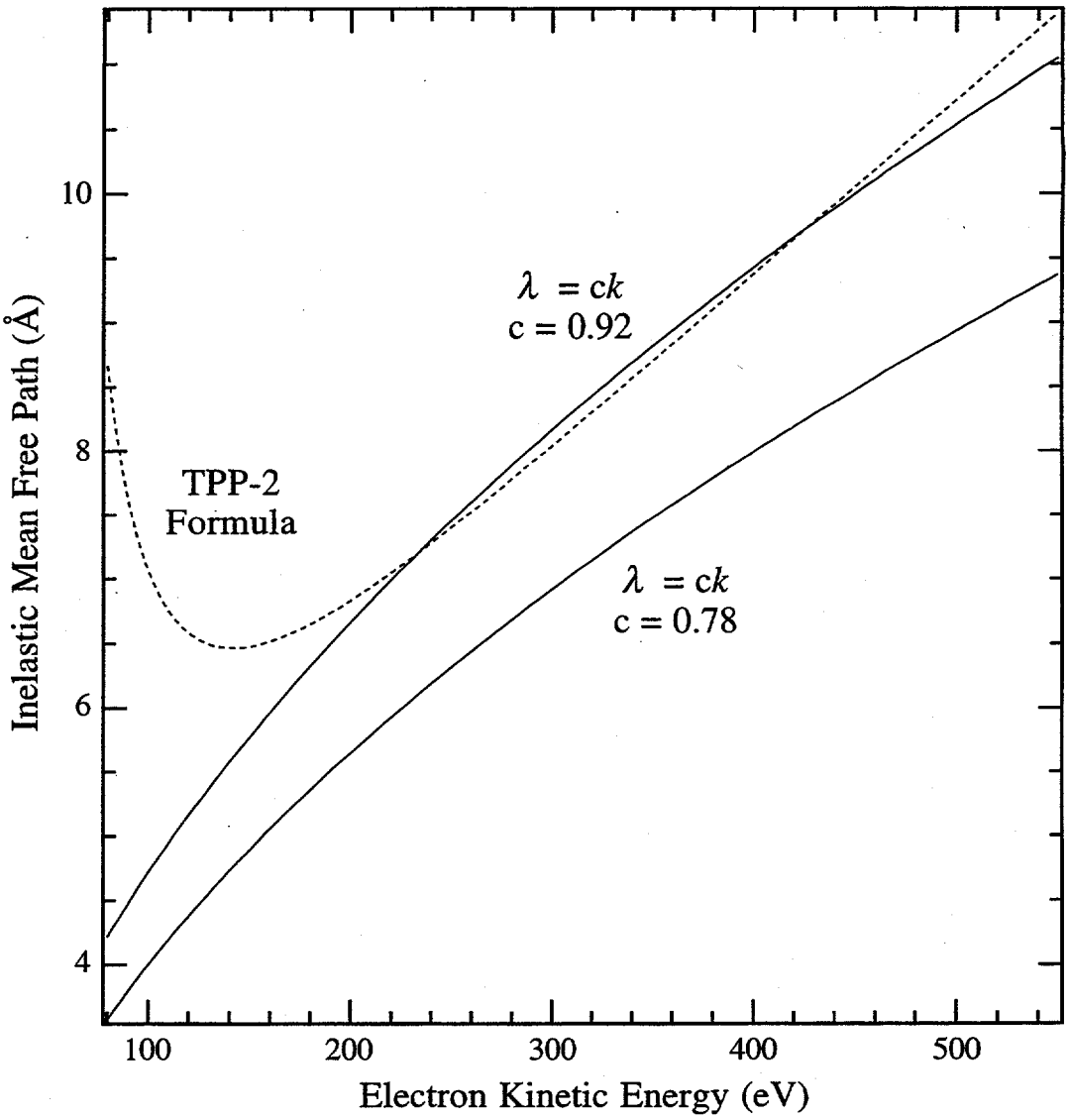

Calculation of the IMFP as proposed in the previous ARPEFS studies involving Ni using $\lambda = ck$ and $c = 0.78$ Å^2. Also plotted is a calculation for $c = 0.92$ Å^2 which better approximates the TPP-2 result (dashed line) for electron energies >200 eV.

Figure 4

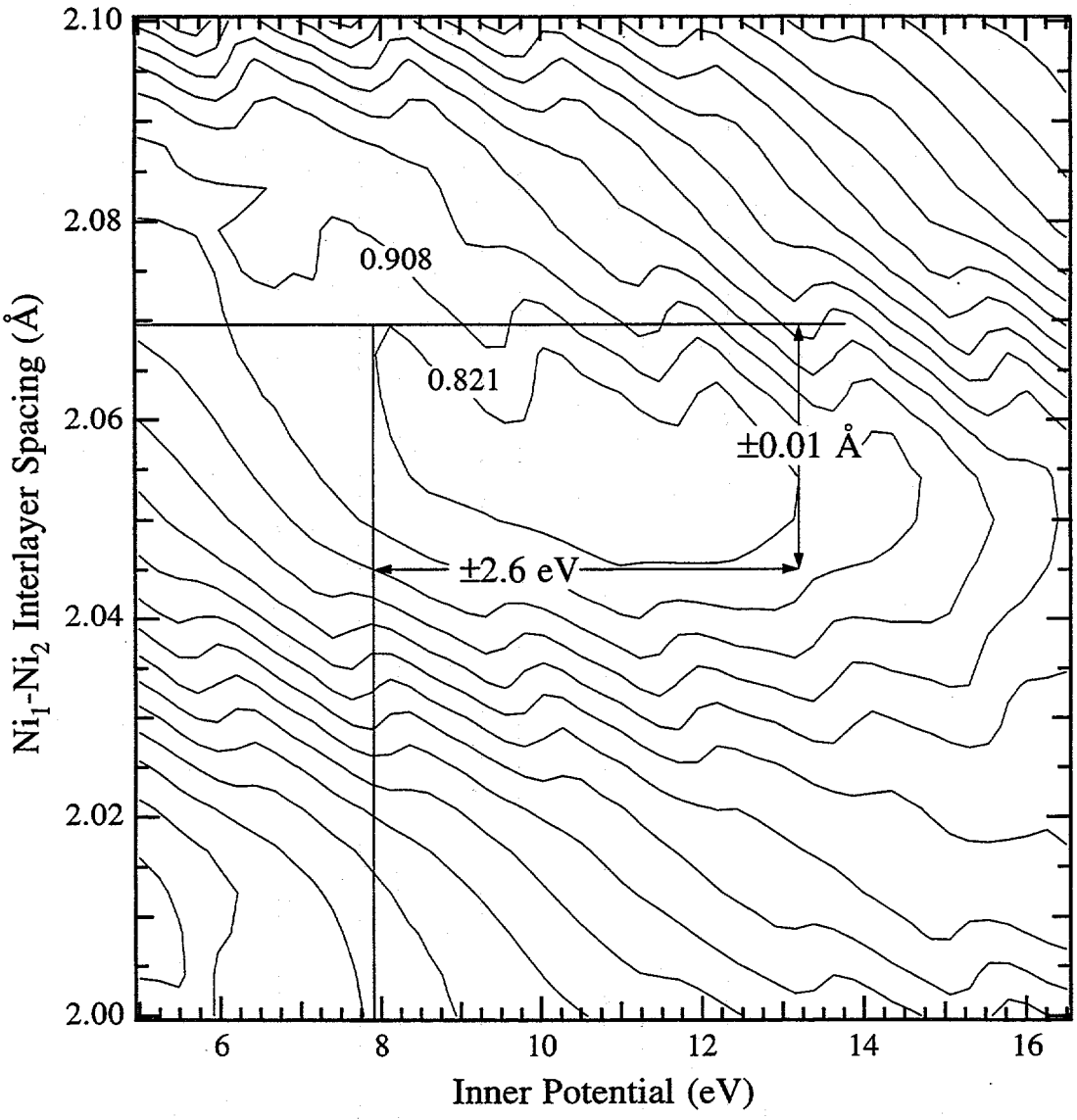

Contour plot showing how the *R*-factor varies with the Ni_1-Ni_2 interlayer spacing and the inner potential. Even with an uncertainty of ±2.6 eV in the inner potential, the precision of ARPEFS is ±0.01 Å.

Figure 5

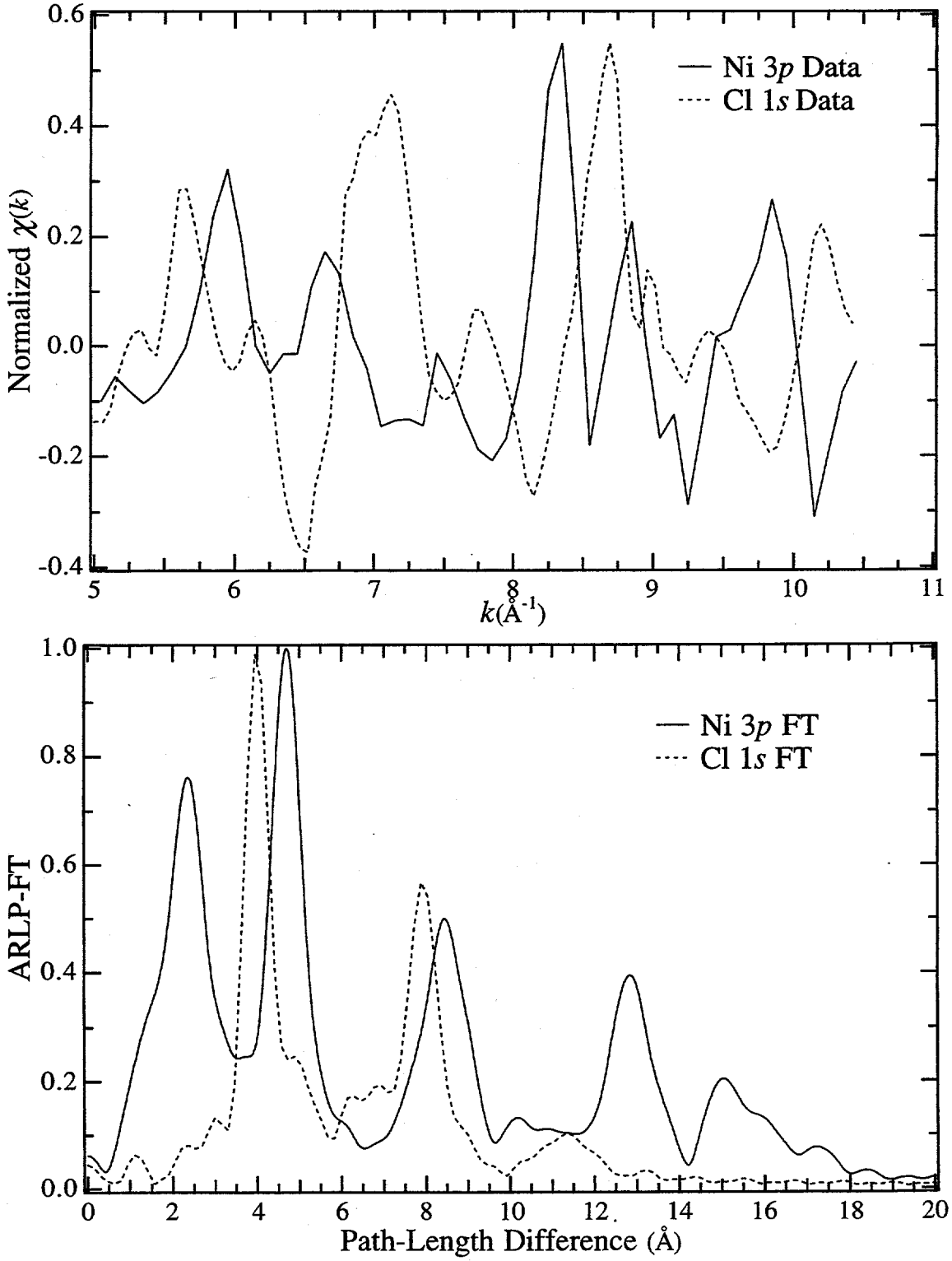

The top panel overlays the $\sqrt{3} \times \sqrt{3}R30°$ Cl/Ni(111) (dashed line) with the Ni 3*p* (solid line) experimental ARPEFS curves. The bottom panel overlays their respective ARLP-based FTs.

Figure 6

REFERENCES

[1]S.D. Kevan, D.H. Rosenblatt, D. Denley, B.C. Lu and D.A. Shirley, Phys. Rev. Lett. **41**, 1565(1978).

[2]J.J. Barton, C.C. Bahr, Z. Hussain, S.W. Robey, J.G. Tobin, L.E. Klebanoff and D.A. Shirley, Phys. Rev. Lett. **51**, 272(1983).

[3]D.P. Woodruff, D. Norman, B.W. Holland, N.V. Smith, H.H. Farrell and M.M. Traum, Phys. Rev. Lett. **41**, 1130(1978).

[4]M. Sagurton, E.L. Bullock and C.S. Fadley, Surf. Sci. **182**, 287(1987).

[5]Y. Zheng and D.A. Shirley, Chem. Phys. Lett. **203**, 114(1993).

[6]J.J. Barton, C.C. Bahr, S.W. Robey, Z. Hussain, E. Umbach and D.A. Shirley, Phys. Rev. B **34**, 3807(1986).

[7]S.W. Robey, C.C. Bahr, Z. Hussain, J.J. Barton, K.T. Leung, J.R. Lou, A.E. Schach von Wittenau and D.A. Shirley, Phys. Rev. B **35**, 5657(1987).

[8]L.Q. Wang, A.E. Schach von Wittenau, Z.G. Ji, L.S. Wang, Z.Q. Huang and D.A. Shirley, Phys. Rev. B **44**, 1292(1991).

[9]Z.Q. Huang, L.Q. Wang, A.E. Schach von Wittenau, Z. Hussain and D.A. Shirley, Phys. Rev. B **47**, 13626(1993).

[10]Z.Q. Huang, Z. Hussain, W.T. Huff, E.J. Moler and D.A. Shirley, Phys. Rev. B **48**, 1696(1993).

[11]Y. Zheng, E. Moler, E. Hudson, Z. Hussain and D.A. Shirley, Phys. Rev. B **48**, 4960(1993).

[12]W.R.A. Huff, Y. Chen, X.S. Zhang, L.J. Terminello, F.M. Tao, Y.K. Pan, S.A. Kellar, E.J. Moler, Z. Hussain, H. Wu, Y. Zheng, X. Zhou, A.E. Schach von Wittenau, S. Kim, Z.Q. Huang, Z.Z. Yang and D.A. Shirley, (to be published).

[13]W.R.A. Huff, Y. Zheng, Z. Hussain and D.A. Shirley, J. Phys. Chem. **98**, 9182(1994).

[14]S.Y. Tong and J.C. Tang, Phys. Rev. B **25**, 6526(1982).

[15]J.C. Tang, Chin. Phys. Lett. **4**, 321(1987).

[16]C.J. Powell, J. Electron Spectrosc. Relat. Phenom. **47**, 197(1988).

[17]A. Jablonski and C.J. Powell, Surf. Interface Anal. **20**, 771(1993).

[18]S. Tanuma, C.J. Powell and D.R. Penn, Surf. Interface Anal. **20**, 77(1993).

[19]L.-Q. Wang, Z. Hussain, Z.Q. Huang, A.E. Schach von Wittenau, D.W. Lindle and D.A. Shirley, Phys. Rev. B **44**, 13711(1991).

[20]B.L. Petersen, L.J. Terminello, J.J. Barton and D.A. Shirley, Chem. Phys. Lett. **213**, 412(1993).

[21]S.D. Kevan, *Ph.D. Thesis*, The University of California, Berkeley, LBL-11017(1980).

[22]J.J. Barton, S.W. Robey and D.A. Shirley, Phys. Rev. B **34**, 778(1986).

[23]J.J. Barton, *Ph.D. Thesis*, The University of California, Berkeley, LBL-19215(1985).

[24]J.J. Barton and D.A. Shirley, Phys. Rev. B **32**, 1892(1985).

[25]Y. Chen, H. Wu and D.A. Shirley, *CWMS Code - Unpublished*, (1995).

[26]J.J. Rehr and R.C. Albers, Phys. Rev. B **41**, 8139(1990).

[27]A. Kaduwela, *Ph.D. Thesis*, University of Hawaii at Manoa, Honolulu, (1991).

[28]D.J. Friedman and C.S. Fadley, J. Electron Spectrosc. Relat. Phenom. **51**, 689(1990).

[29]S.M. Goldberg, C.S. Fadley and S. Kono, J. Electron Spectrosc. Relat. Phenom. **21**, 285(1981).

[30]S.T. Manson and J.W. Cooper, Phys. Rev. **165**, 126(1968).

[31]R.E. Allen, G.P. Alldredge and F.W. de Wette, J. Chem. Phys. **54**, 2605(1971).

[32]S.W. Robey, J.J. Barton, C.C. Bahr, G. Liu and D.A. Shirley, Phys. Rev. B **35**, 1108(1987).

[33]M.P. Seah and W.A. Dench, Surf. Interface Anal. **1**, 1(1979).

[34]V.L. Moruzzi, J.F. Janak and A.R. Williams, *Calculated Electronic Properties of Metals*, (Pergamon Press, Inc., New York, 1978).

[35]S.P. Tear, K. Roll and M. Prutton, J. Phys. C **14**, 3297(1981).

[36]S.A. Lindgren, L. Wallden, J. Rundgren and P. Westrin, Phys. Rev. B **29**, 576(1984).

[37]W.H. Press, S.A. Teukolsky, W.T. Vetterling and B.P. Flannery, *Numerical Recipes in Fortran: The Art of Scientific Computing*, 2 ed., (University Press, Cambridge, 1992).

Chapter 5

A Study of Angle-Resolved Photoemission Extended Fine Structure as Applied to the Cu 3*s* and Cu 3*p* Core-Levels of a Clean Cu(111) Surface

ABSTRACT

A clean Cu(111) single crystal was used to study angle-resolved photoemission extended fine structure (ARPEFS) from non-*s* initial states in a controlled manner. Photoemission data from the Cu 3*s* core-level and the Cu 3*p* core-levels were similar but 180° out of phase as expected. The Fourier transform of these clean surface ARPEFS data resemble data for adsorbate systems, showing strong backscattering signals from atoms up to four layers below the source atoms. In addition to the backscattering, the Fourier transform of the Cu 3*p* data show a peak corresponding to scattering from the six nearest-neighbor atoms in the same crystal layer as the emitting atoms. Evidence was also seen for single-scattering events from atoms laterally distant from the emitting atom as well as double-scattering events. Multiple-scattering modeling calculation results indicate that the Cu 3*p* photoemission intensity has mostly *d*-wave character. Test calculations indicate that Cu 3*s* photoemission scatters from atomic potentials that are laterally distant from the photoemitter. Also, double-scattering events can be observed in the Cu 3*p* Fourier transform. Additional test calculations show that the ARPEFS signal is dominated by photoemission from atoms in the first two crystal layers.

I. INTRODUCTION

Angle-resolved photoemission extended fine-structure (ARPEFS) is a proved technique for determining surface structures.[1-5] ARPEFS has been used to determine the structures of metal and non-metal atomic adsorbate systems as well as molecular adsorbates on conducting single crystal surfaces. ARPEFS yields accurate information about both the local structure around the adsorbates and the adsorbate-induced relaxation of the substrates.[6-12]

In using ARPEFS to study clean surfaces, the photoelectron signals from surface and bulk atoms will in some cases be resolvable, either directly or through fitting procedures. In these cases, the data analysis would be based on two ARPEFS curves. For the more common case in which signals from different layers cannot be resolved, reconstruction or relaxation effects may still be modeled by fitting the single experimental ARPEFS curve.

Most of the previous ARPEFS studies have been based on photoemission data from atomic *s* core-level initial states, for which the selection rules $\Delta\ell_i = \pm 1$, and $\Delta m_i = 0$ give a p_o-wave final state. Experience with ARPEFS data from non-*s* initial states and their Fourier transforms is very limited, however.[13-16] For non-*s* initial states ($\ell_i \neq 0$), partial waves with orbital quantum numbers $\ell_i + 1$ and $\ell_i - 1$ make up the photoemission intensity. There is a phase relationship between them which leads to interference between the partial waves. Note that the allowed m levels will be populated in the final state. Thus, with a p initial state, the partial waves consist of $\ell_f = 0$, $m_f = m_i = 0$ as well as $\ell_f = 2$, $m_f = m_i = 0, \pm 1$. It is important to note that the intensities sum from these different m levels, not the amplitudes.[17] The intensities also sum over the

different emitters, e. Thus, for the given partial waves, $\psi_{\ell_f,m}(\theta,\phi,k)$, the total intensity, $I_{tot}(\theta,\phi,k)$, is

$$I_{tot}(\theta,\phi,k)=\sum_{e}\sum_{m}\left|\sum_{\ell_f}(-i)^{\ell_f}R_{\ell_f}(k)e^{i\delta_{\ell_f}(k)}\left\langle Y_{\ell_f,m}\left|Y_{1,0}\right|Y_{\ell_i,m}\right\rangle\psi_{\ell_f,m}(\theta,\phi,k)\right|^2 \quad (1)$$

$\left\langle Y_{\ell_f,m}\left|Y_{1,0}\right|Y_{\ell_i,m}\right\rangle$ is the overlap integral between the initial and final spherical harmonic wave functions which are functions of θ and ϕ. $R_{\ell_f}(k)$ are the partial wave radial dipole matrix elements and $\delta_{\ell_f}(k)$ are the phase shifts. Despite these complications, there are a number of interesting experimental situations for which ARPEFS studies on a non-*s* initial state may be the only practical method of study.

A clean Cu(111) single crystal was used to study ARPEFS from non-*s* initial states in a controlled manner. Photoemission data were taken from the Cu 3*p* core-levels and subsequently the Cu 3*s* core-level. The two data sets were acquired on the same sample within a few hours of each other. This allows for a direct comparison of the data and the Fourier transforms.

After fitting the data to determine the parameters, two types of test calculations were performed. For the purpose of determining if double-scattering may be detectable directly in the Fourier transform (FT), a cluster was used with a single emitter adsorbed on a layer of scattering potentials. The single-scattering calculation results are compared to the double-scattering calculation results for each initial state. A second test system used a ten layer cluster for full multiple-scattering calculations. A single emitter was placed in the surface layer; the position of this emitter was subsequently moved to each layer ending with the sixth. The intensity as a function of the magnitude of the photoelectron wave vector is plotted to better understand

from where the ARPEFS signal originates. Each of these test systems is useful to study the similarities and differences between photoemission from the two different initial states.

II. EXPERIMENTAL

The experiments were performed using the Advanced Light Source at the E. O. Lawrence Berkeley National Laboratory on beamline 9.3.2. This is a soft x-ray spherical grating monochromator.[18] The accessible photon energy range was 200 - 800 eV using the 600 $^{lines}/_{mm}$ grating. Because this is not a high-resolution study, the entrance slit was set to 1 mm and the exit slit was set to 120 μm to allow the maximum flux with adequate resolution.

The data were collected in an ultra-high vacuum chamber ($P \leq 60$ nPa) which has been described previously.[16,19] The crystal was spotwelded to a molybdenum sample holder using tantalum strips onto a high-precision manipulator (x, y, z, θ, ϕ) equipped with a liquid-helium cooled cryostat. The crystal was cleaned by repetitive cycles of Ar^+ sputtering and subsequent annealing by electron bombardment from behind to 700 °C. The sample cleanliness was monitored using x-ray photoelectron spectroscopy (XPS) and checking for carbon (1s), nitrogen (1s), oxygen (1s), and sulfur (2p). The Cu 3p data were collected first; the data collection time was five hours for each set. Between the data sets, the sample was annealed to a dim orange glow to desorb any contaminants. The crystal was cooled to ~80 K throughout the data collection.

The photoemission spectra were collected using an angle-resolving electrostatic hemispherical electron energy analyzer (mean radius of 50 mm) which is rotatable 360° around the sample's vertical axis and 100° around the

sample's horizontal axis. The analyzer pass energy was set to 32 eV. The angular resolution of the double einzel input lens was ~±3°.

The degree of linear polarization was measured to be ≥0.99 at the endstation of this bending magnet beamline.[18] The angle of incidence of the light on the crystal was oriented 80° from the surface normal. The photon polarization vector, $\vec{\varepsilon}$, was thus oriented 10° from the surface normal (see illustration in figure 2). The analyzer was oriented 5° off-normal from the Cu(111) surface.

III. DATA COLLECTION

The raw data are a series of photoemission spectra. The photoelectron kinetic energy for the respective Cu 3*s* and Cu 3*p* peaks was stepped from ~100 - 540 eV. Using the de Broglie relation

$$k\left(\text{Å}^{-1}\right) = 0.5123\sqrt{E(\text{eV})} \qquad (2)$$

this photoelectron energy range corresponds to the magnitude of the photoelectron wave vector range ~5.0 - 11.9 Å^{-1}. The spectra were recorded across this range in equal 0.10 Å^{-1} steps.

Each Cu 3*s* photoemission spectrum was a 13 eV window as illustrated in figure 1a. Each Cu 3*p* photoemission spectrum was a 20 eV window encompassing the Cu $3p_{3/2}$ and Cu $3p_{1/2}$ peaks as illustrated in figure 1b. The data reduction for these Cu spectra was much easier than for clean Ni photoemission spectra.[16] The two satellites present in the clean Ni data are not present in either of the clean copper data sets. Also, due to the lack of satellites and thus a lower uncertainty in the determined peak area, it is

expected that the resultant ARPEFS $\chi(k)$ curve represents a more accurate diffraction pattern.

The fits used to determine the peak areas are also included in figures 1a and 1b. Each peak was fit with a Lorentzian convoluted with a Gaussian, a Voigt function, to model the natural linewidth and the experimental broadening, respectively. Each Voigt function was added to a Fermi step-function with a step-height scaled to the respective peak intensity and a step-width taken as the Gaussian width of the respective peak. In this way, the step-function models the inelastic scattering background of the photoemission spectrum. Summing these sub-spectra gives the total fit which is the solid line through the data points. Note that two ARPEFS $\chi(k)$ curves were determined for the Cu $3p$ spectra due to the spin-orbit splitting. As was expected, these two curves were nearly identical. Thus, the reported Cu $3p$ $\chi(k)$ curve is the average of the Cu $3p_{3/2}$ and the Cu $3p_{1/2}$ $\chi(k)$ curves.

IV. DATA REDUCTION AND ANALYSIS

After the peak area is determined from fitting the raw spectra, the data are reduced to the $\chi(k)$ diffraction curve which contains the structural information. $\chi(k)$ is defined by[20]

$$\chi(k) = \frac{I(k)}{I_0(k)} - 1 \tag{3}$$

where $I(k)$ is the peak area plotted as a function of the peak position in k-space. $I_0(k)$ is a smooth, slowly varying function with an oscillation frequency much lower than $I(k)$; $I_0(k)$ stems from the contribution of the

inelastic scattering processes and the varying atomic cross section. It is adequate to use a simple polynomial function of energy to fit $I_0(k)$.[21]

Removing $I_0(k)$ results in a removal from the Fourier transform the peaks $\lesssim 2$ Å. Note that this study is of the clean copper surface and thus photoemission occurred from atoms several layers below the surface. Many forward scattering path-length differences from sub-surface emitting atoms will be on the order of $\lesssim 2$ Å. The forward scattering signal is therefore removed during the data reduction along with the standard $I_0(k)$. The resulting experimental ARPEFS $\chi(k)$ curve is thus dominated by backscattering.

Figure 2 overlays the Cu 3*s* and the Cu 3*p* ARPEFS $\chi(k)$ curves. The experimental geometry is also pictured. The data are plotted in this way to clearly illustrate that the ARPEFS data from an *s* atomic core-level are ~180° out of phase from ARPEFS data from a *p* atomic core-level. This result is expected and has been studied previously.[13-16]

A. Fourier Analysis

The auto-regressive linear prediction based FT (ARLP-FT) transforms the data from momentum space to real space. In ARPEFS, the positions of the strong peaks in ARLP-FTs from adsorbate/substrate systems can be predicted with fairly good accuracy using the single-scattering cluster model together with the concept of strong backscattering from atoms located within a cone around 180° from the emission direction.

These FT peaks correspond to path-length differences (PLDs) between the component of the photoemitted wave that propagates directly to the detector and the components which are first scattered by the atomic

potentials within this backscattering cone.[6] The scattering takes place inside the crystal and the ARPEFS data must be shifted from the measured $\chi\left(k_{\text{outside-crystal}}\right)$ to $\chi\left(k_{\text{inside-crystal}}\right)$ to account for the inner potential. In ARPEFS modeling calculations, the inner potential is often treated as an adjustable parameter and is typically 5 - 15 eV. The inner potential is approximately the sum of the work function and the valence band-width.[22] The work function for Cu(111) is ~5 eV and the valence band-width is ~5 eV.[23,24] Thus, before Fourier transformation, the ARPEFS data presented here were shifted by 10 eV to higher kinetic energy.

Figure 3 plots the ARLP-FT of the Cu 3*s* and the Cu 3*p* ARPEFS data. Also illustrated in figure 3 is a schematic of the Cu(111) single crystal, assuming a bulk-terminated fcc surface, with a backscattering cone superimposed. The FT shows peaks due to scattering from atoms up to four layers below the emitting atoms. The depth sensitivity of ARPEFS has been described previously and was found to be enhanced by multiple-scattering effects.[5]

The labeled atoms correspond to the labeled peaks in figure 3. Using the bulk nearest-neighbor spacing, 2.56 Å, and assuming a bulk-terminated surface, the expected peak positions can be calculated using simple geometry. These expected peak positions are listed in table 1 along with the actual peak positions (and corresponding shifts) for the Cu 3*s* and Cu 3*p* data FTs. Also listed in table 1 is an assignment of the peak to single-scattering (SS) or double-scattering (DS) events. Additionally, the number of atomic scattering potentials contributing to each peak is listed in table 1.

The origins of the peaks labeled 2, 3, 4, 5, and 6 are straightforward. If a line is drawn from a surface emitter into the crystal and normal to the (111) plane, peaks 2, 3, and 6 occur due to single-scattering from the three

atoms closest to this line in layers 2, 3, and 5, respectively. Copper is fcc and thus peak 4 is due to direct backscattering (θ_j=180°) from the #4 atom which is in layer 4. Peak 5 is due to single-scattering from the six nearest-neighbors to atom #4, the #5 atoms which are also in layer 4.

Peaks 2' and 3' may be attributed to atoms more laterally distant from the line described above. Peak 2' occurs due to single-scattering from the three second nearest-neighbors to this line in layer 2. Similarly, peak 3' occurs due to single-scattering from the three second nearest-neighbors to this line in layer 3.

Double-scattering may be detectable in the ARLP-FT as evidenced by peaks 2*, 3*, 4*, and 5*. The first event for peak 2*, for example, is scattering by the three #2 atoms. The second event is scattering by the six nearest-neighbors to each #2 atom. An analogous process holds for the 3* peak. Because there is only one #4 atom for each emitter in the fcc ($\dot{a}bc\dot{a}bc$) geometry, only six atoms are in position for the second scattering event to give peak 4*. However, there are six #5 atoms and thus thirty-six atoms for the second scattering event to give peak 5*.

An additional peak is noted in the Cu 3*p* ARLP-FT. The peak labeled 1 is due to single-scattering of the photoemitted wave from the six nearest-neighbor atoms in the same (111) plane as the emitting atoms. This scattering path is not observed in the Cu 3*s* FT and has not been observed previously for *s* initial state data or calculations. The photoemitted p_o-wave final state destructively interferes with itself for the scattering angle $\theta_j = 90°$ due to its negative parity. From the *p* initial state, however, the photoemitted *d* and *s* partial waves which are interfering with themselves and with each other have positive parity. Therefore, they do not cancel upon scattering from atoms in the same (111) plane as the emitting atoms. This result has

been seen previously for ARPEFS data collected from the Ni 3*p* core-level of clean Ni(111).[16]

An interesting feature of the Cu 3*s* FT as compared to the Cu 3*p* FT is the intensity differences between some of the peaks. If the ARPEFS data from these different initial states were identical but out of phase, then their FTs would be identical in peak position and intensity. These data are more than simply out of phase as evidenced by the appearance of peak 1 in the Cu 3*p* FT which is not present in the Cu 3*s* FT. A related study of ARPEFS data collected from the sulfur 1*s* and 2*p* initial states for c(2x2)S/Ni(001) found that the generalized Ramsauer-Townsend effect[25] occurs in the S 1*s* data but not the S 2*p* data.[13]

The total photoemitted intensity, $I_{\text{tot}}(\theta,\phi,k)$, was discussed in the introduction. Given that $I_{\text{tot}}(\theta,\phi,k)$ depends on the initial state, the oscillation magnitudes in the respective $\chi(k)$ curves should be somewhat different. These differences translate to the FT as intensity differences between the two initial state ARPEFS data for a given PLD.

From the single-scattering values listed in table 1, one can see that the structure can generally be determined to ±0.5 Å by simply analyzing the ARLP-FT. Given this accuracy limit, some peaks seem to correlate with double-scattering PLDs. However, these assignments due to double-scattering events are somewhat speculative. To be certain that these small features are not artifacts caused by the finite data range, one must study the FT in more detail than has been done to date. Additionally, one must better understand any slight shifting of the peaks caused by mathematically extending the data range using the ARLP method.

B. Multiple Scattering Analysis

It has become standard to perform modeling calculations in an attempt to simulate ARPEFS $\chi(k)$ curves. Using the single-scattering model of ARPEFS,[6,20] $\chi(k)$ can be written as

$$\chi(k) = \sum_j A_j(k) \cos\left[k\left(R_j - R_j \cos\theta_j\right) + \phi_j\right] \tag{4}$$

where $A_j(k)$ contains experimental geometry factors including the photon polarization direction and the electron emission direction as well as the scattering amplitude, aperture integration, and thermal averaging.

A new code developed by Chen, Wu, and Shirley was used for the calculations presented here.[17,26-28] Fitting calculations can be performed for systems in which the photoemitters are in many layers and the core-level initial state has arbitrary angular momentum. For fitting the Cu $3p$ initial state data, the radial dipole matrix elements, $R_{\ell_i \pm 1}$, and phase shifts, $\delta_{\ell_i \pm 1}$, were obtained from Goldberg, Fadley, and Kono[29] who developed them from Manson and Cooper's earlier work.[30] These values describe the shape and phase relationship between the photoemitted partial waves, $\ell_i \pm 1$.

To account for vibration effects of the bulk atoms, the mean square relative displacement was calculated using equation (33) by Sagurton *et al.*[4] The correlated Debye temperature was 350 K and the sample temperature was 80 K for both data sets. Accounting for the surface atomic vibration has been discussed previously.[12,31]

The inelastic mean free path was included using the exponential damping factor $e^{-r/\lambda}$ where λ was calculated using the Tanuma, Powell, and Penn (TPP-2) formula.[32] The analyzer acceptance angle was set to match the

experiment as described earlier. The atomic-scattering phase shifts were calculated in situ by using the atomic potentials tabulated by Moruzzi *et al.*[33] The emission direction was optimized at 5° off-normal and the polarization direction was optimized at 180°, the [111] direction. Optimization of the emission and polarization angles is discussed in the next section.

Figure 4a overlays the experimental Cu 3*s* ARPEFS data (solid line) with its best fit (dashed line). Figure 4b overlays the experimental Cu 3*p* ARPEFS data (solid line) with its best fit (dashed line). For each fit, a 74 atom cluster was used. During the fitting, the distance between the first two copper layers, $d_{1,2}$,was unusually sensitive to the inner potential.[12,16] This resulted in a large uncertainty in the determined structure. Thus, the inner potential was fixed at 10 eV as discussed above. The modeling calculations determined that $d_{1,2}$ = 2.06(5) Å, a contraction from the bulk value, 2.09 Å. This surface layer contraction is consistent with previous LEED studies which found a contraction of 0.7(5)%.[34,35] By contrast, there is a slight surface *expansion* (+1.5%) of the clean Ni(111) surface; $d_{1,2}$ = 2.06(1) Å while the bulk Ni(111) spacing is 2.03 Å.[16]

C. Discussion of Error

Since the purpose of this work is to study final-state effects in ARPEFS, it is useful to minimize the *R*-factor as a function of the emission angle as measured from the surface normal, θ_e, and the azimuthal angle about the surface normal, ϕ_e. These contour plots are illustrated in figures 5a and 5b for the Cu 3*s* and Cu 3*p* fitting calculations, respectively. The sample's orientation with respect to the photon beam, and thus the photon polarization vector, was maintained constant. θ_e was varied from 0° to +10°

stepping by 1° and ϕ_e was varied from 0° to 180° stepping by 10°. The fcc surface has six-fold symmetry but the bulk only has three-fold symmetry; the surface atoms adsorb in the three-fold hollow site. $\phi_e = 0°$ was chosen to bisect one edge of the equilateral triangle formed by this three-fold hollow site, the [100] direction. Thus, a mirror plane exists which allows the calculations to be symmetrized to obtain the results for $\phi_e = 180°$ to 360°.

Comparing figures 5a and 5b shows some very interesting differences between the Cu 3*s* and the Cu 3*p* ARPEFS data. From figure 5a (the Cu 3*s* contour plot), the *R*-factor minimum is at $\theta_e = 4.5° \pm 1°$. It is a very shallow minimum toward normal emission ($\theta_e = 0°$) but becomes steep more off-normal ($\theta_e > 5°$). When visually inspecting the Cu 3*s* fits, $\theta_e = 5°$ fit was marginally better than the $\theta_e = 0°$. Figure 5b (the Cu 3*p* contour plot) is markedly different due to final-state effects. The *R*-factor minimum is at $\theta_e = 5.5° \pm 0.5°$. It is a very steep minimum both toward and away from normal emission ($\theta_e < 5°, \theta_e > 6°$). For the Cu 3*p*, the $\theta_e = 0°$ fit was very poor while the $\theta_e = 5°$ fit was quite good. This result has significant implications with respect to modeling ARPEFS data from non-*s* initial states. As always, great care must be taken during the alignment of the experimental system. Additionally, because the difference of 1° is so important, the modeling must search angle-space to finally obtain the optimum fit to the data.

Studying how the *R*-factor varies with ϕ_e at different θ_e also shows final-state effects. For both the 3*s* and the 3*p* initial states, the *R*-factor is very insensitive to changing ϕ_e if θ_e is near normal emission ($\theta_e < 5°$). Even at the *R*-factor minimum ($\theta_e \approx 5°$), the *R*-factor remains rather insensitive to changing ϕ_e. However, for the 3*p* initial state, the three-fold symmetry of the adsorption site begins to become evident. As θ_e is increased even more ($\theta_e > 5°$), the *R*-factor begins to vary significantly with changing ϕ_e and the

three-fold symmetry of the adsorption site is evident in both contour plots. This results due to backscattering. As the emission angle becomes more off-normal, backscattering from the second-layer Cu atoms is enhanced in the ARPEFS $\chi(k)$ curve.

As stated above, $\phi_e = 0°$ is toward the [100] direction. This geometry would highlight backscattering from the second-layer Cu atom. Since the best fit to the data is for $\phi_e = 180°$ (as well as +120° and -120° from 180°) it can be concluded that during the experiment, the analyzer was ~5° off-normal toward the [111] direction (away from an edge and toward a point of the equilateral triangle formed by the three-fold hollow adsorption site).

These results from θ_e and ϕ_e indicate that the detected intensity distribution of Cu $3s$ photoemission is less directional than the detected intensity distribution of Cu $3p$ photoemission. As discussed previously, photoemission data from atomic s core-level initial states gives a p_o-wave final state. Thus, the intensity distribution from the Cu $3p$ core-level initial states must have mostly d-wave character. This is not necessarily intuitive because examining the radial dipole matrix elements shows that R_{ℓ_i+1} (d partial-wave) is less than a factor of two greater than R_{ℓ_i-1} (s partial-wave) through almost the entire ARPEFS data range.[13,29]

It should be noted that the calculations can be symmetrized as described above because the photon polarization vector is approximately normal to the surface. Experience with fitting ARPEFS data suggests that the oscillation frequencies of the $\chi(k)$ curve are rather insensitive to the photon polarization vector orientation. However, the oscillation amplitudes are dependent on this orientation. These amplitude variations will change the magnitude of the R-factor and perhaps break this three-fold symmetry.

Thus, if the photon polarization vector is significantly off-normal, then ϕ_e should be calculated from 0° to 360°.

V. DISCUSSION

A. Double Scattering Events

Using the best-fit parameters, some test calculations were completed to study the scattering in more detail. To determine whether double-scattering events can be detected in the ARLP-FT, a test cluster was input with a single emitter adsorbed 2.06 Å above a layer of scattering atomic potentials. The distance and geometry were chosen such that the layer simulated the second layer of the fcc Cu(111). In addition to testing for double-scattering, this test allows for the simulation of the intensity differences between the Cu 3*s* and Cu 3*p* FTs in figure 3. Note that the ARLP method was not applied to these test $\chi(k)$ curves because they were calculated directly over a wide *k*-range (4 - 20 $Å^{-1}$).

With this geometry, peaks are expected to be at PLDs correlating with the 2 and 2' positions for single-scattering and the 2, 2', and 2* positions for double-scattering. Figure 6a plots the Cu 3*s* FT for a single-scattering calculation (solid line) and a double-scattering calculation (dashed line). Figure 6b plots the Cu 3*p* FT for a single-scattering calculation (solid line) and a double-scattering calculation (dashed line). The respective $\chi(k)$ curves are plotted in the insets. The $\chi(k)$ curves were filtered to pass only those PLDs > 3.5 Å to remove some low frequency oscillations unrelated to PDLs. The 2* peak distinctly appears in the FT of the Cu 3*p* double-

scattering calculation even though there appear to be only minor differences in the $\chi(k)$ curves. The 2* peak is not as convincing in the Cu 3*s* FT.

A striking difference between the Cu 3*s* and Cu 3*p* FTs is the occurrence of peaks 2" and 2"' in only the Cu 3*s* FT. Each additional prime represents scattering from the next laterally distant atomic potential. This difference is also observed in the ARLP-FT of the ARPEFS data for the peak $\lesssim$7 Å and is the reason for the chosen 2* position in figure 3. These results again indicate that Cu 3*p* photoemission intensity is more directional than the Cu 3*s* photoemission intensity.

B. Contribution of Emitters in Different Layers

For the study of clean surfaces or multilayers, it is important to understand the contribution of emitters in sub-surface layers to the overall ARPEFS data. For these tests, a ten layer fcc Cu(111) cluster was input with a single emitter. This emitter was subsequently moved from the surface to each layer, ending with the sixth. The cluster was constructed such that the photoemitted wave from the emitter in the sixth layer was subject to the same scattering environment as the photoemitted wave from the emitter in the surface layer. This is true to four layers below the emitter which is the cut-off seen in the ARLP-FT of the ARPEFS data.

Figure 7 shows the multiple-scattering calculation results for this test cluster. The calculation parameters were fixed at the best-fit values discussed previously. The normalized intensity at the detector is plotted as a function of the magnitude of the photoelectron wave vector. The first point to note about these results is that the signal from the Cu 3*s* initial state is a factor of 100 stronger than the signal from the Cu 3*p* initial state. This factor

drops out in equation (2) and is thus not seen in the data $\chi(k)$ curves. The next point to note is that the signal drops off drastically between placing the emitter in the second layer and placing the emitter in the third layer. The signal increases slightly when placing the emitter in the fourth layer due to forward focusing by the surface layer atoms.

When the emitter is placed from the third layer to the sixth layer, the high-frequency oscillations important to ARPEFS become small and the $I(k)$ curves become dominated by the low-frequency oscillations (short path-length differences). This indicates that the signal is becoming dominated by forward scattering.

The bottom panel in figure 7 plots $I_{\text{total}}(k)$ which is the sum of the six calculated $I(k)$ curves. This curve simulates the total intensity that would be collected. The low-frequency oscillations are removed by equation (2) when $I(k)$ is divided by a simple polynomial to fit $I_0(k)$. The forward scattering signal is therefore removed during the data reduction along with the standard $I_0(k)$. The resulting experimental ARPEFS $\chi(k)$ curve is thus dominated by backscattering. Although the signal from the deeper layers may modulate the high-frequency oscillation magnitudes slightly, the signal is principally due to photoemission from the first two crystal layers. Scattering from six or seven layers is therefore adequate to simulate ARPEFS data.

VI. CONCLUSION

A Cu(111) single crystal sample was used to study ARPEFS from non-*s* initial states in a controlled manner. Photoemission data were taken from the Cu 3*p* core-levels and subsequently the Cu 3*s* core-level. These

two data sets were similar but ~180° out of phase as expected. The Fourier transform of these clean surface ARPEFS data resemble data for adsorbate systems, showing strong backscattering signals from atoms up to four layers *below* the source atoms. In addition to the backscattering, the FT of the Cu $3p$ data show a peak corresponding to scattering from the six nearest neighbor atoms in the same crystal layer as the emitting atoms. This result is forbidden by symmetry for s initial state photoemission scattering from a point source but is expected from p initial state photoemission. Evidence was also seen for single-scattering events from atoms laterally distant from the emitting atom as well as double-scattering events.

The R-factor was minimized as a function of ϕ_e and θ_e. These contour plots illustrate the directional nature of the Cu $3s$ as compared to the Cu $3p$ photoemission intensity distribution. For the Cu $3s$ fitting, the R-factor minimum is rather shallow from $0° < \theta_e < 5°$. However, at $\theta_e > 5°$, the Cu $3s$ R-factor rises sharply and changing ϕ_e begins to show the three-fold symmetry of the adsorption site. In contrast, the Cu $3p$ R-factor minimum is very steep for $\theta_e < 5°$ and $\theta_e > 6°$. The three-fold symmetry in ϕ_e is not evident until $\theta_e \geq 5°$. These results indicate that the photoemission intensity from the Cu $3p$ core-levels must have mostly d-wave character. Because $\Delta\theta_e = 1°$ has such a dramatic effect on the quality of the fit, the modeling must search angle-space to obtain the optimum fit to the data.

After fitting the data to determine the parameters, two types of test calculations were performed. For the purpose of determining if double-scattering events may be detectable directly in the FT, a cluster was used with a single emitter adsorbed on a layer of scattering potentials. The 2* peak distinctly appears in the FT of the Cu $3p$ double-scattering calculation even though there appear to be only minor differences in the $\chi(k)$ curves.

The 2* peak is not as convincing in the Cu 3*s* FT. The Cu 3*s* FT, however, indicates scattering from atomic potentials much more laterally distant than the Cu 3*p* FT. These results again indicate that Cu 3*p* photoemission intensity is more directional than the Cu 3*s* photoemission intensity.

A second test system used a ten layer cluster for full multiple-scattering calculations. A single emitter was placed in the surface layer; the position of this emitter was subsequently moved to each layer ending with the sixth. The $I(k)$ curves illustrate that the signal from the Cu 3*s* initial state is a factor of 100 stronger than the signal from the Cu 3*p* initial state. The signal drops off drastically when the emitter is placed below the second layer. From the third layer to the sixth layer, the high-frequency oscillations important to ARPEFS become small and the $I(k)$ curves become dominated by the low-frequency oscillations. Although the signal from the deeper layers may modulate the high-frequency oscillation magnitudes slightly, the photoemission signal comes principally from the first two crystal layers. Scattering from six or seven layers is therefore adequate to simulate ARPEFS data.

Calculated and Actual PLDs

Peak Number	Calculated PLD (Å)	Cu 3*s* Position (Å)	Cu 3*p* Position (Å)	Scattering Process	# of Atomic Potentials
1	2.56	---	2.39 (-0.17)	SS	6
2	4.65	4.15 (-0.50)	4.85 (+0.20)	SS	3
2'	5.71	6.19 (+0.48)	6.26 (+0.55)	SS	3
2*	7.21	7.67 (+0.46)	7.58 (+0.37)	DS	3 × 6
3	8.61	8.36 (-0.25)	8.29 (-0.32)	SS	3
3'	9.30	8.91 (-0.39)	9.37 (+0.07)	SS	3
3*	11.17	10.91 (-0.26)	10.97 (-0.20)	DS	3 × 6
4	12.54	12.10 (-0.44)	12.46 (-0.08)	SS	1
5	13.04	13.20 (+0.16)	13.12 (+0.08)	SS	6
4*	15.10	14.96 (-0.14)	15.13 (+0.03)	DS	1 × 6
5*	15.60	15.77 (+0.17)	15.80 (+0.20)	DS	6 × 6
6	16.85	16.68 (-0.17)	16.99 (+0.14)	SS	3

Scattering paths with the calculated PLD (based on 2.56 Å nearest neighbor spacing) along with the actual peak positions and the respective shifts. Refer to figure 3 for an illustration of the atomic positions.

Table 1

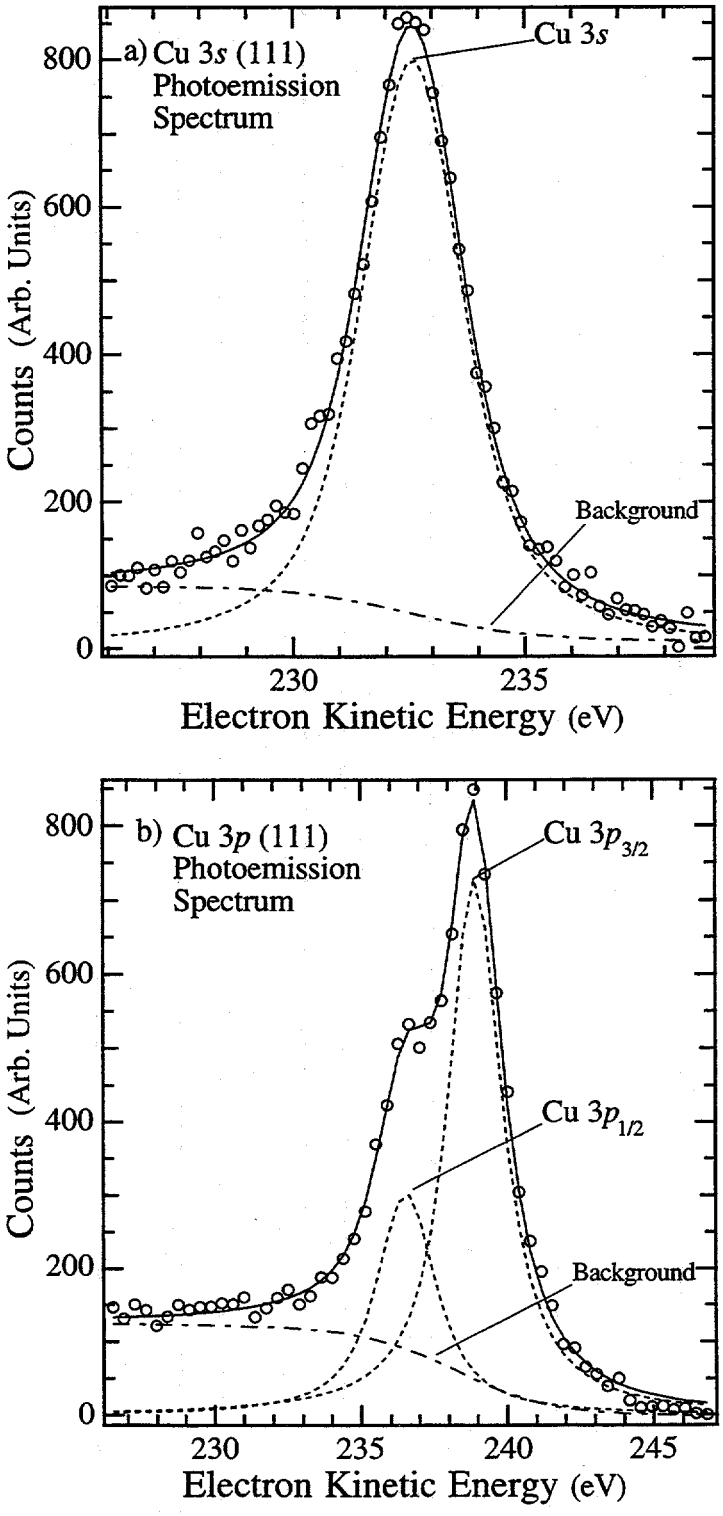

Example photoemission spectrum showing the data as well as the Voigt function(s) and the step function used to fit the a) Cu 3*s* data and b) the Cu 3*p* data.

Figures 1a and 1b

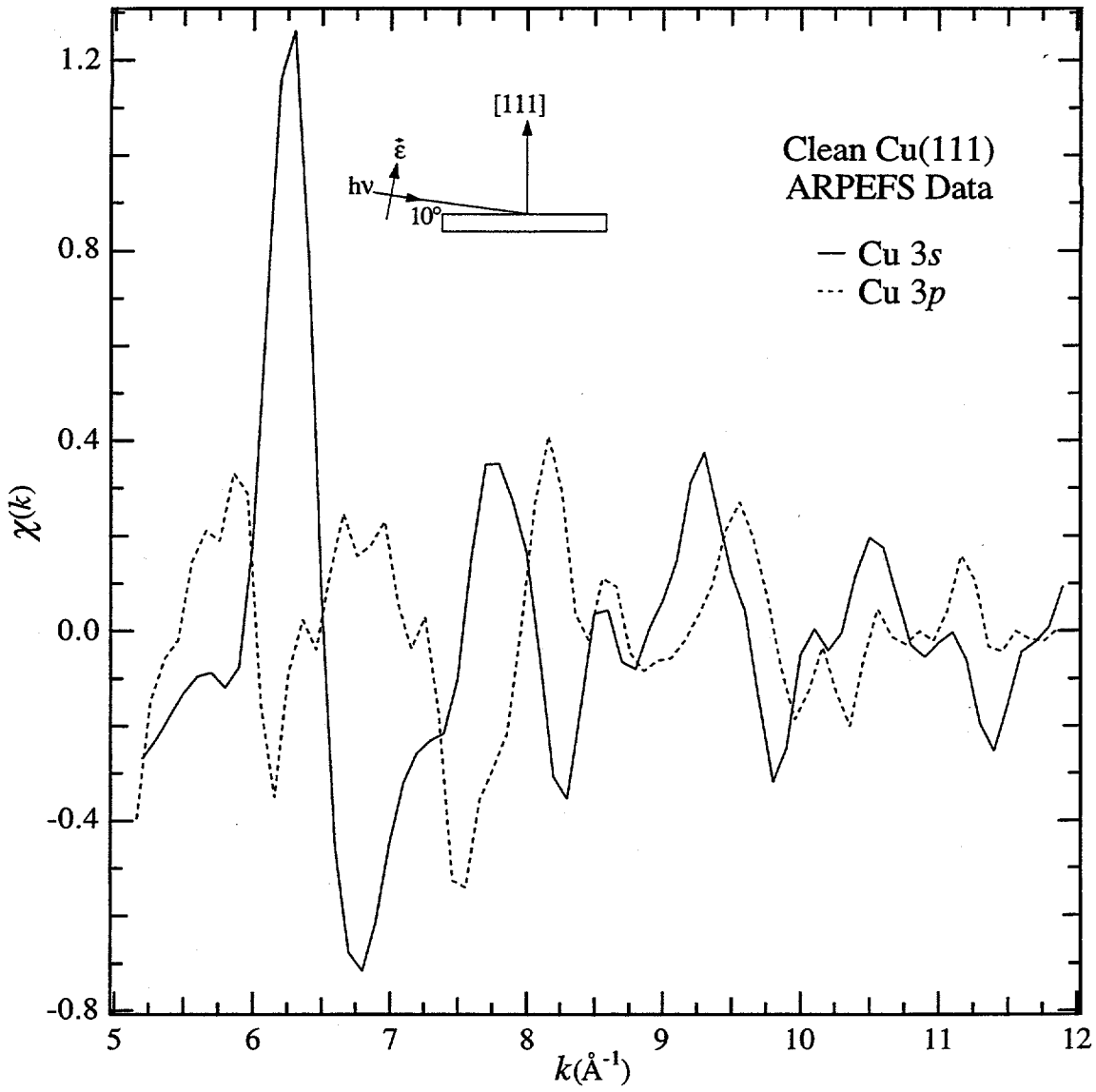

Cu(111) 3*s* ARPEFS data (solid line) and Cu(111) 3*p* ARPEFS data (dashed line). A schematic of the experimental geometry is shown.

Figure 2

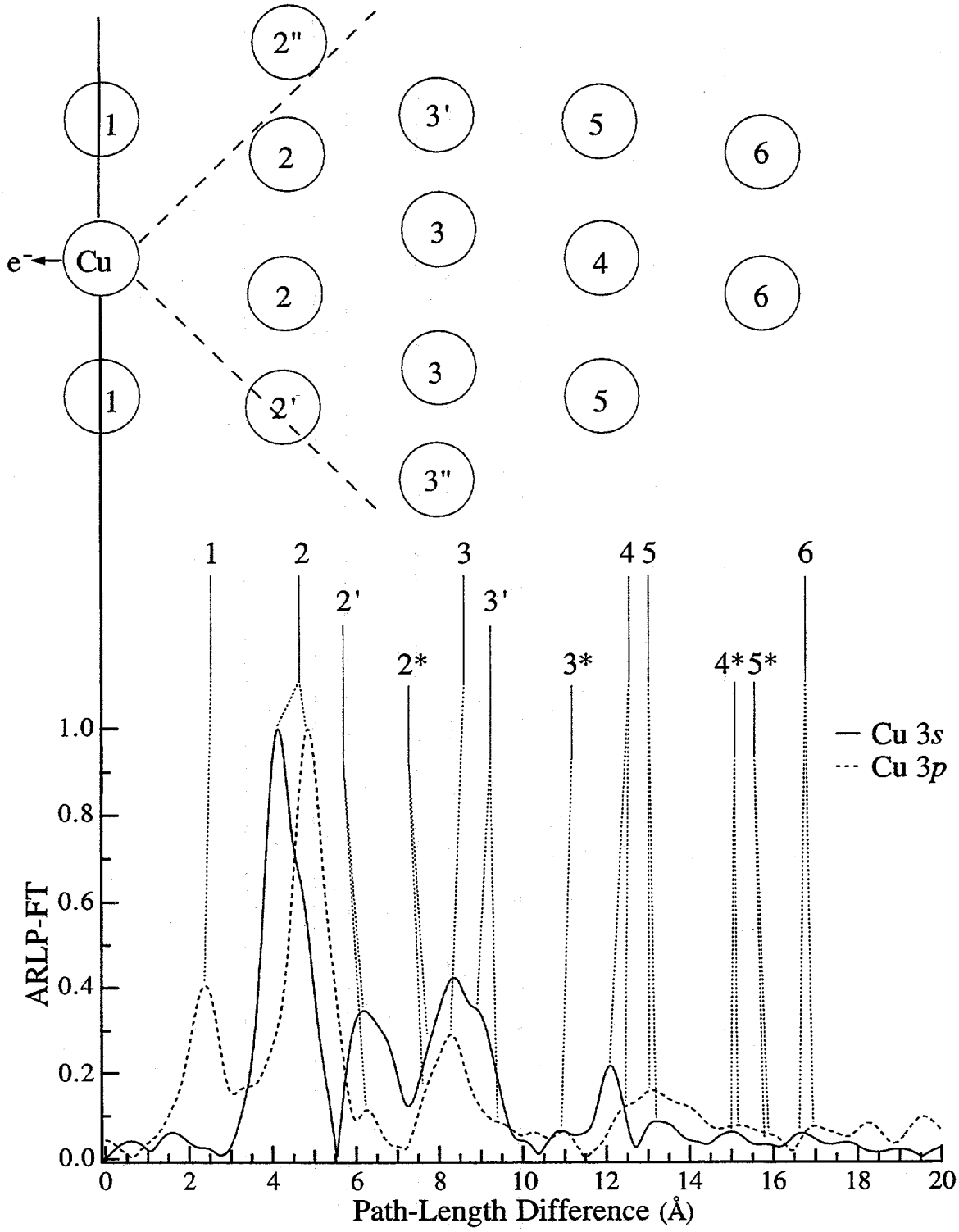

ARLP based FTs of the Cu 3*s* data (solid line) and Cu 3*p* data (dashed line). A model of the lattice with the backscattering cone indicates the scattering atoms corresponding to the FT peaks.

Figure 3

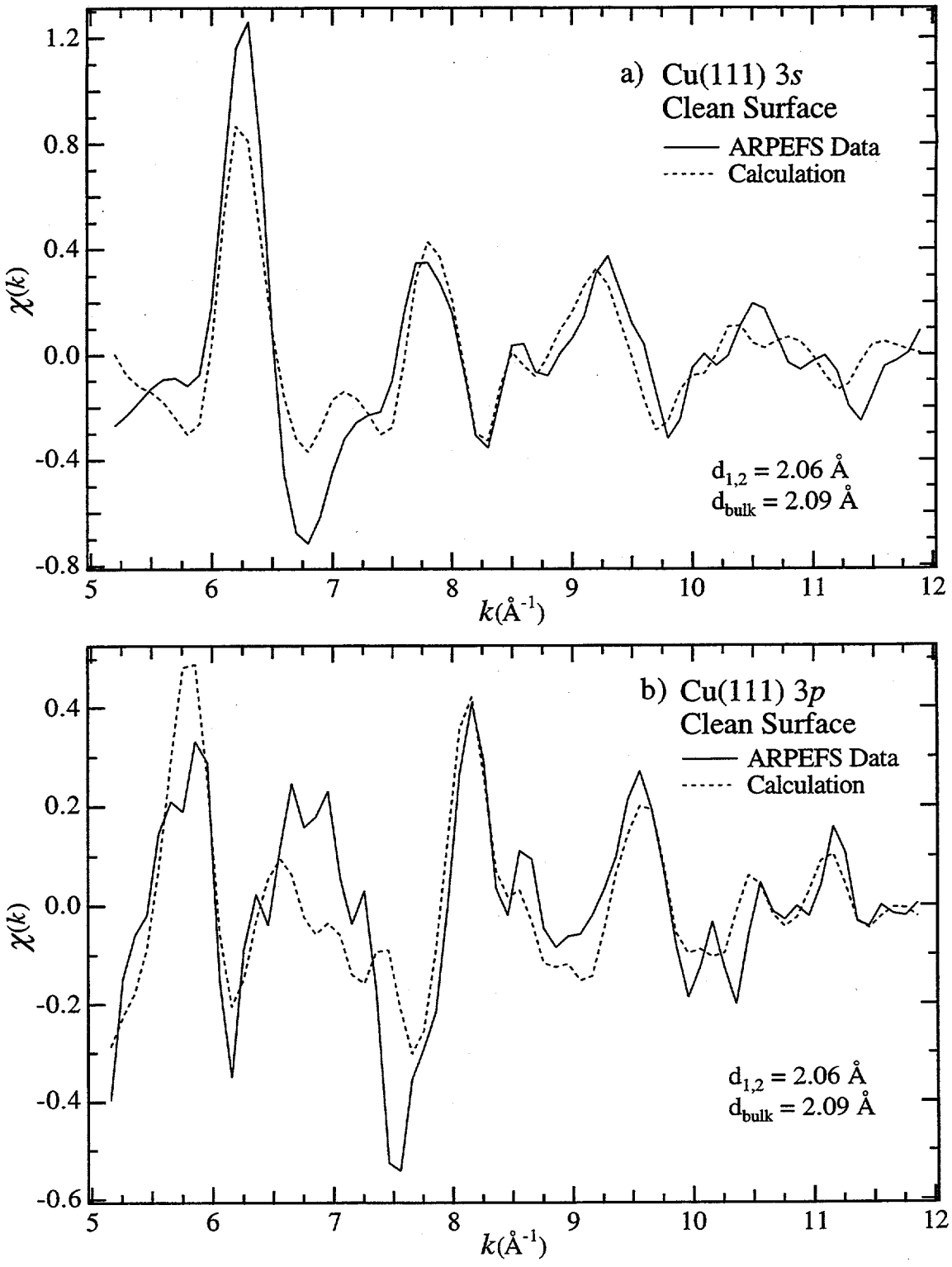

ARPEFS data (solid line) and the MSSW best fit (dashed line) for a) Cu(111) 3*s* and b) Cu(111) 3*p*.

Figures 4a and 4b

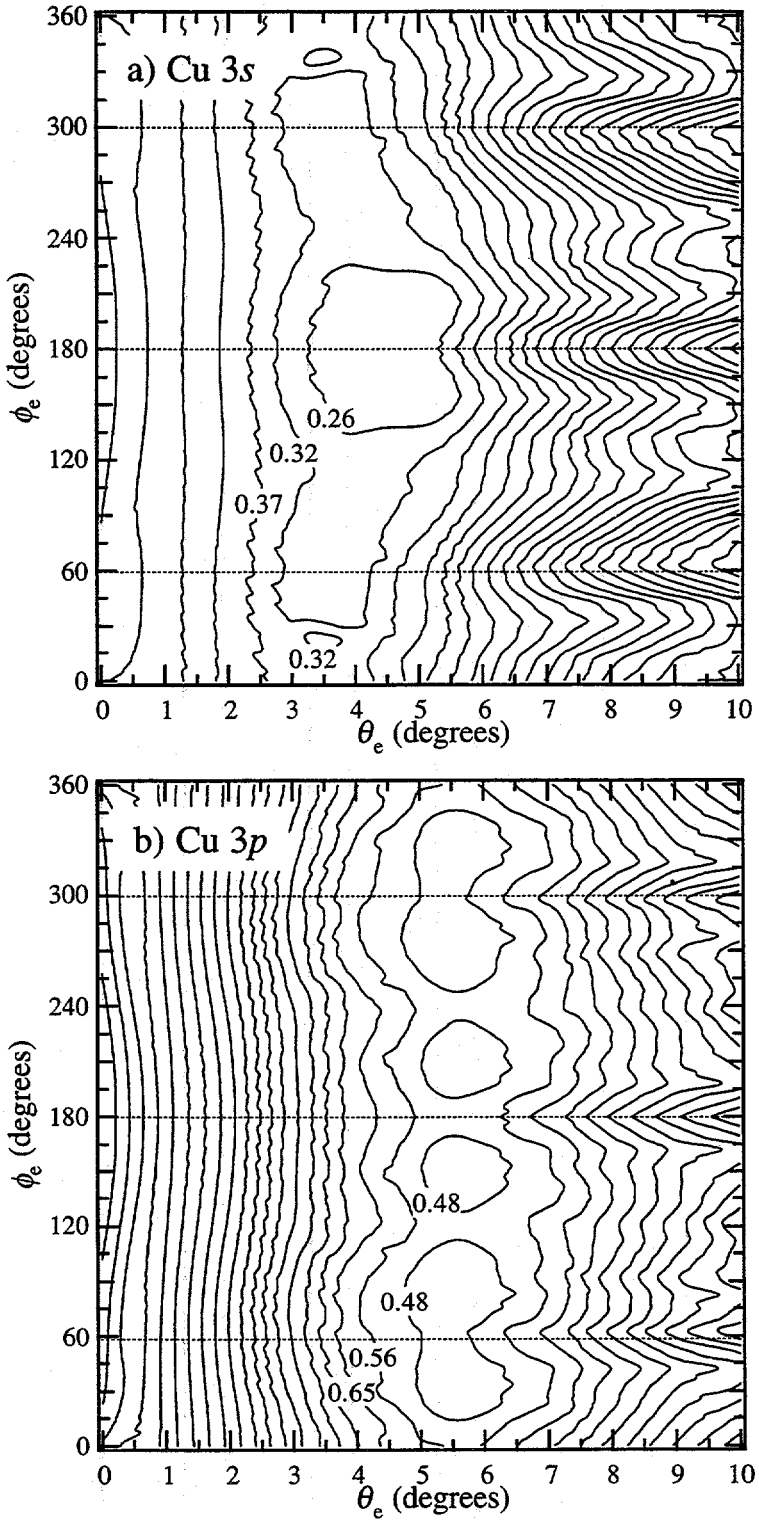

a) Contour plot showing how the *R*-factor varies with ϕ_e and θ_e for a) the Cu 3*s* modeling and b) the Cu 3*p* modeling.

Figures 5a and 5b

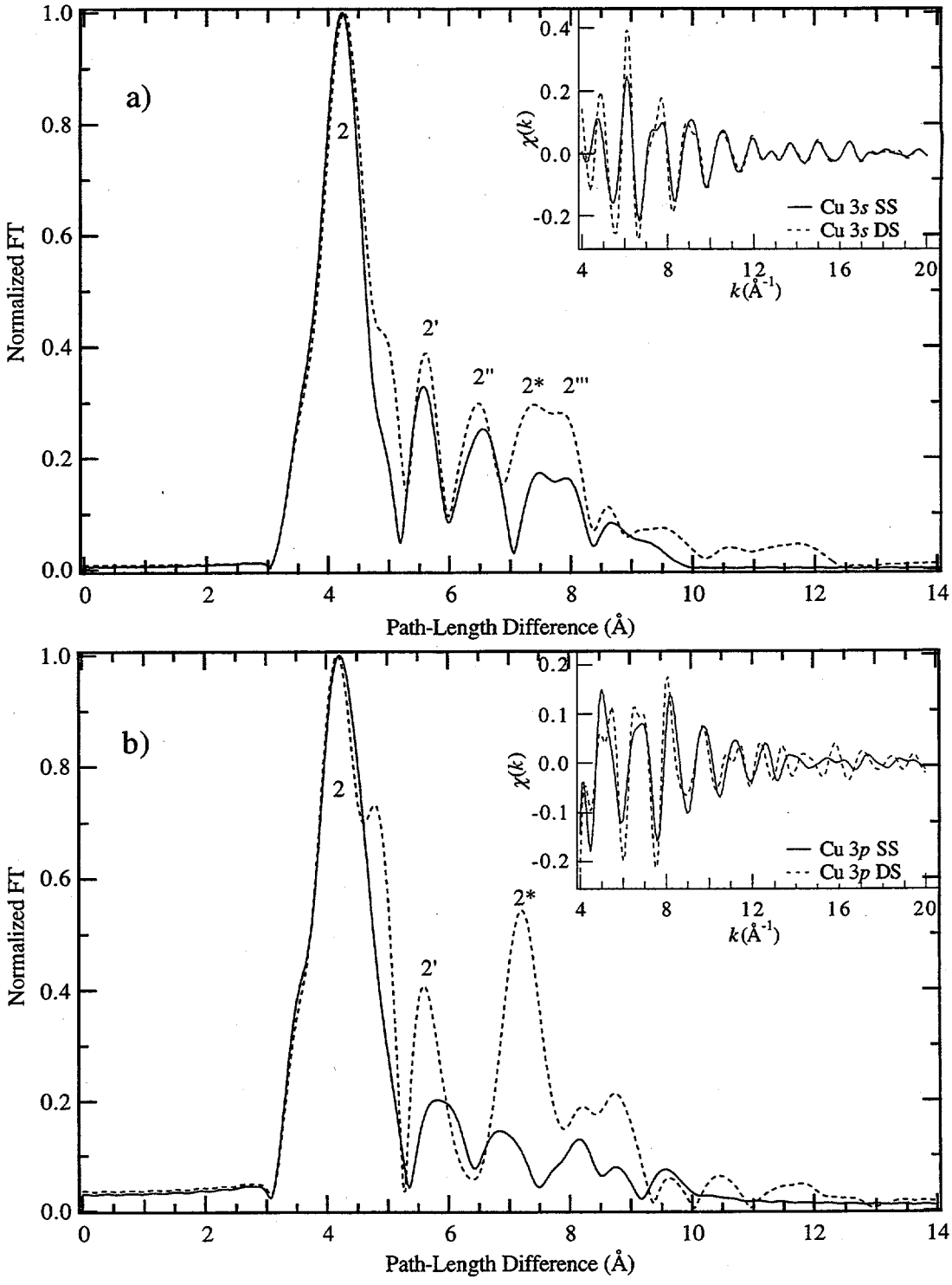

FT of the calculated ARPEFS $\chi(k)$ curves (insets) for a) Cu 3*s* and b) Cu 3*p* where a single emitter was adsorbed 2.06 Å above a layer of scattering potentials for single-scattering (solid line) and double-scattering (dashed line).

Figures 6a and 6b

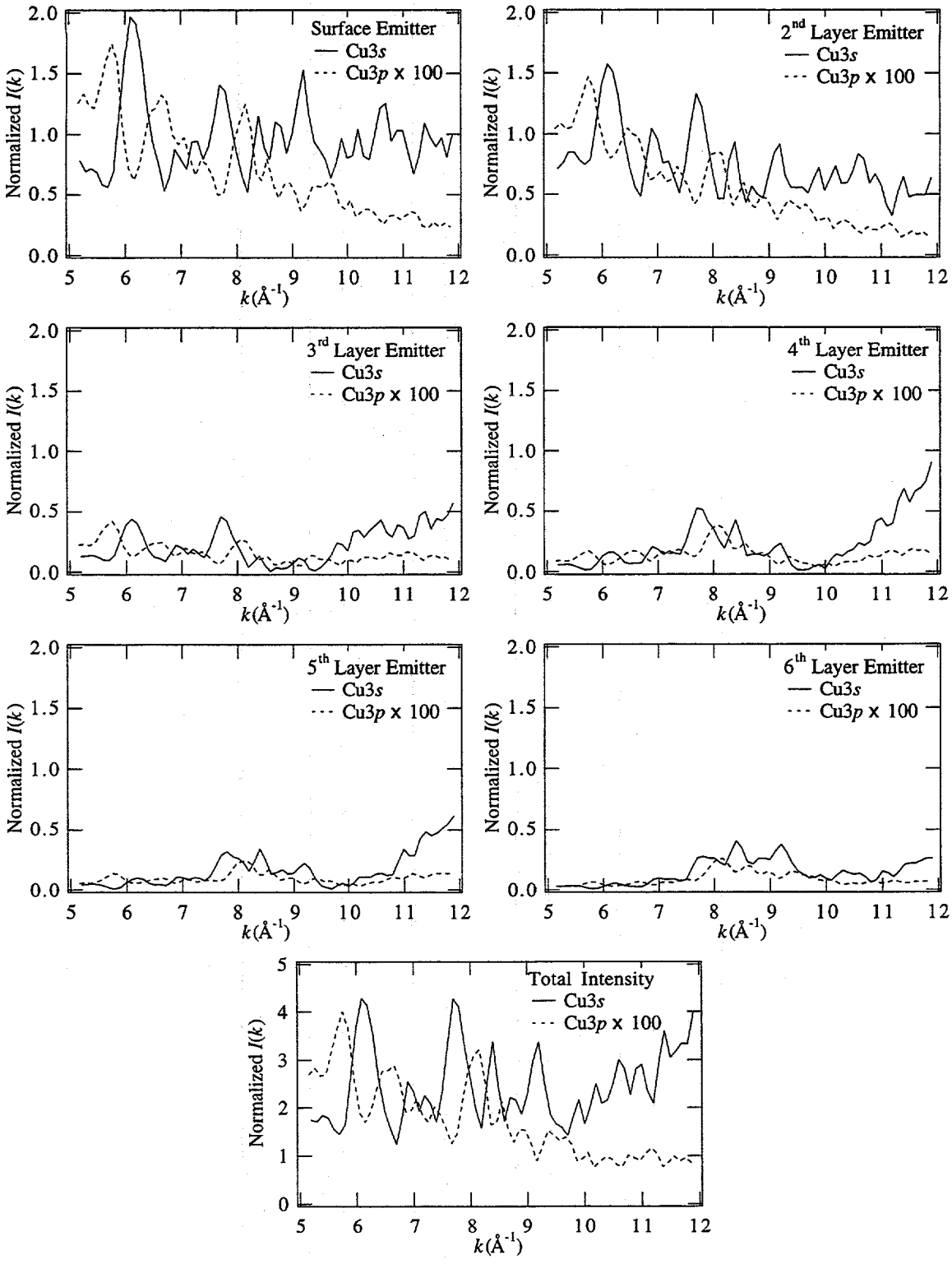

The calculated ARPEFS $I(k)$ curves for Cu 3*s* (solid line) and Cu 3*p* (dashed line) where a single emitter was moved successively to deeper layers.

Figure 7

REFERENCES

[1]S.D. Kevan, D.H. Rosenblatt, D. Denley, B.C. Lu and D.A. Shirley, Phys. Rev. Lett. **41**, 1565(1978).

[2]J.J. Barton, C.C. Bahr, Z. Hussain, S.W. Robey, J.G. Tobin, L.E. Klebanoff and D.A. Shirley, Phys. Rev. Lett. **51**, 272(1983).

[3]D.P. Woodruff, D. Norman, B.W. Holland, N.V. Smith, H.H. Farrell and M.M. Traum, Phys. Rev. Lett. **41**, 1130(1978).

[4]M. Sagurton, E.L. Bullock and C.S. Fadley, Surf. Sci. **182**, 287(1987).

[5]Y. Zheng and D.A. Shirley, Chem. Phys. Lett. **203**, 114(1993).

[6]J.J. Barton, C.C. Bahr, S.W. Robey, Z. Hussain, E. Umbach and D.A. Shirley, Phys. Rev. B **34**, 3807(1986).

[7]S.W. Robey, C.C. Bahr, Z. Hussain, J.J. Barton, K.T. Leung, J.R. Lou, A.E. Schach von Wittenau and D.A. Shirley, Phys. Rev. B **35**, 5657(1987).

[8]L.Q. Wang, A.E. Schach von Wittenau, Z.G. Ji, L.S. Wang, Z.Q. Huang and D.A. Shirley, Phys. Rev. B **44**, 1292(1991).

[9]Z.Q. Huang, L.Q. Wang, A.E. Schach von Wittenau, Z. Hussain and D.A. Shirley, Phys. Rev. B **47**, 13626(1993).

[10]Z.Q. Huang, Z. Hussain, W.T. Huff, E.J. Moler and D.A. Shirley, Phys. Rev. B **48**, 1696(1993).

[11]Y. Zheng, E. Moler, E. Hudson, Z. Hussain and D.A. Shirley, Phys. Rev. B **48**, 4960(1993).

[12]W.R.A. Huff, Y. Chen, X.S. Zhang, L.J. Terminello, F.M. Tao, Y.K. Pan, S.A. Kellar, E.J. Moler, Z. Hussain, H. Wu, Y. Zheng, X. Zhou, A.E. Schach von Wittenau, S. Kim, Z.Q. Huang, Z.Z. Yang and D.A. Shirley, (to be published).

[13]W.R.A. Huff, Y. Zheng, Z. Hussain and D.A. Shirley, J. Phys. Chem. **98**, 9182(1994).

[14]S.Y. Tong and J.C. Tang, Phys. Rev. B **25**, 6526(1982).

[15]J.C. Tang, Chin. Phys. Lett. **4**, 321(1987).

[16]Chapter 4 of this dissertation.

[17]M. Biagini, Phys. Rev. B **48**, 2974(1993).

[18]Chapter 1 of this dissertation.

[19]S.D. Kevan, *Ph.D. Thesis*, The University of California, Berkeley, LBL-11017(1980).

[20]J.J. Barton, S.W. Robey and D.A. Shirley, Phys. Rev. B **34**, 778(1986).

[21]J.J. Barton, *Ph.D. Thesis*, The University of California, Berkeley, LBL-19215(1985).

[22]L.J. Terminello, *Private Communication*, (1996).

[23]R.C. Weast, *Handbook of Chemistry and Physics*, 67th ed., (CRC Press, Boca Raton, FL, 1986-1987).

[24]P. Thiry, *PhD Thesis*, L'Université Pierre et Marie Curie, Paris, France, (1980).

[25]J.J. Barton, Z. Hussain and D.A. Shirley, Phys. Rev. B **35**, 933(1987).

[26]Y. Chen, H. Wu and D.A. Shirley, *CWMS Code - Unpublished*, (1995).

[27]J.J. Rehr and R.C. Albers, Phys. Rev. B **41**, 8139(1990).

[28]D.J. Friedman and C.S. Fadley, J. Electron Spectrosc. Relat. Phenom. **51**, 689(1990).

[29]S.M. Goldberg, C.S. Fadley and S. Kono, J. Electron Spectrosc. Relat. Phenom. **21**, 285(1981).

[30]S.T. Manson and J.W. Cooper, Phys. Rev. **165**, 126(1968).

[31]R.E. Allen, G.P. Alldredge and F.W. de Wette, J. Chem. Phys. **54**, 2605(1971).

[32]S. Tanuma, C.J. Powell and D.R. Penn, Surf. Interface Anal. **20**, 77(1993).

[33]V.L. Moruzzi, J.F. Janak and A.R. Williams, *Calculated Electronic Properties of Metals*, (Pergamon Press, Inc., New York, 1978).

[34]S.P. Tear, K. Roll and M. Prutton, J. Phys. C **14**, 3297(1981).

[35]S.A. Lindgren, L. Wallden, J. Rundgren and P. Westrin, Phys. Rev. B **29**, 576(1984).

Chapter 6

Conclusion

The following is a global conclusion to this dissertation. The purpose here is two-fold. An attempt is made to summarize thoughts about the beamline and about angle-resolved photoemission extended fine structure. Additionally, some suggestions for the future are included and some important points are re-iterated.

I. BEAMLINE 9.3.2

Bending magnet beamline 9.3.2 at the Advanced Light Source (ALS) was designed for high resolution spectroscopy with the capability for delivering circularly polarized light as discussed in chapter 1. BL 9.3.2 was originally installed at the Stanford Synchrotron Radiation Laboratory as a prototype for spherical grating monochromators (SGMs) at the ALS.

The circular polarization aperture has worked as designed and has yielded reproducible results. In the future, this aperture will be modified with a "chopper" to allow for rapid switching between left and right circularly polarized radiation. Although only left or only right circular polarized light will be incident on the sample at any given moment, this chopper will allow a spectrum from each to be acquired simultaneously.

The piezoelectric drive controlling the vertically deflecting/focusing mirror pitch has proven necessary to maintain a stable photon beam flux at the endstation. The feedback loop works reliably for entrance slit widths ≤ 100 μm due to the small vertical divergence of the photon beam.

In chapter 1, it was shown that the true focal point of the vertically focusing mirror, M2, could be determined by scanning the M2 pitch at different entrance slit positions. If the entrance slit had not been translatable, this experimental maximization of the flux could only be accomplished by changing the angle of incidence and the elevation of M2.

Both the entrance and exit slits on BL 9.3.2 are translatable along the photon beam path. Experience suggests that for most applications it is sufficient to maintain a fixed entrance slit while translating only the exit slit. Some of the newer SGMs at the ALS have incorporated this idea by building the monochromator with a fixed entrance slit.

To obtain the highest possible resolution, however, the Rowland circle condition must be satisfied for all photon energies used in a given experiment (Chapter 1, Appendix C). Satisfying the Rowland circle condition at more than a single photon energy requires that both the entrance and exit slits be translatable. If a beamline is being developed for the purpose of high-resolution studies, then the entrance slit should not be fixed. Although some money may be saved by designing a fixed entrance slit, this savings is minor when compared to the total cost of a high-resolution beamline. Additionally, the money value is offset by the scientific value of being able to do high resolution spectroscopy.

Higher orders of diffraction from the grating can be useful in some experiments and detrimental in other experiments. Some possibilities exist for removing the higher orders when desirable:

i) A removable filter could be installed which would be transparent to first order diffraction and opaque to higher photon energies. However, these filters must be the form of thin films which are extremely delicate and subject to failure.

ii) A gas phase filter shown to work well on BL 9.0.2 could be installed. Unfortunately, the pumping requirements and equipment safety considerations are quite expensive.

iii) Removable mirrors could be installed to supply additional photon beam reflections. The reflection angle could be adjusted to filter the higher photon energies. It would be crucial that the photon beam was incident on the refocusing mirror in the same geometry with or without the additional reflections. Such a configuration has been designed by Jim Underwood in the Center for X-Ray Optics.

A piezoelectric drive bending control could be attached to the refocusing mirror, M3. The sagittal radius is fixed by the horizontal focal position of the horizontally deflecting mirror, M1. The exit slit is an aperture defining the vertical source for M3. Because the exit slit is translatable, a fixed M3 tangential radius will cause the M3 vertical focal point to translate. With a fixed sample position, the result is that the beamsize changes with changing photon energy (when the exit slit translates). A piezoelectric drive controlling the M3 tangential radius could be calibrated to the exit slit position. Using such a system, the beamsize at the sample position would be constant for any given energy.

The rotating platform endstation has been a grand success. It has allowed the beam to be used to optimum efficiency by reducing the down time to almost zero due to endstation problems. If one group is having difficulty with their equipment, then the beam is used by the other group. The rotating platform has also allows for mid-week sharing of the synchrotron beam.

Much experience was gained for all those involved during the BL 9.3.2 construction. It is now known that the proper itinerary for building a beamline is:

i) One should first design the mirrors, gratings, and the beamline geometry.

ii) One should then buy the mirrors, gratings, and their respective vacuum tanks with the appropriate specifications.

iii) When the mirrors and gratings are delivered, one should measure the *true* specifications, as compared to what was expected.

iv) After the true optical parameters are known, the vacuum tanks should be positioned on the experimental floor according to these values.

v) Finally, one connects the remaining vacuum hardware.

II. ENERGY-SCANNED PHOTOELECTRON DIFFRACTION

Angle-resolved photoemission extended fine-structure (ARPEFS) is energy-scanned photoelectron diffraction (as compared to angle-scanned photoelectron diffraction). By acquiring diffraction curves from a few angles for a given sample, ARPEFS has been used to determine the structures of metal and non-metal atomic adsorbate systems as well as molecular adsorbates on conducting single crystal surfaces. ARPEFS yields accurate information about both the local structure around the adsorbates and the adsorbate-induced relaxation of the substrates. The chemical specificity of photoelectron diffraction greatly enhances the utility of ARPEFS.

ARPEFS probes the short-range order of a surface. Large, ordered domains are not necessary for the successful application of ARPEFS. One could envision applying ARPEFS to a sample for which a low-energy electron diffraction (LEED) pattern was unattainable. However, one should

be reasonably certain that the surface atoms were locally well-ordered. For example, if a scanning-tunneling microscopy image indicated that all adsorbate atoms bond to the same adsorption site, then ARPEFS would be a good technique to employ, even if the overall adsorbate structure was disordered.

Conversely, if the overall surface structure is well ordered, but the local geometry of each adsorbate atom is not well defined, then ARPEFS is not a useful technique for that system. For example, an incommensurate overlayer is often well ordered, but each atom is in a slightly different adsorption site. For such a sample, the detected ARPEFS signal would be the sum of the signals from each atom. Such a system does not lend itself to a unique structure determination using ARPEFS.

The analysis of the ARPEFS $\chi(k)$ diffraction curves is two-fold as discussed in chapters 2, 3, 4, and 5. The auto-regressive linear prediction based Fourier transform (ARLP-FT) is used to determine a starting point for the subsequent multiple-scattering spherical-wave (MSSW) modeling calculations. The extension of the data range using the ARLP theory is very important to the utility of the FT. Without the ARLP, the FT resolution is sufficiently poor that the FT analysis does not yield conclusive results for a starting point.

The importance of theoretically modeling the experimental data using MSSW calculations cannot be over-stated. Using the modeling code discussed in chapters 2, 4, and 5, ARPEFS data from an arbitrary initial state can be modeled quickly and accurately. Alone, a diffraction curve has little utility. The ARLP-FT of the diffraction curve can be used to determine the adsorption site as well as to determine the bond lengths to ~±0.1 Å. To fully exploit the power of ARPEFS, however, the data must be modeled

theoretically. Careful analysis and good fitting can determine the surface structure to ~±0.01 Å.

Past ARPEFS studies measured the photoemission intensity from *s* atomic core-level initial states. Non-*s* initial state photoemission was studied in this dissertation. It was determined that non-*s* initial state ARPEFS data can be used to determine surface structures. One must be aware that some Fourier transform peak intensities may differ from *s* initial state ARPEFS data. Additionally, the appropriate theory must be used when modeling the data.

The main contributing factors to the precision of ARPEFS are the inner potential, the photoemission angle, the sample temperature, the Debye temperature and the quality of the single crystal. The crystal quality can be checked using Laue backscattering; it is roughly included in the scattering code discussed in chapters 2, 4, and 5 via an optional normalization factor. The oscillation magnitudes in the $\chi(k)$ curve are dampened for ARPEFS data acquired from a substrate which is slightly polycrystalline. A similar dampening is seen in the modeling calculations if the sample temperature is raised or if the Debye temperature is lowered. These three effects are thus coupled. An effort should be made to start with a high-quality crystal. If the sample temperature is known to within ~±20 K, then the Debye temperature is well-defined; the calculations use the ratio of the two.

The photoemission angle can be measured using laser alignment. During this process, the viewports on the chamber are used for reference. Thus, the angles between these viewports should be known to ±1°. For higher precision alignment and to account for the analyzer lens and hemispheres, one should also use photoelectron diffraction from the substrate (Kikuchi band).

The photoemission angle can be allowed to float during the fitting as discussed in chapter 5. This method can be used to define the polar angle to ±1°, especially for non-*s* initial state photoemission. The polar angle is the angle between the surface normal and the analyzer. However, depending on the sample's orientation with respect to the photon polarization vector, fitting may not define the azimuthal angle.

The oscillation frequency of the $\chi(k)$ curve is most sensitive to changes in the inner potential and changes in the surface structure as discussed in chapters 2 and 4. Thus, a more precise estimate of the inner potential means a more precise determination of the surface structure. For c(2x2)P/Fe(100) discussed in chapter 2, determining the inner potential to less than ±1 eV allowed the surface structure to be determined to ±0.02 Å. However, with a similar inner potential precision for the clean Cu(111) discussed in chapter 5, the surface structure precision was ~±0.05 Å. The c(2x2)P/Fe(100) ARPEFS data was collected from two photoemission directions but the clean Cu(111) ARPEFS data was collected from only one photoemission direction. For clean Ni(111) discussed in chapter 4, ARPEFS data was collected from only one photoemission direction and yet the surface structure was determined to ±0.01 Å. This high precision was reached because the structure was very insensitive to the value of the inner potential.

By acquiring ARPEFS data along multiple photoemission directions, the surface structure can be unambiguously defined to very high precision, ~±0.01 Å. The number of different photoemission directions required for a given sample is a valid point to consider. Typically, the sensitivity of the calculated surface structure to the inner potential is not known prior to the experiment. One emission direction is insufficient for an unambiguous and

precise structure determination. Experience modeling ARPEFS data suggests that three different, high-symmetry photoemission directions may be sufficient; an additional three photoemission directions 10° from the high-symmetry directions should certainly be sufficient.

Methods exist for acquiring ARPEFS data very quickly from as many as 200-500 directions. Such k, θ, ϕ data sets contain much information which is useful to study the physics of photoelectron diffraction and photoelectron holography. However, if the purpose of the experiment is to simply determine the surface structure, then such data contains much more information than is required.